



The University of
Nottingham

UNITED KINGDOM CHINA MALAYSIA

Faculty of Engineering

Department of Mechanical, Materials and Manufacturing Engineering

**Experimental and Finite Element Studies of
Creep and Creep Crack Growth in
P91 and P92 Weldments**

Mohammed Saber, BSc.

Thesis submitted to the University of Nottingham
for the degree of Doctor of Philosophy

September 2011

For my wife

ABSTRACT

P91 and P92 steels are two ASTM grades of steel which have been used in high temperature applications, such as fossil-fuelled power stations, nuclear power stations and chemical plants. Operating under creep conditions, i.e. high temperature and/or high stress, the welds made from these steels are potential failure locations and, therefore, life limiting for the entire plant. In this thesis, the results of creep and creep crack growth (CCG) tests, which were carried out on P91 and P92 welds, are reported. These tests were carried out on welds constituents, i.e. parent materials (PM) and weld metal (WM), and across-welds, for the P91 material at 650°C and for the P92 material at 675°C. For the cross-weld tests, interest was focused on the Type IV region, a narrow zone at one end of the heat affected zone (HAZ) at the side of the PM. Also reported, in this thesis, are the results of the Finite Element analyses for predicting the creep and creep crack growth in the P91 and P92 materials.

For the P91 material, CCG tests were carried out on PM and cross-weld CT specimens, at 650°C. The results of the CCG tests for P91 show that the CCG rates for the cross-weld CT specimens are about ten times higher than those for the PM specimens. For P92, uniaxial and notched bar creep tests were carried out on the PM and WM, at 675°C. Cross-weld uniaxial, notched bar and waisted specimens were also tested in order to characterise the creep behaviour of the P92 HAZ material. Impression creep tests were also carried out on the P92 HAZ material. The results of the CCG tests for P92 show that the CCG rates for the cross-weld CT specimens are about two times higher than these for the PM CT specimens.

The fracture mechanics parameter, C^* , was used to correlate the CCG rates in the P91 and P92 CT specimens. The load line displacement rates and the CCG data, for the CT specimens, were used to calculate C^* values according to ASTM

E 1457-00 (2001). The Reference Stress was also found to correlate the CCG rates in the P91 CT specimens. Further, FE analyses were carried out to obtain the values of C^* , based on the steady state value of the contour integral $C(t)$. Stationary crack and growing crack CT models were used to obtain the C^* values.

Damage mechanics theory and equations were used to predict the creep and CCG for the P91 and P92 materials using the commercial FE package, ABAQUS. Both the Kachanov and the Liu and Murakami damage models were used. In order to use these models, material properties have to be determined. The results of creep and creep rupture tests were used to determine those properties. It was found that both damage models could be used to predict the creep behaviour of the tested materials. However, the Liu and Murakami model was favoured over the Kachanov model in predicting the CCG in the CT specimens. The effect of the material multiaxiality is also highlighted.

LIST OF PUBLICATIONS:

Journal articles:

- 1 - Hyde, T. H., **Saber, M.** and Sun, W. (2010) Testing and Modelling of Creep Crack Growth in Compact Tension Specimens from a P91 Weld at 650°C. *Engineering Fracture Mechanics*, 77, 2946-2957.
- 2 - Hyde, T. H., **Saber, M.** and Sun, W. (2010) Creep Crack Growth Data and Prediction for a P91 weld at 650°C. *International Journal of Pressure Vessels and Piping*, 87, 721-729.
- 3 - Hyde, T. H., Li, R., Sun, W. and **Saber, M.** (2010) A simplified Method for Predicting the Creep Crack Growth in P91 Welds at 650°C. *Proceedings of the Institution of Mechanical Engineers, Part L: Journal of Materials: Design and Applications*, 224, 208-219.
- 4 - **M. Saber**, D. W. J. Tanner, T. H. Hyde and W. Sun (2011) Determination of Creep and Damage Properties for P92 at 675°C. *The Journal of Strain Analysis for Engineering Design*. (**Accepted**)

Conferences proceedings:

- 1 - Hyde, T. H., **Saber, M.** and Sun, W. (2009) Creep Crack Growth in a P91 Weld at 650°C. *WELDS 2009*. Sanibel Harbour Resort and Spa, Fort Myers, Florida, USA.
- 2 - W. Sun, C. J. Hyde, T. H. Hyde, A. A. Becker, R. Li and **M. Saber** (2011) Finite Element Analysis of Creep Crack Growth for Compact Tension and Thumbnail Crack Specimens. *Proceedings of ICAPP 2011*, Nice, France, May 2-5, 2011, Paper 11262.

In preparation:

- 1 - **M. Saber**, D. W. J. Tanner, K. Chalk, W. Sun and T. H. Hyde, Creep and Creep Crack Growth of a P92 Weld at 675°C.

ACKNOWLEDGEMENTS

I would like to thank my supervisors, Prof. T. H. Hyde and Dr. Wei Sun, for their endless support and help. Also, great thanks for their sympathy and patience and for encouraging me throughout my study. Socially, they keep asking about my family, especially during the hard time the Egyptians lived early this year (Jan. 2011). Therefore, big thanks are due to them. I would also like to thank Professor Adib Becker for his help, support, guidance and valuable comments.

Thanks are also due to all my friends and colleagues in the Structural Integrity and Dynamics (SID) group, the Department of Mechanical Engineering, The University of Nottingham. Great and special thanks are given to Dr. Anas Yaghi and Dr. David Tanner for their help and support and for providing me with needed data.

Great thanks are offered to Mr. Brian Webster, retired-senior Creep Laboratory technician, and to Mr. Shane Maskill, the active Creep Laboratory technician, for their assistance in the experimental part of my work.

Great thanks are also due to the Egyptian government for offering me this chance to study abroad and for its financial and social support during all my study. I would like to acknowledge the financial and technical support of the SuperGen programme partners and of The University of Nottingham.

In remembrance of my dad, I would like to appreciate all of what he did for the family; his seriousness is still inspiring all of the family members.

Finally yet most importantly, I would like thank my wife, without her love, help, patience and support, it would be difficult to finish this work. My love is to my two kids, Amira and Sara. Great thanks are due to my mother, my brothers and my sisters and to all of my friends back home.

NOMENCLATURE

\dot{V}_c	Creep component of load line displacement rate for compact tension specimens in creep crack growth tests
\dot{V}_p	Plastic component of load line displacement rate
\dot{V}_t	Total load line displacement rate for compact tension specimens in creep crack growth tests
$\dot{\epsilon}_{ave}$	Average creep strain rate
$\dot{\epsilon}_{eq}$	Equivalent creep strain rate
$\dot{\epsilon}_{ij}$	Creep strain rate tensor
$\dot{\epsilon}_{min}$	Minimum creep strain rate
S_{ij}	Deviatoric stress tensor
\dot{V}	Load line displacement rate for compact tension specimens in creep crack growth tests
\dot{a}	Creep crack growth rate
ϵ_p	Plastic strain
σ_{eq}	Equivalent, von Mises, stress
$\Delta\epsilon^c$	Creep strain increment
A	Material constant in Norton's creep law, Kachanov creep damage model, and Liu and Murakami creep damage model
a	Crack length
A'	Material constant in Norton creep model for average strain rate
B	Material constant in Kachanov creep damage model or full thickness of compact tension specimens
B _N	Net thickness of compact tension specimens
C	Material constant in Monkman-Grant relationship
C(t)	Contour integral characterising stresses and strains at the crack tip in creeping cracked bodies
C*	Fracture mechanics parameter used to correlate creep crack growth rates creeping cracked bodies
D	Material constants in the relationship $\dot{a} = D(C^*)^q$
D ₁	Material constant in Ramberg-Osgood relationship
D_i	Inner diameter
D_o	Outer diameter
E	Modulus of elasticity
J	J contour integral
K	Stress intensity factor
M	Material constant in both Kachanov, and Liu and Murakami creep damage models; $M = B(1+\phi)$
n	Material constant in Norton's creep law, Kachanov creep damage model, and Liu and Murakami creep damage model
n'	Material constant in Norton creep model for average strain rate
P	Applied load to compact tension specimens
P_i	Internal pressure

P_L	Limiting load
q	Material constant in the relationship $\dot{a} = D(C^*)^q$
Q	Mismatch factor of heterogamous compact tension specimens
q_2	Material constant in Liu and Murakami creep damage model
t	Time
t_f	Failure time
t_r	Transient time
W	Width of compact tension specimen
X, Y, Z	Cartesian coordinates
α	Multiaxial parameter; material constant
β	Material constant in Monkman-Grant relationship
Δt	Time increment
ν	Poisson's ratio
σ	Stress
σ_1	Maximum principal stress
σ_m	Hydrostatic stress
σ_{non}	Nominal stress
σ_r	Rupture stress
σ_{ref}	Reference stress
σ_{ut}	Ultimate tensile stress
σ_y	Yield stress
χ	Material constant in both Kachanov, and Liu and Murakami creep damage models
ω	Damage parameter, ranging from 0.0 (no damage) to 1.0 (full damage)
ε^c	Creep strain
ε_f	Strain at failure
ϕ	Material constant in Kachanov creep damage model

Abbreviations

2D	Two dimensional
3D	Three dimensional
ASTM	American Society for Testing and Materials
Ave. SR	Average strain rate
CCG	Creep crack growth
CCRB	Circumferential cracked round bar
COD	Crack opening displacement
CT	Compact tension
DC	Direct current
DENT	Double edged notched in tension specimens
EBW	Electron Beam Welding
EDM	Electric discharge machining

FE	Finite element
GTAW	Gas Tungsten Arc Welding
HAZ	Heat affected zone
ID	Inner diameter
LLD	Load line displacement
MMA	Manual metal arc
Mo	Molybdenum
Mod.	Modified
mpc	Multipoint constraint
MSR	Minimum strain rate
OD	Outer diameter
PD	Potential difference
PM	Parent material
RSM	The Reference Stress Method
SEM	Scanning Electron Microscopy
W	Tungsten
WM	Weld metal

TABLE OF CONTENTS

ABSTRACT.....	III
LIST OF PUBLICATIONS:.....	V
ACKNOWLEDGEMENTS	VI
NOMENCLATURE.....	VII
TABLE OF CONTENTS.....	X
LIST OF FIGURES:	XIV
LIST OF TABLES:	XXIII
CHAPTER 1. INTRODUCTION	1
1.1 SUMMARY AND BACKGROUND.....	1
1.2 THESIS OUTLINE.....	4
CHAPTER 2. LITERATURE REVIEW	7
2.1 INTRODUCTION	7
2.2 CREEP	9
2.2.1 <i>Creep mechanisms</i>	9
2.2.2 <i>Creep curves</i>	10
2.2.3 <i>Effect of temperature variation</i>	11
2.2.4 <i>Minimum and average creep strain rates</i>	12
2.2.5 <i>Creep rupture and creep fracture</i>	12
2.3 HIGH TEMPRATURE MATERIALS	13
2.3.1 <i>P91 material</i>	13
2.3.2 <i>P92 material</i>	15

2.4	CREEP IN WELDS	20
2.4.1	<i>Materials of weld region</i>	20
2.5	CRACKS IN WELDED JOINTS	22
2.5.1	<i>Type IV cracks</i>	23
2.6	PREDICTION OF CREEP CRACK GROWTH USING FRACTURE MECHANICS	25
2.6.1	<i>Introduction</i>	25
2.6.2	<i>C* derivation background</i>	26
2.6.3	<i>C*, C(t) and K to correlate creep crack growth</i>	28
2.6.4	<i>Creep crack growth prediction using C*</i>	35
2.6.5	<i>FE prediction of C*</i>	37
2.7	PREDICTION OF CREEP CRACK GROWTH USING DAMAGE MECHANICS.....	39
2.7.1	<i>Introduction</i>	39
2.7.2	<i>Material properties</i>	41
CHAPTER 3. EXPERIMENTAL WORK.....		47
3.1	INTRODUCTION	47
3.2	WELDS AND SPECIMENS	48
3.2.1	<i>P91 welds</i>	48
3.2.2	<i>Specimens for creep and creep rupture tests</i>	48
3.2.3	<i>P91 CT specimens</i>	53
3.2.4	<i>P92 weldments</i>	56
3.2.5	<i>P92 uniaxial and notched bar specimens</i>	58
3.2.6	<i>P92 CT specimens</i>	58
3.3	CREEP TESTING ARRANGEMENTS	61
3.4	EXPERIMENTAL RESULTS	63
3.4.1	<i>P91 experimental results</i>	63
3.4.2	<i>P92 experimental results</i>	81
3.5	DISCUSSION	94
3.5.1	<i>P91 creep crack growth</i>	94
3.5.2	<i>P92 uniaxial results</i>	96

3.5.3	<i>P92 creep crack growth</i>	97
CHAPTER 4. FRACTURE MECHANICS APPROACH TO PREDICTING CREEP CRACK GROWTH.....99		
4.1	INTRODUCTION	99
4.2	MATERIALS PROPERTIES	100
4.3	C* CALCULATIONS FOR P91 AND P92 WELDMENTS.....	102
4.3.1	<i>Validity of the Test Results</i>	102
4.3.2	<i>C* calculations</i>	104
4.3.3	<i>C* for the P91 CT specimens</i>	105
4.3.4	<i>C* for the P92 CT specimens</i>	109
4.3.5	<i>Discussion and Conclusions</i>	111
4.4	FE C* PREDICTION.....	123
4.5	STATIONARY CRACK CT MODELS	124
4.5.1	<i>C* for P91 PM CT specimens with stationary crack</i>	126
4.6	GROWING CRACK CT MODELS	128
4.6.1	<i>FE modelling</i>	128
4.6.2	<i>C* calculations</i>	131
4.6.3	<i>Load line displacement (LLD)</i>	133
4.6.4	<i>C* using the growing crack model and the experimental creep crack growth curve</i>	135
4.7	REFERENCE STRESS APPROACH TO PREDICT CREEP CRACK GROWTH IN P91 WELDMENTS.....	140
4.7.1	<i>Introduction</i>	140
4.7.2	<i>Reference Stress for thick-walled pipes</i>	141
4.7.3	<i>Prediction of creep crack growth using the Reference Stress Method</i>	143
4.7.4	<i>Discussion and Conclusions</i>	146
CHAPTER 5. DETERMINATION OF MATERIALS' CREEP AND DAMAGE PROPERTIES.....147		
5.1	INTRODUCTION	147

5.2	DAMAGE MECHANICS MODELS	148
5.2.1	<i>Kachanov damage model</i>	148
5.2.2	<i>Liu and Murakami model</i>	149
5.3	DETERMINATION OF MATERIAL CONSTANTS FOR DAMAGE MODELS.....	150
5.3.1	<i>P91 material constants</i>	150
5.3.2	<i>P91 FE uniaxial creep strain</i>	158
5.3.3	<i>P92 material constants</i>	161
5.3.4	<i>P92 FE uniaxial creep strain</i>	173
5.4	DISCUSSION AND CONCLUSIONS.....	175
 CHAPTER 6. CREEP CRACK GROWTH PREDICTION USING DAMAGE MECHANICS		181
6.1	INTRODUCTION	181
6.2	PARENT MATERIAL CT MODEL.....	182
6.3	CROSS-WELD CT MODEL.....	184
6.4	P91 FE PREDICTIONS.....	186
6.4.1	<i>P91 PM</i>	186
6.4.2	<i>P91 cross weld</i>	189
6.5	P92 FE PREDICTIONS.....	193
6.5.1	<i>P92 PM</i>	193
6.6	DISCUSSION AND CONCLUSION.....	197
 CHAPTER 7. DISCUSSION, CONCLUSIONS AND FUTURE WORK		199
7.1	DISCUSSION	199
7.2	CONCLUSIONS.....	203
7.3	FUTURE WORK	204
 REFERENCES... ..		208
 APPENDICES... ..		214

LIST OF FIGURES:

Fig. 2-1:	View of a typical header (Viswanathan <i>et al.</i> , 2008).....	8
Fig. 2-2:	creep mechanisms.....	10
Fig. 2-3:	A typical uniaxial creep strain curve.....	11
Fig. 2-4:	Creep ahead of the crack tip in a cracked body (Anderson, 2005).....	11
Fig. 2-5:	Comparison of allowable stress for P91 (Mod. 9Cr-1Mo) and P92 (NF616) (Ohgami <i>et al.</i> , 1997).....	16
Fig. 2-6:	Comparison of a pipe wall thickness if it is made of P91 (Mod.9Cr-1Mo) or of P92 (NF616) (Ohgami <i>et al.</i> , 1997).....	17
Fig. 2-7:	Creep results for T/P92 for various temperatures tests, (Vaillant <i>et al.</i> , 2008).	17
Fig. 2-8:	P92 weldment cross-section (Tabuchi <i>et al.</i> , 2010).....	19
Fig. 2-9:	Schematic cross section of a weld showing typical microstructural zones, (Storesund and Tu, 1995).	22
Fig. 2-10:	Types of cracking in weld joint of steels on service exposure (Laha, 2007).	23
Fig. 2-11:	Creep crack growth in P91 tested pipe, at 625°C; the crack grew in Type IV region (Shibli and Le Mat Hamata, 2001). EDM refers to the Electric Discharge Machining process used to cut the notch.	25
Fig. 2-12:	Arbitrary contour around the crack tip used to obtain J contour integral, (Anderson, 2005).....	27
Fig. 2-13:	A single material compact tension (CT) specimen.....	29
Fig. 2-14:	Creep crack growth (CCG) for a creep ductile material, Cr-Mo-V, and a creep brittle material, IN 100. 1 = steady state CCG; 2 = accelerated CCG; t_f = fracture life, (Yokobori, 1999).	30
Fig. 2-15:	Three regimes of creep deformation in a structural element with a crack-like defect, (Landes and Schwalbe, 2004).....	35
Fig. 2-16:	Relationship between C^* and creep crack growth for P91 weldment at different temperatures (Yamamoto <i>et al.</i> , 2010).....	37
Fig. 2-17:	da/dt against C^* for P92 at different temperatures for (a) base material and (b) weld joints (Tabuchi <i>et al.</i> , 2010).	37
Fig. 2-18:	FE results of the CCRB analyses.	39

Fig. 2-19:	Small specimens types (Hyde and Sun, 2009b):	42
Fig. 2-20:	Ring specimens, (Hyde and Sun, 2009b).	43
Fig. 2-21:	Relationship between creep crack growth path of CT specimen, Vickers hardness and stress triaxiality (Sugiura <i>et al.</i> , 2010).	46
Fig. 3-1:	P91 weldment from which all the specimens were cut (Hyde <i>et al.</i> , 2004a).	51
Fig. 3-2:	Uniaxial creep test specimen.	52
Fig. 3-3:	Notched bar specimen (dimensions in mm).	52
Fig. 3-4:	Cross-weld waisted specimen (dimensions in mm).	52
Fig. 3-5:	Cross-weld uniaxial specimen.	53
Fig. 3-6:	HAZ impression creep specimens and their positions in the weldments, tested from the PM side.	53
Fig. 3-7:	Parent metal CT specimen. Plain specimen's front view (Left) and grooved specimen's side view (Right). (dimensions in mm).	54
Fig. 3-8:	Schematic drawing of the P91 weldment and cross-weld CT specimen (dimensions in mm).	55
Fig. 3-9:	Cross-weld CT specimen consisting of PM, HAZ and WM (dimensions in mm).	56
Fig. 3-10:	The P92 weld cross section.	57
Fig. 3-11:	Sampling for the P92 PM CT specimens.	59
Fig. 3-12:	Sampling for the P92 cross-weld CT specimens.	60
Fig. 3-13:	The P92 cross-weld CT specimens were cut perpendicular to the welding cross section with the initial crack located on the PM/HAZ boundary.	60
Fig. 3-14:	Initial cracks in P92 cross -weld CT specimens were allowed to grow in the welding direction and opposite to the welding direction.	61
Fig. 3-15:	Loading arrangements for testing CT specimens.	62
Fig. 3-16:	Potential difference measuring arrangements.	62
Fig. 3-17:	Creep strain curves for the P91 PM at 650°C, (Hyde <i>et al.</i> , 2004b).	64
Fig. 3-18:	Creep strain curves for the P91 WM, at 650°C, (Hyde <i>et al.</i> , 2004b). .	64

Fig. 3-19:	Impression deformation versus time curves for the P91 HAZ material, at 650°C, subjected to steady loading from the parent material side, (Hyde <i>et al.</i> , 2004b).....	65
Fig. 3-20:	Failed CT specimen (CT5).....	68
Fig. 3-21:	Load line displacement for the P91 PM CT specimens, at 650°C.....	69
Fig. 3-22:	Load line displacement for the P91 cross-weld CT specimens, at 650°C.....	69
Fig. 3-23:	Creep crack growth in the P91 PM CT specimens at 650°C.....	72
Fig. 3-24:	Calibration factors for the P91 cross-weld CT specimens.....	72
Fig. 3-25:	Creep crack growth for the P91 CT5, CT7 and CT8 with and without using CT6 calibration factor (CF).....	73
Fig. 3-26:	Creep crack growth for the P91 cross-weld CT specimens at 650°C.....	73
Fig. 3-27:	Cracked surfaces of the P91 PM CT1 specimen.....	75
Fig. 3-28:	Cracked surfaces of the P91 PM CT specimens.....	75
Fig. 3-29:	Cracked surfaces of the P91 cross-weld CT specimens.....	76
Fig. 3-30:	Schematic drawing showing the planes where the hardness was measured.....	77
Fig. 3-31:	A tested cross-weld CT specimen cut into slices.....	78
Fig. 3-32:	Polished and etched slices of a cross-weld CT5 specimen.....	78
Fig. 3-33:	Vickers' hardness results for cross-weld CT specimens, CT5 and CT7.....	79
Fig. 3-34:	Sub cracks were found close to the crack line in CT7.....	80
Fig. 3-35:	Micro cracks appear next to the crack line in high density.....	80
Fig. 3-36:	Creep strain curves for the P92 PM at 675°C.....	83
Fig. 3-37:	Failure times against stresses for the P92 PM at 675°C.....	83
Fig. 3-38:	Creep strain curves for the P92 WM , at 675°C.....	84
Fig. 3-39:	85 PM failed cross-weld uniaxial specimen.....	84
Fig. 3-40:	Creep strain curves for P92 cross-weld uniaxial test at 675°C.....	84
Fig. 3-41:	Results of the impression creep test for the P92 HAZ material, at 675°C, subjected to steady loading from the parent material side. ...	86

Fig. 3-42:	Load line displacement for the P92 PM CT specimens tested at 675°C.	88
Fig. 3-43:	Load line displacement for the P92 cross-weld CT specimens tested at 675°C.....	88
Fig. 3-44:	Raw and refined data for P92 CT1.....	90
Fig. 3-45:	Creep crack growth for P92 PM CT specimens at 675°C.....	91
Fig. 3-46:	Creep crack growth for the P92 cross-weld CT specimens at 675°C.....	91
Fig. 3-47:	Cracked surfaces of P92 CT specimens, PM specimen CT1-CT5 and cross-weld CT specimens CT6-CT11.....	92
Fig. 3-48:	Hardness test results for the P92 weld before creep testing.	93
Fig. 3-49:	Experimental results of nominally identical CT tests, CT6, CT9 and CT10: (a) Load line displacement and (b) Creep crack growth.....	95
Fig. 3-50:	Experimental results of nominally identical CT tests, CT8 and CT11; (a) Load line displacement and (b) Creep crack growth.	95
Fig. 3-51:	Creep strain curves for P92 PM and WM at 675°C.	96
Fig. 3-52:	Effect of the welding direction on load line displacement for the P92 cross-weld CT specimens. Cracks grew opposite to the welding direction in CT6 and CT7 while they grew in the welding direction in CT8 and CT8.	97
Fig. 3-53:	Effect of the welding direction on creep crack growth for the P92 cross-weld CT specimens. Cracks grew opposite to the welding direction in CT6 and CT7 while they grew in the welding direction in CT8 and CT8.	98
Fig. 4-1:	Definition of minimum creep strain and "average" creep strain rate.	101
Fig. 4-2:	Creep crack growth rates, da/dt , against C^* values for the P91 PM CT specimens, at 650°C.	106
Fig. 4-3:	Creep crack growth, da/dt , against C^* for the P91 cross-weld CT specimens, using specimens own calibration factors.	108
Fig. 4-4:	Creep crack growth, da/dt , against C^* for the P91 cross-weld CT specimens, at 650°C, when CT6 CF was used for CT5, CT7 and CT8.	108
Fig. 4-5:	Creep crack growth rate, da/dt , against C^* obtained from P92 PM CT specimens, at 675°C.	110

Fig. 4-6:	Creep crack growth rate, da/dt , against C^* obtained from P92 cross-weld CT specimens, at 675°C	110
Fig. 4-7:	Function g vs. the mismatch factor Q for CT specimen, (Tu, 2002).	112
Fig. 4-8:	Creep crack growth rates, da/dt , against C^* for the P91 PM and cross-weld CT specimens at 650°C	113
Fig. 4-9:	Creep crack growth rates, da/dt , against C^* for the P92 PM and cross-weld CT specimens at 650°C	114
Fig. 4-10:	Creep crack growth rates, da/dt , against C^* for the P91 and P92 PM CT specimens.....	115
Fig. 4-11:	Creep crack growth rates, da/dt , against C^* for the P91 and P92 cross-weld CT specimens.....	116
Fig. 4-12:	P91 PM stress-strain curve at 650°C	119
Fig. 4-13:	P91 plastic stress-strain curve at 650°C	119
Fig. 4-14:	Plastic strain against plastic stress for P91 at 650°C	120
Fig. 4-15:	C^* values calculated using total LLD rate, V_t , and the creep component of LLD rate, V_c , for P91 PM CT4	122
Fig. 4-16:	C^* values calculated using total LLD rate, V_t , and the creep component of LLD rate, V_c , for P91 cross-weld CT7	123
Fig. 4-17:	Single material (PM) CT model using collapsed elements ahead of the crack tip.....	125
Fig. 4-18:	Single material (PM) FE CT model using quadrilateral 4-node elements ahead of crack tip.	125
Fig. 4-19:	Contour integral, $C(t)$, against time for collapsed element and 4-node elements for P91 CT4 at $a = 15.5$	126
Fig. 4-20:	Changing of time increment, Δt , and the contour integral, $C(t)$, with time for CT4 specimen with initial crack length of 16 mm.	127
Fig. 4-21:	FE C^* against crack length for CT4 using stationary crack models for P91, at 650°C , compared to Exp. results.	127
Fig. 4-22:	FE mesh for growing crack model.....	130
Fig. 4-23:	Mesh ahead of the crack tip showing crack increments.....	130
Fig. 4-24:	Deformed shape of the growing crack model showing the released boundary conditions.....	131

Fig. 4-25:	Contour integral, $C(t)$, for the growing crack model using CT4 loading conditions.	132
Fig. 4-26:	C^* for the stationary crack models and the growing crack model compared to the experimental results for CT4.	132
Fig. 4-27:	FE load line displacement for the growing crack model, using plane strain elements , and the experimental results for CT4.	134
Fig. 4-28:	FE load line displacement for growing crack model, using plane strain and plane stress elements , compared to the experimental results for CT4.	134
Fig. 4-29:	FE load line displacement using the average strain rates constants, A' and n'	135
Fig. 4-30:	Creep crack growth curve for CT4 used to calculate the step time, Δt	137
Fig. 4-31:	FE C^* results for stationary crack and growing crack models compared to experimental results.	138
Fig. 4-32:	Creep crack growth rate, da/dt , against C^* for the growing crack model and experimental results of CT4.	138
Fig. 4-33:	Load line displacement for the growing crack model compared to the experimental results.	139
Fig. 4-34:	Creep crack growth of P91 at 650°C against the Reference Stress. ...	145
Fig. 4-35:	Creep crack growth against Reference Stress using plane strain and plane stress conditions.	145
Fig. 5-1:	Creep strain curves fitted to the experimental creep curve at $q_2 = 3.2$ for P91 PM	153
Fig. 5-2:	Minimum Strain Rates (MSR) against applied stress for P91 WM at 650°C.	154
Fig. 5-3:	Uniaxial failure times against applied stress for P91 WM at 650°C.	154
Fig. 5-4:	Creep strain curves fitted to the experimental creep curve at $q_2 = 5.0$ for P91 WM using FE analyses.	155
Fig. 5-5:	Reproduced creep strain curves using Kachanov damage model and Liu and Murakami damage model at $q_2 = 2.8$ for the P91 HAZ material.	156
Fig. 5-6:	FE notched bar failure times, for different α values, using the Liu and Murakami damage model for P91 WM at 650°C.	157

Fig. 5-7:	FE uniaxial model	159
Fig. 5-8:	Experimental and FE uniaxial creep strain curves for P91 PM at 650°C.....	159
Fig. 5-9:	Experimental and FE uniaxial creep strain curves for P91 WM at 650°C.....	160
Fig. 5-10:	Minimum strain rates (MSR) against stress(σ) for P92 PM , at 675°C.	162
Fig. 5-11:	Minimum strain rates(MSR) against stress(σ) for P92 WM , at 675°C.	162
Fig. 5-12:	Failure time (t_f) against applied stress (σ) for the P92 PM uniaxial creep tests at 675°C.	163
Fig. 5-13:	Failure time (t_f) against applied stress (σ) for the P92 WM uniaxial creep tests at 675°C.	164
Fig. 5-14:	Calculated creep strain curves fitted to the experimental creep curves, for the P92 PM , at $\phi = 8.3$	166
Fig. 5-15:	Calculated creep strain curves fitted to the experimental creep curves, or the P92 WM , at $\phi = 7.5$	166
Fig. 5-16:	FE notched bar model.....	169
Fig. 5-17:	FE notched bar failure times, for different α values, using the Kachanov model for P92 PM at 675°C.....	170
Fig. 5-18:	FE notched bar failure times, for different α values, using the Liu/Murakami for P92 PM at 675°C.	170
Fig. 5-19:	FE notched bar failure times, for different α values, using the Kachanov model for P92 WM at 675°C.....	171
Fig. 5-20:	FE notched bar failure times, for different α values, using the Liu/Murakami model for P92 WM at 675°C.	171
Fig. 5-21:	Creep strain curves fitted to experimental creep curves at $q_2 = 3.0$, for P92 PM at 675°C.....	172
Fig. 5-22:	Creep strain curves fitted to experimental creep curves at $q_2 = 3$, for P92 WM at 675°C.	173
Fig. 5-23:	Experimental and FE creep strain curves using the Kachanov and the Liu and Murakami Damage models for P92 PM at 675°C.....	174
Fig. 5-24:	Experimental and FE creep strain curves using the Kachanov and the Liu and Murakami Damage models for P92 WM at 675°C.	175

Fig. 5-25:	Minimum creep strain rates, ϵ_{min} , against stress, σ , for the P91 weldment, at 650°C, (Hyde <i>et al.</i> , 2004a).....	177
Fig. 5-26:	Minimum creep strain rates, ϵ_{min} , against stress, σ , for the P92 weldment, at 675°C.....	177
Fig. 5-27:	Failure times, t_f , against stresses for the P91 weldment, at 650°C....	179
Fig. 5-28:	Failure times, t_f , against stresses for the P92 weldment, at 675°C....	180
Fig. 6-1:	PM CT specimen.	183
Fig. 6-2:	Boundary conditions applied to the planes of symmetries.	183
Fig. 6-3:	The cross-weld CT model.	185
Fig. 6-4:	The loading and boundary conditions at the load points.	185
Fig. 6-5:	The boundary conditions were applied to the plane of symmetry.	186
Fig. 6-6:	Mesh for the 3D PM CT model showing damage contours.....	188
Fig. 6-7:	FE damage contours for a plane CT model, CT1, and a side grooved CT model, CT4.....	188
Fig. 6-8:	Damage zones at various α values for the P91 PM CT model CT4.	188
Fig. 6-9:	FE creep crack growth for P91 PM CT3 compared to the experimental results.....	189
Fig. 6-10:	Predicted damage zones on the PM/HAZ boundary for the CT9, with various α values for the HAZ material.	191
Fig. 6-11:	Damage accumulation, indicating the progression of the creep crack growth with time, for CT9 with $\alpha = 0.52$, for various times, t , relative to the failure time, t_f	192
Fig. 6-12:	Experimental and FE creep crack growth for the P91 CT9 and CT10 with various α values.	192
Fig. 6-13:	Experimental and FE creep crack growth for CT7 and CT8 with $\alpha = 0.48$	193
Fig. 6-14:	Experimental and FE creep crack growth for the P92 CT2 with $\alpha = 0.383$	195
Fig. 6-15:	Experimental and FE creep crack growth for the P92 CT3 with $\alpha = 0.383$	195
Fig. 6-16:	FE creep crack growth with various α values compared to the P92 CT3 results.	196

Fig. 6-17: FE creep crack growth rates for various α values, using CT3 loading conditions. 196

Fig. 6-18: FE notched bar failure times, for different α values, using the **Kachanov** model for the P91 **cross-weld**, at 650°C. 198

Fig. 7-1: Proposed CT specimens sampling..... 205

Fig. 7-2: It is suggested to cut impression creep specimens in one go; to obtain consistent specimens. 207

LIST OF TABLES:

Table 2-1: Tensile properties of P22, X20 and P91 at room temperature (Saha, 2003).	15
Table 2-2: Limits of the chemical composition of P91 and P92 (weight %) (Jason Dobson, 2006) and (Vaillant <i>et al.</i> , 2008).	18
Table 3-1: Chemical composition of P92 PM and WM (%Wt).	57
Table 3-2: Creep rupture data (in hours) for P91 at 650°C.	67
Table 3-3: CT experimental test conditions and main results.	67
Table 3-4: Creep rupture data(in hours) for P92 at 675°C.	85
Table 3-5: Testing conditions and main results of the P92 creep crack growth tests.	87
Table 3-6: Variation in the calibration factors for the P92 CT specimens.	90
Table 4-1: Materials constants A , n , A' and n' for P91, at 650°C, and for P92, at 675°C (stress in MPa, time in h and ϵ_{min} in h^{-1}).	101
Table 4-2: h_1 (a/W , m) values for CT specimens under plane strain conditions; reproduced from the one given in (ASTM E 1457-00, 2001).	118
Table 4-3: h_1 for P91 CT specimen, at 650°C, and different crack length to the specimen width ratios, at $m = 18.558$	121
Table 4-4: C^* values and the transient times for CT4, with nine initial crack lengths using stationary crack models (MSR constants were used to obtain C^* values).	128
Table 4-5: Load for CT4 and material constants for P91 at 650°C.	130
Table 4-6: Correlation between the reference stress, σ_{ref} , and the mean diameter hoop stress, σ_{mdh}	142
Table 5-1: P91 Material constants for damage models at 650°C (σ in MPa and time in h)	157
Table 5-2: P92 Material constants for damage constitutive equations at 675°C (σ in MPa and time in h).	173

CHAPTER 1.

INTRODUCTION

1.1 SUMMARY AND BACKGROUND

The objective of this thesis is to study and predict creep and creep crack growth (CCG) in P91 and P92 high temperature steels. P91 and P92 are two ASTM high Cr creep resistant steels that are used in the manufacturing of main steam pipes in power plants. They are also used in chemical plants and nuclear power plants. Studying of creep and CCG in high temperature materials helps in predicting residual life of the components, that were made of these materials, and, hence, the residual life of plant itself. Accurate and reliable prediction of residual life (or remaining life) provides a basis for timely, safe and economic replacement or repair of key components which helps to maximise a plant's usefulness by eliminating unnecessary replacement and reducing costly unscheduled outages caused by in-service failure (Ling *et al.*, 2000).

The development of new, high temperature, materials is essential to withstand the higher temperatures and the high pressure of steam, e.g. about 650°C and 350 bar, used for ultra-supercritical power stations. The objective of the use of these new materials is to maximize plant thermal efficiency by minimising fuel consumption and, therefore, the CO₂ emission. Examples of such new materials are the Mod. 9Cr-1Mo (P91) and 9CrW steel, NF616 (P92) (Ohgami *et al.*, 1997).

Most of, for example, power plants components, with complex geometries, operate under multiaxial stress states. Hence, testing of such components under operating conditions is a challenge. Instead, specimens cut from the materials of these components are used to characterise the behaviour of such components.

These specimens are tested under conditions more severe than the actual components in terms of temperatures and stresses. Throughout this thesis, and in many of the published papers, standard specimens have been tested and their results have been used to describe the creep behaviour of the materials from which the specimens were cut. One important question arose; how can these results be applied, with confidence, to the real components? Le Mat Hamata and Shibli (2001) stated some assumptions under which results obtained from testing specimens could be applied to actual components. These assumptions are that (i) the metallurgical structures, for specimens and components, are similar, (ii) the crack positions are the same and cracks grow in the same orientation through the structure, and (iii) the stress distribution within the specimens and the components are similar. However, these assumptions are rarely met.

On one hand, efforts have been made to replicate the severe operating conditions, that these and other components are subjected to, in power stations, to the laboratory testing. In this respect, Le Mat Hamata and Shibli (2001) tested the CCG in P22 and P91 pipes. They found good correlation with conventional data generated using compact tension (CT) specimens. Moreover, they carried out another set of tests, on pipes, at low frequency cyclic load (10^{-4} Hz), which is similar to, or a slightly higher than, that in the power plants. They also found no effect of such cyclic loading on creep crack growth when compared to the static load tests.

On the other hand, the Finite Element (FE) method has been widely used to predict the failure life and the potential failure position in welded pipes, e.g. (Hyde *et al.*, 2004a, Hyde *et al.*, 2006b, Hyde *et al.*, 2006d, Sun *et al.*, 2000). The FE method can also be used to model components that are more complex and are subjected to more complex loading conditions. However, for accurate

predictions, using the FE method, reliable material models and material properties are needed.

The determination of material properties is extremely important for the prediction of material creep behaviour. Minimum creep strain rates, $\dot{\epsilon}_{min}$, induced in a material are related to the applied stress, σ , by the well known Norton's relationship, for example:-

$$\dot{\epsilon}_{min} = A\sigma^n \quad (1-1)$$

where A and n are material constants. Moreover, the minimum creep strain rate can also be related to failure time, t_f , by the well-known Monkman-Grant relationship:-

$$(\dot{\epsilon}_{min})^\beta t_f = C \quad (1-2)$$

where β and C are material constants. These material constants can be determined using the results of uniaxial creep tests. More sophisticated material models, e.g. the Kachanov creep/damage model, can be used to predict damage initiation and progression in a material. To employ these models, more material constants are needed.

Steady state creep behaviour of a component can be predicted by, for example, the Norton law. Material constants A and n can be obtained by using either the minimum creep strain rates or the average creep strain rates (definitions are given in Section 2.2). The prediction of creep behaviour using average creep strain rates is more conservative. However, damage mechanics based material models, such as the Kachanov and the Liu and Murakami models (both are detailed in Section 5.2), can be used to predict the full creep behaviour, i.e. primary, secondary and tertiary creep stages, of a component.

Creep crack growth in a component can be predicted by using fracture mechanics parameters, such as K , $C(t)$, and C^* (reviewed in Section 2.6) or by using damage mechanics (as given in Chapter 6). C^* was found to correlate CCG rates better than other parameters. C^* can be calculated using experimental results from, for example, compact tension (CT) specimens. C^* can be also obtained using the FE method. Stationary crack and growing crack CT models were used to obtain the C^* values. Nodes releasing technique was used to grow cracks in the FE models. A fracture criterion, such as experimental CCG, should be imposed in the FE analyses in order to grow cracks. CCG can also be predicted using the damage mechanics approach. In this thesis, CCG was predicted for P91 and P92 materials using the Liu and Murakami damage model; details are given in Chapter 6. The Liu and Murakami model has been used for parent material specimens and for welded specimens, too.

1.2 THESIS OUTLINE

Following this introduction, the literature review in Chapter 2 is divided into three themes. The first covers, in some detail the general background to creep, high temperature materials and creep in welds, including Type IV cracks. The second reviews the prediction of CCG using fracture mechanics parameters. The third reviews the prediction of CCG using a damage mechanics approach. The effects and determination of material properties are also included in the third theme.

Chapter 3 contains details of the experimental programme of creep and CCG testing of P91 and P92 materials and welds. This chapter is also divided into three main parts. The first focuses on the P91 and P92 welds, from which all the specimens were cut, and introduces the geometries and dimensions of uniaxial, notched bar, cross-weld notched bar, cross-weld waisted and impression creep specimens. The second presents the experimental results obtained from all the

creep, creep rupture and CCG tests for the P91 steel, followed by those for the P92 steel. The third part of the chapter is the discussion and conclusions including comments on the effects of material variability on the CCG results.

Chapter 4 discusses the prediction of CCG, in P91 and P92 CT specimens, using fracture mechanics. The fracture mechanics parameter, C^* , was used to correlate the CCG rates for PM and for cross-weld CT specimens. The first three sections of Chapter 4 are concerned with the calculation of C^* values using experimental results, i.e. load line displacement rates and CCG, for both PM and cross-weld CT specimens. The CCG tests and the calculation of C^* values were carried out in accordance with (ASTM E 1457-00, 2001). The following three sections contain reports on the prediction of C^* using FE analyses. Stationary crack models and growing crack models are presented and their results are compared. The last section of Chapter 4 contains the description of the use of the Reference Stress method to correlate the CCG rates in CT specimens.

The fracture mechanics approach, used to predict the CCG in P91 and P92 CT specimens, is presented in Chapter 4. Chapter 5 and Chapter 6 are concerned with the use of the damage mechanics method for predicting the creep and CCG in P91 and P92 materials. Firstly, Chapter 5 presents two damage mechanics models, namely the Kachanov and the Liu and Murakami models. Moreover, it explains how the material constants needed to use these models are determined. Chapter 5 also presents the validation of the damage models and the material constants by comparing the FE uniaxial creep data to the corresponding experimental creep data.

In Chapter 6, the CCG data were predicted for the P91 PM and cross-weld CT specimens and for the P92 PM CT specimens. The effects of the multiaxiality

parameter, α , on the damage initiation and evolution in the CT specimens were also detailed.

Finally, Chapter 7 presents a general discussion, main conclusions and the future work.

CHAPTER 2.

LITERATURE REVIEW

2.1 INTRODUCTION

Electricity (Power) is the backbone of industry and most of everyday activities. The power generation involves burning huge amounts of fossil fuel. In coal-fired power stations, heat produced by burning coal is used to heat up water, in boilers, to produce steam with high temperature and high pressure. Steam is then used to operate turbines which rotate alternators to produce electricity.

The boilers are crucial components in power stations. Within boilers, water passes through a wall of welded tubes, known as water wall. Combustion gases, produced from the burning of coal, flow through the furnace and evaporate the water into steam inside the furnace water walls. This steam is then further superheated in a superheater and delivered to high-pressure turbines via main steam pipes. Low pressure steam exhausted from the high pressure turbines is reheated again, in a reheater, and is delivered to low pressure turbines (Viswanathan *et al.*, 2008).

Tubes and thick-walled pipes of a boiler are subjected to extremely harsh working conditions, i.e. high temperatures and/or high pressures. Thick-walled pipes are generally known as headers; to collect or distribute steam, or steam pipes; to transfer steam to turbines, while tubes refers to furnace water wall, superheater tubes or reheater tubes. Fig. 2-1 shows a typical header. As it can be seen, headers are thick-walled extruded pipes where steam is collected and

homogenized. Headers could be inlet headers, steam goes into them, or outlet headers, steam goes out of them (Viswanathan *et al.*, 2008).

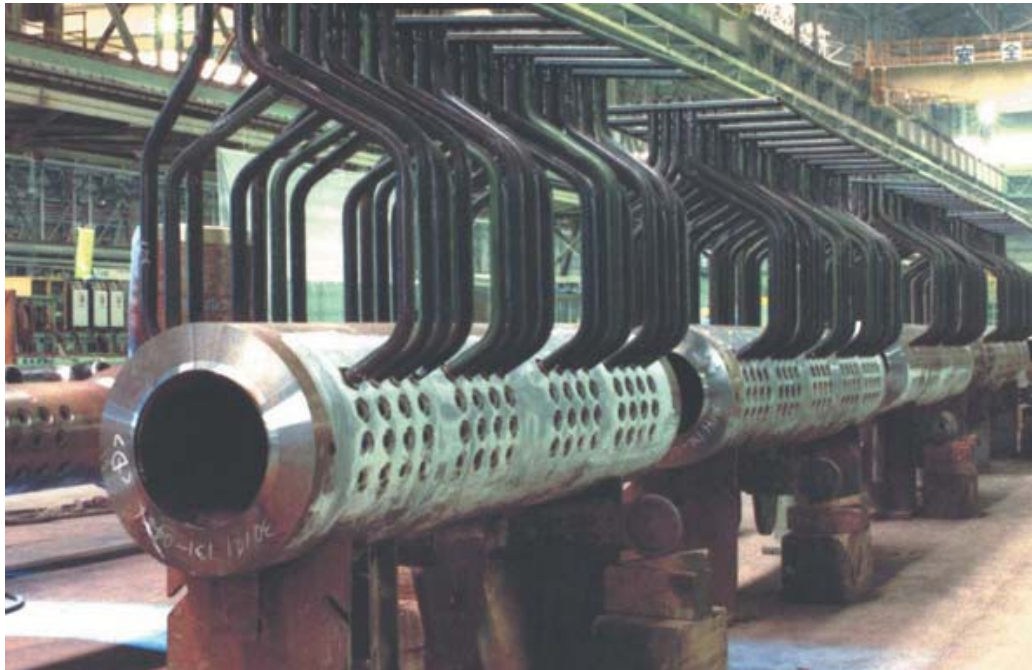


Fig. 2-1: View of a typical header (Viswanathan *et al.*, 2008).

This thesis is focused on two of high temperature materials, i.e. P91 and P92, and their welds, which are used for manufacturing thick-walled main steam pipes. Creep and creep crack growth (CCG) of these two materials are studied. Fracture mechanics and damage mechanics methods have been used to predict the CCG in standard compact tension (CT) specimens. Using the materials constants, obtained as a part of the investigation, it is shown that the methodology can be used for the modelling of P91 and P92 pipes, headers or thin-walled tubes.

2.2 CREEP

Creep is defined as the time-dependent non-reversible deformation that occurs when materials are subjected to stresses lower than its yield stress for a long period. Creep could happen at any temperature above the absolute zero, i.e. 0.0 K (-273.15°C). However, from a practical point of view, it is much more significant at high temperatures, normally 0.3 to 0.5 of the melting point (Evans and Wilshire, 1985, Laha, 2007, Nikbin, 2009).

2.2.1 Creep mechanisms

At high temperatures, the atoms of metals are active enough to move from one position to another within metal crystals. With load applied to the material over long time, the movements of the atoms result in creep of the material. This movement, of atoms, is caused by diffusion. Vacancy diffusion occurs when an atom moves from its position to a vacancy which may be the same size as the atom itself, as shown in Fig. 2-2(a). Interstitial diffusion occurs when small atoms moves into spaces between large atoms, as shown in Fig. 2-2(b). Diffusion at grain boundaries, as shown in Fig. 2-2(c), or down cores of dislocations, as shown in Fig. 2-2(d), is much easier and may be 10^6 times faster than that within a crystal. This is because of the large and/or irregular atomic spacings present in these regions. At high stresses, dislocation is the dominant creep mechanism while at low stresses and high temperatures the diffusion creep is the dominant creep mechanism (Ashby and Jones, 1996).

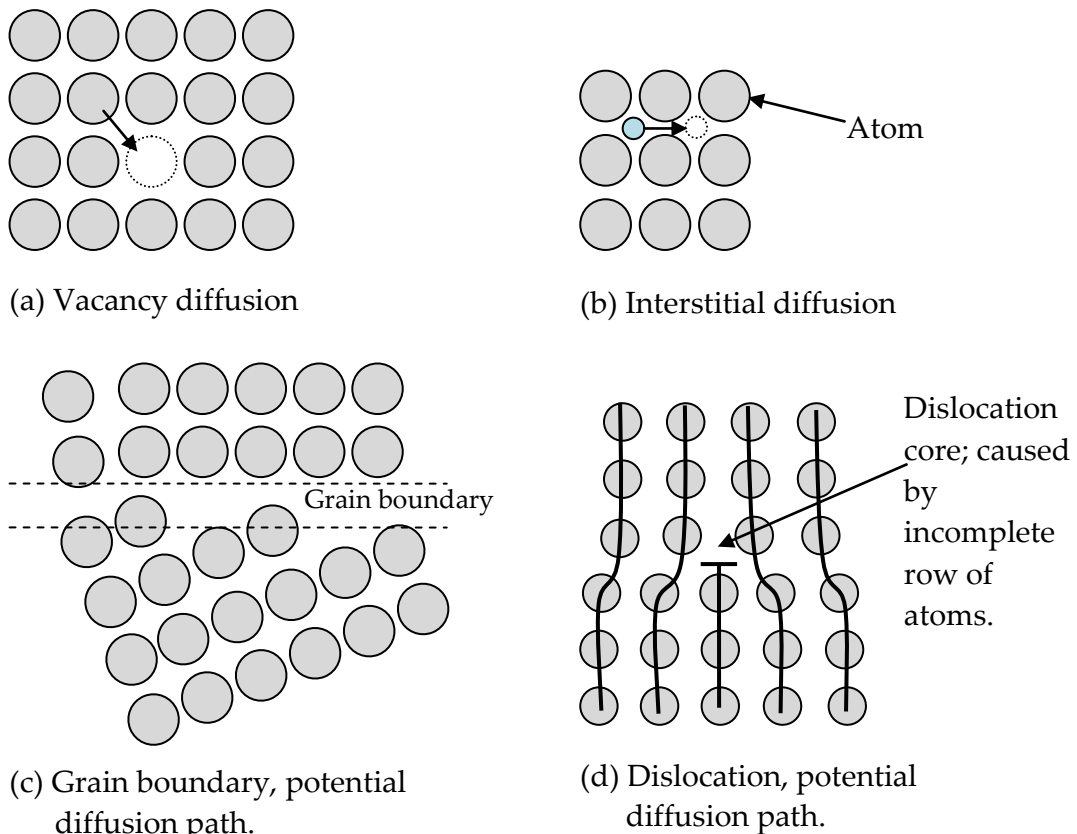


Fig. 2-2: Creep mechanisms.

2.2.2 Creep curves

A typical creep curve mainly consists of three distinct regions, i.e. primary creep, secondary creep and tertiary creep, see Fig. 2-3. The primary creep region is a period of decreasing creep rate during which work-hardening processes dominate and cause dislocation movements to be prevented or limited. The secondary creep region, also known as steady state creep, usually takes the longest time of the creep process and the material creeps with a constant creep rate, $\dot{\epsilon}_{min}$. The final stage, of the creep process, is the tertiary creep stage in which the material creeps at an increasing rate until specimens fail. For cracked bodies, for example, all three-creep regions may be found at the same time as shown in Fig. 2-4.

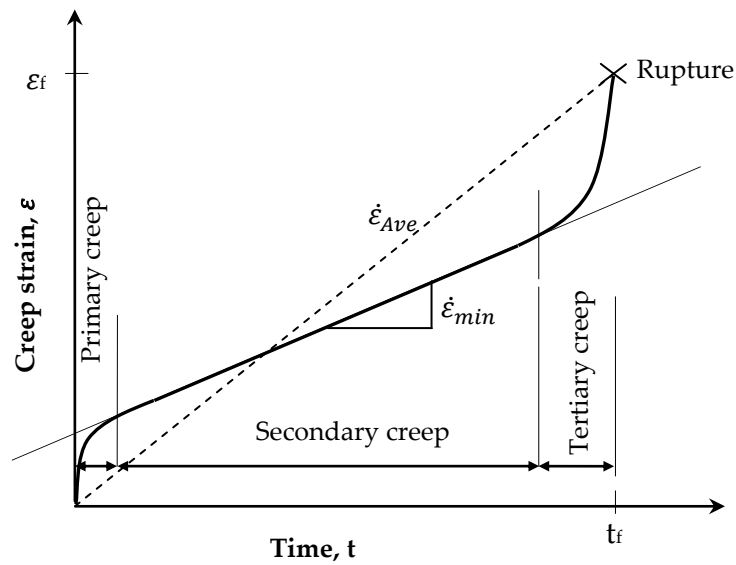


Fig. 2-3: A typical uniaxial creep strain curve.

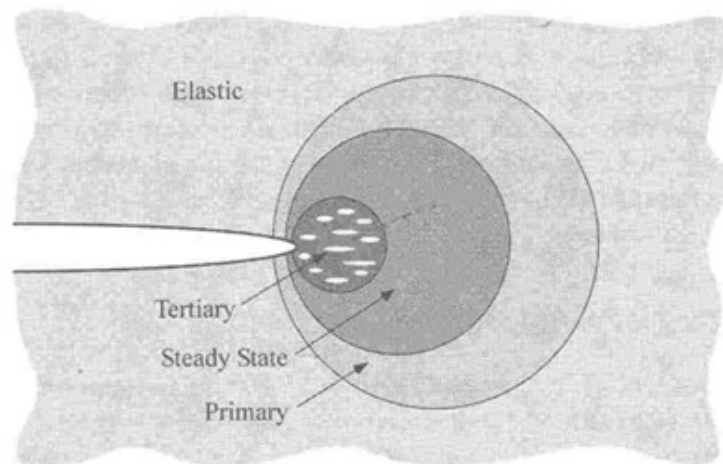


Fig. 2-4: Creep ahead of the crack tip in a cracked body (Anderson, 2005).

2.2.3 Effect of temperature variation

Creep tests are, normally, carried out at constant stress and constant temperature, usually in the range 0.3 to 0.5 of the material absolute melting temperature. Further, high temperature materials often operate at nominally constant temperatures. However, creep strains, and hence lifetimes, are exponentially dependent on testing (or operating) temperature, (Hayhurst,

2001). Subjected to an inadequate temperature control, results of creep tests could change significantly.

2.2.4 Minimum and average creep strain rates

Creep strain rates are of the most effective features of creep curves. The minimum creep strain rate (MSR), $\dot{\epsilon}_{min}$, and the average creep strain rate (Ave. SR), $\dot{\epsilon}_{Ave}$, are indicated in Fig. 2-3 and are detailed in Section 4.2. Materials that exhibit low values of $\dot{\epsilon}_{min}$ or $\dot{\epsilon}_{Ave}$ are known as creep resistant materials when compared to those which exhibit higher values of $\dot{\epsilon}_{min}$ or $\dot{\epsilon}_{Ave}$ at the same stress and temperature. The MSR characterizes the behaviour of materials in the secondary creep region. The average creep strain rate is related to rupture data, i.e. strain at failure, ϵ_f , and failure time, t_f . Therefore, the average creep strain rate accounts for all the three stages of creep curves.

Yatomi *et al.* (2003) found that, for Carbon-Manganese steel at 360°C, the failure strains are stress independent. Therefore, they noted scatter when ϵ_f was plotted against applied stresses, σ . In order to overcome this scatter, they averaged the failure strains, and the average value was then taken as the failure strain for all of the tests. The average creep strain rate for the P91 material was used to determine material constants which are used to calculate fracture mechanics parameter C^* using FE methods, see Section 4.4.

2.2.5 Creep rupture and creep fracture

Creep rupture is the failure of initially crack-free bodies under creep conditions. The failure can be creep ductile or creep brittle in nature. Creep ductile failure is, usually, accompanied by high local deformation while creep brittle failure is accompanied by the initiation and growth of voids, i.e. of failed (or damaged) materials within the structure. Creep damage in creeping components, for example welded pipes, can be quantitatively measured by considering density

number and area fraction of voids in potentially failed regions. By analysing the image data of microstructure of a failed region, number density and area fraction can be determined as follows (Hongo *et al.*, 2009):-

Number density of creep voids = S / A_t

Area fraction of creep voids = $\sum_{i=1}^S A_i / A_t$

where S is the number of voids, A_i is the area of void i , and A_t is the measured area over which the study was carried out. The region of the highest number density is the likely failure position.

Creep fracture is the failure of bodies that contain cracks. Those cracks may be produced from manufacturing processes, such as the welding process or the forging process. The growth of these cracks could be slower or faster than the accumulation of damaged material ahead of the crack tip (Wilshire and Owen, 1983).

2.3 HIGH TEMPRATURE MATERIALS

2.3.1 P91 material

P91 material is an ASTM grade of steel used to manufacture main steam pipes, that are used in the fossil-fuel and nuclear power plants. This material was first developed in the US in the early 1980s and was introduced to the industry in the early 1990s (Vaillant *et al.*, 2008). P91 material is a modified form of P9 (9Cr 1Mo steel) material. P91 material has higher allowable stress than that of its predecessor, eg P22 material. The high allowable stress, of P91 material, enabled engineers to design pipes with thinner walls, saving plant owners a substantial amount of money in material cost. In addition, thinner pipes cost less in fabrication and installation. They also need less energy for preheating, welding

and post-weld heat treatment. Moreover, thinner pipes store less thermal energy and, hence, are subjected to lower thermal stresses. The higher creep-rupture strength of P91 allows piping made of it to survive higher temperatures and pressures than pipes constructed of other steels, e.g. P22. P91 material has higher corrosion-oxidation resistance than that of P22 (Jason Dobson, 2006). Working under high pressures and temperatures has enabled power stations to achieve higher thermal efficiencies and this has resulted in lower fuel costs and reduces pollutants, because less fuel is burned (Saha, 2003).

P91 material was introduced to power stations, replacing components which were made of X20; X20 had been introduced to replace components which were made of P22.

Table 2-1 compares the tensile properties of these three materials at room temperature (Saha, 2003).

Though P91 material has been successfully used internationally in power industries since the 90s, it has drawbacks that prevent it from being applied to supercritical and ultra-supercritical power stations. That is, supercritical and ultra-supercritical power stations operate at 600°C and pressures of 25 MPa or higher. At that temperature, the allowable stress of P91 falls dramatically, to about 50 MPa, so that the piping made of P91 material would have to be several inches thick (Jason Dobson, 2006). Therefore, P92 material was introduced for use in supercritical and ultra-supercritical power stations. The chemical composition of P91 is given in Table 2-2.

Steel Grade	0.2% yield stress, σ_y , MPa	Ultimate tensile stress, σ_{ut} , MPa	% of elongation (gauge length)
P22	205	415	30(2")
X20	490	690	17(5×d)
P91	415	585	20(2")

Table 2-1: Tensile properties of P22, X20 and P91 at room temperature (Saha, 2003).

2.3.2 P92 material

P92 is a relatively newly developed material for use in manufacturing boiler components of supercritical and ultra-supercritical power stations. P92 material was obtained by partially substituting Molybdenum (Mo), in P91 material, by tungsten (W). Tungsten, when added to 9Cr materials, such as P92, produces low thermal expansion, high thermal conductivity, good steam corrosion resistance and excellent creep properties (Wang *et al.*, 2009).

Steam oxidation plays an important role in defining the maximum allowable temperature for each grade of steel. The maximum allowable temperature for T91 is 610°C while it is 620°C for T92, (Vaillant *et al.*, 2008). It should be noted that, according to the ASTM coding, the letter P, in P91 and P92, refers to pipes while the letter T, in T91 and T92, refers to tubes.

Fig. 2-5 compares the allowable stresses for P91 and P92 materials at different temperatures. The nominal working temperature for P91 steel is about 593°C. At that temperature, the allowable stress for P92 material is about 87 MPa, which is about 25% higher than that of P91 material. The (expected) working temperature, in the supercritical and ultra-supercritical power stations, is about 620°C. At that temperature, the allowable stress for P92 material is about 70 MPa, which is more than 50% higher than that of the P91 material (Ohgami *et al.*, 1997). Fig. 2-6 compares, quantitatively, the wall thickness of a pipe if it is made of P91 material and if it is made of P92 material, subjected to the same

working conditions. It can be seen that the wall thickness of the P91 pipe is about 150% of that of the P92 pipe (P. Jason Dobson, 2006, Ohgami *et al.*, 1997). Therefore, the use of P92 material at high temperature can save money in terms of the material used, its manufacturing and processing. Moreover, using thinner tubes of P92 enhances the thermal efficiency of plants because of its higher thermal conductivity. Fig. 2-7 shows the uniaxial creep failure time against applied stress for P92 at different temperatures, (Vaillant *et al.*, 2008).

Table 2-2 compares the chemical compositions of P92 material to that of P91 material. It can be seen that the chemical composition for P92 is similar to that for P91; the key exception is the presence of tungsten (W) and less molybdenum (Mo) in P92 (Jason Dobson, 2006) and (Vaillant *et al.*, 2008).

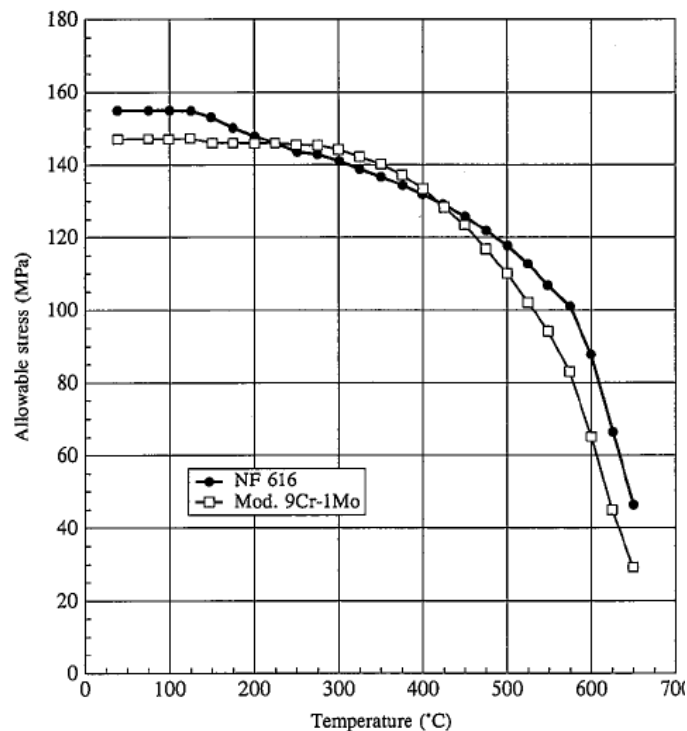


Fig. 2-5: Comparison of allowable stress for P91 (Mod. 9Cr-1Mo) and P92 (NF616) (Ohgami *et al.*, 1997).

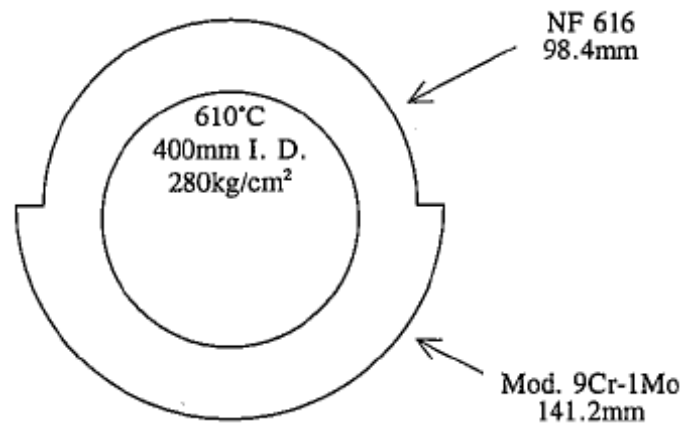


Fig. 2-6: Comparison of a pipe wall thickness if it is made of P91 (Mod.9Cr-1Mo) or of P92 (NF616) (Ohgami *et al.*, 1997).

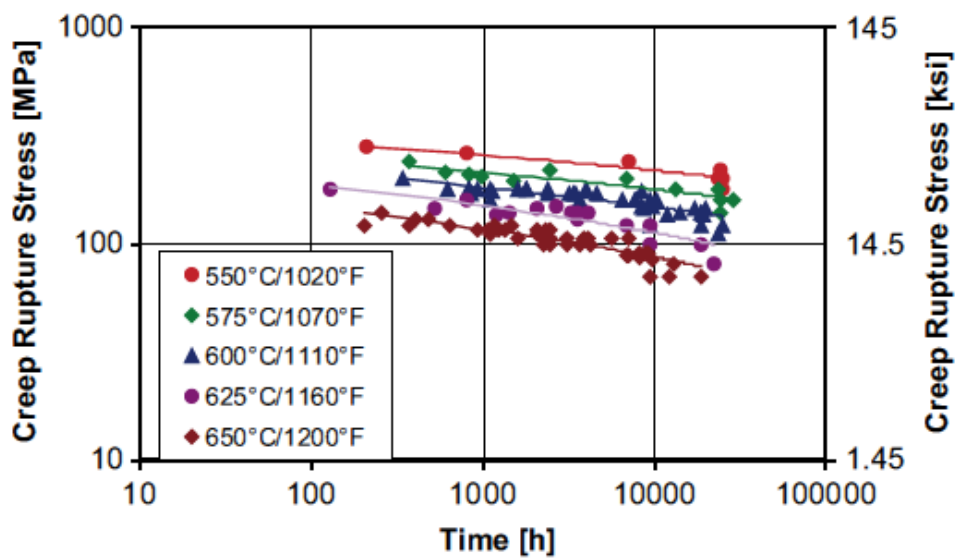


Fig. 2-7: Creep results for T/P92 for various temperatures tests, (Vaillant *et al.*, 2008).

Grade	C	Mn	P	S	Si	Cr	W	Mo	V	Nb	N	B	Al	Ni
P91														
Min%	0.08	0.3	-	-	0.2	8	-	0.85	0.18	0.06	0.03	-	-	-
Max%	0.12	0.6	0.02	0.01	0.5	9.5	-	1.05	0.25	.1	0.07	-	0.04	0.4
P92														
Min%	0.07	0.3	-	-	-	8.5	1.5	0.3	0.15	0.04	0.03	0.001	-	-
Max%	0.13	0.6	0.02	0.01	0.5	9.5	2	0.6	0.25	0.09	0.07	0.006	0.04	0.4

Table 2-2: Limits of the chemical composition of P91 and P92 (weight %) (Jason Dobson, 2006) and (Vaillant *et al.*, 2008).

Kim and Lim (2008) carried out detailed studies on the local creep characteristics of P92 weldments at 600°C using small punch creep tests. They found that the Type-IV region, a very narrow zone in the heat affected zone (HAZ) close to the parent material (PM), is the weakest of all the weld zones, i.e. PM, weld metal (WM), coarse grained HAZ and fine-grained HAZ, and it is the place where creep cavities (damage) are concentrated.

Creep and CCG in P92

Kim *et al.* (2008) were amongst the first who studied the creep and creep crack growth in P92 welds. They found that creep damage was concentrated in the Type IV region and causes failure of the cross-weld, uniaxial, creep specimens at that region. They, also, found that cracks in cross-weld CT specimens grew in the Type IV region. Further, their results showed that the P92 HAZ is less ductile than the PM material; as most of the life (80-90%) of the tested cross-weld CT specimens was consumed before the crack growth accelerated.

Tabuchi *et al.* (2010) tested creep crack growth in P92 welds at different temperatures and loads using CT specimens and sharply notched bars. They

used P92 material constants that were obtained from uniaxial tests carried at 650°C. They tested both PM CT specimens and cross-weld CT specimens. For the cross-weld specimen, they located initial cracks in the middle of the HAZ region and allowed the crack to grow out of the plane of the welding cross section, see Fig. 2-8. For the notched bar specimen they allocated the sharp notch in the middle of the HAZ specimen. They found that the cracks deviated from the middle of the HAZ material and grew into the Type IV region. Further, though they carried out CCG tests at different temperatures, they obtained a unique relationship between C^* (a fracture mechanics parameter used to correlate the CCG rates) values and the creep crack growth rates, da/dt . From the $da/dt-C^*$ curve, they concluded that the creep crack growth rates in the cross-weld CT specimens are higher than these in the PM CT specimens. This could be attributed to the high multiaxiality produced in Type IV region in the cross-weld CT specimens.

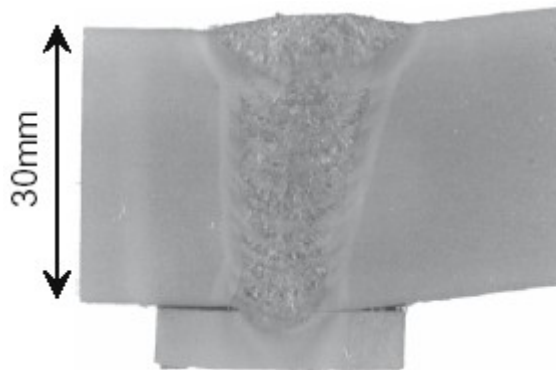


Fig. 2-8: P92 weldment cross-section (Tabuchi *et al.*, 2010).

2.4 CREEP IN WELDS

2.4.1 Materials of weld region

A typical weld consists of parent material (PM), weld metal (WM) and heat affected zone (HAZ) materials, as shown in Fig. 2-9. The PM and the WM may have similar compositions (*similar weld*) or different compositions (*dissimilar weld*). Whether it is a similar weld or a dissimilar weld, the weld constituents have different creep properties. Further, the HAZ region may be divided into several different sub-regions, i.e. coarse-grained zone (close to the fusion line), fine-grained zone (in the middle of HAZ) and intercritical zone, usually referred to as the Type IV region (close to the PM/HAZ boundary), as shown in Fig. 2-9. The presence of all of these materials in the weld region makes a weld a highly complex heterogeneous structure (Hyde *et al.*, 1998, Hyde and Sun, 2000). The different creep deformations of each of these individual zones results in the constraint of transverse deformation during long-term service. Hence, a multiaxial stress state exists which may become even more complex due to mismatching in the welds. Further, the different creep rates of each of these materials lead to stress redistribution. This stress redistribution enhances the multiaxial state of stress (Perrin and Hayhurst, 1999). The intercritical zone is the weakest region of a weld and represents a service life limiting zone of a component associated with the so called Type-IV cracking, which may develop early in service life (Seliger and Gampe, 2002).

In this thesis, compact tension (CT) specimens have been used to study the creep crack growth in P91 and P92 materials. It is obvious that, when testing creep crack growth using CT specimens, this only approximates to the actual life of cracked components. That is, actual components, for example, in power plants, operate under multiaxial stress conditions and at very severe working environments. It is not common practice to simulate these conditions in

laboratories. Therefore, it is essential to obtain creep and creep crack growth data using standard specimens and standard testing methods, e.g. (ASTM E 1457-00, 2001). Results obtained from such creep tests and creep crack growth tests could be applied, with some assumptions, to actual components. These assumptions include that the metallurgical structure for the component and the specimens are identical and that the crack position in the specimens is the same as that in the component and grows in a similar manner and direction (Le Mat Hamata and Shibli, 2001).

Though the testing of actual pipes is very expensive and time-consuming, Le Mat Hamata and Shibli (2001) tested the creep crack growth in two pipes made of P22 (at 565°C) and P91 (at 625°C), under steady and cyclic loads. For the P91 pipes, they found that, while starter cracks initiated in the middle of the HAZ material, it grew into Type IV region. Moreover, they found that the creep crack growth in the Type IV region is about ten times higher than that in the parent material. They, also, found that the low cyclic creep/fatigue (0-11 MPa at 10⁻⁴ HZ) has a similar effect as creep in terms of the creep crack growth.

Another approach to predict creep failure in actual components is presented in (Ogata *et al.*, 2009) where they tested creep rupture in P91 cross-weld uniaxial specimens and in seam welded P91 tubes, at 650°C. They calculated the nominal stress in the tubes using the following relationship:

$$\sigma_{nom} = P_i \left(\frac{D_o}{2t_w} - y \right) \quad (2-1)$$

where P_i is the internal pressure, D_o is the tube outer diameter, t_w is the tube wall thickness and y is a constant (0.38 in their studies). They found that, the calculated nominal stresses and failure times obtained for the tubes are coincident with those for the uniaxial cross-weld specimens. That means that the

results of the cross-weld uniaxial specimens can be used directly to obtain the rupture life of the tubes. In addition, they investigated the microstructure of a failed tube and found that creep voids, and hence sub-cracks, initiated in the mid-thickness of the tube, in the Type IV region, and progressed towards the outer surface of the tube.

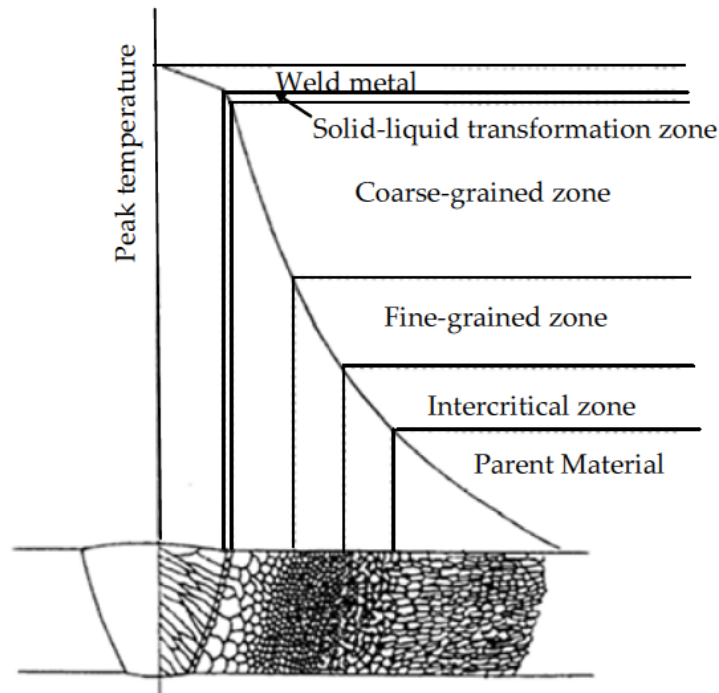


Fig. 2-9: Schematic cross section of a weld showing typical microstructural zones, (Storesund and Tu, 1995).

2.5 CRACKS IN WELDED JOINTS

Cracks in welded joints are classified according to their positions. Type I and Type II cracks occur within weld metal; Type I is confined to weld metal whereas Type II may grow outside the weld metal and into the parent material. Type III cracks occur in coarse grained HAZ. Type IV cracks initiate and grow in a narrow zone of HAZ material, adjacent to the PM/HAZ boundary. Type IV cracking is the most severe form of cracks because it results in the highest rate of

void formation, leading to early failure, when compared with creep tests on the unwelded, homogenous, specimens (Francis *et al.*, 2006), see Fig. 2-10.

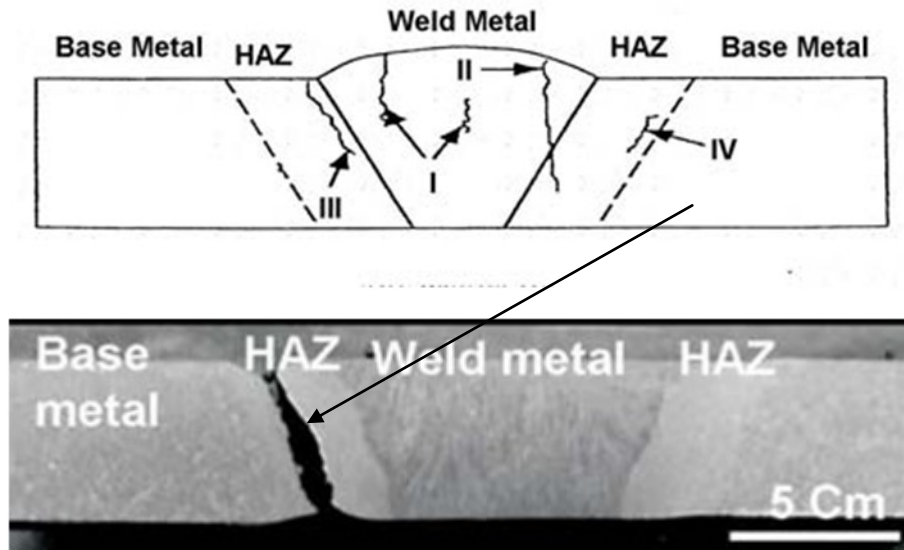


Fig. 2-10: Types of cracking in weld joint of steels on service exposure (Laha, 2007).

2.5.1 Type IV cracks

Type-IV cracks appear in the intercritical region of the HAZ in welded components, that operate under creep conditions. Hongo *et al* (2009) carried out uniaxial creep tests on welded specimens, made from P91 material, with different weld groove configurations, i.e. single U groove and double U groove welds. They found that all of the tested specimens failed in the Type IV region with Type IV cracks. Using the FE method, they predicted the damage position to be the same as in the experiments. Hyde and Sun (2000) also predicted Type IV cracking in a CrMoV pipe weld using damage mechanics FE analyses. They found that, damage initiated in regions near the outer surface of the pipe and move inwards. They also carried out a set of FE analyses using the Kachanov damage model (Kachanov damage model is detailed in Section 5.2.1) and they found that the value used for the multiaxial stress state factor, α , is very

important to being able to predict the fracture location and the life of components that are made from high Cr steel welds. Tabuchi *et al.* (2001) studied the effect of the welding process on Type IV cracking by comparing the creep failure in cross-weld uniaxial specimens cut from Gas Tungsten Arc Welding (GTAW) and Electron Beam Welding (EBW) weldments. They found that in both of the weldment types, the specimens failed in the Type IV regions. However, the width of the HAZ region of the EBW is one-fifth that of the GTAW. Shibli and Le Mat Hamata (2001) performed tests and measured the creep crack growth in a P91 welded pipe; they applied internal gas pressure, at 625°C. The initial cracks were situated in the middle of the HAZ region. They found that the initial cracks deviated until they reached the Type IV region, and then they remained in that region, see Fig. 2-11.

Observation of the creep and creep crack growth in P92 welds suggested that failure in cross-weld uniaxial or CT specimens occurs in the fine-grained HAZ region close to the PM, i.e. the Type IV region (Kim *et al.*, 2008, Falat *et al.*, 2009, Tabuchi *et al.*). Tabuchi *et al.* (2010) and Yamamoto *et al.* (2010) noted that even if the initial cracks were located in the middle of the HAZ region, they deviated to, and grew into, the Type IV region.

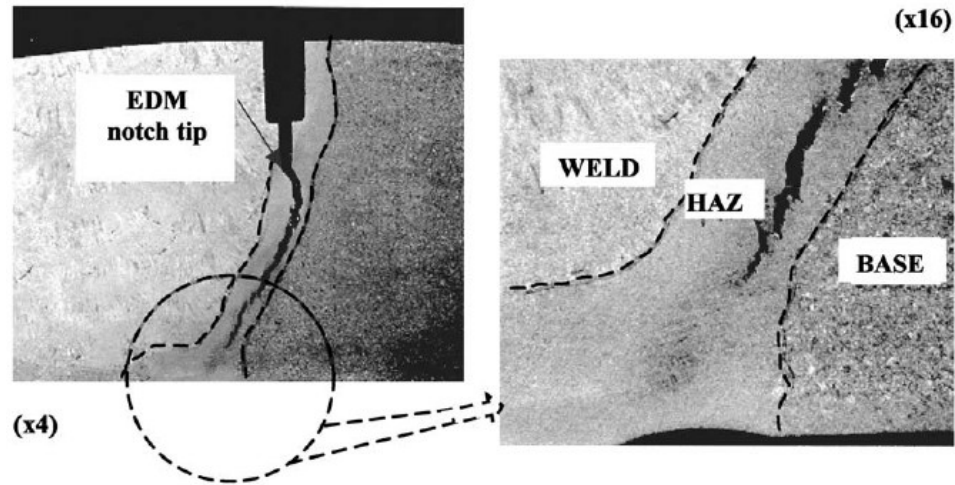


Fig. 2-11: Creep crack growth in P91 tested pipe, at 625°C; the crack grew in Type IV region (Shibli and Le Mat Hamata, 2001). EDM refers to the Electric Discharge Machining process used to cut the notch.

2.6 PREDICTION OF CREEP CRACK GROWTH USING FRACTURE MECHANICS

2.6.1 Introduction

C^* is a fracture mechanics contour integral that can be used to correlate the creep crack growth which occurs in cracked bodies, under mode I loading conditions, through use of the equation:-

$$\dot{a} = D(C^*)^q \quad (2-2)$$

where, \dot{a} is the creep crack growth rate, D and q are material constants.

Material constants D and q can be determined by plotting $\text{Log}(\dot{a})$ against $\text{Log}(C^*)$. The gradient of the plot is the q and the intercept is $\text{Log}(D)$. By determining the values of D and q , it is possible to calculate creep crack growth rates at specific C^* values. Then, it is possible to predict the remaining life of cracked bodies.

2.6.2 C* derivation background

To characterise the stresses and strains ahead of a crack in a cracked body, several parameters can be used. Stress intensity factor, K , can be used for the linear elastic material. For elastic plastic materials, a J contour integral can be used; the J contour integral was firstly proposed by (Rice, 1968). It is defined as a line integral along a contour encompassing the crack tip, starting from the lower surface of the crack and ends at the upper surface, see Fig. 2-12. J integral was found to be path independent and it is given by, (Anderson, 2005), i.e.

$$J = \int_{\Gamma} \left(w dy - T_i \frac{\partial u_i}{\partial x} ds \right) \quad (2-3)$$

where w is the strain energy density, T_i is a traction vector, ds is a small length increment along the contour Γ and u_i is a displacement vector.

The traction vector T_i can be defined as:-

$$T_i = \sigma_{ij} n_j \quad (2-4)$$

where σ_{ij} are the components of stresses, n_j are the components of the unit vector normal to Γ .

The strain energy density, w , is defined as:-

$$w = \int_0^{\varepsilon_{ij}} \sigma_{ij} d\varepsilon_{ij} \quad (2-5)$$

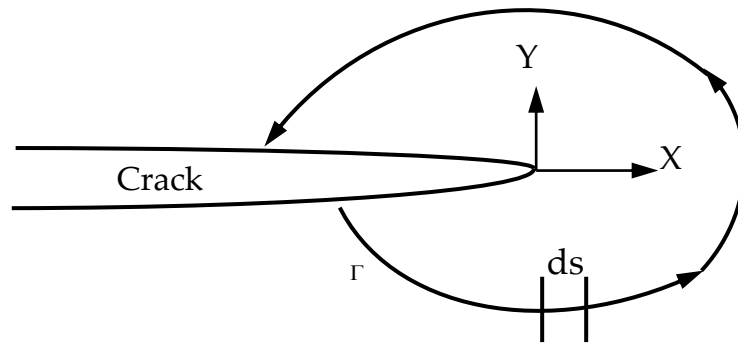


Fig. 2-12: Arbitrary contour around the crack tip used to obtain J contour integral, (Anderson, 2005).

Components which operate at high temperatures, relative to the absolute melting point of the material, are likely to fail due to slow and stable extension of macroscopic cracks (Anderson, 2005). Growth of cracks under steady state creep can be correlated using the C^* parameter. As with J , C^* is a line integral along a contour encompassing the crack tip, starting from the lower surface of the crack and ending at the upper surface of the crack. Because of the fact that creep behaviour is time dependent, strain rates replaced the strains and displacement rates replaced the displacement in the J contour integral, i.e.

$$C^* = \int_{\Gamma} \left(\dot{w} dy - T_i \frac{\partial \dot{u}_i}{\partial x} ds \right) \quad (2-6)$$

and

$$\dot{w} = \int_0^{\dot{\epsilon}_{ij}} \sigma_{ij} d\dot{\epsilon}_{ij} \quad (2-7)$$

It has been shown that C^* is, similarly to J , path independent, e.g. (Halighongde, 2009).

ASTM E 1457-00 (2001) provided a standard method for the measurement of C^* values for CT specimens, shown in Fig. 2-13, using load line displacement rates and creep crack growth data. The load line displacements are measured using extensometers attached to the specimen. The creep crack growth can be monitored using the direct current potential difference (DCPD) technique. Details of methods used to obtain the experimental C^* values, for the P91 and P92 CT specimens, are given in Chapter 4.

2.6.3 C^* , $C(t)$ and K to correlate creep crack growth

The stress intensity factor (K), the contour integral ($C(t)$) and steady state contour integral (C^*) are three parameters that have been used to correlate the creep crack growth rates in cracked bodies. C^* and $C(t)$ are used for ductile creep; $C(t)$ for small-scale creep and C^* for extensive creep. The stress intensity factor, K , is used for creep brittle materials.

C^* values can be calculated from the results of tests on different specimen types, e.g. CT, thumbnail and circumferential cracked round bar (CCRB) specimens. Hyde (1988) calculated C^* using thumbnail and CT specimens. He concluded that, the use of CT specimens remains the simplest and most accurate technique that can be used to calculate C^* values. C^* values, obtained from CT specimen test results, correlate the creep crack growth data better than other specimens do. Standards have been set up for the creep crack growth testing using CT specimens, e.g. (ASTM E 1457-00, 2001).

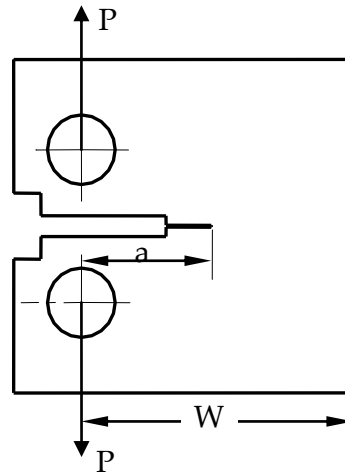


Fig. 2-13: A single material compact tension (CT) specimen.

From the results of creep crack growth tests, it is possible to distinguish between the creep ductile and creep brittle behaviour of materials using the creep crack growth and the load line displacement records. For creep ductile materials, creep crack growth is accompanied by substantial time-dependent creep strain in the region near the crack tip. Further, in creep ductile behaviour the accelerated creep crack growth begins at relatively early stage of creep rupture life, say 40% and occupies most of the fracture life, see Fig. 2-14, (Yokobori, 1999). Creep crack growth in creep ductile materials can be correlated by using the C^* or $C(t)$ parameters. For creep brittle materials, creep crack growth occurs with low creep strain around the crack tip. This means that, the creep strains are comparable to or dominated by the accompanying elastic strains local to the crack tip. Further, accelerated creep crack growth starts at a later stage of the creep rupture life, i.e. approximately 90% of fracture life, see Fig. 2-14, (Yokobori, 1999). Under such steady state creep brittle conditions, K is used as the correlating parameter (ASTM E 1457-00, 2001).

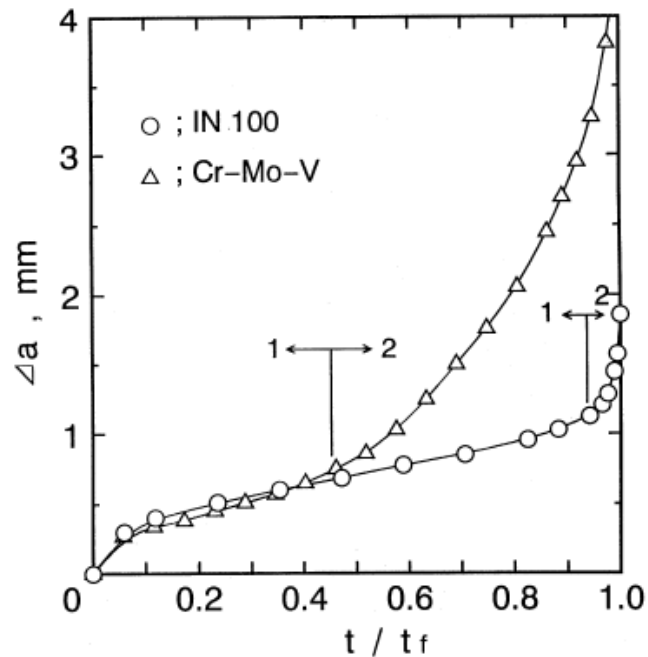


Fig. 2-14: Creep crack growth (CCG) for a creep ductile material, Cr-Mo-V, and a creep brittle material, IN 100. 1 = steady state CCG; 2 = accelerated CCG; t_f = fracture life, (Yokobori, 1999).

Tabuchi *et al* (2009) noticed the creep brittle behaviour which occurred in circumferentially notched round bar specimens made from P92 steel. These specimens were cut from base metal and from welded joints and were tested at different loads and temperatures. They noticed that, for long-term tests, the crack growth was more brittle than that for short-term tests. Under these creep brittle conditions, they also noticed that the crack length and displacement scarcely increase during a steady-state (incubation) period and once cracks began to grow they rapidly accelerated until the final failure happened in a short time later. They attributed that brittle behaviour to the high stress triaxiality in the HAZ ahead of the crack tip.

Sugiura *et al.*(2010) performed tests on the creep crack growth of both P92 PM and cross-weld CT specimens. They found that the PM was more ductile than the HAZ material. That is, the accelerated region of the creep crack growth rate

is about 50-60%, of the total creep crack growth life, for the PM CT specimens and about 20% for the cross-weld CT specimens. Moreover, they concluded that, the incubation time, i.e. the time to reach the accelerated crack growth region, is a key for being able to accurately define the remaining life of cross-weld specimens.

2.6.3.1 Small scale creep

In the small-scale creep of cracked specimens, only a small region of the uncracked ligament, near the crack tip, experiences significant creep deformation, see Fig. 2-15(a). The contour integral, $C(t)$, correlates the creep crack growth occurring in the small scale creep zone. For compact tension specimens, $C(t)$ is given in (ASTM E 1457-00, 2001) as follows:-

$$C(t) = \frac{P\dot{V}_c}{(BB_N)^{\frac{1}{2}}W} (\dot{F}/F) \quad (2-8)$$

and

$$\dot{F}/F = \left[\frac{1}{2(1+a/W)} + \frac{3}{2(1-a/W)} \right] + \frac{\dot{f}(a/W)}{f(a/W)} \quad (2-9)$$

$$\dot{f}(a/W) = 4.64 - 26.64(a/W) + 44.16(a/W)^2 - 22.4(a/W)^3 \quad (2-10)$$

$$f(a/W) = 0.886 + 4.64(a/W) - 13.32(a/W)^2 + 14.72(a/W)^3 - 5.6(a/W)^4 \quad (2-11)$$

where P is the applied load, \dot{V}_c is the creep component of the load line displacement rate, B_N is the net section thickness of side grooved specimens, B is the specimen thickness, W is the specimen width and a is the crack length.

2.6.3.2 Transition creep

Fig. 2-15(b) shows a creep regime for which creep deformation dominates, compared with the elastic and plastic zones, but cannot be said to dominate the entire uncracked ligament of the body, (Landes and Schwalbe, 2004). This creep regime is called the transition creep regime. In transition creep, $C(t)$ is used to characterize the instantaneous field of a stationary crack tip as it approaches the C^* value as time elapses. Using the FE method, it is possible to calculate $C(t)$ for stationary cracks. $C(t)$ reaches a constant value after a long creeping time (Park *et al.*, 2001). $C(t)$ is usually much higher than C^* . $C(t)$ is given as follows for plane strain small scale creep conditions :-

$$C(t) = \frac{K^2(1-\nu^2)}{E(n+1)t} \quad (2-12)$$

where K is the stress intensity factor, ν is Poisson's ratio, E is the modulus of elasticity, n is the creep exponent in Norton's law and t is the time.

From equation (2-12), the transition time from small scale creep to steady state creep is defined by the time at which $C(t)$ becomes equal to C^* and hence it is given by:-

$$t'_T = \frac{K^2(1-\nu^2)}{E(n+1)C^*} \quad (2-13)$$

This equation is used to calculate t'_T for each C^* value, then t_T is the maximum value of t'_T .

Park. *et. al.* (2001), carried out creep crack growth tests on CT specimens cut from the base metal and weld joints of an X20CrMOV121 steel. They calculated

the transition time from small scale to extensive creep. It was found to range from 0.3% to 0.8% of the specimen failure time. It is worth noting that, for CT creep crack growth tests, C^* increases with time and crack length. Therefore, as C^* is in the denominator of the above equation, t_T decreases as C^* increases.

2.6.3.3 Extensive Creep

Extensive creep occurs when the entire uncracked ligament undergoes creep deformation as shown in Fig. 2-15(c). In this case, the region dominated by creep deformation is significant in size in comparison to the crack size and to the uncracked ligament size (ASTM E 1457-00, 2001).

Load line displacement rates, \dot{V} , is time-dependent and so is C^* . Therefore, C^* is, sometimes, designated by $C^*(t)$, e.g. (Park *et al.*, 2001). When the crack growth is slow compared to the expansion of the creep zone, the crack tip is surrounded by an extensive creep zone, and C^* values are, usually, found to correlate the corresponding creep crack growth rates. ASTM E 1457-00 calculates C^* for compact tension specimens as follows:-

$$C^* = \frac{n}{n+1} \frac{P\dot{V}}{B_N(W-a)} \left(2 + 0.522 \left(1 - \frac{a}{W} \right) \right) \quad (2-14)$$

where n is the creep exponent in Norton's creep law, i.e. $\dot{\epsilon}_{min} = A\sigma^n$, P is the applied load, \dot{V} is the load line displacement rate, B_N is the net section thickness of side grooved specimens, W is the specimen width and a is the crack length.

Laiarinandrasana *et al.* (2006) investigated the relationship between creep crack growth rate, \dot{a} , and C^* values, in 316L steel. Though they used different specimen geometries and carried out CCG tests at different loads and different temperatures, they obtained almost a unique relationship. They then collected

all the curves in one curve and considered that curve to be the master curve for the tested material. Similarly, Yamamoto *et al.* (2010) studied the creep crack growth in Mod. 9Cr-1Mo, using PM and cross weld CT specimens, at different temperatures, and constructed a master curve. The master curve can be used to predict creep crack growth rates for cracked bodies that do not have C^* formula, by carrying out FE analyses and obtaining the C^* value and then use the master curve to obtain the corresponding \dot{a} . Further, Tabuchi *et al.* (2001) tested the effects of welding processes on the correlation between \dot{a} and C^* values. They tested the creep crack growth in P122 cross-weld CT specimens. Those welds were made using gas tungsten arc welding and using electron beam welding. No difference has been found between the \dot{a} vs. C^* curves for these two weldments. Shibli and Le Mat Hamata (2001) mentioned that there is no effect of microstructure on the da/dt vs. C^* correlation. They obtained this result by testing CCG in P22 cross weld CT specimens, at 550°C, where the initial cracks were located in the fine-grained HAZ region for some specimens and in the coarse-grained HAZ region for others.

The formulas available for calculating C^* have been developed for standard specimens geometries, e.g. equation (2-14), these were mainly derived for homogenous CT specimens. Load line displacement rates from CT specimen testing are needed in order to calculate C^* values using equation (2-14). However, for non-standard specimens or when load line displacements are not available, the Reference Stress Method can be used. Hyde (1988) used the Reference Stress Method to calculate C^* for thumbnail surface cracked tensile specimens. He found that Reference Stress based C^* values can be used to reasonably accurately to correlate creep crack growth data and to predict creep crack growth rates in engineering components.

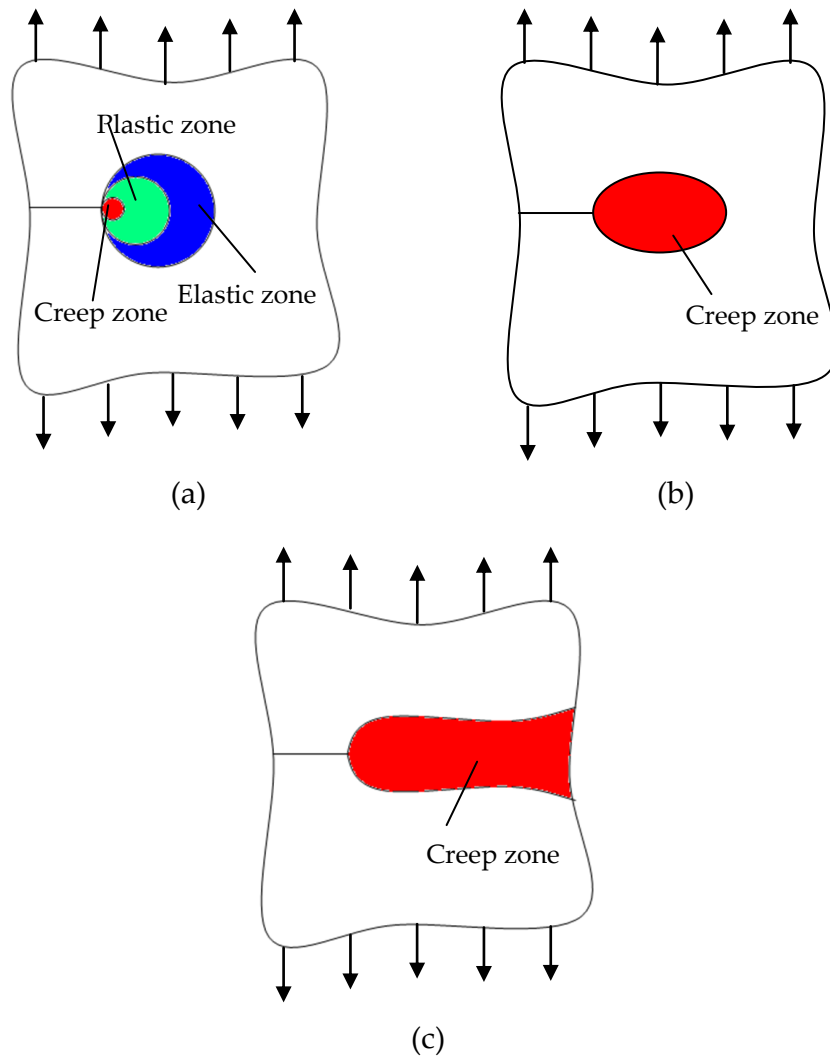


Fig. 2-15: Three regimes of creep deformation in a structural element with a crack-like defect, (Landes and Schwalbe, 2004).
(a) Small scale creep, (b) Transition creep, (c) Extensive creep.

2.6.4 Creep crack growth prediction using C^*

C^* is used to predict the creep crack growth in materials which operate at high temperatures. Studies have been carried to investigate the applicability of C^* and other parameters, that could be used to correlate the creep crack growth for different materials. For example, Dogan and Petrovski (2001) correlated the creep crack growth in P91, at 600°C, to both C^* and K . They found that, C^* showed less scatter and more accurate correlation. Xia *et al.* (1998) obtained the

same conclusion when they studied the creep crack growth in Wospaloy, at 700°C.

The C^* parameter was originally developed to correlate creep crack growth in homogenous materials, (ASTM E 1457-00, 2001). However, it is now being applied to heterogeneous materials, e.g. weldments. Experimental studies, e.g. (Dogan and Petrovski, 2001, Yamamoto *et al.*, 2009, Park *et al.*, 2001), showed that, C^* values correlate the creep crack growth in cross-weld CT specimens. Numerical studies, e.g. (Halighongde, 2009), have shown that C^* for heterogeneous material is path independent, under some circumstances. Therefore, C^* has been used to predict the creep crack growth in welded components.

Creep crack growth tests are, generally, carried out at a constant temperature and for a range of loads. However, for example, (Yamamoto *et al.*, 2010) carried out creep crack growth tests on P91 weldments with various loads and temperatures. The results are shown in Fig. 2-16, where good correlation, between the C^* values and the creep crack growth rates, can be seen. Moreover, the relationship between C^* values and creep crack growth rates, for both the base material (BM) and the weld joint (WJ) support the use of the C^* parameter for the heterogeneous specimens. Similarly, Tabuchi *et al* (2010) studied the creep crack growth for P92 PM and cross-weld CT specimens, at different temperatures and loads. They also obtained a unique relationship between the da/dt and the C^* values, see Fig. 2-17. They concluded that the fracture life for the cross-weld specimens is 1/4 to 1/2 those of the parent material specimens.

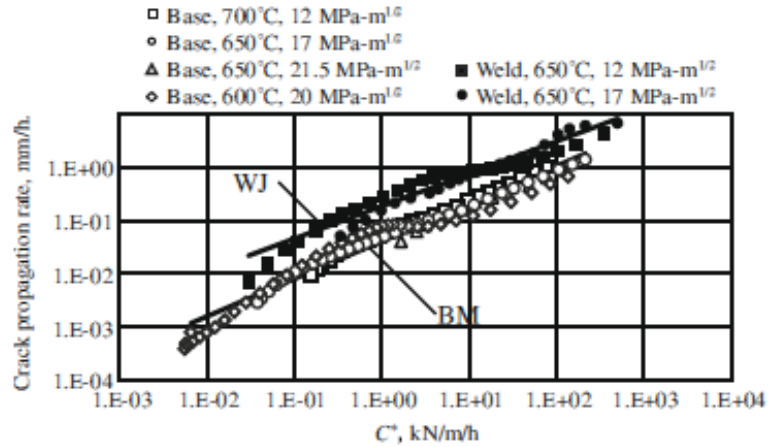


Fig. 2-16: Relationship between C^* and creep crack growth for P91 weldment at different temperatures (Yamamoto *et al.*, 2010).

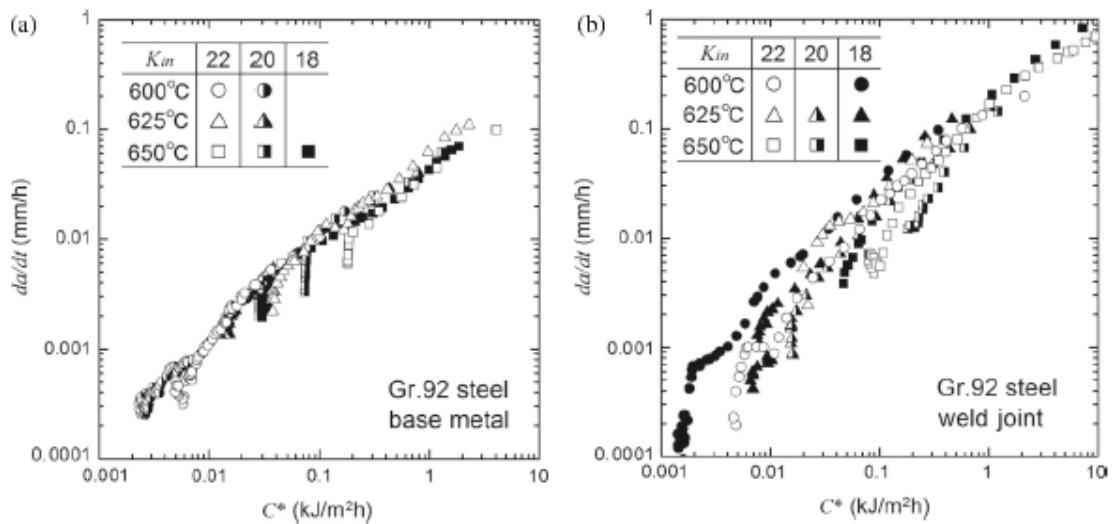


Fig. 2-17: da/dt against C^* for P92 at different temperatures for (a) base material and (b) weld joints (Tabuchi *et al.*, 2010).

2.6.5 FE prediction of C^*

The FE method can be used to obtain C^* values for cracked bodies, working under creep conditions. A commercial FE package, ABAQUS, has been used to obtain contour integral, $C(t)$, using a built-in function or by using the load line displacement rates of specimens, e.g. Xia *et al.* (1998).

Tabuchi *et al.*(2010) used the FE method to obtain C^* values for P92 weld CT specimens. They used 2D stationary crack models, where the crack length was kept the same during each analysis, with plane strain elements and with plane stress elements. Further, the C^* values for the cross-weld CT specimens were from 2 to 4 times higher than those of the PM specimens.

Creep crack growth in CT specimens can be modelled, within ABAQUS, using a nodes release technique. Zhao *et al.* (2001) modelled the creep crack growth in CT specimens made of Nickel based super alloy, Waspaloy, at 650°C. Due to the symmetry of PM CT specimen, they modelled only one-half of it. They modelled a rigid body and paired it to the plane of symmetry of the CT specimen. Then they allowed the nodes, on the plane of symmetry, to be released, from that rigid body. In order to ease the creating of the model and releasing the nodes; they used linear elements.

Another example of the use of the nodes releasing technique, to simulate the creep crack growth, is given in (Laiarinandrasana *et al.*, 2006). They modelled circumferential cracked round bars (CCRB) using axisymmetric elements. They used an experimental creep crack growth curve as the fracture criterion. They obtained the crack opening displacement (COD) against time data which was then used to calculate C^* values. They obtained good agreement between the C^* values obtained using the experimental load line displacement rates and those obtained using the FE COD rates. They also used the same nodes releasing technique with CT specimens. Fig. 2-18 shows the deformed and undeformed shapes of the CCRB specimens using the nodes release technique and the results are compared with the corresponding experimental results. The nodes release approach has also been used by other workers, for example, (Xia *et al.*, 1998) (Halighongde, 2009).

The nodes release technique has been used, in this thesis, to simulate the creep crack growth in P91 PM CT specimens. 2D plane strain and plane stress elements have been used with various material constants. Creep crack growth data have been used as fracture criterion. The nodes release technique and its application to CT specimens are detailed in Section 4.6.1.

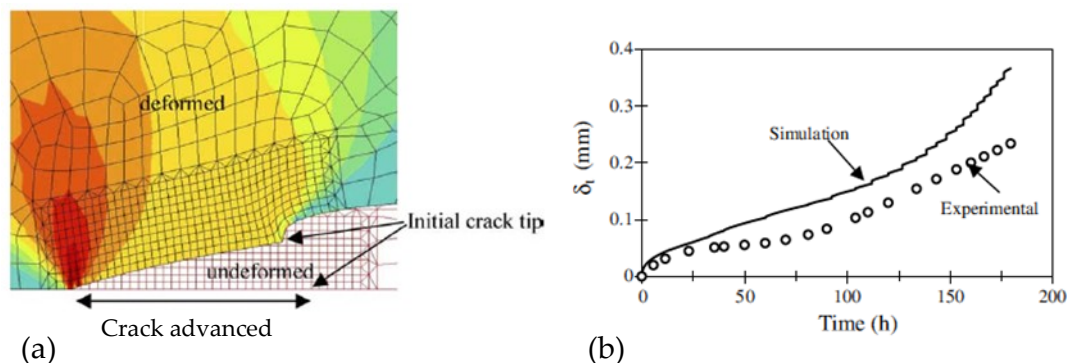


Fig. 2-18: FE results of the CCRB analyses.

- (a) deformed and undeformed mesh ahead of the crack tip, and
- (b) FE and experimental crack opening displacement (Laiarinandrasana *et al.*, 2006).

2.7 PREDICTION OF CREEP CRACK GROWTH USING DAMAGE MECHANICS

2.7.1 Introduction

The damage mechanics approach accounts for the loss in the load carrying capacity during the creep process due to material deterioration. This loss, in the load carrying capacity, is due to the coalescences of the voids and microcracks that are formed on grain boundaries and to the material degradation which occurs. The generalised damage mechanics approach can be used to predict progressive deterioration and ultimate failure in components working under creep conditions. Kachanov (1958) was the first to model the deterioration of a creeping material by using a single parameter known as the damage parameter, ω , where ($0 < \omega < 1.0$). Kachanov's model was, then, generalised to multiaxial

stress cases by Hayhurst (1972). The Kachanov damage model is detailed in Section 5.2.1. A three state variables model has been developed by Perrin and Hayhurst (1996). The three state variables model accounts for the strain hardening occurred during primary creep, the evolution of carbide precipitates and intergranular cavitation damage. The three-variables constitutive equations are given by (Perrin and Hayhurst, 1999):-

$$\dot{\epsilon}_{ij} = \frac{3S_{ij}}{2\sigma_{eq}} A \sinh \left[\frac{B\sigma_{eq}(1-H)}{(1-\phi)(1-\omega)} \right] \quad (2-15)$$

$$\dot{H} = (h\dot{\epsilon}_{eq}/\sigma_{eq})(1 - (H/H^*)) \quad (2-16)$$

$$\dot{\phi} = (K_c/3)(1 - \phi^4) \quad (2-17)$$

$$\dot{\omega} = CN\dot{\epsilon}_e(\sigma_1/\sigma_{eq})^v \quad (2-18)$$

where A , B , C , h , H^* and K_c define the uniaxial creep behaviour, and the stress state index v defines the multiaxial stress rupture criterion. σ_1 is the maximum principal stress and σ_{eq} is the von Mises stress. S_{ij} is the deviatoric stress tensor. $N = 1$ for $\sigma_1 > 0$ and $N = 0$ for $\sigma_1 < 0$. H , ϕ and ω are the three state variables which account for strain hardening, carbide precipitate spacings and damage integration criterion, respectively. H represents the strain hardening which occurs during primary creep. It ranges from zero, initial condition, to, as strain is accumulated, H^* . ϕ accounts for the carbide precipitates and ranges from zero to one. ω defines the damage cavitation and ranges from 0, no damage, to 1/3, full damage. More details of the three state variables model can be found in (Perrin and Hayhurst, 1996, Perrin and Hayhurst, 1999).

Hyde *et al.* (2006c) used uniaxial and notched bar creep test data to establish the materials behaviour models for two P91 pipes using the Kachanov model and

the three variables model. They found that, within the range of the applied stresses, both models resulted in similar failure times and minimum creep strain rates. Moreover, the two models predicted the same failure location for the notched bar specimens. They also found that, the three-variable model could accurately predict failure life for stresses outside the stress range used to calculate the material constants. However, the one-variable model is used widely due to its simplicity and ease in determination of its material properties.

Another single variable damage model was proposed by Liu and Murakami (1998). Liu and Murakami found that, for crack situations, the Kachanov model is mesh dependent and the damage is localised into a single row of elements. They considered the main causes of the mesh dependency of the Kachanov model to be the stress singularity in front of crack-tip and stress sensitivity of damage evolution equation (the Kachanov model is described in detail in Section 5.2.1). Liu and Murakami investigated their proposed model by studying creep crack growth in a perforated plate under tension. The results obtained indicated that the Liu and Murakami model is relatively mesh independent. A detailed study of creep crack growth in CT specimens using the Liu and Murakami model is given in Chapter 6.

2.7.2 Material properties

Accurate determination of material properties plays an important role in the modelling and predicting of materials, and hence components, behaviours. Whatever material model to be used, i.e. one-variable damage model or three-variable damage model, a set of material constants must be determined. Data obtained from uniaxial and notched bar creep tests are used to determine the material properties for both damage models (Hyde *et al.*, 2006c, Hyde *et al.*, 2010, Hyde *et al.*, 2004a). Standard uniaxial and notched bar specimens are used when sufficient test material is available. However, other techniques and specimen

designs are needed if sufficient test material is not available, or if it is needed to test, for example, materials removed from a running power plant. Further, different techniques are needed to test the small material zones within a HAZ.

Small specimen types can be used to obtain creep properties when it is not possible to use other conventional specimens. Fig. 2-19 and Fig. 2-20 show the geometries of a conventional sub-size uniaxial specimen, an impression creep specimen, a small punch specimen, and a ring specimen. The importance of the use of small specimens is that it can be used to measure local creep properties of materials. The ring specimen, Fig. 2-20, was introduced, recently, by Hyde and Sun (2009b), where different designs, of the ring specimens, have been shown and investigated. Ring specimens are easy to manufacture, compared to other specimens. The loading system, experimental and alignment procedures used are simple to operate. Creep tests on small specimens measure creep strain in the conventional sub-size specimens while it measures displacements of indenter, punch and loading pins in impression, small punch and ring creep specimens, respectively. These displacements are converted to the equivalent uniaxial creep strain using suitable conversion factors. Details of the displacements conversion factors can be found in (Hyde and Sun, 2009b).

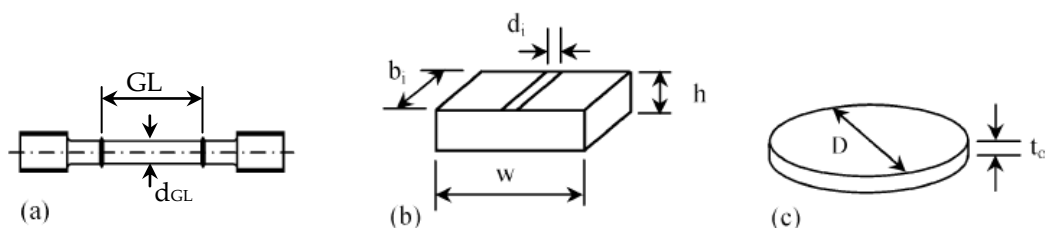


Fig. 2-19: Small specimen types (Hyde and Sun, 2009b):

- (a) conventional sub-size uniaxial specimen ($GL \approx 5\text{--}12\text{mm}$, $d_{GL} \approx 1\text{--}3\text{mm}$).
- (b) impression creep specimen ($w = b_i \approx 10\text{mm}$, $d_i \approx 1\text{mm}$, $h \approx 2.5\text{mm}$, loading area is $b_i \times d_i$).
- (c) small punch specimen ($D \approx 8\text{mm}$, $t_o \approx 0.5\text{mm}$).

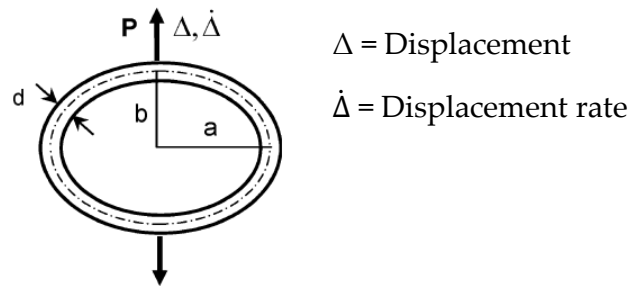


Fig. 2-20: Ring specimens, (Hyde and Sun, 2009b).

As mentioned, the HAZ region may be divided into several different sub-regions, i.e. a coarse-grained zone, a fine-grained zone and an intercritical zone, usually referred to as the Type IV region, as shown in Fig. 2-9. The intercritical zone is the weakest region of a weld. Therefore, it is very important to accurately determine the material properties for the Type IV region. Some workers suggest simulating HAZ material by heat treatment of PM until it has the same microstructure as the Type IV region, and then using conventional test specimens and methods to obtain creep properties for the simulated Type IV material, e.g. (Smith *et al.*, 2003, Tabuchi *et al.*, 2010, Hongo *et al.*, 2009). The simulated Type IV material is, usually, the weakest condition that can be obtained from the PM (Perrin and Hayhurst, 1999). Other workers, simply, used the results of cross-weld conventional creep specimens to determine the material properties for the Type IV region, e.g. (Falat *et al.*, 2009). Storesund and Tu (1995) compared the results of simulated Type IV specimens to those of cross-weld specimens. they found that the failure times of simulated Type IV tests are similar to those of cross weld tests.

Sometimes and due to material limitations, material constants for HAZ material and/or WM must be taken as those for PM, for simplification. Hyde *et al.* (2006a) carried out creep damage analyses on an Inco718 welded sheet at 620°C. They used the material creep and damage constants for the HAZ and the WM as

those for the PM. They, also, carried out hardness tests across the HAZ, WM and PM to identify the variation of the material properties across the weld. Their results indicated that the variations of creep properties across the weld are likely to be insignificant. Further, Hayhurst (2001) presented the results of FE analyses which were carried out on a branched pipe with the use of three-variables damage model. In those analyses, a four materials model, i.e. PM, WM, HAZ and Type IV material was used and it was assumed that the material constants for the HAZ material are the same as those for the PM.

2.7.2.1 Multiaxiality

Multiaxial stress states exist in creep tests if the specimen has cross sectional discontinuities, e.g. notches or cracks, or when the specimen consists of more than one material with different creep properties, e.g. cross-weld specimens which include PM, WM, and HAZ, (Smith *et al.*, 2003). For example, the Type IV regions of cross-weld specimens are constrained by stronger materials, i.e. PM and WM, resulting in the creation of a multiaxial state stress; this may play a big role in the Type IV cracking which is observed. Multiaxial parameters, such as the following, have been introduced to allow the characterization of its effect, (Seliger and Gampe, 2002):

$$TF = \frac{\sigma_1 + \sigma_2 + \sigma_3}{\sigma_{eq}} \quad (2-19)$$

where TF refers to Triaxiality Factor, and

$$\sigma_{eq} = \sqrt{\frac{1}{2} [(\sigma_1 - \sigma_2)^2 + (\sigma_1 - \sigma_3)^2 + (\sigma_2 - \sigma_3)^2]} \quad \text{is the von Mises stress}$$

and σ_1 , σ_2 and σ_3 are the principal stresses.

The multiaxial parameter, α , is described, in detail, in Chapter 5. The rupture stress, σ_r , which controls the failure of a component, is defined as:

$$\sigma_r = \alpha\sigma_1 + (1 - \alpha)\sigma_{eq} \quad (2-20)$$

where σ_1 is the maximum principal stress.

The determination of α for single materials, e.g. PM and WM, can be achieved by use of notched bar specimens test results and FE analyses. The α value that gives the FE failure time the same as the experimental failure time is taken as the correct α value. The more experimental tests for which results are obtained, the more accurate the α value that will be obtained. However, even, one experimental test can be used to estimate the α value, e.g. (Hyde *et al.*, 1996).

Hongo *et al.* (2009) studied, experimentally and using the FE method, the creep damage in cross-weld specimens made of a 9Cr-1Mo steel. They found that the maximum creep damage occurred at the same location where the triaxial factor, TF , is maximum. Moreover, they found that the FE failure times were practically the same as the experimental failure times when $\alpha = 0.4$. They have determined this value of α by fitting the failure times of an FE cross-weld uniaxial specimen to the corresponding experimental failure times. Hyde *et al.* (2010) fitted FE creep crack growth for the 316 stainless steel, using CT specimens, to corresponding experimental results, at 600°C; these were used to obtain the value of α . To validate the value of α obtained, they predicted the creep crack growth in thumbnail specimens and obtained very good agreement between the predicted and the experimental results. The approach used is described in detail in Chapter 6 for P91 at 650°C and for P92 at 675°C.

Ogata *et al.*(2009) studied creep rupture behaviour in cross-weld P91 uniaxial specimens, at 650°C. In order to clarify creep voids formation and accumulation,

they interrupted creep tests at 20%, 40%, 60% and 80% of failure time. Moreover, they carried out stress analyses for these tests. They found that the location of the maximum number of creep voids, in the experiments, was the same as the location of the highest triaxiality, in the analyses. Moreover, the tested specimens failed in the Type IV region, which is where creep voids and stress triaxiality are greatest.

Sugiura *et al.* (2010) studied the relationship between the multiaxial parameter, TF , and the creep crack growth in P92 weldments. They found that the triaxiality for the cross-weld CT specimen is higher than that for the PM CT specimens. Moreover, they found that, for the cross-weld CT specimens, the maximum triaxiality occurred in the Type IV region, where the hardness is at its minimum, see Fig. 2-21. Further, they found that the time at which the triaxiality reached its maximum value, in the Type IV region, is the same as the experimental incubation time. Therefore, they concluded that, it is possible to predict the incubation time by carrying out FE analyses.

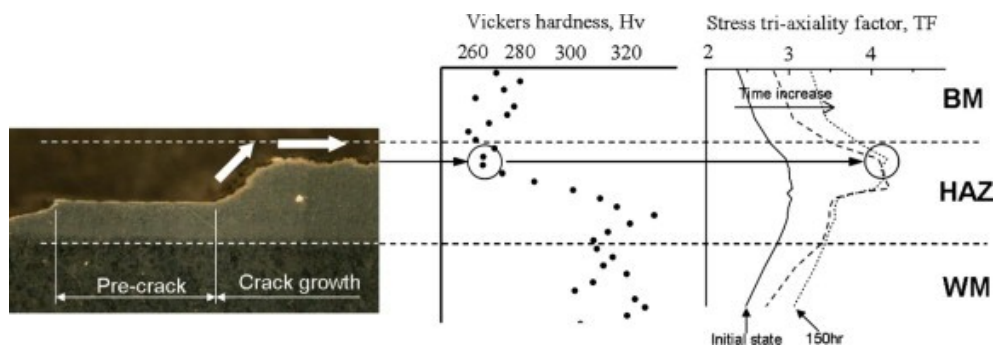


Fig. 2-21: Relationship between creep crack growth path of CT specimen, Vickers hardness and stress triaxiality (Sugiura *et al.*, 2010).

CHAPTER 3.

EXPERIMENTAL WORK

3.1 INTRODUCTION

This chapter details the experimental programme of creep and creep crack growth (CCG) testing of P91 and P92 materials and welds. Uniaxial and notched bar specimens were tested to obtain the materials creep and creep rupture data for parent material (PM) and weld metal (WM). Creep data for HAZ material was obtained using impression creep tests and cross-weld uniaxial, waisted and notched bar specimens. Compact tension (CT) specimens were used to study CCG in P91 and P92 weldments. Creep and CCG tests were carried out at 650°C for the P91 material and at 675°C for the P92 material. Load line displacements were recorded from testing the CT specimens and crack length was monitored using the potential difference (PD) method. The load line displacement rates and the corresponding crack lengths were then used to calculate C^* , a fracture mechanics parameter used to correlate creep crack growth rates of cracks in cracked specimens such as CT specimens.

CT specimens were cut from the P91 and P92 PM and from across the welds. The initial cracks in the cross-weld CT specimens were located on the boundary between the PM and HAZ material, i.e. in the Type IV region. Macrostructure analyses and hardness tests were carried out on some of the CT specimens to verify the correct locations of the initial cracks. The effects of side grooves, materials variability and welding direction on the CCG were also investigated.

3.2 WELDS AND SPECIMENS

3.2.1 P91 welds

A disc type weldment of thickness 50 mm was made of P91 parent material using a suitable consumable, i.e. a 9CrMoNbV weld metal, provided by Metrode. This welding was made using the manual metal shielded arc welding process. Fig. 3-1 shows schematic diagrams of the P91 weldment, welding grooves geometry and the polished and etched welding cross section. The weldment was then heat-treated at 761°C for three hours to relieve the welding induced residual stresses. Therefore, this weldment will be practically free of any residual stresses.

3.2.2 Specimens for creep and creep rupture tests

Uniaxial, notched bar, waisted and impression creep specimens were used to obtain creep and creep rupture data for the P91 and P92 materials. These specimens were cut from the P91 weld, shown in Fig. 3-1, and from a P92 welded pipe; details of the P92 welded pipes is given in Section 3.2.4. Fig. 3-2 shows a standard uniaxial creep test specimen with a gauge length of 50mm and gauge length diameter of 10mm. These uniaxial specimens were used to obtain the P91 and P92 creep data.

Determination of creep and creep rupture properties for the HAZ material is more difficult than that for PM or for WM. Impression creep tests are currently used to obtain the creep data for HAZ material, while the creep rupture data can be determined using cross-weld uniaxial, notched bar and waisted specimens. Other small specimens technologies, such as small punch and ring specimen testing can be used to determine the creep behaviour of the HAZ material. Finite element analyses are required together with the results of cross-weld specimen tests to accurately define and verify the HAZ material constants.

Creep rupture test data were obtained using notched bar specimens. The geometry and dimensions of the notched bar specimen are shown in Fig. 3-3. The stress applied to the notched bar specimens was calculated at the notch cross-section. Single material and cross-weld notched bar specimens were tested. The single material notched bar specimens were used to obtain rupture data for the PM and WM of both the P91 and P92 steels. The cross-weld notched bar specimens were used to obtain rupture data which were related to the HAZ material properties. A cross-weld notched bar specimen consists of PM, HAZ and WM with the centre of the notch being positioned on the boundary between the PM and HAZ material. Therefore, the creep rupture data obtained is related to Type IV material. Results for the P91 single material and cross-weld notched bar specimen tests have been reported in (Hyde *et al.*, 2004a) and are included in Table 3-2. The results of the notched bar specimen tests for the P92 weldment are given in Table 3-4.

In addition to the cross-weld notched bar specimens, cross-weld waisted specimens were also used to obtain creep rupture data for the HAZ material. The geometry and dimensions of the cross-weld waisted specimens are shown in Fig. 3-4. In these specimens, the PM/HAZ boundary was positioned in the centre of the waisted section. P91 cross-weld waisted specimens were tested and their results were reported in (Hyde *et al.*, 2004a) and are included in Table 3-2. The results of the waisted specimen tests for the P92 weldment are given in Table 3-4.

Cross-weld uniaxial specimens have been used to obtain creep and creep rupture data for the P92 HAZ material. The cross-weld uniaxial specimen has the same geometry and dimensions as the single material uniaxial specimens but it consists of PM, HAZ and WM, see Fig. 3-5. The results of the creep tests, carried out on the cross-weld uniaxial specimens, are in the form of strain-time

records. The applied stresses and failure times are used to obtain the creep rupture data, for the HAZ material, while the applied stress and the minimum creep strain are used to obtain the material constants A and n .

Impression creep specimens, shown in Fig. 3-6, were used to obtain creep data for HAZ material. Square specimens with dimensions of $w \times b \times h = 10 \times 10 \times 2.5$ mm and $d = 1$ mm were used for the P91 HAZ material. These dimensions are $8 \times 8 \times 2$ and $d = 0.8$ mm for the P92 HAZ material. Definitions of w , b , h , and d are given in Fig. 3-6. Constant loads were applied to the specimens via a rectangular indenter from the PM side; to relate the obtained material data to the Type IV region; often the weakest region of a weld. Details of impression creep tests can be found in (Hyde and Sun, 2009a). From Impression creep tests, the displacement of the indenter against time is measured. This displacement-time relationship is related to creep properties of a relatively small volume of material in the immediate vicinity of the indenter. The relationship between load applied to the specimen and the equivalent uniaxial stress is given by, (Hyde and Sun, 2009a):-

$$\sigma = \eta \frac{P}{ab} \quad (3-1)$$

where, σ is the equivalent uniaxial stress, η is a conversion factor equals to 0.43 for the dimensions used for the impression creep test specimens, P is the applied load, d is the indenter width and b is the specimen length, see Fig. 3-6. It is worth noting that η is geometry dependent and it is 0.43 for the specific geometry and dimensions shown in Fig. 3-6, where $h/d = 2.5$ and $w/d = 10$.

The indenter displacement can be converted to an equivalent creep strain using the following relationship:-

$$\varepsilon^c = \frac{\Delta^c}{\beta d} \quad (3-2)$$

where ε^c is the equivalent uniaxial strain, Δ^c is the indenter displacement, β is a conversion factor equal to 2.18 for the dimensions used for the impression creep specimens (where $h/d = 2.5$ and $w/d = 10$), d is indenter width. Similar to η , β is geometry dependent.

Results of P91 creep and creep rupture tests, at 650°C , are reported in (Hyde *et al.*, 2004a) and summarised again in Section 3.4. These results will be used in this study to obtain the P91 material constants for the Liu and Murakami damage model (the Liu and Murakami damage model is detailed in Section 5.2.2).

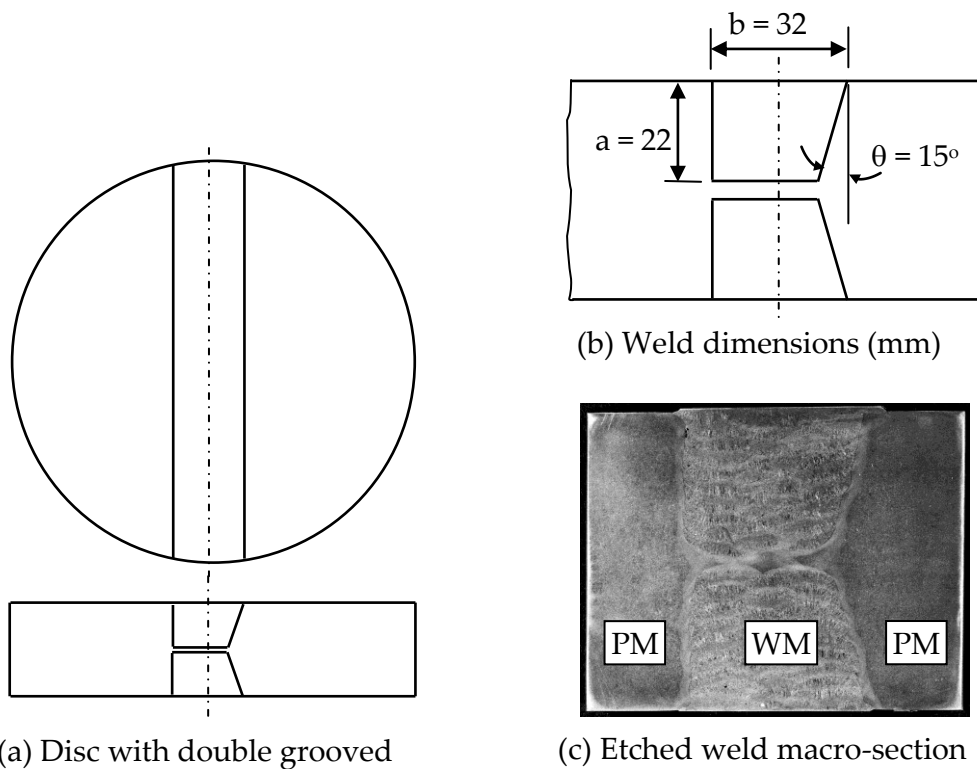


Fig. 3-1: P91 weldment from which all the specimens were cut (Hyde *et al.*, 2004a).

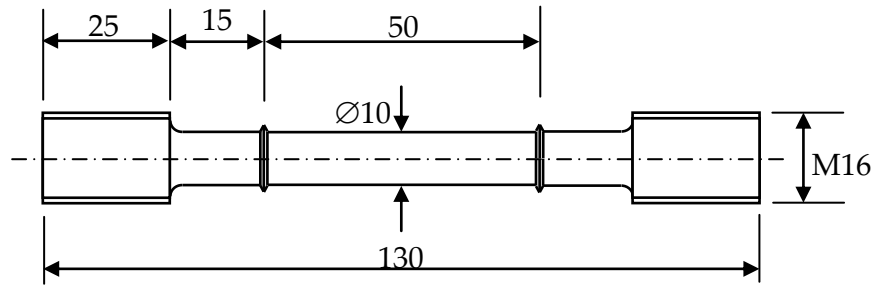


Fig. 3-2: Uniaxial creep test specimen.

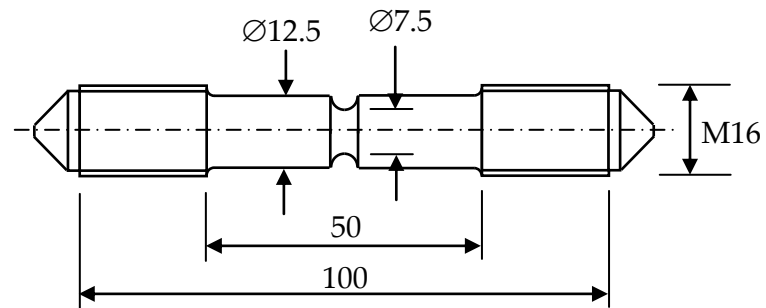


Fig. 3-3: Notched bar specimen (dimensions in mm).

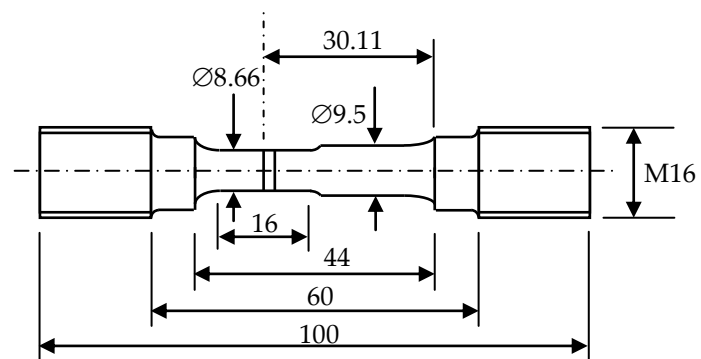


Fig. 3-4: Cross-weld waisted specimen (dimensions in mm).

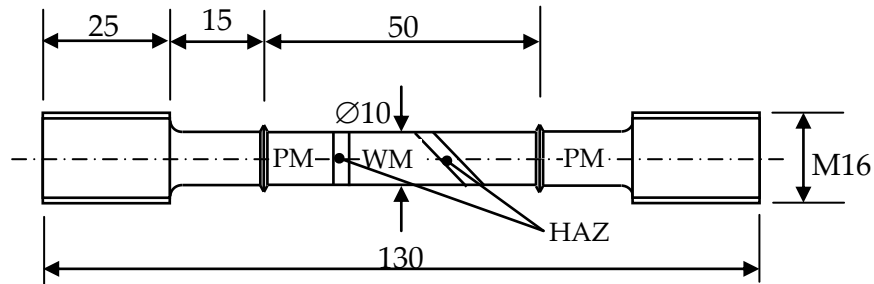


Fig. 3-5: Cross-weld uniaxial specimen.

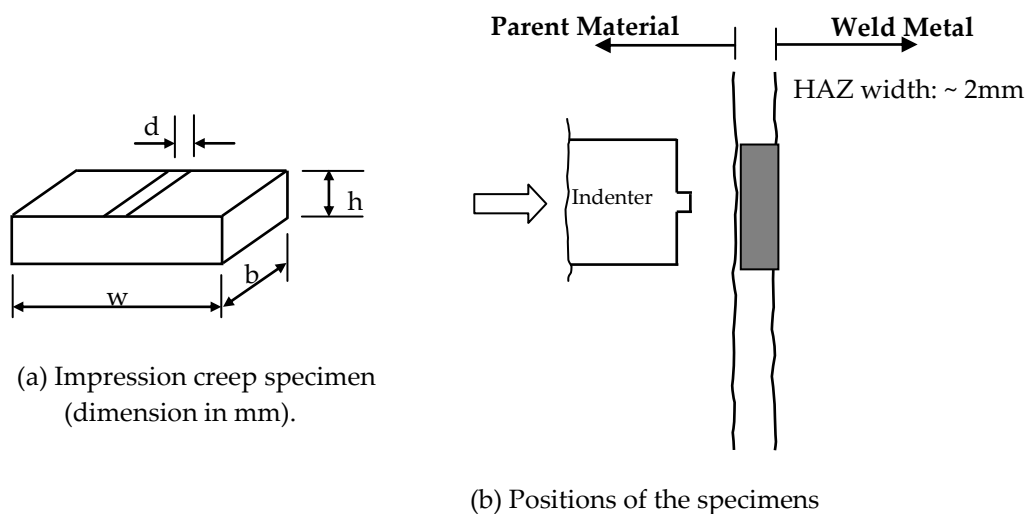


Fig. 3-6: HAZ impression creep specimens and their positions in the weldments, tested from the PM side.

3.2.3 P91 CT specimens

CT specimens were used to study creep crack growth in P91 weldments. These specimens were cut from the P91 PM and across the P91 weld. Fig. 3-7 shows the geometry and dimensions of a CT specimen. These CT specimens conform with the ASTM standard (ASTM E 1457-00, 2001). The CT specimen's width, W , is a characteristic dimension of CT specimens and, in general, it should be as large as practically possible. The length is determined based on the testing facility and the availability of tested materials. W is 32 mm for all of the CT specimens tested in this study. The crack length, a , for these specimens is the distance between the loading point and the crack tip. B is the specimen's

thickness and if the specimen is side grooved, then the net section thickness is B_N , as shown in Fig. 3-7.

Four P91 PM CT specimens were tested, i.e. CT1, CT2, CT3 and CT4. CT1 was a plain specimen, i.e. without side grooves. CT2 was partially side grooved, i.e. the depth of the groove on each side of the specimen was 5% of the specimen's original thickness (B). CT3 and CT4 were fully side grooved, i.e. the depth of the groove on each side of the specimen was 10% of the specimen's original thickness. The side grooves are recommended by ASTM (ASTM E 1457-00, 2001) to ensure that a straight crack front is produced, these avoiding crack tunnelling. These variations of side groove depths were chosen to investigate the effects of the side grooves on creep crack growth. The output of these investigations are given in the experimental results sections. ASTM E 1457-00 (2001) specifies the groove depth to be 10% of the specimen's original thickness.

Electric Discharge Machining (EDM), also known as wire erosion machining, was used to cut the initial cracks. The wire diameter, 0.25 mm, was the smallest size available. This method enabled the initial crack length and position to be accurately defined prior to the test commencement.

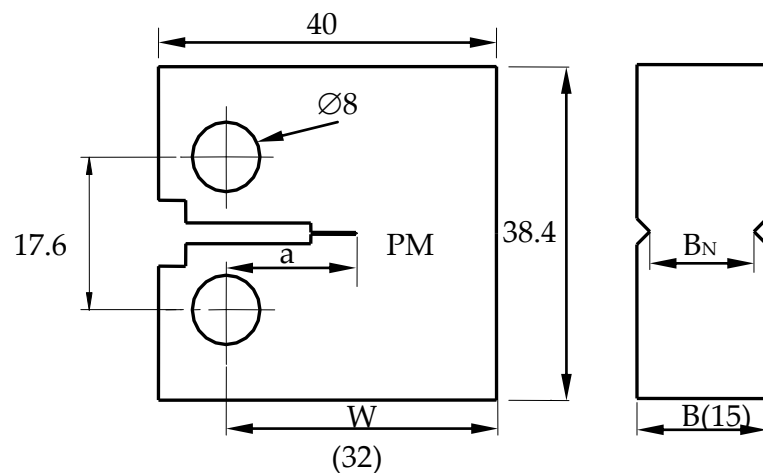


Fig. 3-7: Parent metal CT specimen. Plain specimen's front view (Left) and grooved specimen's side view (Right). (dimensions in mm).

P91 PM and cross-weld CT specimens were cut from a P91 weldment. The P91 PM CT specimens were cut from the PM side of the P91 weldment, shown in Fig. 3-1, while the cross-weld specimens were cut across the weld. Therefore, the cross-weld CT specimens consist of PM, HAZ material, and WM. The cross-weld CT specimens were cut so that the initial cracks were located, as far as practically possible, on the PM/HAZ boundary, i.e. in the Type IV region. In order to accurately position the initial cracks, the cross-weld CT specimens were, firstly, polished and etched to show the PM/HAZ boundary then wire erosion machining was used to cut the initial cracks. Fig. 3-8 shows a schematic drawing of the P91 weldment and the sampling position for the cross-weld CT specimens. Fig. 3-9 shows the geometry and dimensions of the cross-weld CT specimens. All of the P91 cross-weld CT specimens were fully side grooved.

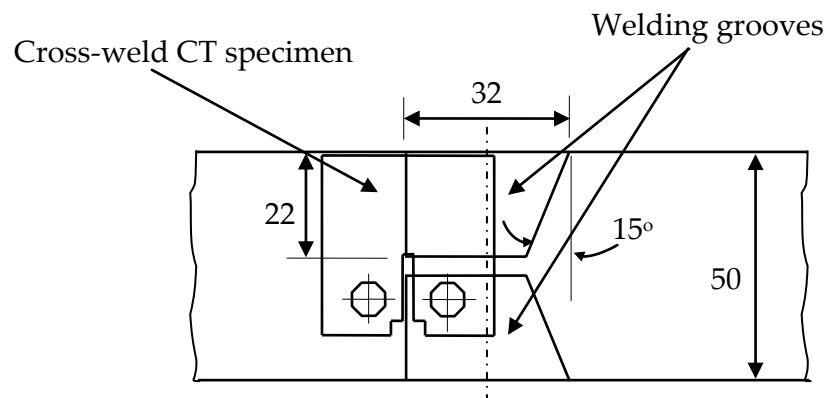


Fig. 3-8: Schematic drawing of the P91 weldment and cross-weld CT specimen (dimensions in mm).

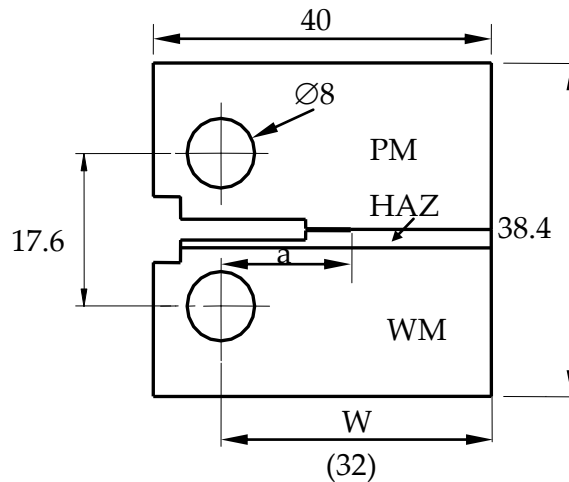


Fig. 3-9: Cross-weld CT specimen consisting of PM, HAZ and WM (dimensions in mm).

3.2.4 P92 weldments

P92 material was provided in the form of a normalised (1070°C/45mins) and tempered (780°C/105mins) PM pipe with an outer diameter (OD) of 355mm and inner diameter (ID) of 295mm. The welding consumable used was Thermanit MTS 616, which has a composition designed to match that of the parent pipe (Table 3-1). A 400×175×30mm WM pad was manufactured by Doosan Babcock Energy Ltd. (UK), by depositing 4mm diameter flux-coated consumable stick electrodes onto a carbon-manganese steel base plate using the manual metal arc (MMA) procedure with DC+ polarity and a current of 150-165A. Approximately 30 runs were made per layer, and the pad consisted of 10 layers. The deposition was performed in the 400mm direction only, at speeds around 190-210 mm/min. A preheat/interpass temperature between 200-300°C was maintained throughout the welding process, measured using temperature indicating crayons. Chipping/wire brushing was performed where necessary.

No non-destructive testing was performed on the weld pad but no defects were observed during the manufacture of test specimens. Cross sections studied contained very little to no weld porosity and no residual austenite. To help

ensure consistent test results and to avoid the effect of dilution with the steel base plate, material close to the weld start and stop edges of the pad and material comprising the innermost and outermost beads was not used. Both the PM and WM were heat treated at $760\pm 10^\circ\text{C}$ for 1.5 hours (minimum) to relax welding-induced residual stress and to temper the martensitic structure.

A similar welded P92 pipe was made and used to manufacture cross weld specimens, such as cross-weld uniaxial, shown in Fig. 3-5, and cross-weld CT specimens, shown in Fig. 3-9. Impression creep specimens were also cut from the HAZ material of the pipe weld. The P92 welded pipe was subjected to the same heat treatment as the PM pipe and WM block. Fig. 3-10 shows the P92 welding cross section where the three weld regions, i.e. PM, WM and HAZ, can be clearly seen.

	C	Mn	P	S	Si	Cr	W	Mo	V	Nb	N	B	Al	Ni
PM	0.11	0.45	0.015	0.001	0.43	8.76	1.87	0.32	0.20	0.074	0.05	0.0034	0.015	0.27
WM	0.09	0.73	0.007	0.005	0.26	8.47	1.67	0.47	0.189	0.042	0.046	-	-	0.65

Table 3-1: Chemical composition of P92 PM and WM (%Wt).

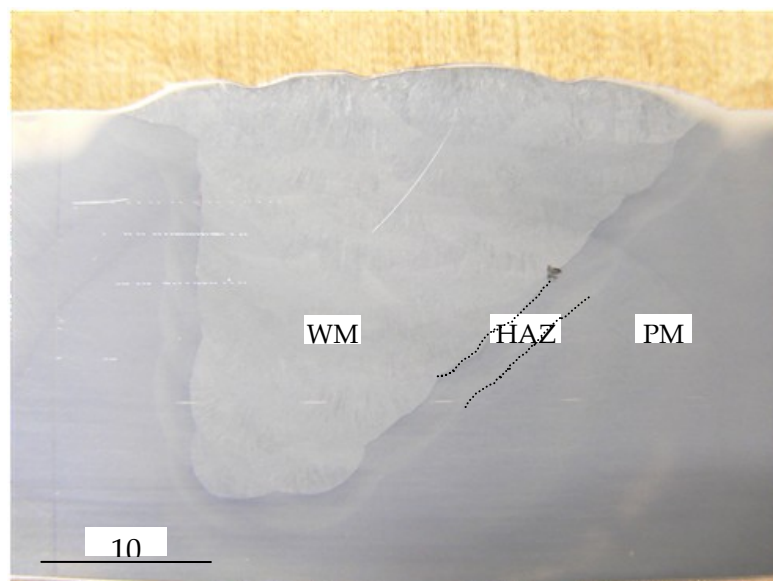


Fig. 3-10: The P92 weld cross section.

3.2.5 P92 uniaxial and notched bar specimens

Uniaxial and notched bar specimens were cut from the P92 PM pipe and WM block. The PM specimens were cut parallel to axis of the pipe while the WM specimens were cut in the transverse direction, i.e. in a direction perpendicular to the welding direction. The P92 uniaxial and notched bar specimens have the same geometry and dimensions as the corresponding P91 specimens, see Fig. 3-2 and Fig. 3-3. Cross-weld uniaxial, notched and waisted specimens were also tested. The geometry and dimensions of the cross-weld waisted and uniaxial specimen are shown in Fig. 3-4 and Fig. 3-5, respectively.

3.2.6 P92 CT specimens

CT specimens were used to study creep crack growth in the P92 weldment. The geometry and dimensions of the P92 CT specimens are the same as those of the P91 CT specimens, see Fig. 3-7 and Fig. 3-9. The P92 PM CT specimens were cut from P92 PM pipe. Fig. 3-11 shows the sampling method used to cut the P92 PM CT specimens. It can be seen that, the CT specimens were cut so that it will be loaded in the pipe's axial direction. The P92 cross-weld CT specimens were cut from P92 welded pipe. Fig. 3-12 shows the sampling method for the P92 cross-weld CT specimens. Cross-weld CT specimens were also loaded in the pipe's axial direction. While P91 cross-weld CT specimens were cut parallel to the welding cross section, as shown in Fig. 3-8, P92 cross-weld CT specimens were cut perpendicular to the P92 welding cross section, as seen in Fig. 3-13. Similar to the P91 cross-weld CT specimens, initial cracks in the P92 cross-weld specimens were positioned on the PM/HAZ boundary.

The creep crack growth test programme for the P92 welds consisted of testing five PM CT specimens and eight cross-weld CT specimens. Side grooves were introduced to some of the CT specimens while other specimens were plane. This was to check the effect of the grooves on the values of the obtained C^* values. In

this respect, the first two PM CT specimens, i.e. CT1 and CT2, were plane specimens, i.e. no side grooves applied to the specimens. However, all of the other PM CT specimens are fully side-grooved specimens, i.e. the depth of the side groove is 10% of the specimen original thickness. Cross-weld specimens CT6 and CT8 were plain specimen while all of the other cross-weld specimens were fully side grooved.

The effect of the welding direction on creep crack growth in the cross-weld CT specimens was investigated. Initially cracks were cut so that they would grow in a direction opposite to the welding direction, as in CT6 and CT7, and in the direction of the welding, as in CT8 and CT 9. Locating CT6 and CT8 with respect to the welding direction is shown in Fig. 3-14.

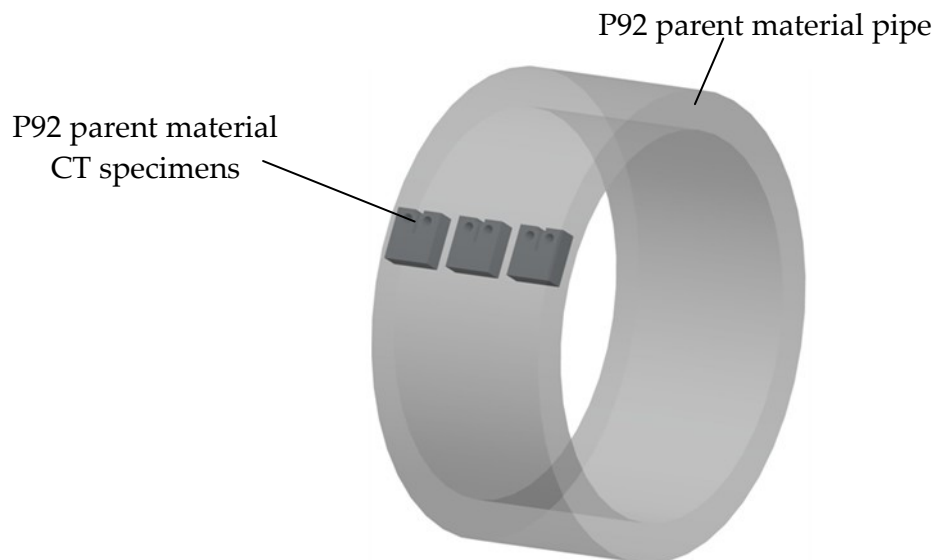


Fig. 3-11: Sampling for the P92 PM CT specimens.

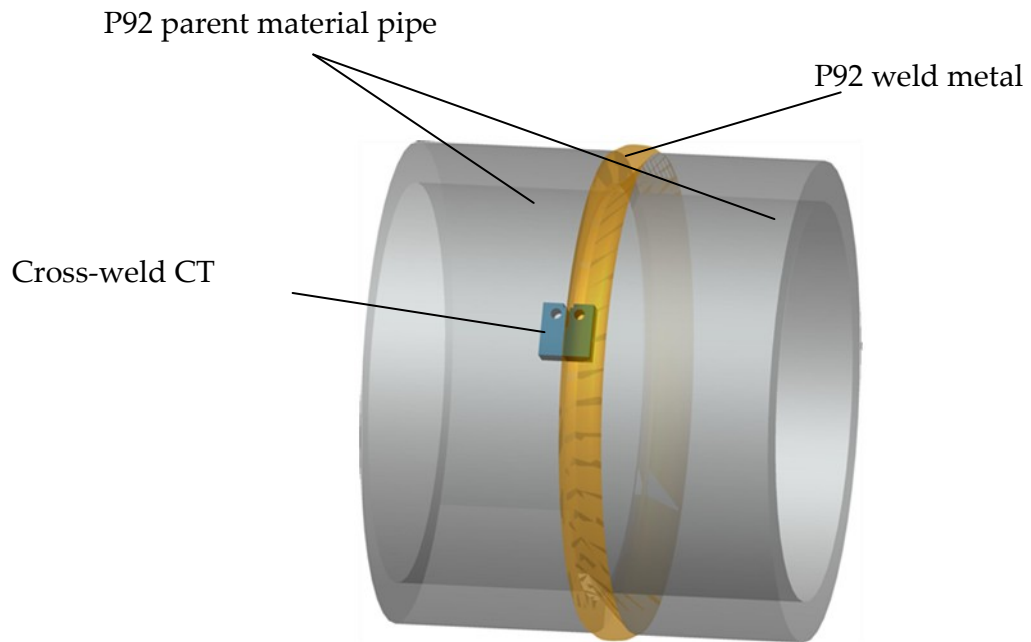


Fig. 3-12: Sampling for the P92 cross-weld CT specimens.

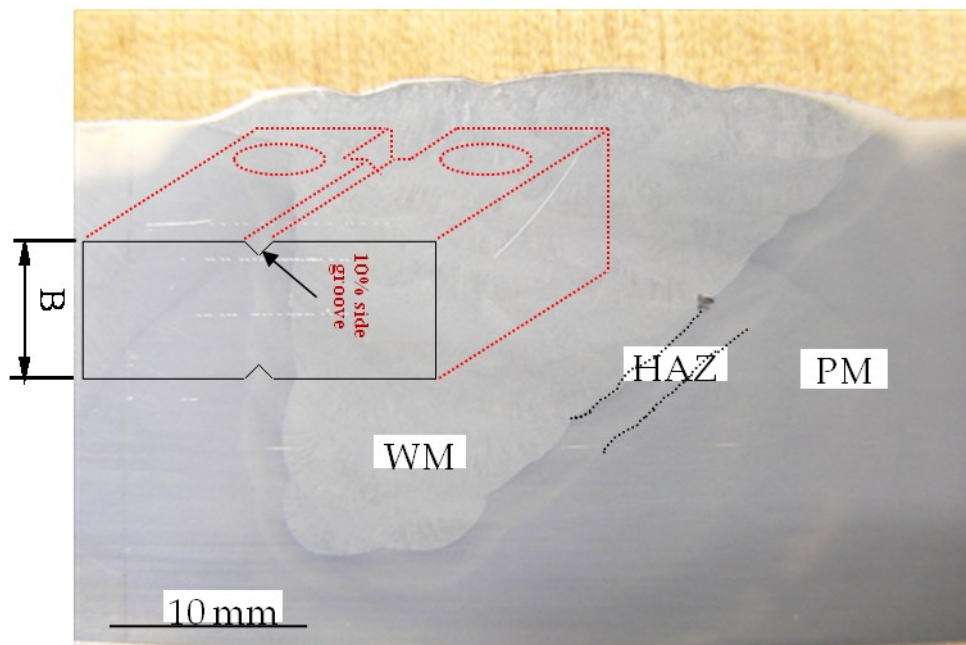


Fig. 3-13: The P92 cross-weld CT specimens were cut perpendicular to the welding cross section with the initial crack located on the PM/HAZ boundary.

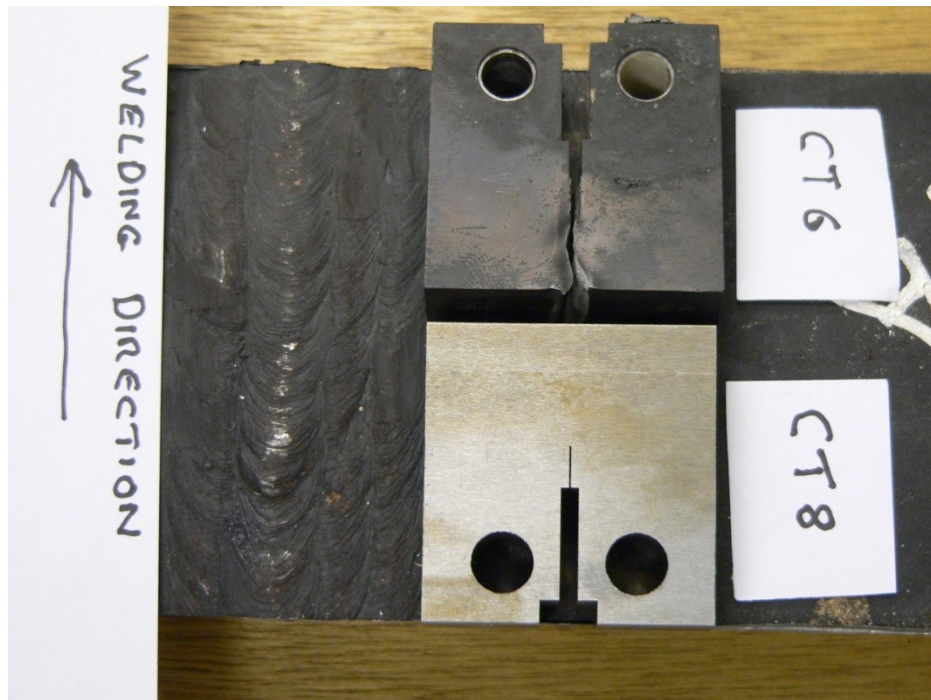


Fig. 3-14: Initial cracks in P92 cross-weld CT specimens were allowed to grow in the welding direction and opposite to the welding direction.

3.3 CREEP TESTING ARRANGEMENTS

The creep testing machines used in this study were 5 tons, dead weight, lever machines. Loading arrangements for CT specimens are shown in Fig. 3-15. Load is applied to the upper hole, in the CT specimen, via a pin attached to the upper grip, while the lower hole is kept fixed. Displacement of the load point was measured by a pair of extensometers and transducers, which monitored using a data logger.

Potential difference measurements were used to monitor creep crack growth in, for example, CT specimens. Once the CT specimen was set up in the creep testing machine, potential difference accessories were attached to the specimen. DC input wires were attached to the CT specimen; one on each side, and output wires were attached to the front of the specimen, as shown in Fig. 3-16. As the

crack grows, potential difference increases. Ceramic bushes were used to insulate the specimen from the loading pins.

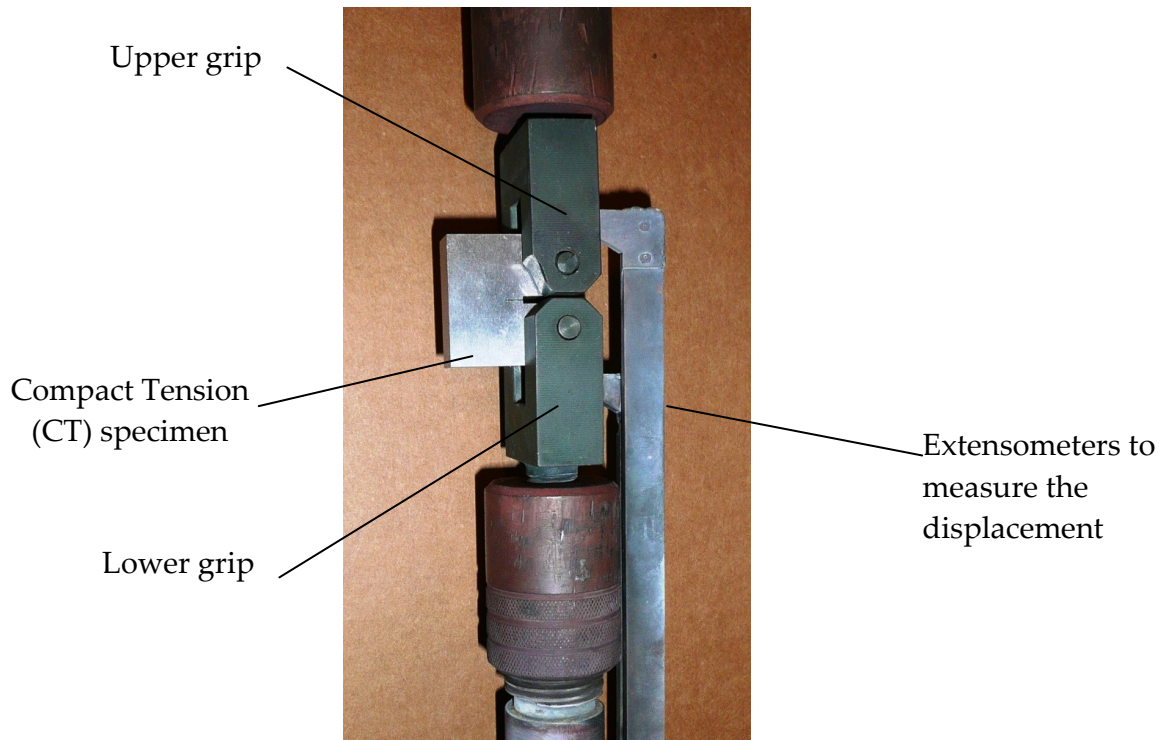


Fig. 3-15: Loading arrangements for testing CT specimens.

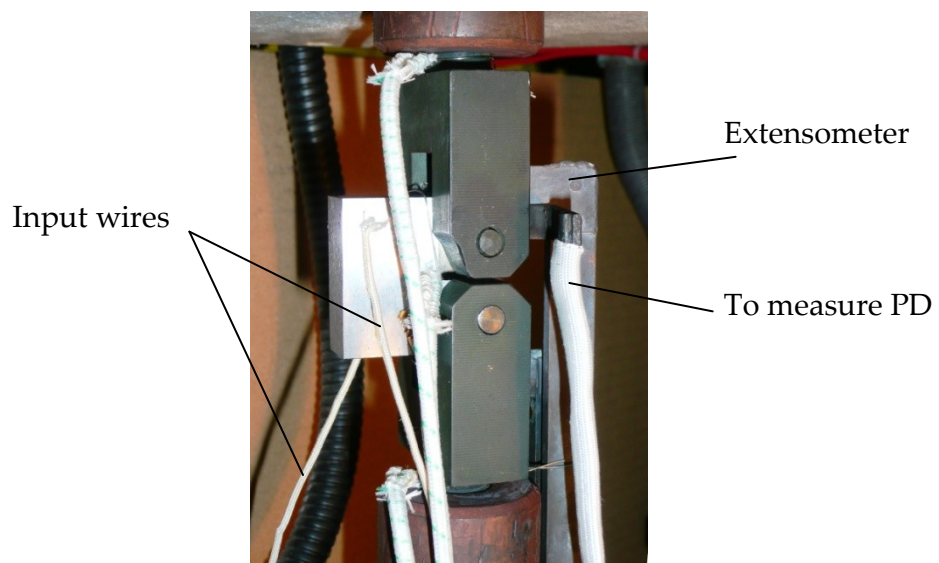


Fig. 3-16: Potential difference measuring arrangements.

3.4 EXPERIMENTAL RESULTS

3.4.1 P91 experimental results

3.4.1.1 P91 uniaxial creep

Creep tests were carried out on uniaxial, notched bar and waisted specimens cut from P91 PM, WM and across the P91 weldment. These tests were carried out at a temperature of 650°C, which is higher than the nominal working temperature of P91 material (593°C), and at stresses equivalent to the working stresses of actual P91 pipes. One of the reasons of testing at temperatures and/or stresses higher than their working temperatures and/or stresses is to reduce the testing time. That is, development of a new high temperature material could take many years if it is tested at the actual temperature and stress. Results of the P91 creep tests have been reported in (Hyde *et al.*, 2004b) and were used to calculate the P91 material creep and damage constants. Those experimental results have been used, in this thesis, to obtain a different set of the P91 material constants. Fig. 3-17 shows the uniaxial creep curves for the P91 PM. It can be seen that, all of the curves exhibit relatively small primary creep and comparatively long secondary and tertiary regions. Pronounced tertiary creep begins at a strain level of about 5%. The failure strains are generally around 35%. Fig. 3-18 shows the uniaxial creep curves for the P91 WM at 650°C (Hyde *et al.*, 2004b). It can be seen that the WM exhibits low ductility when compared to the PM. Ogata *et al.*(2009) found that the rupture life of the P91 PM creep specimens is about five times higher than that of the cross-weld creep specimens. This reduction in creep rupture time, for the cross-weld specimens, can be attributed to the high triaxiality found in the Type IV region due to constraints from the PM and WM. This high triaxiality causes the initiation and accumulation of creep voids at the Type IV region. Impression creep tests were carried out on specimens cut from the P91 HAZ materials and the results were given in (Hyde *et al.*, 2004b) and are shown

in Fig. 3-19. The results obtained from the P91 notched bar and waisted specimens are included in Table 3-2.

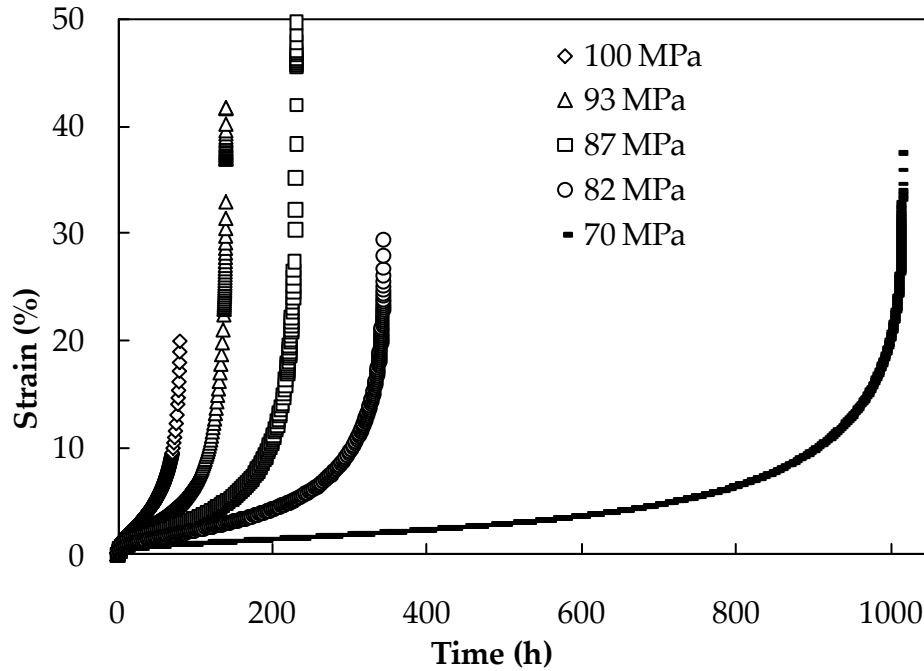


Fig. 3-17: Creep strain curves for the P91 PM at 650°C, (Hyde *et al.*, 2004b).

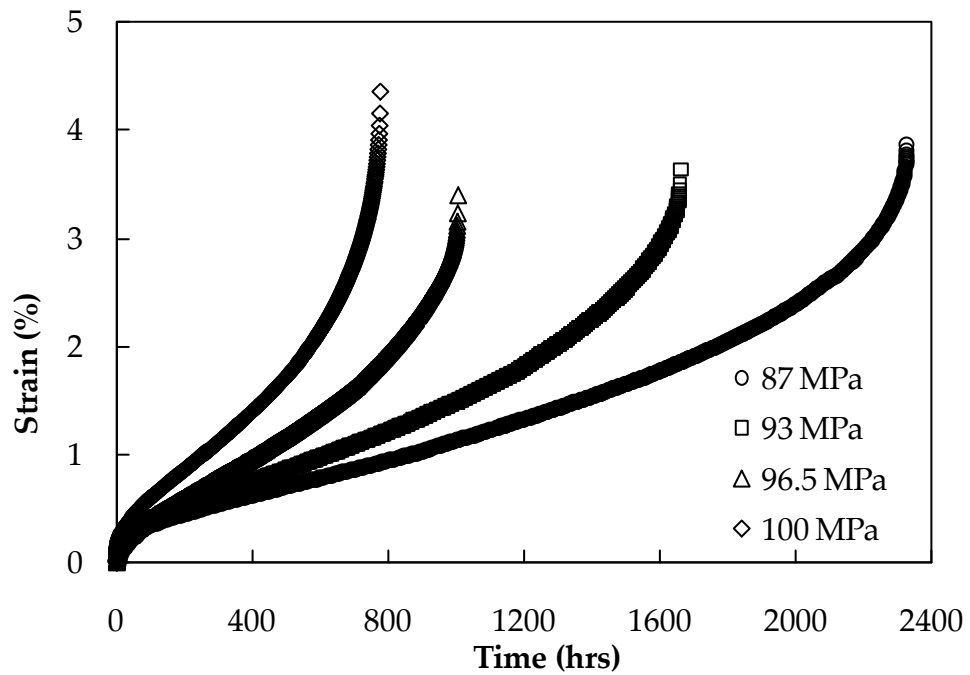


Fig. 3-18: Creep strain curves for the P91 WM, at 650°C, (Hyde *et al.*, 2004b).

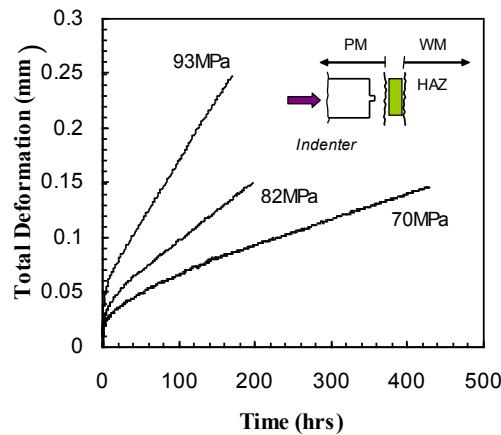


Fig. 3-19: Impression deformation versus time curves for the P91 HAZ material, at 650°C, subjected to steady loading from the parent material side, (Hyde *et al.*, 2004b).

3.4.1.2 P91 creep crack growth

Experimental creep crack growth data, normally, exhibits significant scatter. This scatter is due to microstructural variations, load variations, displacement and crack length measurement accuracy and data processing techniques. Thus, several tests are generally carried out at a given test temperature in order to improve the confidence level in the interpretation of the test data (Gopala Krishna *et al.*, 1998).

P91 creep crack growth tests were carried out in air, to simulate the actual operating conditions of the real components such as main steam pipes of power plants. These test were carried out at 650°C on PM and cross-weld CT specimens. The PM CT specimens are CT1-CT4 and the cross-weld CT specimens are CT5-CT11. Load line displacements and creep crack growth were measured for each test. Table 3-3 summarises the testing conditions, duration and the average final crack growths from the P91 creep crack growth tests. An example of a failed, fully side grooved, CT specimen, CT5, is shown in Fig. 3-20.

The nominal, elastically calculated, stress applied to the crack tip of the CT specimens consists of a tensile stress component and a bending stress component, i.e,

$$\sigma_{nom} = \sigma_{tensile} + \sigma_{bending} \quad (3-3)$$

where

$$\sigma_{tensile} = \frac{P}{B_N(W - a)} \quad (3-4)$$

and

$$\sigma_{bending} = \frac{6P \left(a + \frac{W - a}{2} \right)}{B_N(W - a)^2} \quad (3-5)$$

where P is the applied load, B_N is the specimen's net thickness, W is the specimen's width and a is the crack length.

The nominal stress in the cross-weld CT specimens ranged from 68 to 80 MPa. These stress values are within the range of stresses applied to the P91 uniaxial creep tests, i.e. 70 to 100 MPa. It should be noted that the nominal stresses apply to the conditions at the beginning of the tests when $a = 15.5$ mm, and these stresses increase dramatically as the crack length increases.

Load line displacement and creep crack growth curves for the P91 CT tests are given and discussed in the following two sections.

σ (MPa)	Parent Material		WM		Cross-Weld	
	Uniaxial	Notched	Uniaxial	Notched	Waisted	Notched
70	1010.4	----	----	----	535.1	593.5
82	343.54	2012.1	----	----	250	310.6
87	230.6	----	2328.6	----	----	----
93	140	1037.2	1662	----	112.3	218.4
96.5	----	----	1005	----	----	----
100	78.6	----	776.82	1550	----	----
107	----	----	----	724	----	----

Table 3-2: Creep rupture data (in hours) for P91 at 650°C.

Specimen	CT Material	Side groove depth each side	Load (N)	Test duration (h)	Δa (mm)
CT1	PM	None	5000	98.5	2.83
CT2	PM	5%	4000	184.5	5.26
CT3	PM	10%	3600	210	5.46
CT4	PM	10%	3000	410	6.94
CT5	Cross-weld	10%	3000	154	7.65
CT6	Cross-weld	10%	1700	1533	5.75
CT7	Cross-weld	10%	2500	260	9.44
CT8	Cross-weld	10%	2000	767	9.81
CT9	Cross-weld	10%	1700	1230	4.10
CT10	Cross-weld	10%	1700	1032	2.47
CT11	Cross-weld	10%	2000	904.5	4.29

Table 3-3: CT experimental test conditions and main results.



Fig. 3-20: Failed CT specimen (CT5).

Load line displacement

Load line displacement curves, obtained from the P91 PM CT specimens, are shown in Fig. 3-21. CT1 was initially loaded by 2000N applied for about 74 hours; the load was then increased to 5000N. Therefore, the displacement curve for CT1 exhibits two stages. However, only the data points for the second stage, i.e. when the load was 5000N, were used to calculate the displacement rates.

Load line displacement curves for the P91 cross-weld CT specimens are shown in Fig. 3-22. Specimens CT5, CT7 and CT8, were tested until well into tertiary (i.e. creep crack growth acceleration region). This resulted in a very large displacements at which point they include significant plastic deformation near the end of the test. Tests CT6, CT9, CT10 and CT11, were stopped near the

beginning of tertiary region in order to ensure that the resulting displacements, and the corresponding crack growth, are predominantly due to creep ones.

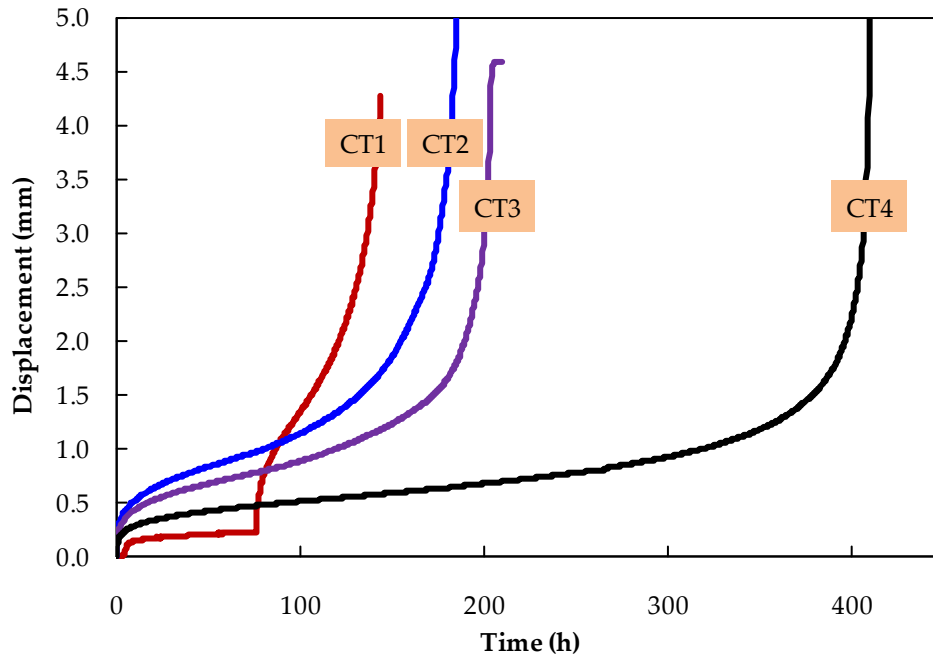


Fig. 3-21: Load line displacement for the P91 PM CT specimens, at 650°C.

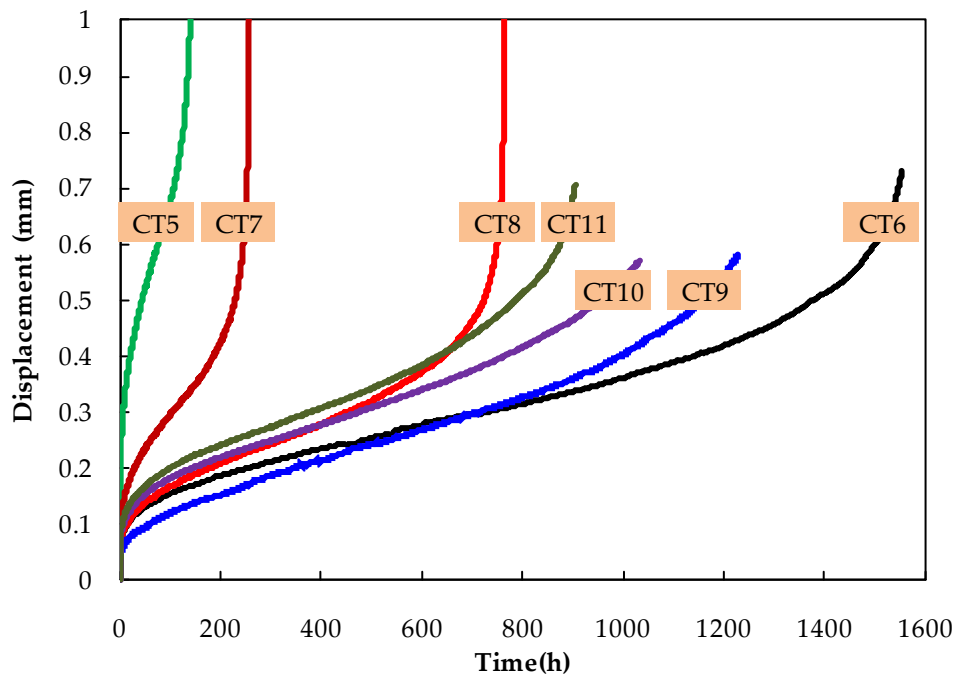


Fig. 3-22: Load line displacement for the P91 cross-weld CT specimens, at 650°C.

Crack length

Creep crack growth in the CT tests was monitored using the DC PD technique. DC current input and PD measuring positions are shown in Fig. 3-16. On completion of the creep crack growth tests, CT specimens were subjected to fatigue loading to expose final creep crack extension and to measure the crack surfaces. The crack length is defined by average of the crack lengths at nine points. In addition, an image analysis package was used to measure the crack area. The final crack length was then calculated by dividing the cracked area by the specimen's thickness (B). No significant difference was observed in the results obtained using these two methods, to measure the final crack length.

A linear relationship was assumed to exist between the potential difference and crack length. Hence, crack length, a , is obtained as follows:-

$$a(t) = a_0 + \frac{\Delta a}{\Delta V} (V(t) - V_0) \quad (3-6)$$

where a_0 is the initial crack length (a_0 is 15.5 mm in all of the CT specimens used in this research), Δa is the overall increment of crack length (as measured from the cracked surface), ΔV is the overall potential difference (in μV), $V(t)$ is the instantaneous potential difference and V_0 is the initial potential difference.

Creep crack growth curves for the P91 PM CT specimens tested at 650°C are given in Fig. 3-23. Data included in these curves were used to calculate the creep crack growth rates and the C^* values.

$\Delta V/\Delta a$ ($\mu\text{V}/\text{mm}$) is the calibration factor. This factor was calculated for each CT specimen. The final crack lengths in some of the specimens were well into tertiary region, i.e. CT5, CT7 and CT8. Other tests were stopped shortly after the tertiary region started, i.e. CT6, CT9, CT10 and CT11. Fig. 3-24 shows the

relationship between the measured Δa and the calibration factor for the cross-weld CT specimens, i.e. CT5 to CT11. It can be seen that when the tests were allowed to continue well until the tertiary region, the apparent calibration factor for these tests is about four times higher than that when the tests were stopped in the early tertiary region. It can also be seen that, the calibration factors for CT6, CT9, CT10 and CT11 are consistent. Therefore, the calibration factor for CT6 was used to determine creep crack growth during the early stages of the tests on specimens CT5, CT7 and CT8. The data well into the tertiary range for specimens CT5, CT7 and CT8 were discarded.

The creep crack growth curves for CT5, CT7 and CT8, using their own calibration factors, and using CT6 calibration factor are shown in Fig. 3-25. A significant difference can be seen between the creep crack growth curves obtained using the specimens' own calibration factors and those obtained using the CT6 calibration factor. Fig. 3-26 shows the creep crack growth for the P91 cross-weld CT specimens at 650°C. Data included in these curves were used to calculate C^* and to obtain the creep crack growth rates. The full procedure, used to calculate C^* , is described in Chapter 4.

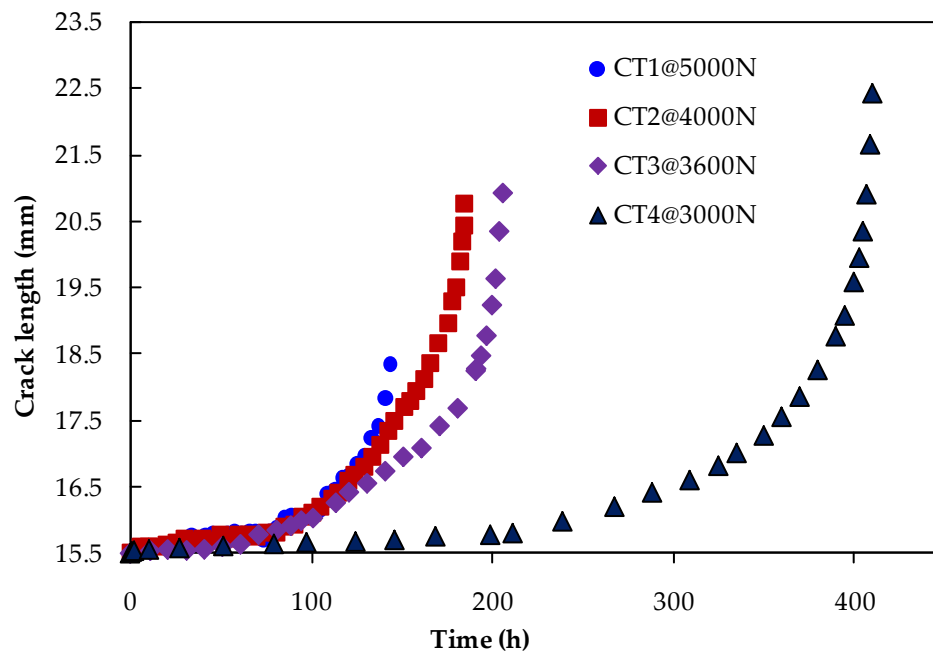


Fig. 3-23: Creep crack growth in the P91 PM CT specimens at 650°C.

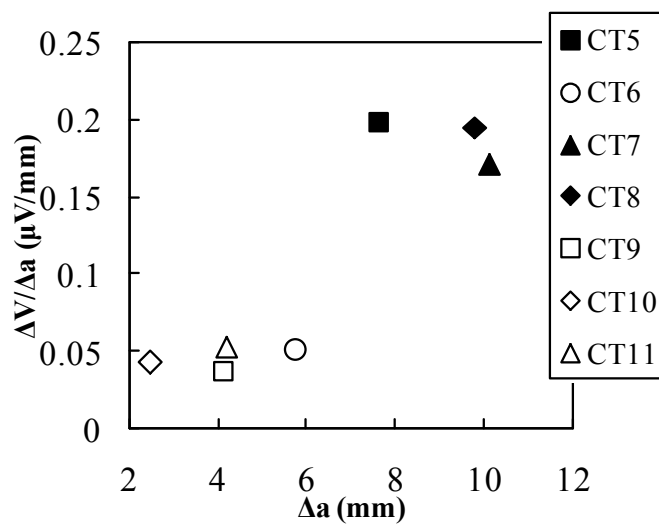


Fig. 3-24: Calibration factors for the P91 cross-weld CT specimens.

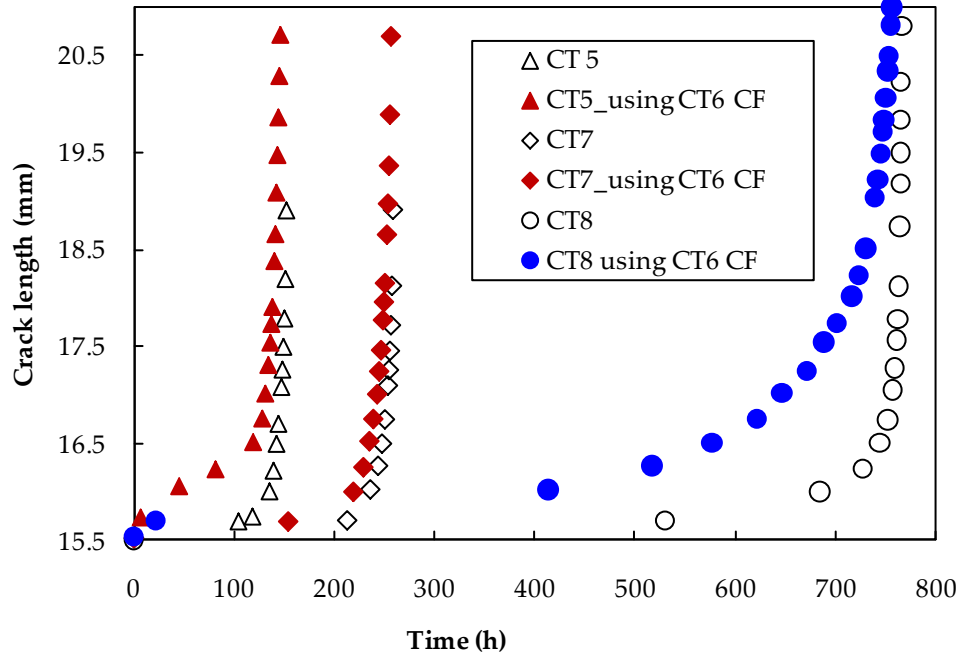


Fig. 3-25: Creep crack growth for the P91 CT5, CT7 and CT8 with and without using CT6 calibration factor (CF).

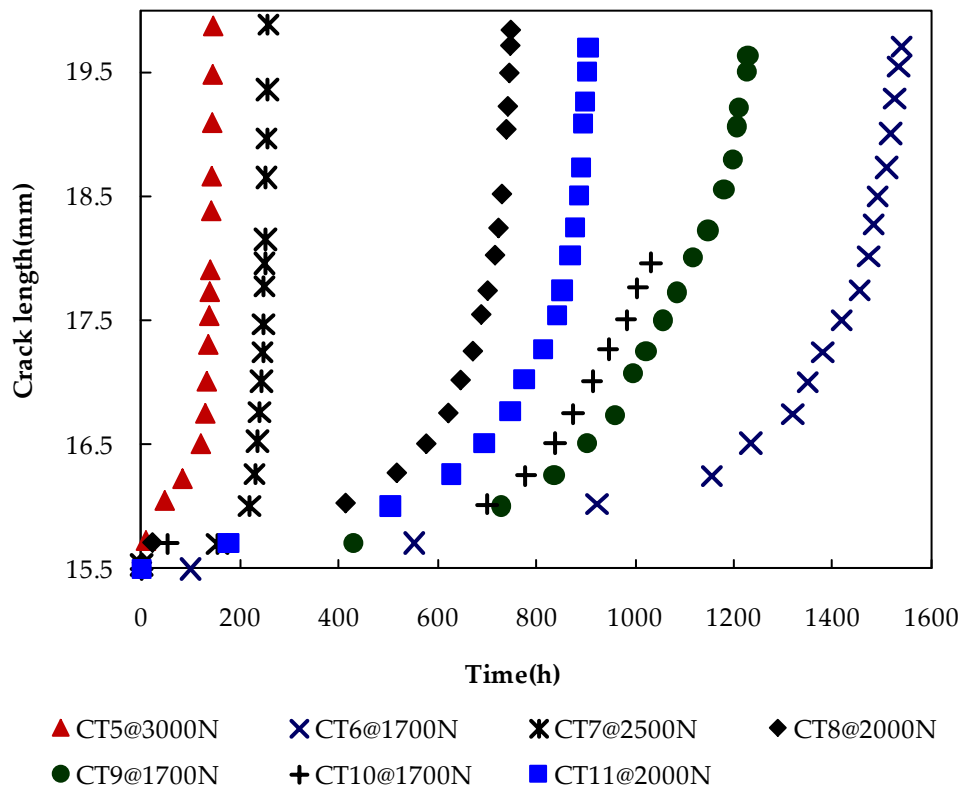


Fig. 3-26: Creep crack growth for the P91 cross-weld CT specimens at 650°C.

3.4.1.3 Macro and microstructure study

Fractured surfaces

On completion of each creep crack growth test, the CT specimen was broken into two halves using a fatigue machine. The fractured surface was then photographed using a high-resolution digital camera. Fig. 3-27 shows the fractured surfaces of CT1. Three distinctive areas can be seen. The first area to the bottom is the starter (initial) crack surface, which was produced using the electric discharge machining. The next upward zone is the creep-cracked surface, which was formed during the creep crack growth. The outermost area is the fatigue cracked area, which resulted from the opening fatigue of the CT specimens.

Side grooves affect the overall crack length increment and the crack shape. Fig. 3-28 compares the creep crack surfaces for the P91 PM CT specimens. It can be seen that, as CT1 was a plain specimen, i.e. without side grooves, the crack front has a thumbnail shape. This feature is known as crack tunnelling. It is believed that the crack tip at the middle of the specimen's thickness was subjected to plane strain conditions and higher stress multiaxiality due to the constraint of the surrounding material. However, the stress state near the free surfaces is close to plane stress conditions. Therefore the creep crack growth rates near the specimen's free surfaces are lower than those at the specimen's mid-thickness. ASTM E 1457-00 (2001) recommends cutting grooves on both sides of the specimen. The depth of these side grooves is 10% of the specimen's original thickness, on each side. These grooves ensure a more uniform growth of the crack and hence obtain a practically straight crack front. CT2 was a partially side grooved specimen, i.e. the depth of the groove was only 5% of the specimen's original thickness on each side. The CT2 crack front, as seen in Fig. 3-28, is somewhere between crack tunnelling and straight crack front. Fully grooved

specimens, e.g. CT3 and CT4, have almost uniform crack fronts. The uniform crack front suggested plane strain controlled the creep crack growth in fully side grooved CT specimens (Yamamoto *et al.*, 2010).

Fig. 3-29 shows the fractured surfaces of the P91 cross-weld CT specimens, i.e. CT5 to CT11. All of these CT specimens are fully side grooved specimens. It can be seen that cracks grew uniformly in all of these specimens and so the crack fronts are almost straight. It can also be seen that specimens CT5, CT7 and CT8 show larger crack surfaces compared to the other cross-weld specimens. This reflects the higher displacements obtained in the CT5, CT7 and CT8 specimens.

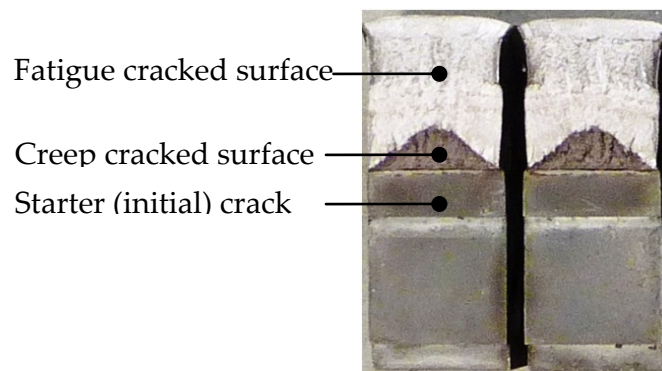


Fig. 3-27: Cracked surfaces of the P91 PM CT1 specimen.

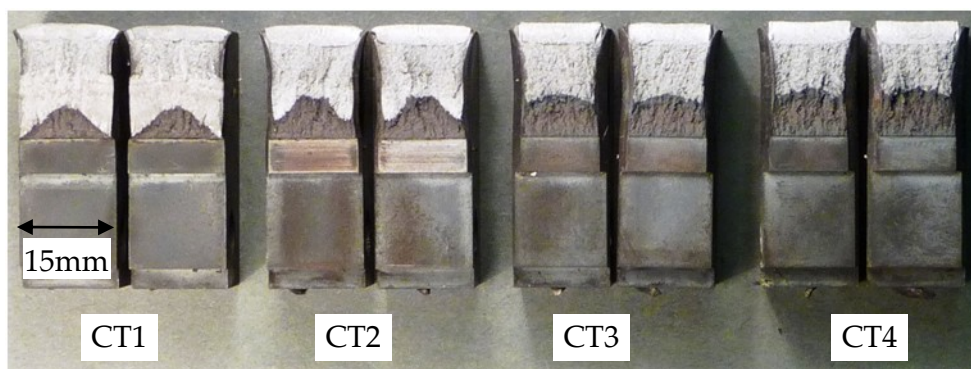


Fig. 3-28: Cracked surfaces of the P91 PM CT specimens.

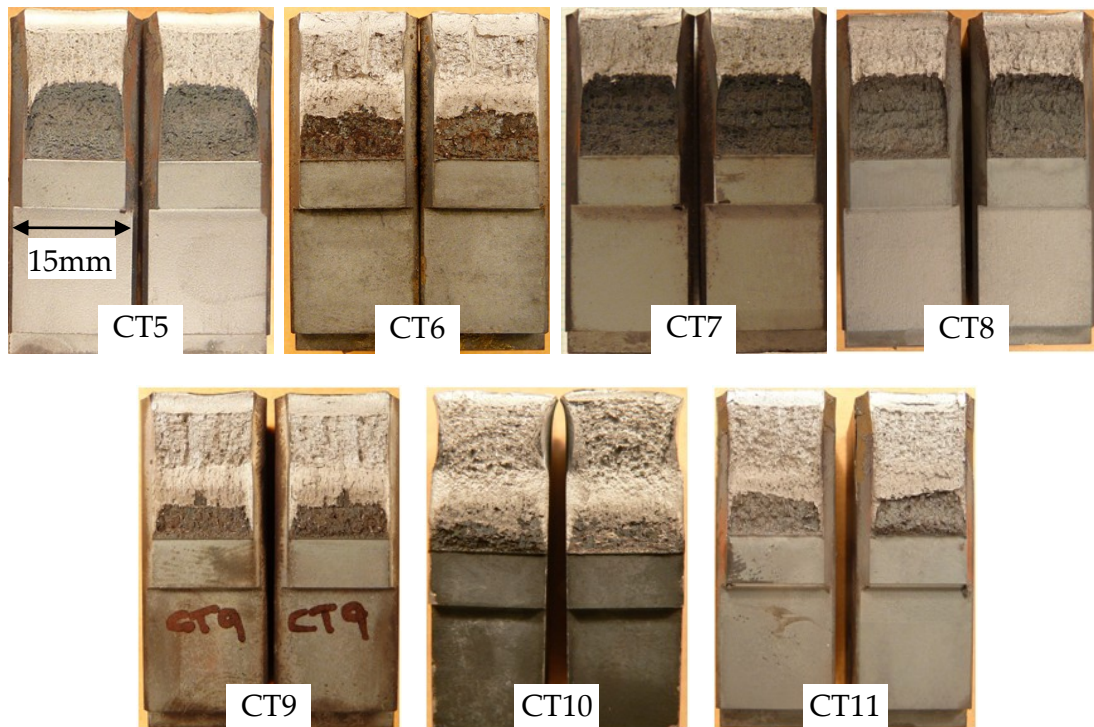


Fig. 3-29: Cracked surfaces of the P91 cross-weld CT specimens.

Hardness test

Hardness tests were carried out on P91 cross-weld CT specimens. These specimens consist of PM, HAZ material and WM. Initial cracks in these specimens were located on (or near to) the boundary between the PM and the HAZ material, i.e. the Type IV region, which is the weakest region in the weld and the potential failure location. Micro hardness tests were carried out on cross-weld CT specimens to check the accuracy of the positioning and growth of these initial cracks.

After measuring the average (final) crack lengths of the cross-weld CT specimens, they were cut into slices, as shown in Fig. 3-30 and Fig. 3-31. These slices were then polished to 1 μm surface roughness and etched using ferric chloride (FeCl_3). Macroscopic investigations were carried out in order to check the crack path produced in these specimens. Fig. 3-32 shows polished and etched slices for cross-weld CT5. The weld beads can be clearly seen and the

fusion line can be easily distinguished. The HAZ region is about 2-3 mm wide as measured from the fusion line. The PM can be distinguished from the WM and the HAZ material. It can also be seen that, as the cracks grew, they remained roughly the same distance away from the fusion line. This indicates that the crack that was initiated in Type IV region continued in the same region.

Vickers' hardness tests were carried out on specimens CT5 and CT7, using micro hardness testing machine. The hardness measurements were taken on a line which started in the WM, passed through the HAZ material and ended in the PM. Results obtained from the hardness tests, for CT5 and CT7, are shown in Fig. 3-33. Also shown are the observed positions of the cracks in these two specimens. It can be seen that the average hardness in the WM is higher than that of the PM and the HAZ material. Moreover, the hardness of the HAZ material reduces gradually from the fusion line to the PM/HAZ boundary. It can also be seen that the cracks, in both specimens, grew in or very close to the region with the minimum hardness. Results shown in Fig. 3-32 and Fig. 3-33 suggest that the initial cracks, in the P91 cross-weld CT specimen, were successfully located and grown in the Type IV region.

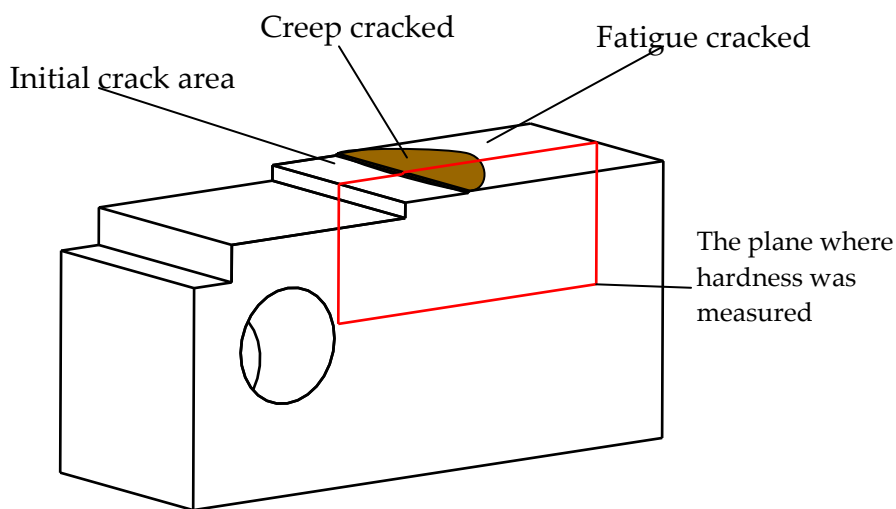


Fig. 3-30: Schematic drawing showing the planes where the hardness was measured.



Fig. 3-31: A tested cross-weld CT specimen cut into slices.

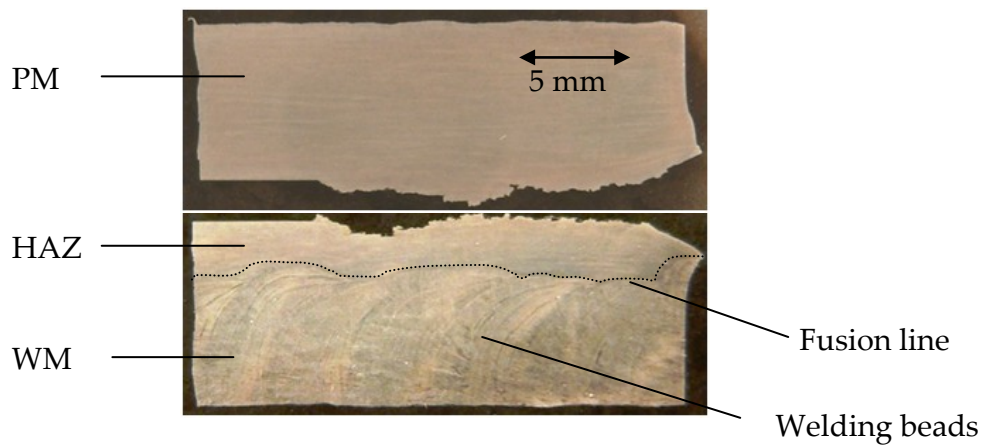


Fig. 3-32: Polished and etched slices of a cross-weld CT5 specimen.

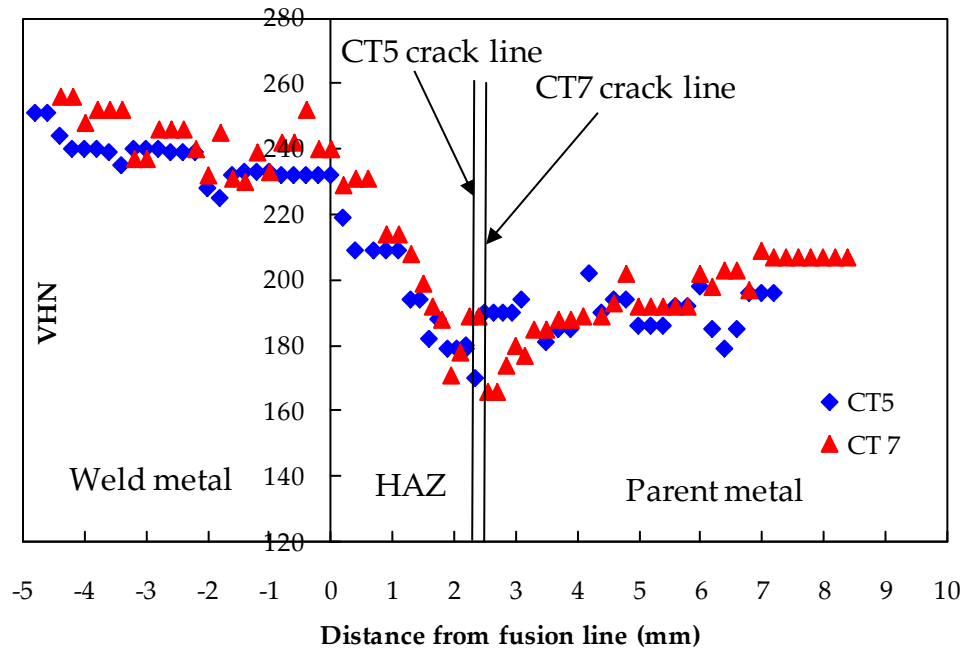


Fig. 3-33: Vickers' hardness results for cross-weld CT specimens, CT5 and CT7.

Micro cracks distribution

Optical microscopy and Scanning Electron Microscopy (SEM) were used to study the micro-cracks distribution in the failed P91 CT specimens. The optical microscopy investigation showed a distribution of sub cracks close to the main crack path as seen in Fig. 3-34. However, dense distribution of micro cracks may be observed by using the SEM, these are also found to occur around the crack path, see Fig. 3-35. These micro-cracks join together to form sub cracks, which lead to the growth of a macro crack. The density of the micro cracks decreases with increasing distance from the crack line.

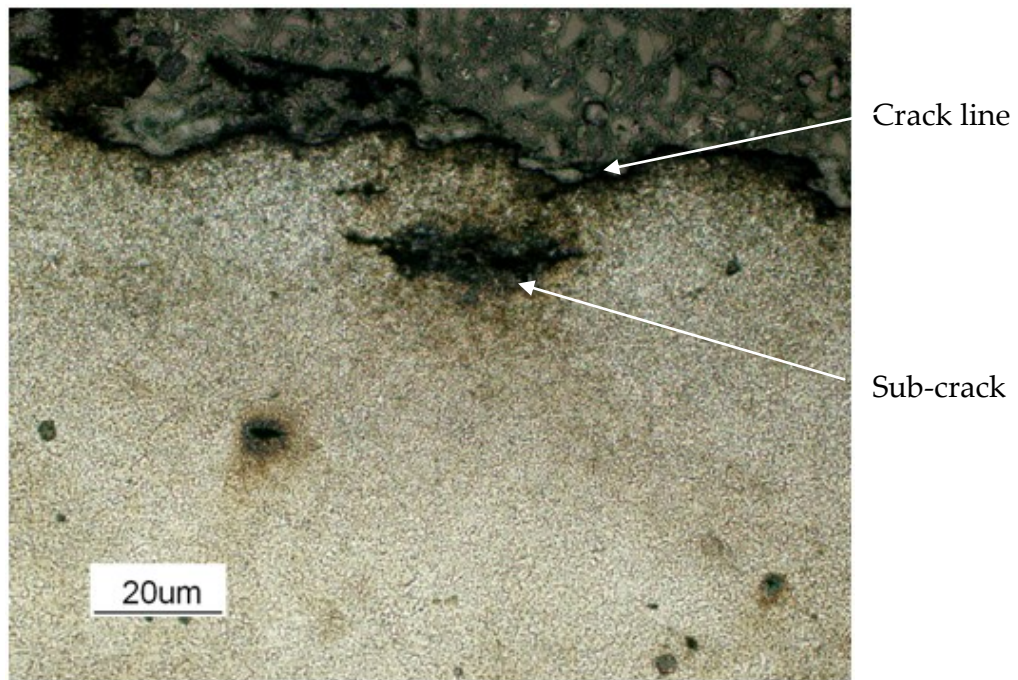


Fig. 3-34: Sub cracks were found close to the crack line in CT7.

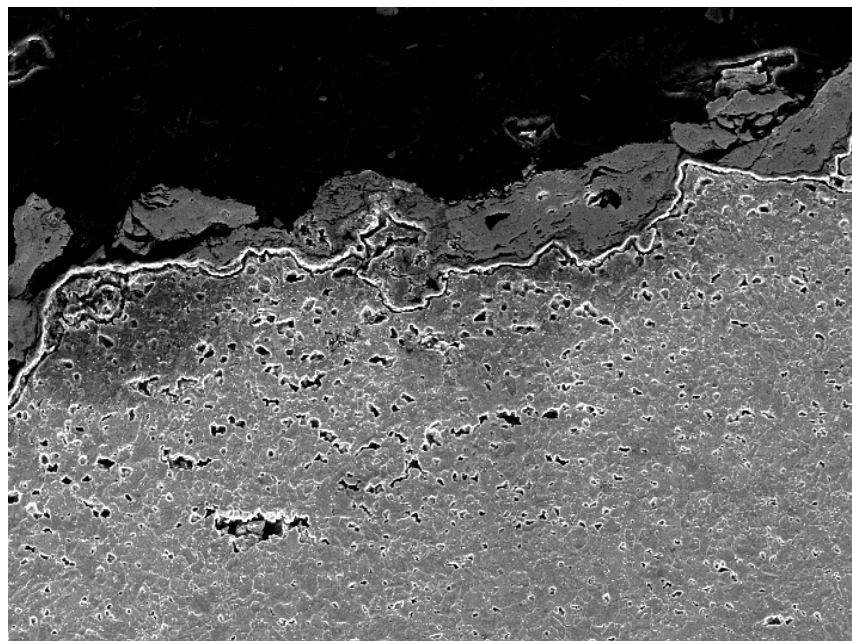


Fig. 3-35: Micro cracks appear next to the crack line in high density.

3.4.2 P92 experimental results

3.4.2.1 P92 uniaxial results

Five uniaxial creep tests were carried out on each of the P92 PM and WM, at 675°C, and at stress levels of 80, 85, 90, 95 and 100 MPa. These stresses span the service conditions used for the P92 material. Fig. 3-36 shows the creep strain against time curves for the P92 PM. It can be seen that all of the curves exhibit primary, secondary and tertiary creep regions. Moreover, for lower stress levels, a linear relationship exists between failure times and applied stress. However, for high stresses, this relationship tends to be non-linear, see Fig. 3-37. Failure time for the 85 MPa test was estimated as the disc (of the data logger), to which the test data were recorded, failed after 1172 hrs. A characteristic creep curve was used to define the strain and the failure time for the rest of the test. The average strain at failure for all the tests is about 22%.

Uniaxial creep strain curves for the P92 WM, at 675°C, are shown in Fig. 3-38. As with the P92 PM, the P92 WM exhibits typical creep strain curves, i.e. they include primary, secondary and tertiary creep stages. The average strain at failure for all of the tests is about 18%, indicating a slightly less ductile behaviour than the PM.

P92 uniaxial creep curves, shown in Fig. 3-36 and Fig. 3-38, have been used to obtain the P92 creep and damage material constants. Six material constants, A , n , B , ϕ , q_2 and χ are to be determined from these curves. The determination of these constants is detailed in Chapter 5.

Cross-weld uniaxial specimens were also tested to obtain creep and creep rupture data for the P92 HAZ material. Two specimens were tested at 85 and 80 MPa. The geometry and dimensions of these specimens are shown in Fig. 3-5.

The 85 MPa specimen failed on a plane that is 45° to the loading direction, as seen in Fig. 3-39, while the 80 MPa specimen failed on a plan perpendicular to the loading direction. Both of the specimens failed in the HAZ region. Creep strain curves for the cross-weld uniaxial tests are shown in Fig. 3-40. It can be seen that the 80 MPa test experienced a more sudden failure than the 85 MPa tests did. It can be also seen that the average failure strain is about 2%, for the two tests. This value is very low when compared to those for the PM (22%) and the WM (18%). This can be explained as the HAZ is the weakest material in a weldment and it is sandwiched between two strong materials, i.e. the PM and the WM. The deformation associated with these tests mainly occurred in the HAZ and then divided by the specimens gauge length (50mm). This resulted in low values of overall strain. Further, it can be seen that the failure times for the uniaxial specimens at 80 MPa and 85 MPa are 1540 hrs and 1247 hrs, respectively, for P92 PM and 382 hrs and 324 hrs, respectively, for the cross-weld, at 675°C. This means that the cross-weld specimens are about 4 times weaker than the PM specimens are. This causes concerns for the integrity of in service weldments and highlights the need for the development of appropriate lifetime assessment procedures (Perrin and Hayhurst, 1999).

Notched bar specimens were tested in order to obtain creep rupture data for the P92 material. Results obtained from the notched bar specimens are used in conjunction with FE analyses to define the PM and WM multiaxiality parameters. To define the HAZ material multiaxiality, results obtained from cross-weld waisted and notched bar specimens are needed. Table 3-4 summaries the failure times of all of the creep and creep rupture tests carried out on the P92 PM, WM and cross the P92 weld.

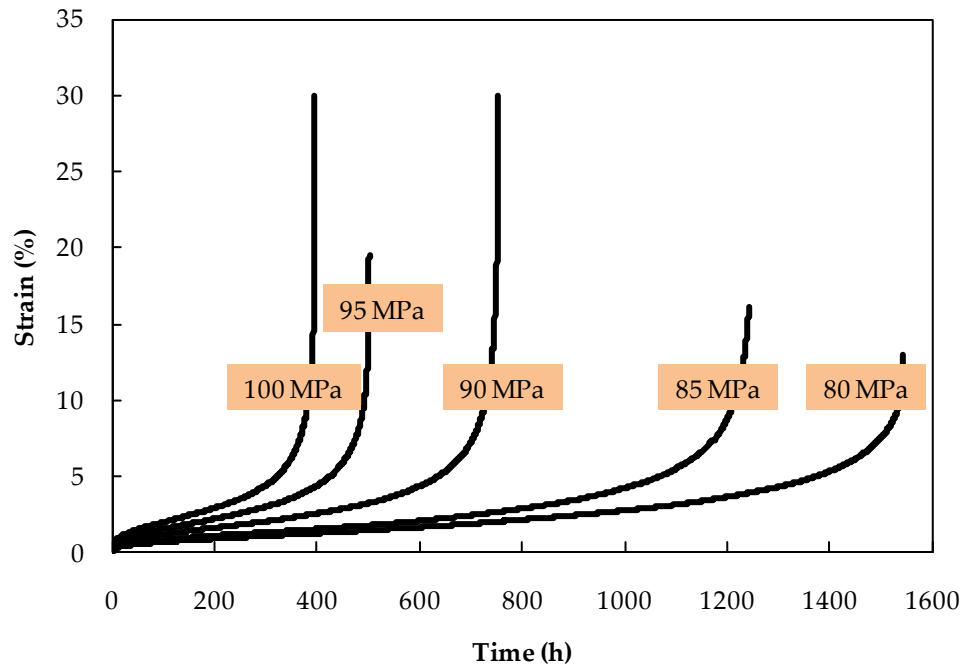


Fig. 3-36: Creep strain curves for the P92 PM at 675°C.

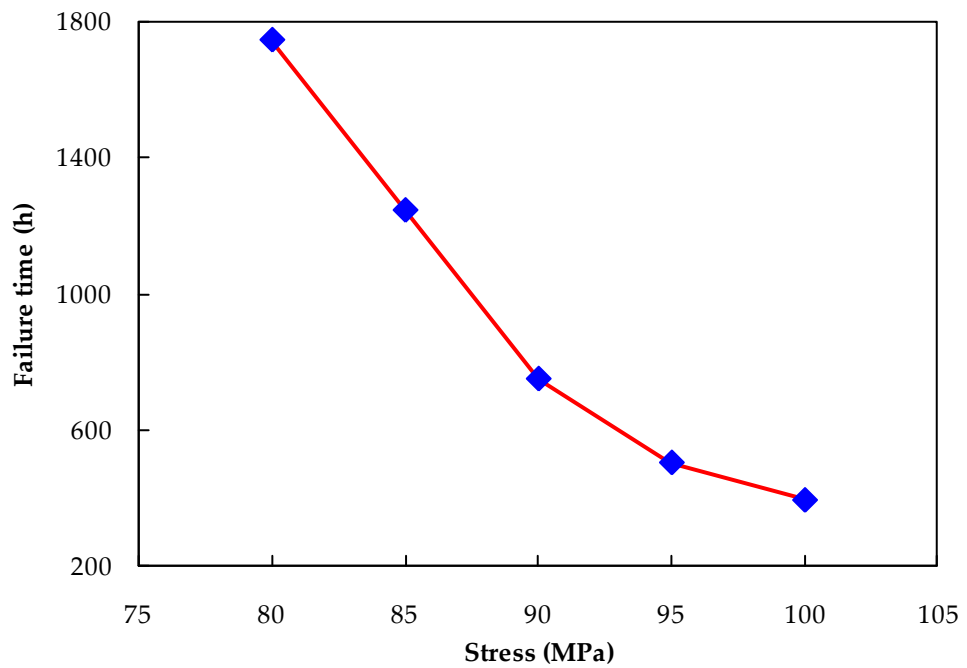


Fig. 3-37: Failure times against stresses for the P92 PM at 675°C.

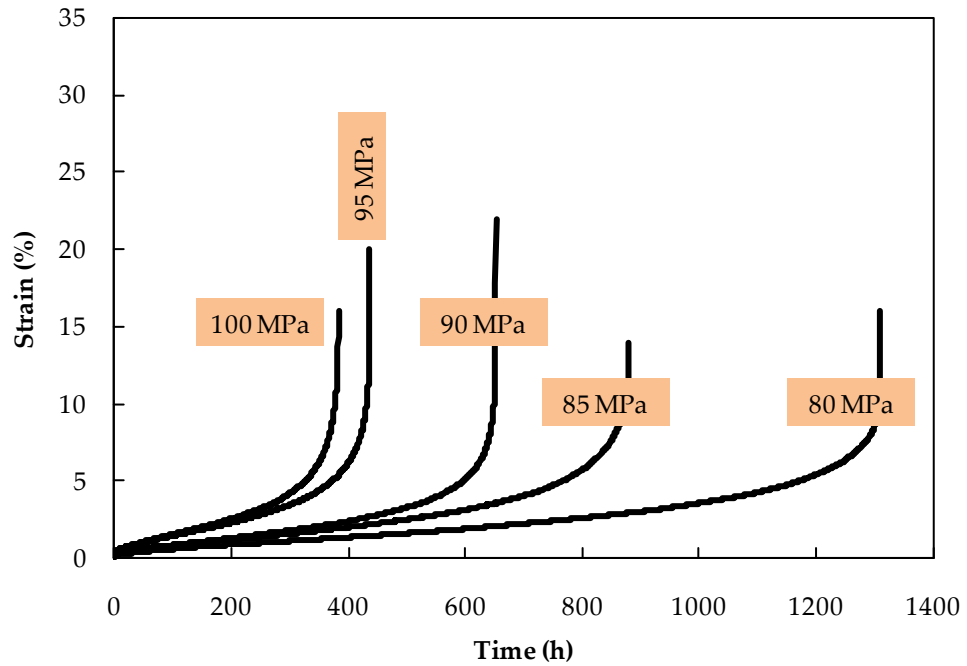


Fig. 3-38: Creep strain curves for the P92 WM, at 675°C.



Fig. 3-39: 85 PM failed cross-weld uniaxial specimen.

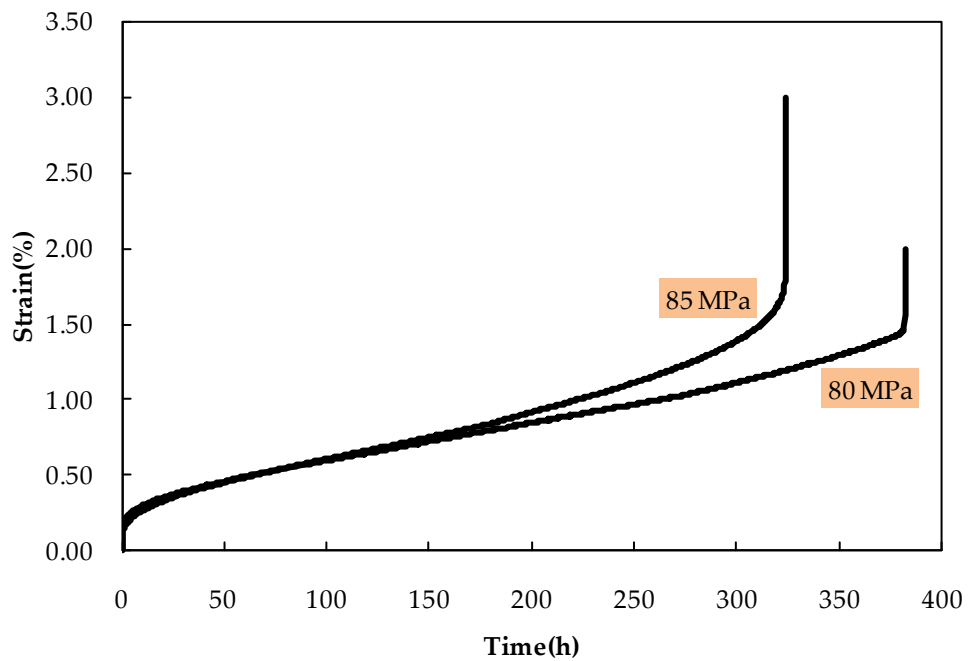


Fig. 3-40: Creep strain curves for P92 cross-weld uniaxial test at 675°C.

σ (MPa)	Failure time (h)						
	PM		WM		Cross-Weld		
	Uniaxial	Notched	Uniaxial	Notched	Uniaxial	Notched	Waisted
60	----	----	----	----	----	----	1005
70	----	----	----	----	----	526	593
80	1541	----	1308	----	382	379	421
85	1210	----	878	----	324	266	336
90	751	----	653	----	----	----	----
95	504	----	436	----	----	----	----
100	394	876	384	----	----	----	----
110	----	697	----	1063	----	----	----
125	----	350	----	498	----	----	----

Table 3-4: Creep rupture data(in hours) for P92 at 675°C.

3.4.2.2 Impression creep test results

Creep and creep rupture data for HAZ material can be determined using impression creep test and cross weld uniaxial ,waisted and notched bar specimens. Impression creep specimens, shown in Fig. 3-6, were used to obtain secondary creep data while cross-weld uniaxial, waisted and notched bar specimens were used to obtain creep rupture data.

Impression creep tests were carried out on the P92 HAZ material at the equivalent uniaxial stresses of 80, 90, and 100 MPa. In impression creep tests, the indenter displacement is recorded against time, as seen in Fig. 3-41, for the P92 HAZ material. This displacement-time record is related to the creep properties of a relatively small volume of material in the immediate vicinity of the indenter, (Hyde and Sun, 2009a). Conversion factors were used to determine the impression creep loading and to obtain the HAZ material strain from the indenter displacement. Application of these conversion factors has been described earlier in Section 3.2.2.

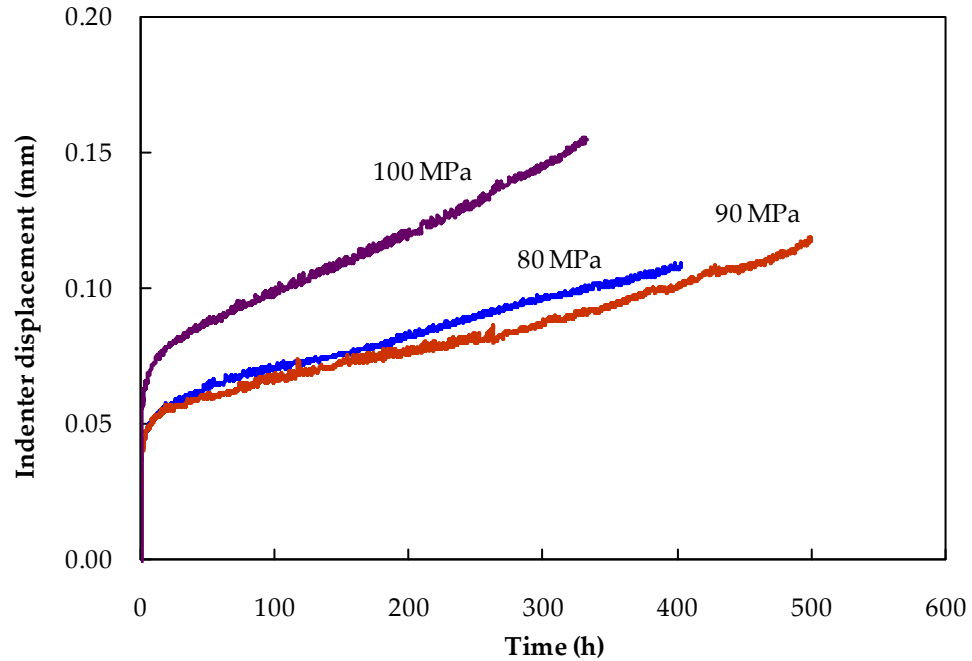


Fig. 3-41: Results of the impression creep test for the P92 HAZ material, at 675°C, subjected to steady loading from the parent material side.

3.4.2.3 P92 creep crack growth

PM and cross-weld CT specimen tests were used to study the CCG in P92 material, at 675°C. The geometry and dimensions of the CT specimens are given in Section 3.2.3. Five PM CT specimens were tested, i.e. CT1, CT2, CT3, CT4 and CT5. The loads, test conditions and main results, for the P92 CCG tests, are given in Table 3-5. Test CT4 was scrapped due to problems experienced within the creep machine furnace control unit. Eight cross-weld CT specimens were tested, i.e. CT6-CT13. Initial cracks in the cross-weld specimens were located on the PM/HAZ material boundary. Moreover, the initial cracks were cut in the welding direction for some cross-weld specimens and in the opposite direction to the welding directions in others. Load line displacements were measured and PD readings were recorded and used to monitor the crack progression.

Specimen	Material	Side groove depth	Load (N)	Test duration (h)	Δa (mm)
CT1	PM	None	5000	60	5.90
CT2	PM	None	4000	166	7.32
CT3	PM	10%	3000	470	7.70
CT4	PM	10%	3500	Scrapped	
CT5	PM	10%	3500	267	7.82
CT6*	Cross-weld	None	3000	281	8.50
CT7*	Cross-weld	10%	3000	123	12.00
CT8**	Cross-weld	None	3000	280	7.5
CT9**	Cross-weld	10%	3000	124	8.3
CT10	Cross-weld	10%	2500	262	8.9
CT11	Cross-weld	10%	2000	614	9.8
CT12	Cross-weld	10%	1700	1099	6.32
CT13	Cross-weld	10%	2000	620	9.95

* The initial crack was allowed to grow, during the test, opposite to the welding direction.

** The initial crack was allowed to grow, during the test, in the welding direction.

Table 3-5: Testing conditions and main results of the P92 creep crack growth tests.

Load line displacement

Load line displacement curves for the P92 PM CT specimens, tested at 675°C, are shown in Fig. 3-42. It can be seen that, all of the specimens exhibit primary, secondary and tertiary stages; the tertiary part is being large in all of the tests. It was found to be difficult to stop the manually operated creep machine at the beginning of tertiary stage. Fig. 3-43 shows the load line displacement curves for the P92 cross-weld CT specimens. CT6, CT7, CT8 and CT9 tests were carried out at the same load to study the effect of the direction of initial crack. Comparing the load line displacement curves for the PM and cross-weld CT specimens, it can be seen that the cross-weld specimens are less "ductile" than the PM specimens. Tertiary stage starts at about 1 mm extension in the PM specimen and at about 0.5 mm extension in the cross-weld specimens. The ductility of the cross-weld CT specimens affects the creep crack growth behaviour.

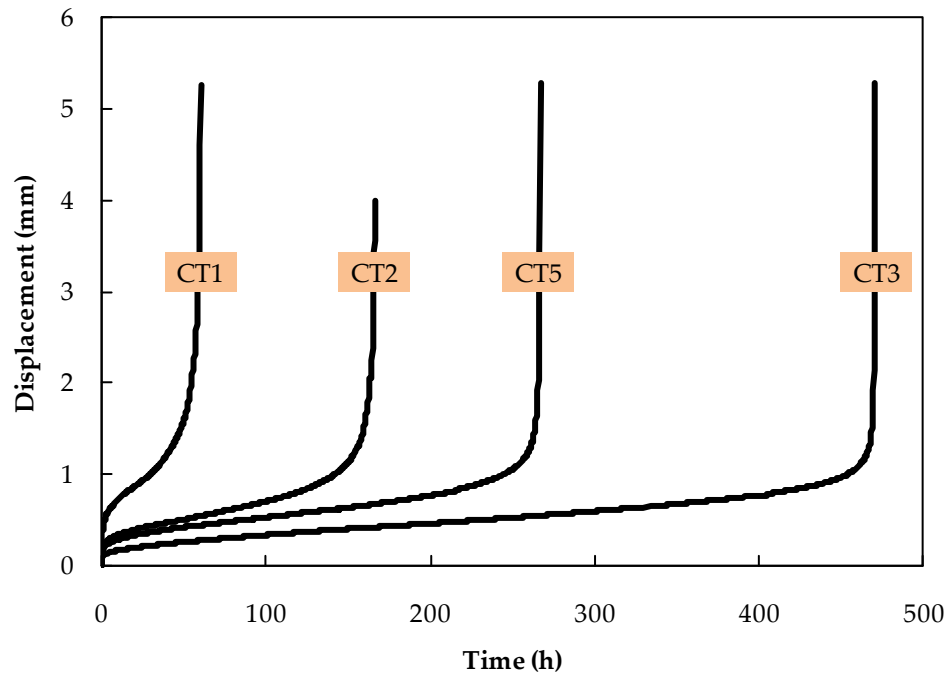


Fig. 3-42: Load line displacement for the P92 PM CT specimens tested at 675°C.

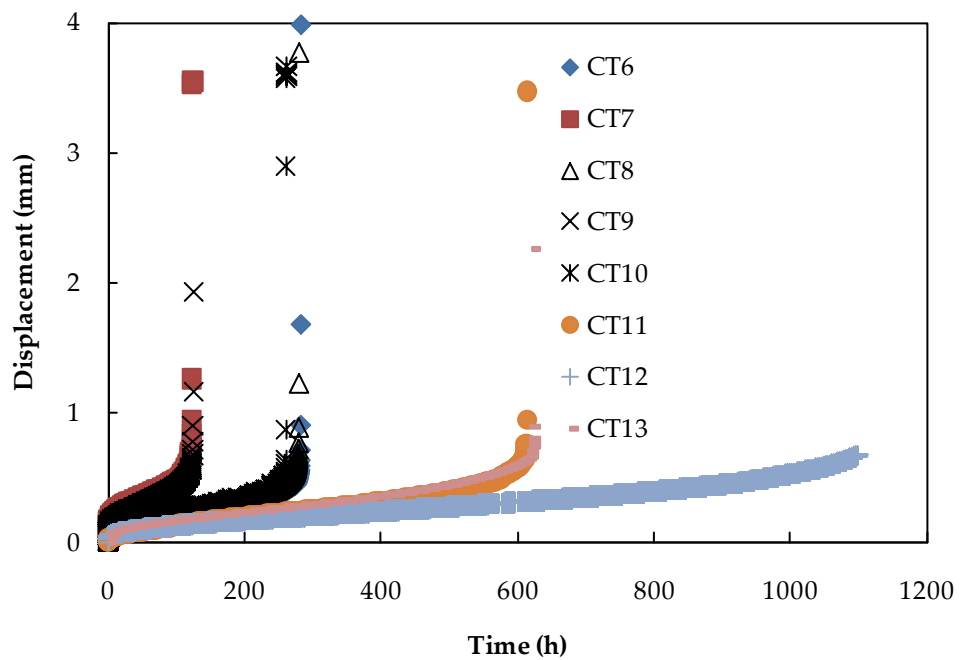


Fig. 3-43: Load line displacement for the P92 cross-weld CT specimens tested at 675°C.

Crack length

As with the P91 CCG testing, the DC potential drop (PD) technique was used to monitor crack progression in the P92 CCG tests. A linear relationship, given in equation (3-6), between the PD and the crack length, was used to obtain the instantaneous crack length. Table 3-6 shows the overall crack extension, the corresponding potential difference and the calibration factor obtained for each CT specimen. The ASTM E 1457-00 (2001) criterion, for defining valid data points, was applied. This criterion indicates that data obtained before the first 0.2 mm crack extension has occurred should be excluded. Furthermore, the minimum crack extension between successive data points is 0.25mm and the maximum is $0.02W$, i.e. 0.64mm in this study where $W = 32$ mm. Fig. 3-44 shows the raw and refined CCG data for the P92 CT1. Refined creep crack growth data was used in calculating C^* and for validating the FE damage predictions. Creep crack growth data for all of the P92 PM CT specimens are shown in Fig. 3-45. Fig. 3-46 shows the creep crack growth curves for the P92 cross-weld CT specimens. Comparing the creep crack growth of the PM and the cross-weld CT specimens, it can be seen that the cross-weld CT specimen are less ductile than the PM CT specimens are. This can be seen from the gradual increase in the crack length, with time, in the PM CT specimens while it is faster in the cross-weld specimens.

3.4.2.4 Macro and microstructure investigation

Fractured surfaces

Photography of the fractured surfaces, for the P92 failed CT specimens, are shown in Fig. 3-47. It can be seen that, the fractured surfaces of the PM CT specimens, i.e. CT1, CT2, CT3 and CT5, are fairly flat while those of the cross-weld CT specimens, i.e. CT6-CT11, are rougher. The roughness pattern seems to

follow the welding beads. The P92 cross-weld CT specimens were cut perpendicular to the welding cross section, as shown in Fig. 3-13.

Specimen	Load (N)	Δa (mm)	Δv (μV)	Calibration factor ($\mu\text{V}/\text{mm}$)
CT1	5000	5.90	0.96275	0.163
CT2	4000	7.32	0.8308	0.114
CT3	3000	7.70	1.52354	0.198
CT4	3500	Scrapped		
CT5	3500	7.82	1.2238	0.157
CT6*	3000	8.5	1.34035	0.157
CT7*	3000	12	1.364	0.114
CT8**	3000	7.5	1.45558	0.194
CT9**	3000	8.3	1.52932	0.184
CT10	2500	8.9	1.59674	0.179
CT11	2000	9.8	2.0616	0.210
CT12	1700	6.32	0.22521	0.035634
CT13	2000	9.95	1.69227	0.170077

* Initial crack was allowed to grow opposite to the welding direction.

** Initial crack was allowed to grow in the welding direction.

Table 3-6: Variation in the calibration factors for the P92 CT specimens.

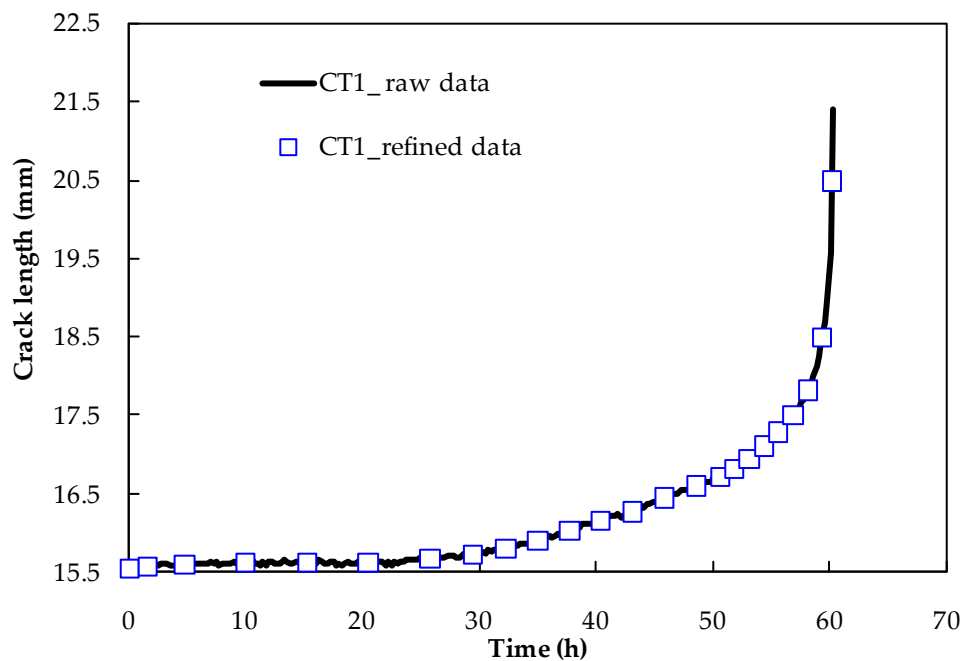


Fig. 3-44: Raw and refined data for P92 CT1.

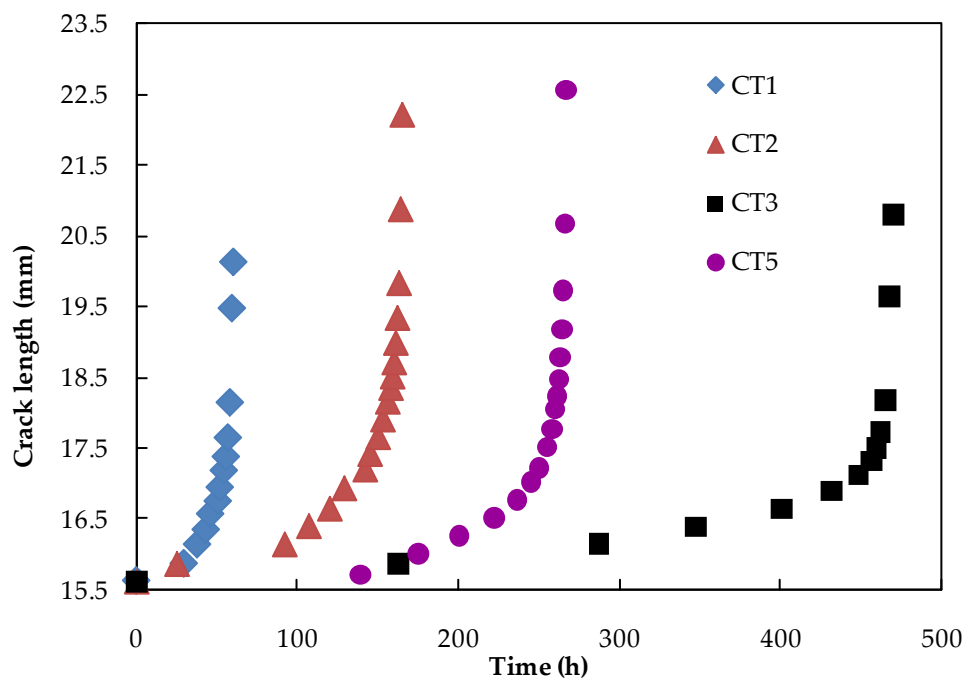


Fig. 3-45: Creep crack growth for P92 PM CT specimens at 675°C.

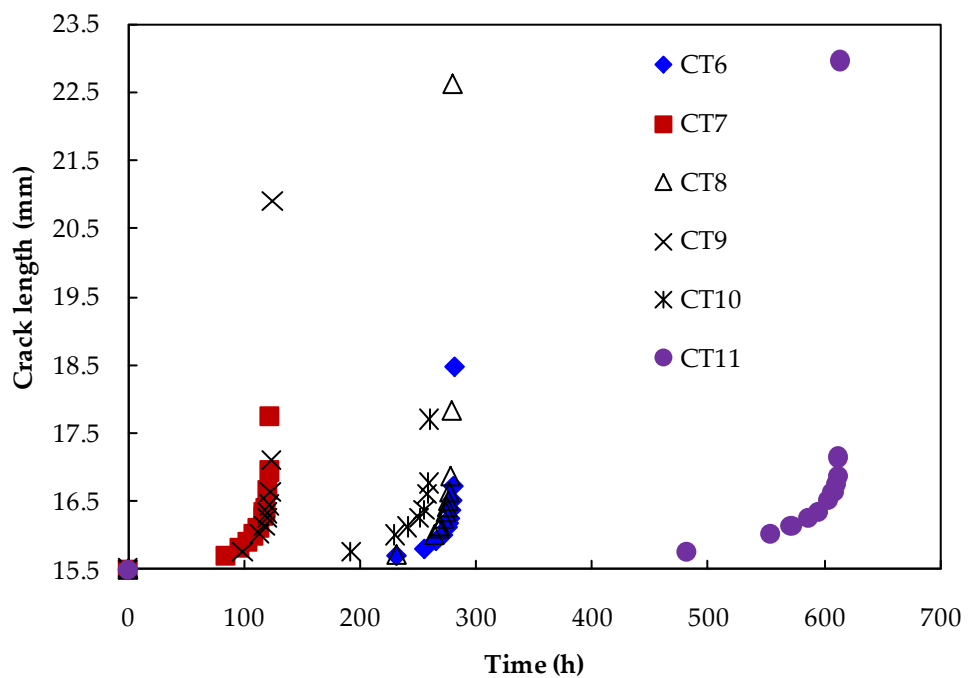


Fig. 3-46: Creep crack growth for the P92 cross-weld CT specimens at 675°C.

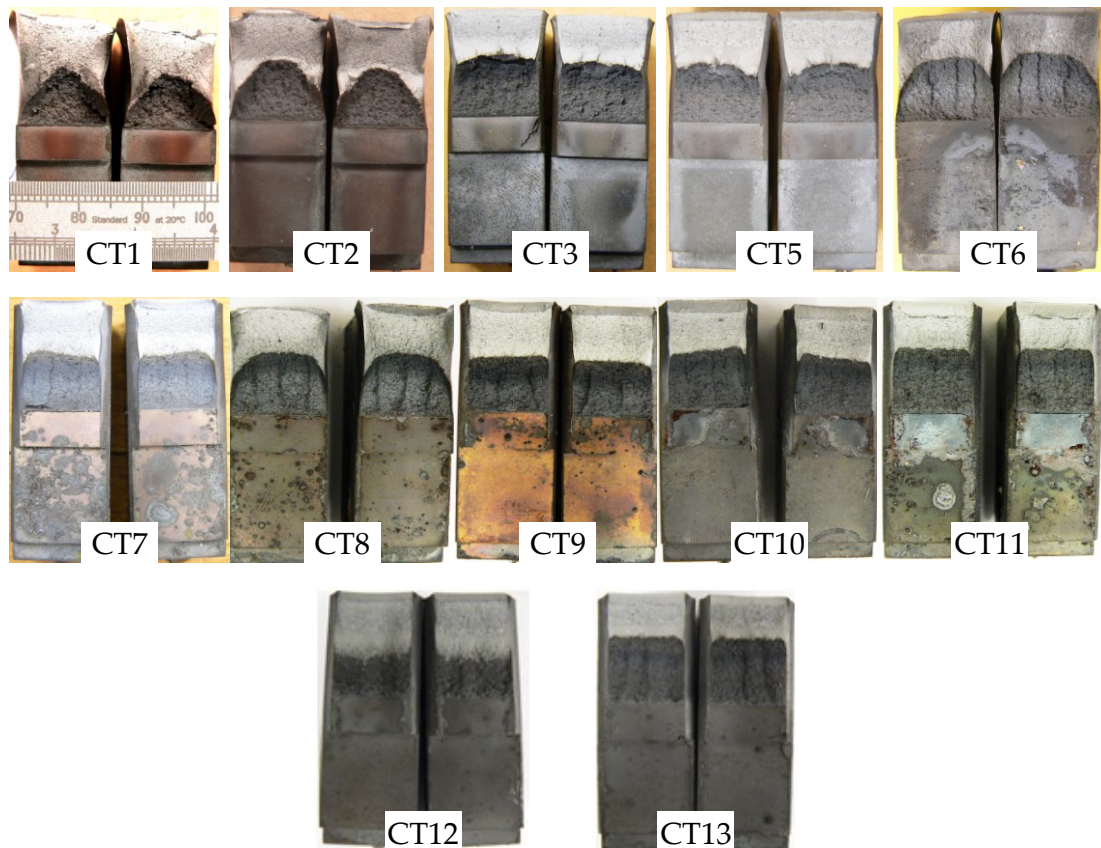


Fig. 3-47: Cracked surfaces of P92 CT specimens, PM specimen CT1-CT5 and cross-weld CT specimens CT6-CT11.

Hardness tests

Vickers' hardness test was carried out on a sample of the P92 weld. The hardness was measured on a line which started in the WM and ended in the PM, passed across the HAZ material. Results of the hardness tests for the P92 weld is shown in Fig. 3-48. It can be seen that the average hardness in the WM is higher than that in the PM and it decreases in the HAZ towards the PM side. Moreover, it can be seen that, the maximum hardness recorded is close to the HAZ/WM boundary, i.e. near the fusion line; where coarse grains are found. Furthermore, the lowest hardness recorded is in the Type IV region; where fine grains are found. The same observations were reported by Falat *et al.* (2009), where they measured the hardness for a creep tested cross-weld uniaxial specimen, at 625°C. This cross-weld uniaxial specimen were tested at 120 MPa

and failed after 1174 hrs. Further, (Sugiura *et al.*, 2010) tested the creep crack growth in P92 CT specimens where the initial crack was located in the middle of HAZ region. They found that the crack grew into the region of the minimum hardness near the boundary between HAZ and PM, i.e. Type IV region.

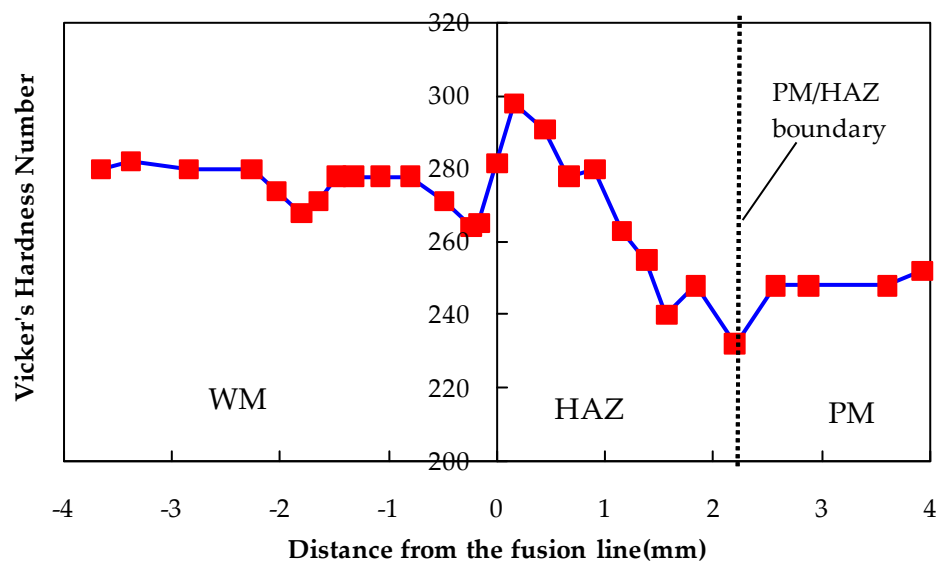


Fig. 3-48: Hardness test results for the P92 weld before creep testing.

3.5 DISCUSSION

One of the purposes of this thesis is to study and evaluate the creep, creep rupture and creep crack growth behaviours of P91 and P92 steels. Therefore, testing programmes have been conducted on these materials. For P91, all of the creep and creep rupture tests were carried out in an earlier test programme and their results have been reported elsewhere, e.g.(Hyde *et al.*, 2004a). P91 creep crack growth tests were carried out and are detailed in this thesis. For the P92 weld, creep and creep rupture tests are completed for the PM , WM and across P92 weld. Creep crack growth tests are also completed for the P92 PM CT specimens and for the P92 cross-weld specimens. Further, impression creep tests were carried out on the P92 HAZ material.

3.5.1 P91 creep crack growth

Creep crack growth tests involve many parameters that could affect their results. They include: changes in room temperature near the test machine, changes in furnace temperatures, resistance of electrodes connected to specimen (to measure the PD), positioning of initial crack in cross-weld CT specimens, etc. However, it is possible to control most of these variables and estimate their effects on results. Nevertheless, the effect of the variations in the material properties from one region to another (material variability), due to its manufacturing procedure, heat-treatment process or even the CT specimen manufacturing processes, may also be significant and cannot be easily predicted.

In order to assess the effects of P91 material variability, three specimens, i.e. CT6, CT9 and CT10, were tested under the same conditions. For the same purpose, CT8 and CT11 were also tested under the same testing conditions. The results obtained from all of these tests show different behaviours of each

specimen in terms of the creep crack growth, the load line displacement and the failure time.

Fig. 3-49 shows the load-line displacements and the creep crack growth data for specimens CT6, CT9 and CT10. Results for specimens CT8 and CT11 are shown in Fig. 3-50. The discrepancies shown in Fig. 3-49 and Fig. 3-50 can, in part, be attributed to the variability of the material properties in the immediate vicinity of the crack tip or to the slight variability of the initial crack tip position relative to the Type IV zone, caused initially by the difficulty in accurately identifying the Type IV region when machining the cracks into the specimens.

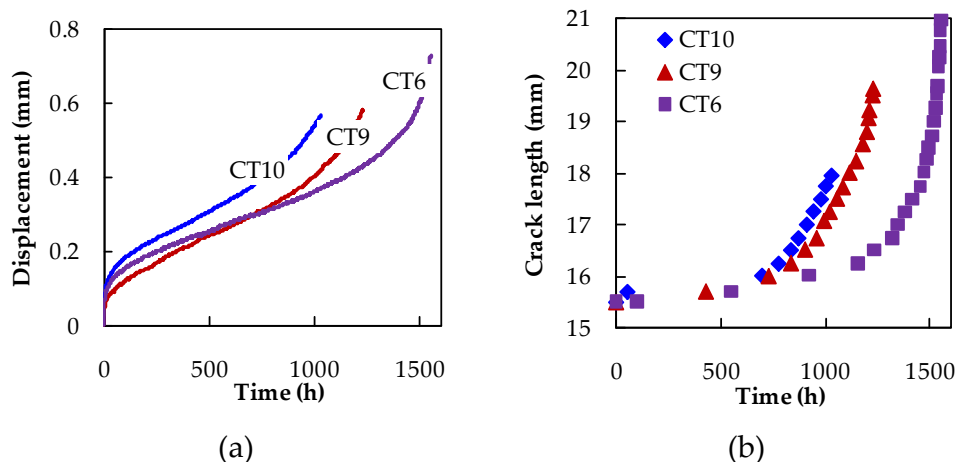


Fig. 3-49: Experimental results of nominally identical CT tests, CT6, CT9 and CT10: (a) Load line displacement and (b) Creep crack growth.

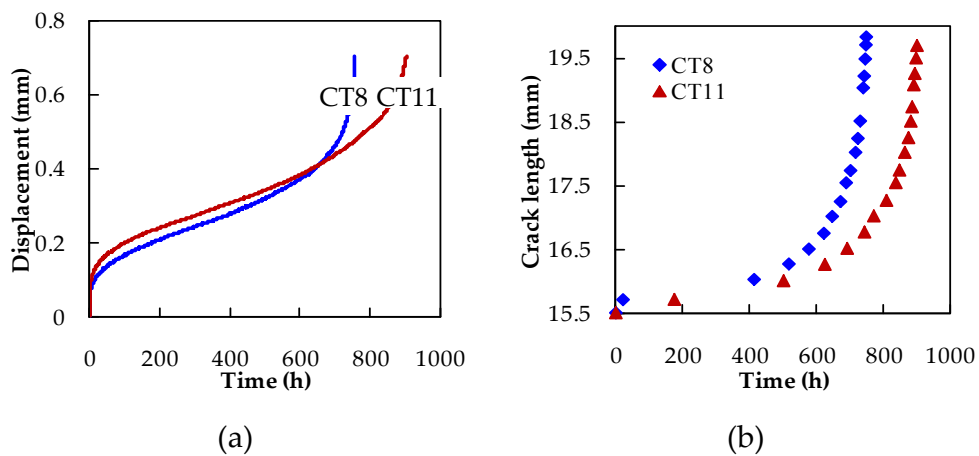


Fig. 3-50: Experimental results of nominally identical CT tests, CT8 and CT11; (a) Load line displacement and (b) Creep crack growth.

3.5.2 P92 uniaxial results

Uniaxial and notched bar specimens were cut from the P92 PM pipe and the WM block. These specimens were tested at 675°C. This temperature was higher than that used for the P91 as the P92 is much stronger than the P91 material; the allowable stress of the P91 and the P92 material, at 650°C, are 30 MPa and 76 MPa, respectively. Moreover, the proposed working temperature of the P92 is 620°C. Therefore, in order to minimize the testing time, a higher temperature (675°C) was chosen to test P92 at. The uniaxial creep curves for the P92 PM and WM, at 675°C, are shown in Fig. 3-51 (a) and (b), respectively. It can be seen that the PM exhibits more ductility and lower steady-state creep strain rates than the WM. In addition, the average strain to failure for the PM is approximately 22%, while it is approximately 18% for the WM. Moreover, the failure times for the PM are higher than those for the WM. The difference between the failure times of the PM and the WM increases as the applied stress decreases.

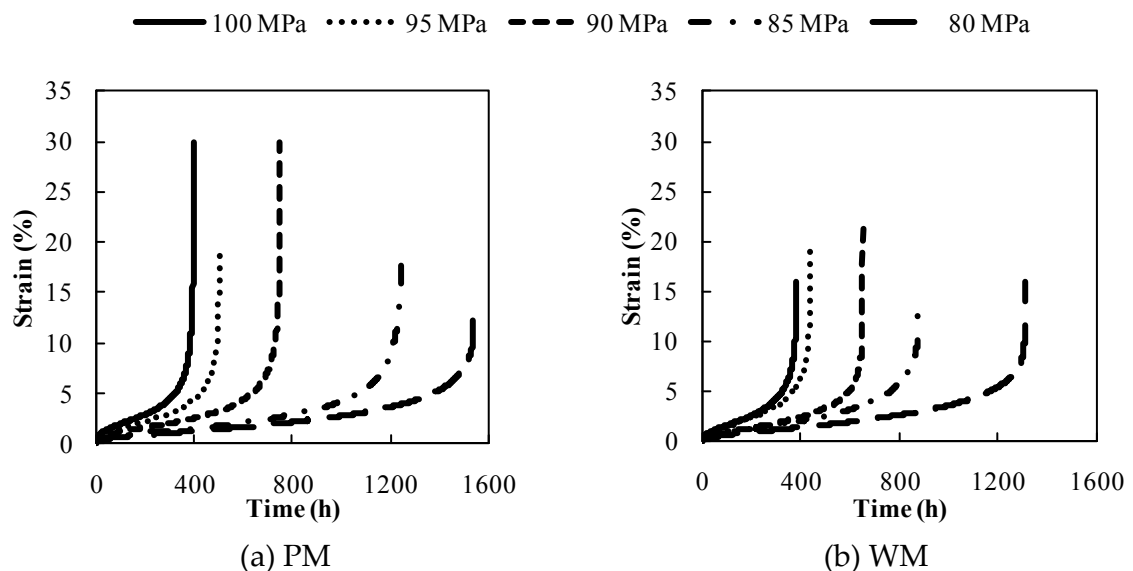


Fig. 3-51: Creep strain curves for P92 PM and WM at 675°C.

3.5.3 P92 creep crack growth

It has been found that the direction of the initial crack with respect to the welding direction affects the creep cracking behaviour of the P92 cross-weld CT specimens. Fig. 3-52 compares the LLD of CT6 and CT7, where the initial cracks grew opposite to the welding direction, and CT8 and CT9, where the initial cracks grew in the welding direction. It can be seen that the LLD curves are smooth when the initial cracks grew in the welding direction (i.e. CT8 and CT9) while they experience little bumps when the initial cracks grew opposite to the welding direction (i.e. CT6 and CT7). It is worth noting that the welding effect has been noticed in both plain specimen (CT6) and side grooved specimens (CT7). However, the crack growth along or opposite the welding direction did not appear to affect the failure time of the specimens and the overall trend of the LLD curves. Furthermore, no effect of the welding direction on the creep crack growth curves has been noticed, see Fig. 3-53.

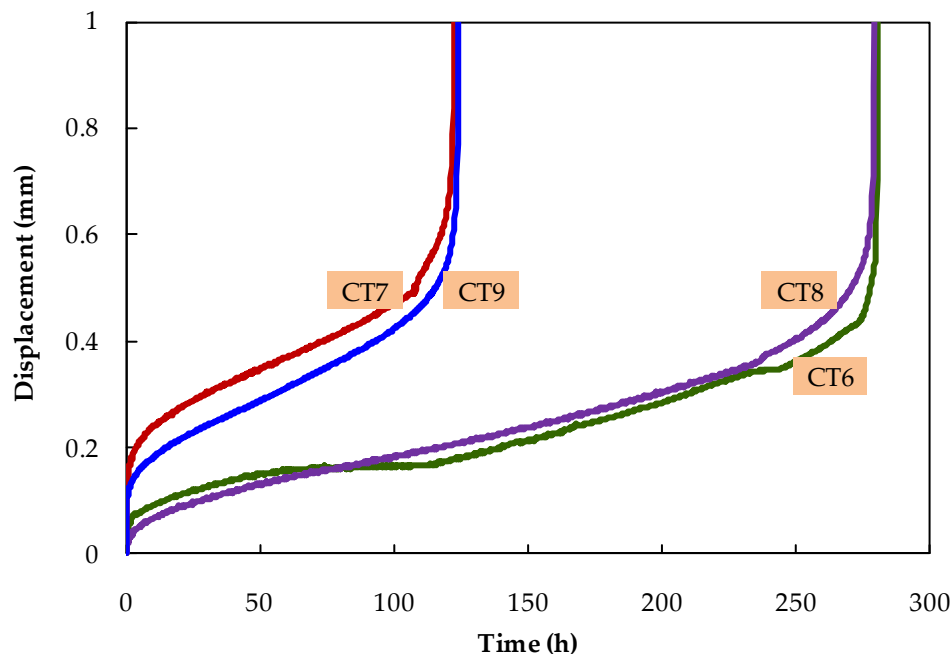


Fig. 3-52: Effect of the welding direction on load line displacement for the P92 cross-weld CT specimens. Cracks grew opposite to the welding direction in CT6 and CT7 while they grew in the welding direction in CT8 and CT8.

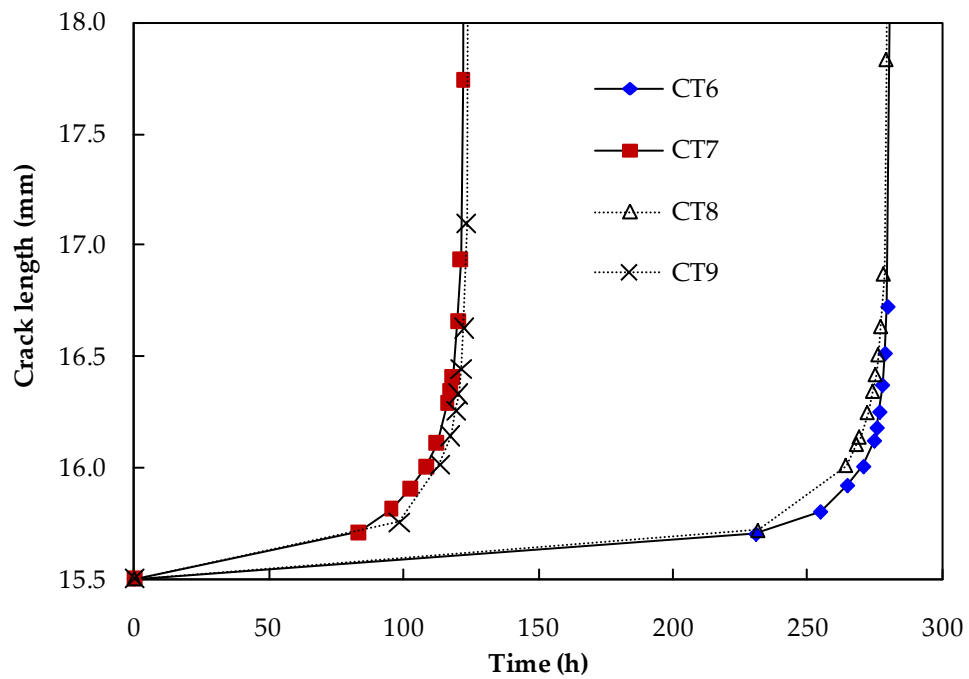


Fig. 3-53: Effect of the welding direction on creep crack growth for the P92 cross-weld CT specimens. Cracks grew opposite to the welding direction in CT6 and CT7 while they grew in the welding direction in CT8 and CT8.

CHAPTER 4.

FRACTURE MECHANICS APPROACH TO PREDICTING CREEP CRACK GROWTH

4.1 INTRODUCTION

This chapter discusses the prediction of the creep crack growth, in P91 and P92 CT specimens, using C^* , a fracture mechanics parameter which correlates the creep crack growth rates. For CT specimens, C^* values were calculated using experimental load line displacement rates and creep crack growth data, and equation (4-10), (ASTM E 1457-00, 2001). Calculated C^* values were then used to correlate the creep crack growth rates. Creep crack growth rates were found to be correlated to C^* , i.e. by $\dot{a} = DC^{*q}$, where D and q are material constants at specific temperature. Creep crack growth rates for PM CT specimens were compared to those for cross-weld CT specimens for both P91 and P92 materials. In addition, the creep cracking resistance of P91 material was compared to that of the P92 material.

FE analyses were also used to obtain C^* for PM CT specimens. Stationary crack models and growing crack models were used. Results obtained from these models are consistent and comparable to the experimental results. This validates the usage of stationary crack models to model the behaviour of cross-weld CT specimens. One advantage of using the growing crack model is the ability to compare the load line displacement of the model to that of the experimental tests.

FE C^* analyses are steady state analyses that require the material Norton's creep constants A and n to be predetermined. These material constants are determined using material creep strain curves. Details of calculating creep and damage material constants, for P91 and P92 materials, are given in Section 5.3. However, a brief description of the derivation procedure for A , n , A' and n' is given below.

4.2 MATERIALS PROPERTIES

It is assumed that the P91 and P92 can be represented by power law material behaviour models, i.e.

$$\dot{\epsilon}_{min} = A\sigma^n \quad (4-1)$$

where $\dot{\epsilon}_{min}$ is the minimum creep strain rate (MSR), defined in Fig. 4-1, σ is the applied stress and A and n are material constants.

Taking the $\text{Log}()$ of both sides of equation (4-1) gives

$$\text{Log}(\dot{\epsilon}_{min}) = \text{Log}(A) + n\text{Log}(\sigma) \quad (4-2)$$

then by plotting $\text{Log}(\dot{\epsilon}_{min})$ against $\text{Log}(\sigma)$, from the straight line of the best fit to the test data, the slope of the line is n and the intercept of the line is $\text{Log}(A)$

Predictions of deformation in a component will be lower bounds when using equation (4-1). That is because the components of deformation related to tertiary and primary creep are neglected; only the steady state deformation is considered. Therefore, if Norton's equation is to be used to predict deformation, an "average" strain rate (Ave. SR), defined in Fig. 4-1, would be an alternative method which would produce more representative deformation rates for longer times. The Norton equation for average strain rates is:-

$$\dot{\epsilon}_{ave} = A' \sigma^{n'} \quad (4-3)$$

where $\dot{\epsilon}_{ave}$ is the average creep strain rate and A' and n' are material constants. A' and n' are obtained in a similar way to that used to obtain A and n .

Table 4-1 includes the values of A , n , A' and n' for the P91 materials, at 650°C, and for the P92 materials, at 675°C. These material constants were used for steady state FE analyses to obtain the C^* values.

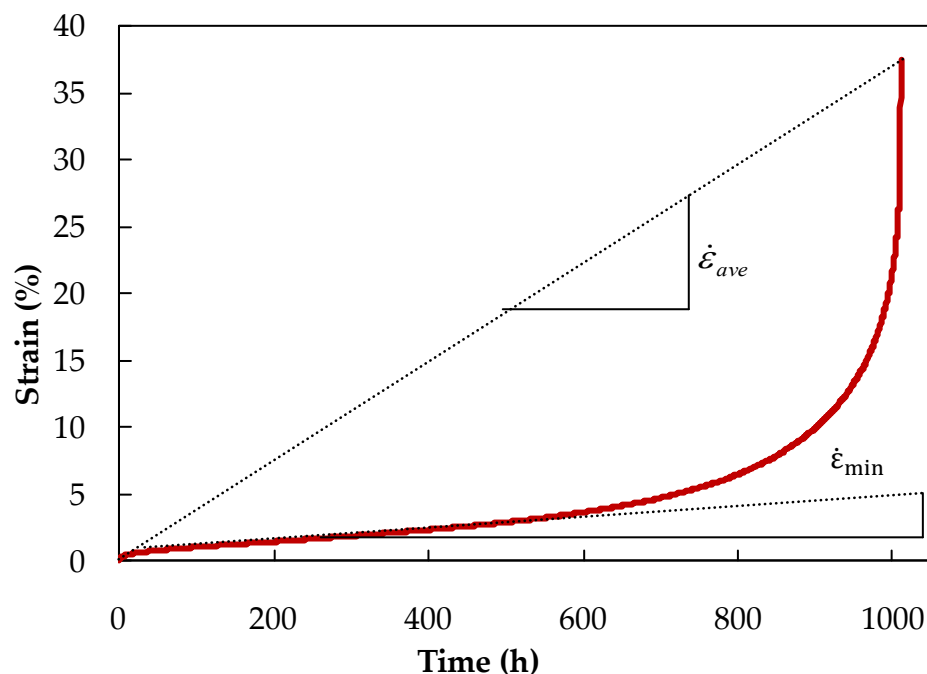


Fig. 4-1: Definition of minimum creep strain and "average" creep strain rate.

Material		A	n	A'	n'
P91	PM	1.092×10^{-20}	8.462	1.0280×10^{-14}	5.7214
	WM	1.370×10^{-20}	7.65	1.9231×10^{-22}	8.7043
	HAZ	2.300×10^{-20}	8.462	-----	-----
P92	PM	4.335×10^{-20}	7.659	6.886×10^{-21}	8.463
	WM	1.065×10^{-17}	6.485	1.559×10^{-19}	7.77

Table 4-1: Materials constants A , n , A' and n' for P91, at 650°C, and for P92, at 675°C (stress in MPa, time in h and $\dot{\epsilon}_{min}$ in h^{-1})

4.3 C* CALCULATIONS FOR P91 AND P92 WELDMENTS

Fracture mechanics parameters, such as K , $C(t)$ and C^* , can be used to correlate creep crack growth. The choice of these parameters depends on the material creep behaviour. K , the stress intensity factor, is applicable for creep brittle materials while the contour integrals, $C(t)$, and C^* are used for more ductile materials. Creep ductile and creep brittle are discussed in the following section. $C(t)$ is used in the small scale creep region and C^* is used for steady state creep. Definitions of small scale and steady state creep are presented in Section 2.6.3.

Hyde (1988) correlated the creep crack growth in Steel 316 using different specimens, i.e. CT specimens and thumbnail specimens, and different parameters, such as K , Reference stress (σ_{ref}), and C^* . He found that, C^* , rather than other parameters, is capable of correlating the creep crack growth in all the tested specimens. Therefore, in this thesis, the C^* parameter is used to correlate creep crack growth rates in CT specimens cut from the P91 and P92 weldments. Results of the creep crack growth tests, presented in Section 3.4, have been processed in accordance to the (ASTM E 1457-00, 2001) to calculate C^* values and the corresponding creep crack growth rates in P91 and P92 CT specimens.

4.3.1 Validity of the Test Results

The following criteria, defined by (ASTM E 1457-00, 2001), have been conformed with in order to validate the results obtained:

- Data points prior the first 0.2mm crack growth has been excluded. Time for this 0.2mm increase in crack length is known as the crack initiation time.

- Only data points that exceed the transition time, t_T , were considered. ASTM E 1457-00 (2001) defines the transition time, for plane strain conditions, as follows:

$$t'_T = \frac{K^2(1-\nu^2)}{E(n+1)C^*} \quad (4-4)$$

where ν is the Poisson's ratio, E is the modulus of elasticity, n is the creep exponent in Norton's creep law, C^* and K are the C^* -parameter and stress intensity factor, respectively, and K is given by :

$$K = \frac{P}{(BB_N)^{1/2}W^{1/2}} \frac{2+a/W}{(1-a/W)^{3/2}} f(a/W) \quad (4-5)$$

and

$$f(a/W) = 0.886 + 4.64(a/W) - 13.32(a/W)^2 + 14.72(a/W)^3 - 5.6(a/W)^4 \quad (4-6)$$

where P is the applied load, a is the instant crack length, W is the specimens width, B is the CT specimen full thickness, i.e. without side grooves, B_N is the CT specimen net thickness, i.e. with side grooves .

Equation (4-4) is used to calculate t'_T then t_T is the maximum value of t'_T .

- ASTM E 1457-00 (2001) describes the creep process as ductile if $\dot{V}_c/\dot{V}_t > 0.5$, where \dot{V}_c is the creep component of the load line displacement rate and \dot{V}_t is the total load line displacement rate. For all of the creep tests carried out in this thesis, it was found that \dot{V}_c is almost equal to \dot{V}_t . Similar results have been obtained by (Yamamoto *et al.*, 2010) for P91

PM and cross-weld CT specimens. They found that the \dot{V}_c/\dot{V}_t is in range of 0.91 - 0.99 at all the duration in all the experiments.

These criteria were applied to all of the creep crack growth tests conducted on the P91 and P92 materials. Crack lengths, used in C^* calculation, have been chosen so that the difference between every two consecutive points lies between 0.25mm and 0.02W; $W = 32$ mm for all of the CT specimens used in this thesis. Corresponding load line displacement points have been taken. The Secant method has been used to obtain the creep crack growth rates and the corresponding load line displacement rates. In the Secant method, the slope of a line connecting every two consecutive points was taken as the rate at an average point which lies in between these two points, i.e.

$$\left(\frac{da}{dt}\right)_{\tilde{a}} = \frac{(a_{i+1} - a_i)}{(t_{i+1} - t_i)} \quad (4-7)$$

and

$$\left(\frac{dV}{dt}\right)_{\tilde{a}} = \frac{(V_{i+1} - V_i)}{(t_{i+1} - t_i)} \quad (4-8)$$

and

$$\tilde{a} = (a_{i+1} + a_i)/2 \quad (4-9)$$

The values of \tilde{a} and $\left(\frac{dV}{dt}\right)_{\tilde{a}}$ were then used to calculate C^* value, at this crack length, which was then correlated with the value of $\left(\frac{da}{dt}\right)_{\tilde{a}}$.

4.3.2 C^* calculations

The contour integral, C^* , is a mathematical expression, a line or surface integral that encloses the crack front. For CT specimens, C^* can be calculated experimentally using load line displacement rates and corresponding creep

crack lengths. C^* values can be calculated, for homogenous material CT specimens, using the following relationship, (ASTM E 1457-00, 2001):

$$C^* = \frac{n}{n+1} \frac{P\dot{V}}{B_N(W-a)} \left(2 + 0.522 \left(1 - \frac{a}{W} \right) \right) \quad (4-10)$$

where n is the creep exponent as given in Norton's creep law, $\dot{\epsilon} = A\sigma^n$, P is the applied load, \dot{V} is the load line displacement rate, B_N is the net section thickness of side grooved specimen, W is the specimen width and a is the instant crack length.

4.3.3 C^* for the P91 CT specimens

For the P91, creep crack growth tests were carried out on four PM CT specimens and seven cross-weld CT specimens, at 650°C. Load line displacement rates and creep crack growth rates were calculated and used to obtain C^* values. The calculated C^* values were correlated to the corresponding creep crack growth rates.

4.3.3.1 P91 PM CT specimens

Fig. 4-2 shows the correlation between C^* and the corresponding creep crack growth rates obtained from PM CT specimen tests, at 650°C. Scatter can be seen to exist in the data, especially at the lower values of C^* (or at the lower values of creep crack growth rates). Similar scatter has been noticed in testing P91 at 600°C by (Dogan and Petrovski, 2001). This scatter can be, partially, attributed to the variability which exists in the experimental creep crack growth curves. Creep crack growth rates are correlated with the C^* values using $da/dt = D(C^*)^q$, where D and q are material constants defined at the specific temperature. Curve fitting facility, available in Microsoft spreadsheet, was used to fit straight lines of the form $y=ax^b$. This facility is based on the least squares

method. This curve fitting technique was applied to all of the $da/dt - C^*$ curves throughout this thesis.

The data shown in Fig. 4-2 can be represented well using the following power law:-

$$da/dt = 0.0316 (C^*)^{0.6335} \quad (4-11)$$

from which, $D = 0.0316$ and $q = 0.6335$. Similar results were obtained for Mod. 9Cr-1Mo steel, tested at different temperatures by (Yamamoto *et al.*, 2010). They obtained $D = 0.0407$ and $q = 0.705$. Using equation (4-11), for cracked bodies, at a specific C^* value, the corresponding creep crack growth rate can be calculated, and hence the failure time for a component can be predicted.

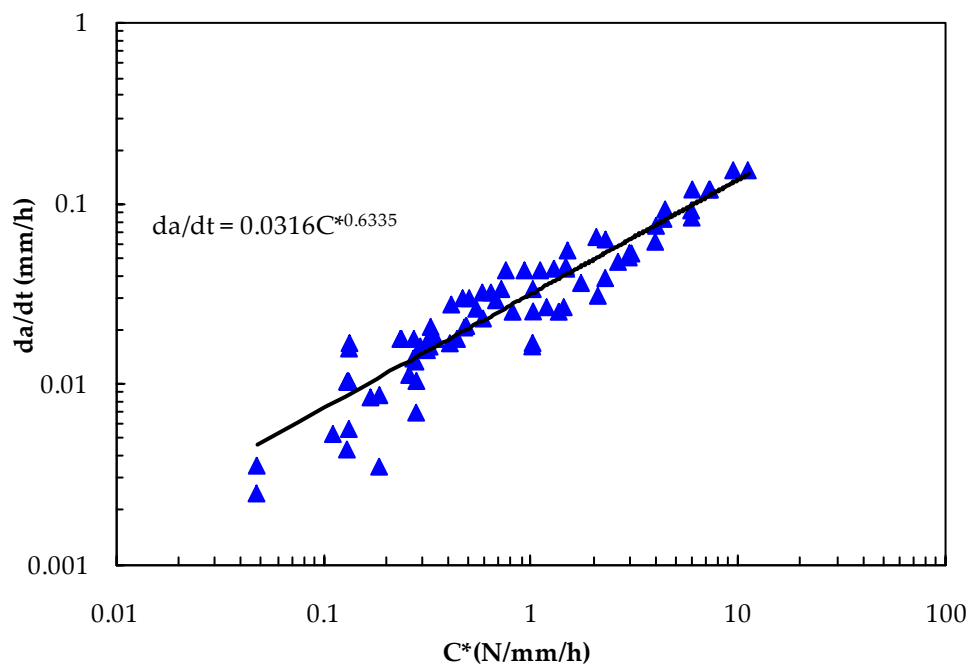


Fig. 4-2: Creep crack growth rates, da/dt , against C^* values for the P91 PM CT specimens, at 650°C.

4.3.3.2 P91 cross-weld CT specimens

Many factors can affect the accuracy of the calculated C^* values for the cross-weld CT specimens. These factors include the accuracy of the positioning of the initial cracks with respect to the Type IV region, variation of the material in the welded zone, variation of material properties at the crack tip, and variation of the testing conditions. It was found that if the tests were left until failure occurred, variations in creep crack growth rates were much more significant. The effects of calibration factors (CF) on calculating creep crack growth (and hence its rates) has been detailed in Section 3.4.1.2. Fig. 4-3 shows the relationship between C^* and the creep crack growth rates for the P91 cross-weld CT specimens, i.e. CT5-CT10, for which each specimen's own CF was used to calculate the creep crack growth. Good correlation can be seen between C^* and da/dt for each of the specimens. However, discrepancies can be seen between the results. As mentioned in Section 3.4.1.2., CT6, CT9 and CT10 were tested at the same load level and gave approximately the same CF. Therefore, their results are consistent and the CF for CT6 was used to calculate the creep crack growth for CT5, CT7 and CT8.

Fig. 4-4 shows the relationship between the creep crack growth rates and C^* values for the P91 cross-weld CT specimens when the CF for CT6 was used to obtain the creep crack growth for CT5, CT7 and CT8. Results of CT11 are also included in Fig. 4-4. The data shown in Fig. 4-4 can be accurately represented using the following power law:-

$$da/dt = 0.374C^{*0.9081} \quad (4-12)$$

from which $D = 0.374$ and $q = 0.9081$.

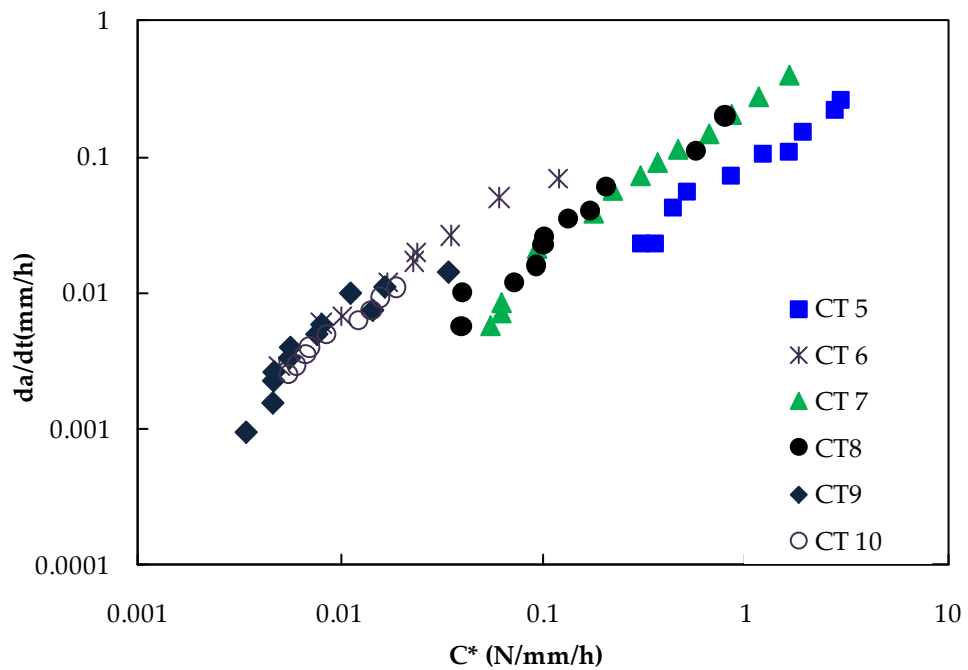


Fig. 4-3: Creep crack growth, da/dt , against C^* for the P91 cross-weld CT specimens, using specimens own calibration factors.

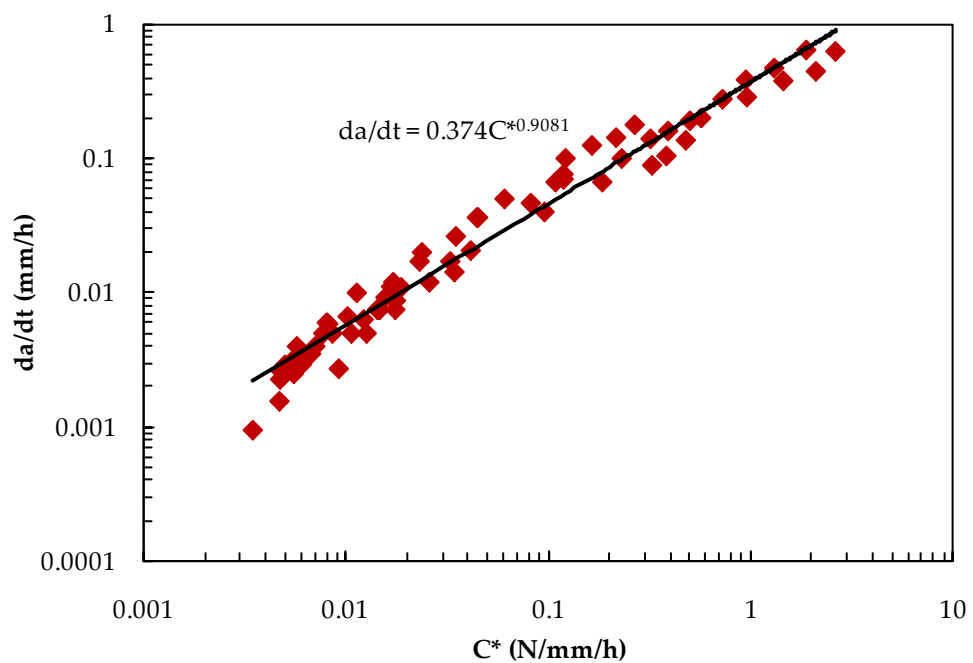


Fig. 4-4: Creep crack growth, da/dt , against C^* for the P91 cross-weld CT specimens, at 650°C, when CT6 CF was used for CT5, CT7 and CT8.

4.3.4 C* for the P92 CT specimens

4.3.4.1 P92 PM CT specimens

As with the P91 CT specimens, the ASTM procedures were followed to calculate C* for P92 PM CT specimens. Fig. 4-5 shows the relationship between creep crack growth rates, da/dt, and corresponding C* values for the P92 PM CT specimens, at 675°C. It can be seen that the C* values correlate well the creep crack growth rates. All of the experimental data has been processed in the same way. However, scatter can be seen to exist in the data. The data shown in Fig. 4-5 can be accurately represented using the following power law:-

$$da/dt = 0.0693C^{*0.7606} \quad (4-13)$$

from which $D = 0.0693$ and $q = 0.7606$.

4.3.4.2 P92 cross-weld CT specimens

Creep crack growth in cross-weld CT specimens is higher than that in single material CT specimens. That is because, in cross-weld specimens, initial cracks were positioned in Type IV region, which is the weakest region in a weld. Fig. 4-6 shows the relationship between the creep crack growth rates against C* for the P92 cross-weld CT specimens. It is worth noting that the n value for the P92 HAZ material is taken as that for the P92 PM; no creep data are available at the moment for the P92 HAZ material. The data shown in Fig. 4-6 can be accurately represented using the following power law:-

$$da/dt = 0.1686C^{*0.9287} \quad (4-14)$$

from which $D = 0.1686$ and $q = 0.9287$.

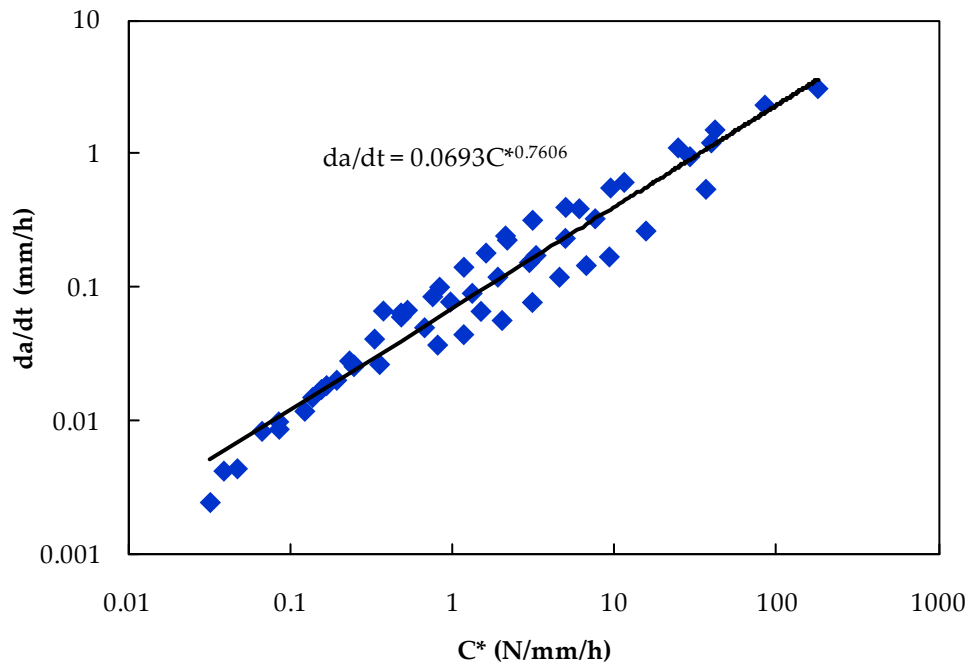


Fig. 4-5: Creep crack growth rate, da/dt , against C^* obtained from P92 PM CT specimens, at 675°C.

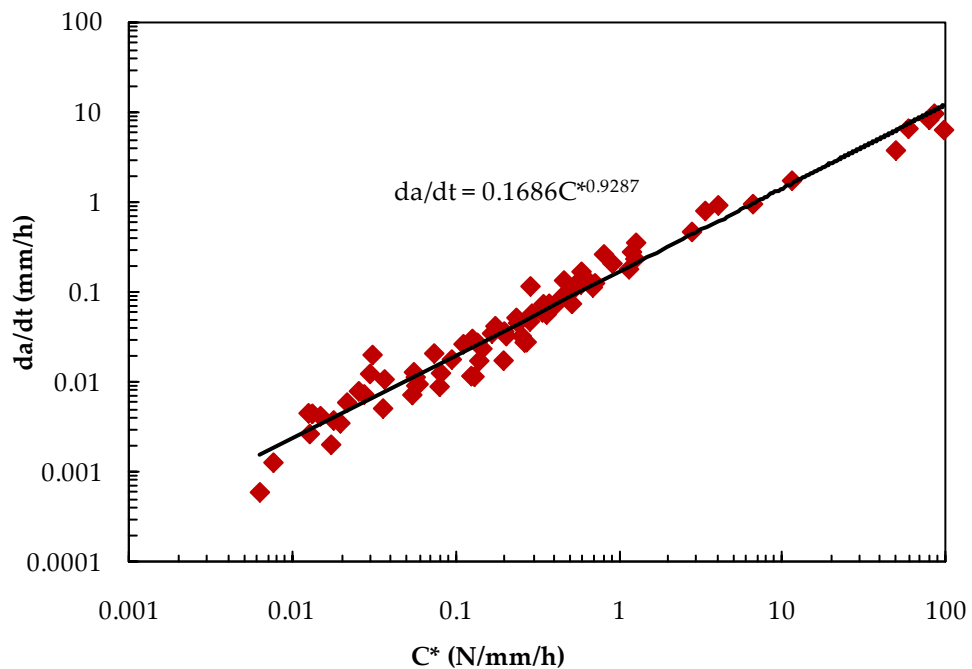


Fig. 4-6: Creep crack growth rate, da/dt , against C^* obtained from P92 cross-weld CT specimens, at 675°C.

4.3.5 Discussion and Conclusions

4.3.5.1 P91 PM against cross-weld

The ASTM equation used to calculate C^* , equation (4-10), is used mainly for homogenous CT specimens, such as the PM CT specimens in this thesis. However, it has also been used to calculate C^* for heterogeneous CT specimens, i.e. cross-weld CT specimens in this thesis, (e.g. (Dogan and Petrovski, 2001, Yamamoto *et al.*, 2009, Park *et al.*, 2001)). Calculated C^* values for cross-weld CT specimens were found to correlate the creep crack growth data very well.

Usage of equation (4-10) to calculate C^* for heterogeneous material CT specimen was tested numerically by (Tu, 2002). He suggested that a scaling factor, known as the g function, could apply to this equation. This function depends on material mismatch, $Q = A_1/A_2$, where A_1 and A_2 are creep coefficients for two adjacent materials make the tested specimen. The g function also depends on a/W and h where a is the crack length, W is the specimen width and h is the distance between the crack plane and the material interface. Therefore, the corrected C^* has the form:-

$$C^*_W = g\left(Q, \frac{a}{W}, h\right) \eta\left(\frac{a}{W}, n\right) \frac{P\dot{V}}{B_N(W-a)} \quad (4-15)$$

Where C^*_W is C^* -contour integral for welded CT specimen, $g\left(Q, \frac{a}{W}, h\right)$ is a function of Q , a/W and h , n is material constant, P is the applied load, \dot{V} is the load line displacement rate, B_N is the specimen net thickness, W is the specimen width and a is the crack length

For cross-weld CT specimens, initial cracks were intended to be located on the boundary between the PM and the HAZ material. Therefore, according to (Tu, 2002), $h = 0.0$ and, therefore, has no effect on the C^* values calculated using equation (4-10). n values for the P91 PM, HAZ and WM are quite large values and hence have their effect on C^* values is insignificant. The mismatch factor Q between the P91 HAZ and PM materials is about 2.1. This mismatch value produces C^* values which are about 0.98 of those calculated using equation (4-10). Therefore, it is justified to use equation (4-10) to calculate C^* for cross-weld CT specimens. Fig. 4-7 shows the variation of the g function with the mismatch factor Q .

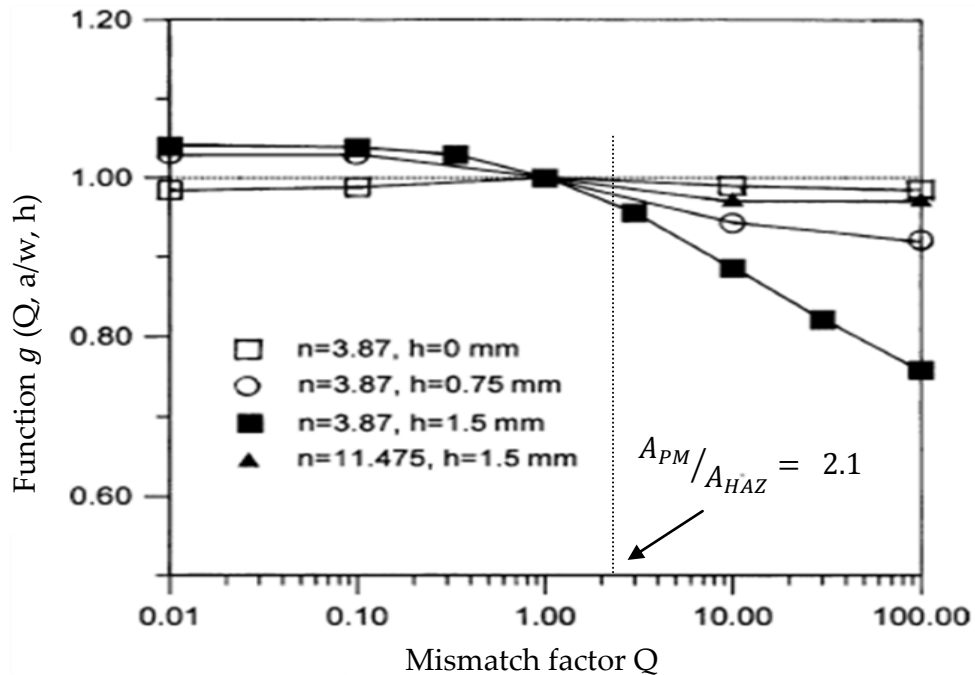


Fig. 4-7: Function g vs. the mismatch factor Q for CT specimen, (Tu, 2002).

Fig. 4-8 compares the creep crack growth rates, da/dt , against C^* for the P91 PM and cross-weld CT specimens. It can be seen that, the creep crack growth rates for the cross-weld specimens are about ten times higher than those for the PM specimens, at the same C^* . Yamamoto *et al.* (2010) studied creep crack growth in Mod. 9Cr-1Mo, i.e. P91, at different temperatures and loads. They found that the

creep crack growth rates of the cross-weld CT specimens are 3 to 10 times faster than that of the PM CT specimens. Therefore, cracks in P91 welded components are likely to grow ten times faster than those in PM components do. Shibli and Le Mat Hamata (2001) tested creep crack growth in a P91 seam welded pipe by applying high pressure gas, at 625°C. They located the initial crack in the middle of the HAZ. Their results showed that the creep crack growth rate in the welded pipe is about 10 times higher than that of the PM pipe, tested under same testing conditions. However, when they compared creep crack growth rates in P91 cross-weld CT specimens to those of parent material CT specimens, they found less difference between both of them.

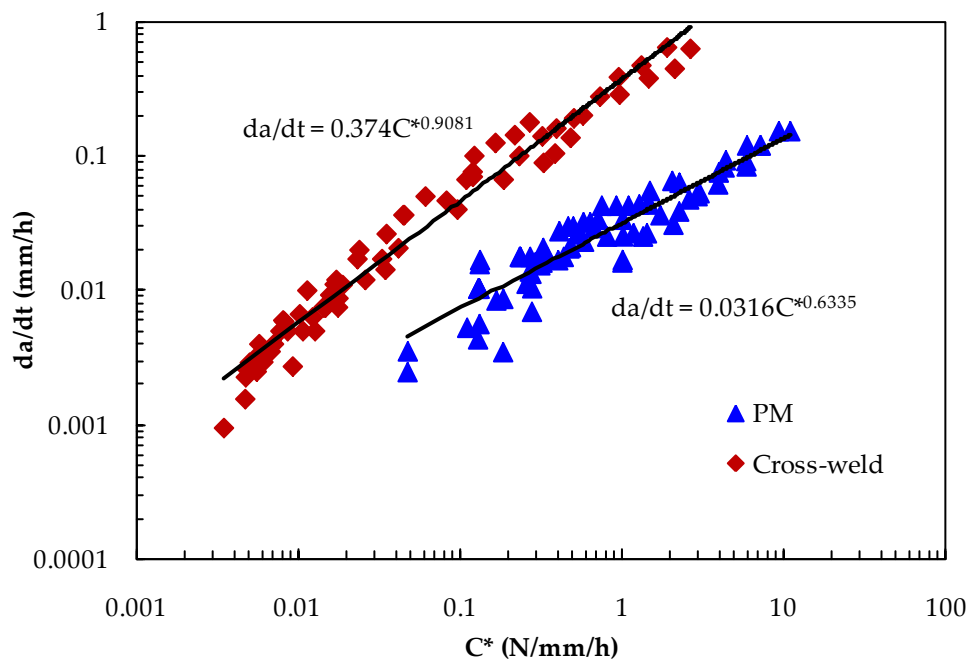


Fig. 4-8: Creep crack growth rates, da/dt , against C^* for the **P91 PM** and **cross-weld CT** specimens at 650°C.

4.3.5.2 P92 PM against cross-weld

Fig. 4-9 compares the creep crack growth for the P92 PM and cross-weld CT specimens. It can be seen that the difference in the creep crack growth rates between the PM and cross-weld CT specimens is less significant in P92 than that in P91, see Fig. 4-8. Moreover, the creep crack growth rates in the P92 cross-weld CT specimens are about two times higher than that in the PM CT specimens, at the same C^* value.

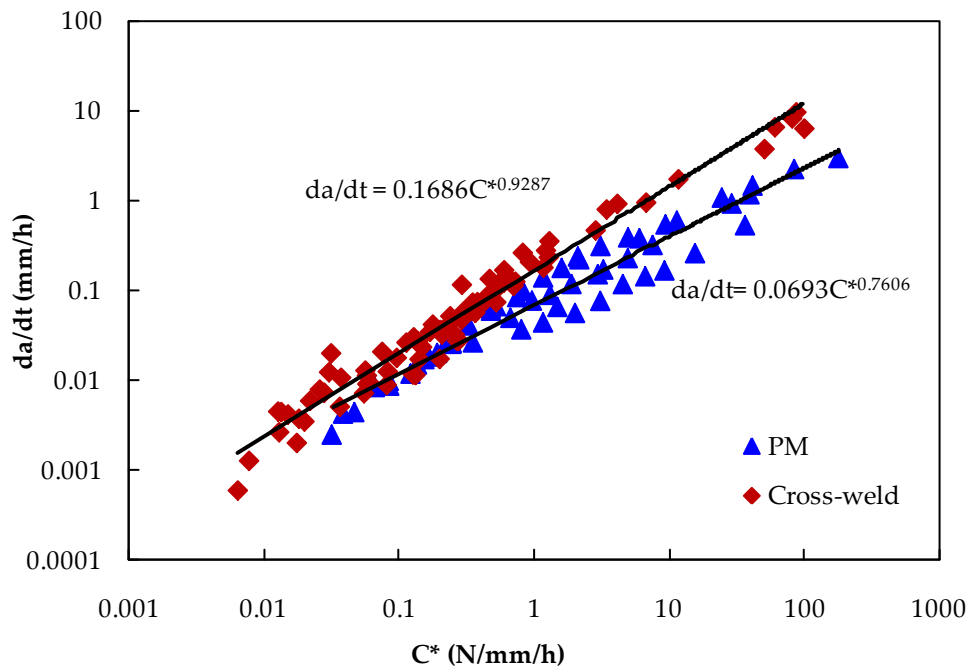


Fig. 4-9: Creep crack growth rates, da/dt , against C^* for the **P92 PM** and **cross-weld CT** specimens at 650°C.

4.3.5.3 P91 against P92

Creep crack growth in the P91 materials, at 650°C, was compared to the creep crack growth in the P92 materials, at 675°C, see Fig. 4-10. It can be seen that the creep crack growth rates for the P92 PM CT specimens are about two times that for the P91 PM CT specimens. However, it should be noted that, the P91 creep crack growth tests were carried out at 650°C while the P92 creep crack growth

tests were carried out at 675°C. Therefore, this difference in the creep crack growth rates may be attributed to the testing temperatures. Conversely, the creep crack growth in the P92 cross-weld CT specimens was found to be less than that in the P91 cross-weld CT specimens, see Fig. 4-11. These results indicate that creep resistance for the P92 welds is higher than that of the P91 material and hence, in that respect, it can be successfully used to replace P91 material.

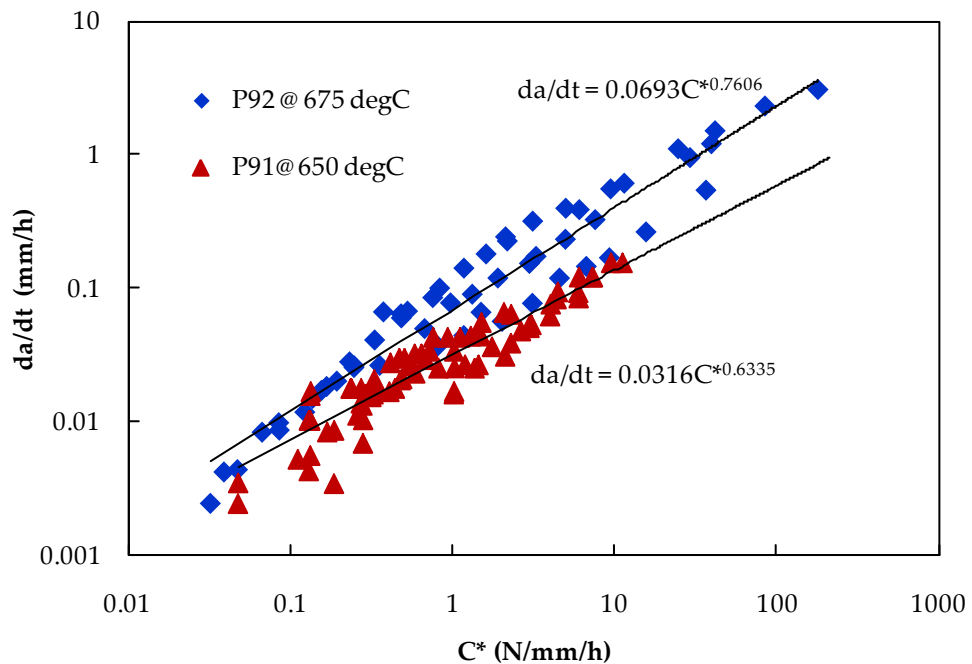


Fig. 4-10: Creep crack growth rates, da/dt , against C^* for the P91 and P92 PM CT specimens.

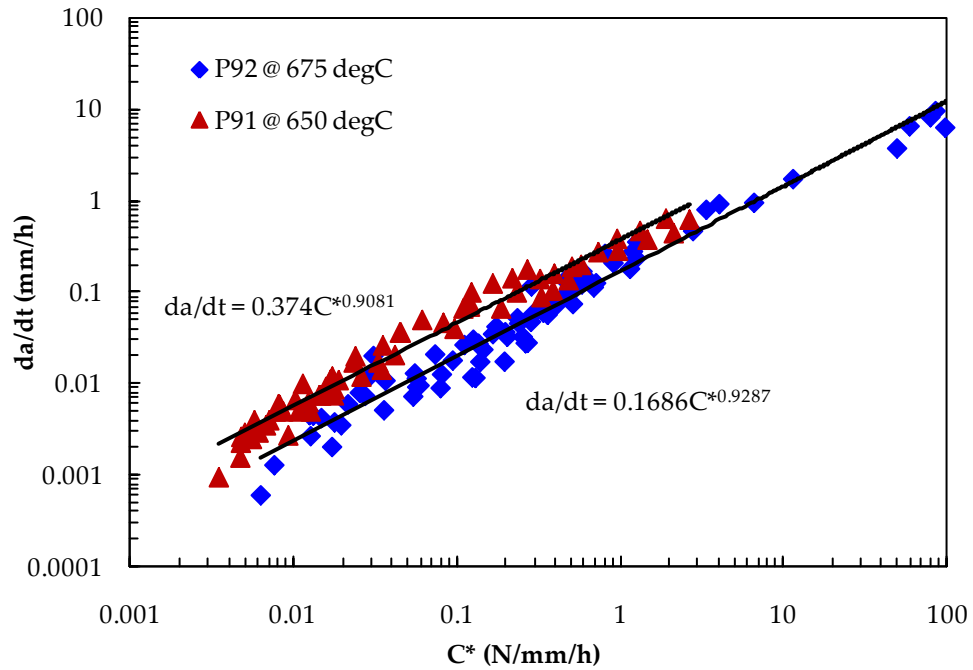


Fig. 4-11: Creep crack growth rates, da/dt , against C^* for the **P91** and **P92 cross-weld** CT specimens.

4.3.5.4 Plasticity in the P91 creep crack growth tests

Load line displacement rates in creep experiments mainly consist of three components, i.e. an elastic component, a creep component and a plastic component, (ASTM E 1457-00, 2001). Summation of these components is the total load line displacement rate as follows:

$$\dot{V}_t = \dot{V}_e + \dot{V}_c + \dot{V}_p \quad (4-16)$$

where \dot{V}_t , \dot{V}_e , \dot{V}_c , and \dot{V}_p are the total, elastic, creep and plastic load line displacement rates, respectively. The creep component of the displacement rate can be obtained using, (ASTM E 1457-00, 2001):

$$\dot{V}_c = \dot{V}_t - \frac{\dot{a}B_N}{P} \left(\frac{2K^2}{E} + (m+1)J_p \right) \quad (4-17)$$

where \dot{a} is the creep crack growth rate, B_N is the CT specimens net section thickness, P is the applied load, K is the stress intensity factor, E is the modulus of elasticity, m is the stress exponent in the Ramberg-Osgood stress-strain relationship and J_p is the fully plastic contribution to the J-integral.

Ramberg-Osgood stress-strain is given by:

$$\varepsilon_p = D_1 \left(\frac{\sigma}{\sigma_y} \right)^m \quad (4-18)$$

where D_1 is a material constant related to its stress-strain behaviour. σ_y is the yield stress and σ is the stress at the uncracked ligament of CT specimens.

J_p can be obtained using the following formula:-

$$J_p = \frac{D_1 h_1 \left(\frac{a}{W}, m \right)}{(\sigma_y (W - a))^m} \left(\frac{P}{1.455 B_N \alpha} \right)^{m+1} \quad (4-19)$$

where h_1 is a function of a/W (given in Table 4-2), a and W are the crack length and the specimen's width, respectively. α is given by:

$$\alpha = (\phi^2 + 2\phi + 2)^{1/2} - (\phi + 1) \quad (4-20)$$

where,

$$\phi = \frac{2a}{(w - a)} \quad (4-21)$$

Determining D_1 and m

Fig. 4-12 shows stress-strain curve for P91 at 650°C. It can be seen that the 0.2% yield stress is about 262 MPa and the ultimate tensile stress is about 281 MPa.

Based on this curve, a pure plastic stress-strain curve has been obtained by subtracting the elastic strain from the total strain at stresses higher than the yield stress according to:

$$\varepsilon_p = \varepsilon_t - \frac{\sigma}{E} \quad (4-22)$$

Where ε_p and ε_t are the plastic and total strain, respectively. $E = 132$ GPa, for the P91 at 650°C. The resultant plastic strain curve is given in Fig. 4-13.

a/W	h_1								
	$m=1$	$m=2$	$m=3$	$m=5$	$m=7$	$m=10$	$m=13$	$m=16$	$m=20$
0.25	2.23	2.05	1.78	1.48	1.33	1.26	1.25	1.32	1.57
0.375	2.15	1.72	1.39	0.970	0.693	0.443	0.276	0.176	0.098
0.5	1.94	1.51	1.24	0.919	0.685	0.461	0.314	0.216	1.132
0.625	1.76	1.45	1.24	0.974	0.752	0.602	0.459	0.347	0.248
0.75	1.71	1.42	1.26	1.033	0.864	0.717	0.575	0.448	0.345
1.0	1.57	1.45	1.35	1.18	1.08	0.950	0.850	0.730	0.630

Table 4-2: h_1 (a/W , m) values for CT specimens under plane strain conditions; reproduced from the one given in (ASTM E 1457-00, 2001).

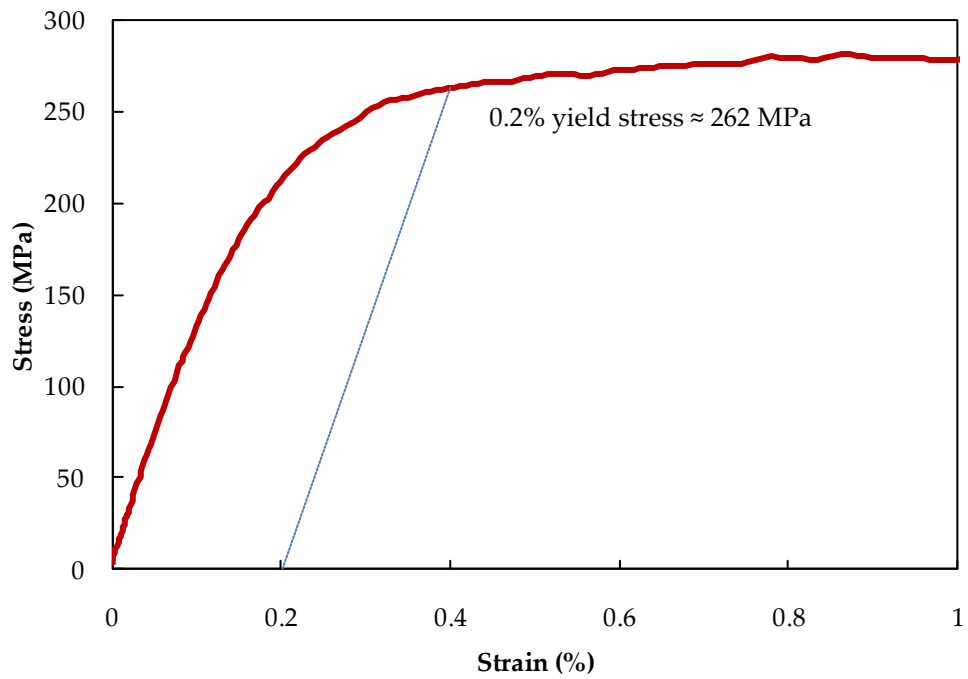


Fig. 4-12: P91 PM stress-strain curve at 650°C.

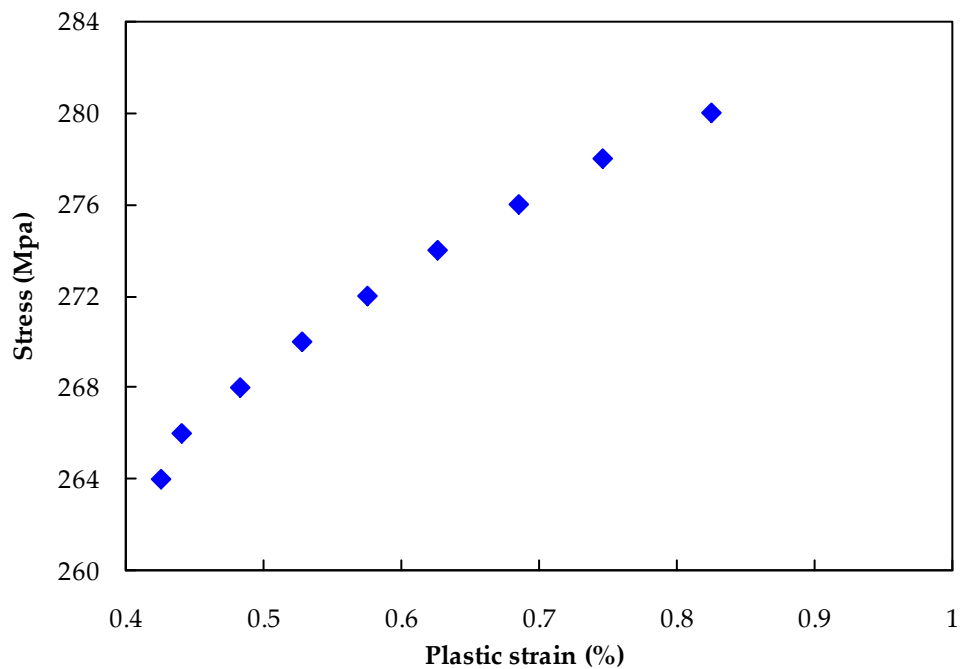


Fig. 4-13: P91 plastic stress-strain curve at 650°C.

Ramberg-Osgood stress strain relationship is given in (ASTM E 1457-00, 2001) as follows:

$$\varepsilon_p = D_1 \left(\frac{\sigma}{\sigma_y} \right)^m \quad (4-23)$$

By taking the logarithm of both sides yields:

$$\log(\varepsilon_p) = \log D_1 + m \log \left(\frac{\sigma}{\sigma_y} \right) \quad (4-24)$$

Therefore, a plot of $\log(\varepsilon_p)$ against $\log \left(\frac{\sigma}{\sigma_y} \right)$ can be used to obtain the $\log(D_1)$ (intercept) and m (gradient). Fig. 4-14 shows $\log(\varepsilon_p)$ against $\log \left(\frac{\sigma}{\sigma_y} \right)$ and the corresponding linear fitting. It was found that $D_1 = 1.8134 \times 10^{-3}$ and $m = 18.558$.

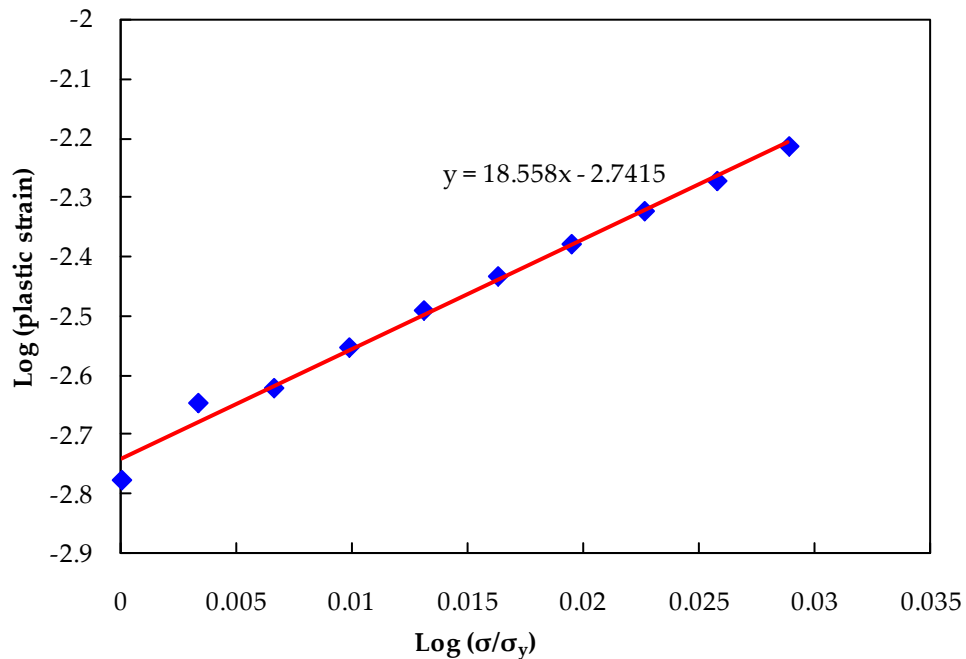


Fig. 4-14: Plastic strain against plastic stress for P91 at 650°C.

Determining h_1

h_1 in equation (4-19) is a function of m and a/W . m is a material constant ($m = 18.558$ for P91 at 650°C) while a/W is increasing as the crack length increases. Values of h_1 are known for $m = 16$ and $m = 20$ (m values that enclose $m = 18.558$ for P91) at different crack lengths, see Table 4-2. Linear interpolations have been assumed to obtain the values of h_1 at $m = 18.558$. Table 4-3 defines h_1 values for the P91 CT specimens at $m = 18.558$. Data given in Table 4-3 was used to define the h_1 at any a/W ratio using linear interpolation.

a/W	0.25	0.375	0.5	0.625	0.75	1
h_1	1.35125	0.16625	0.3305	0.334625	0.435125	0.7175

Table 4-3: h_1 for P91 CT specimen, at 650°C , and different crack length to the specimen width ratios, at $m = 18.558$.

All of the previously mentioned constants and functions were inserted into equation (4-17) to calculate creep component of the load line displacement rates, \dot{V}_c . Creep components of the load line displacement rates were then used to calculate C^* for the CT specimens. C^* values calculated using the creep components of the LLD rates, \dot{V}_c , were compared to those calculated using the total load line displacement rates, \dot{V}_t .

Results for P91 CT4, for example, were used to demonstrate the effect of plasticity on creep crack growth tests. Fig. 4-15 shows the creep crack growth rates, da/dt , against C^* for the P91 PM CT4 using the total load line displacement rates and creep component of the load line displacement rates, calculated using equation (4-17). Fig. 4-16 shows the same for the P91 cross-weld

CT specimen CT7; it has been assumed that the PM and the HAZ material have the same stress-strain curves. No difference can be seen between the C^* values obtained using the total and the creep component of the load line displacement for the PM and the cross-weld CT specimens. This means that elastic and plastic displacements, which contribute only a very small amount, can be neglected, in the total load line displacement. This implies that using \dot{V}_t in calculating C^* is justified for the P91 material. Similar results were obtained by (Yamamoto *et al.*, 2010) for Mod. 9Cr-1Mo steel. They found that creep component of the load line displacement rates is about 91 - 99% of the total load line displacement rates.

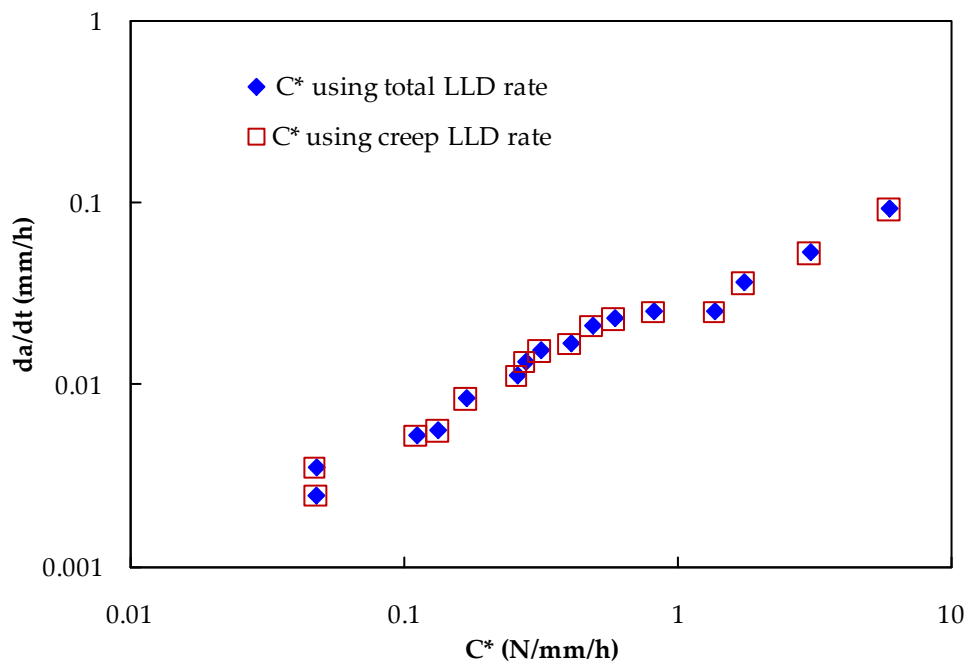


Fig. 4-15: C^* values calculated using total LLD rate, \dot{V}_t , and the creep component of LLD rate, \dot{V}_c , for P91 PM CT4.

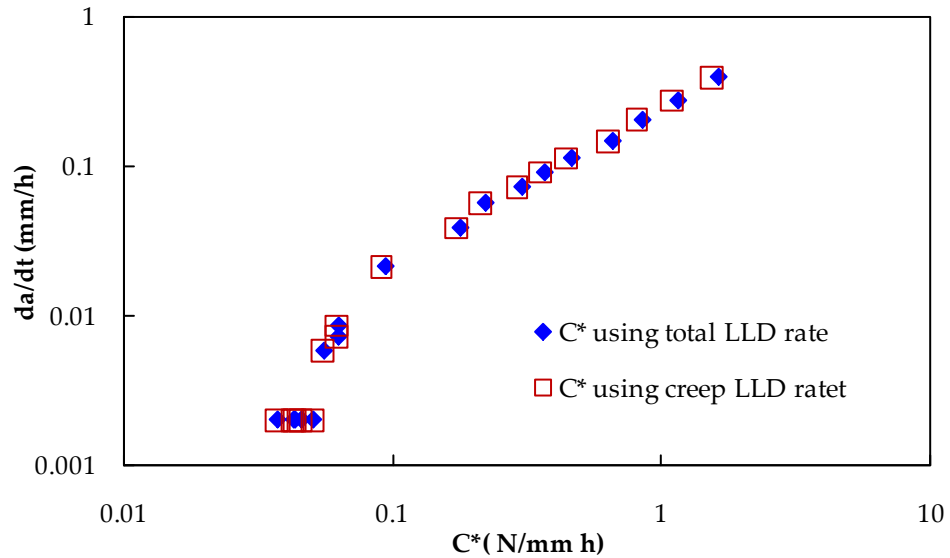


Fig. 4-16: C^* values calculated using total LLD rate, \dot{V}_t , and the creep component of LLD rate, \dot{V}_c , for **P91 cross-weld CT7**.

4.4 FE C^* PREDICTION

The FE method has been extensively used to calculate C^* using CT specimens. Firstly, it was used to obtain FE steady state load line displacement rates, for CT specimens, which were then used to calculate C^* , e.g. (Xia *et al.*, 1998). Recent versions of some FE packages, e.g. ABAQUS, have built-in functions to calculate the contour integral, $C(t)$. In creep analysis, $C(t)$ approaches a constant value when the analysis reaches steady state creep. This constant value of $C(t)$ is C^* . Whether using FE load line displacement rates or the built-in contour integral function, $C(t)$, to obtain C^* , FE analyses have been carried out using stationary crack CT specimens. Halighongde *et al.* (2010) showed the results of an extensive study of the effect of crack position and direction on calculated C^* values for heterogeneous CT specimens. They found that C^* values are path independent when the crack plane is parallel to material interface, while it is path dependent when the crack plane is inclined to the material interface.

In the following sections, FE determined C^* values, based on steady state values of $C(t)$, for P91 CT specimens at 650°C, are presented. Stationary crack analyses

were performed firstly, and these were used to predict growing crack behaviour.

4.5 STATIONARY CRACK CT MODELS

Stationary crack models were used to obtain C^* values based on the steady state values of contour integral $C(t)$. ABAQUS (2007) suggests the use of collapsed elements (singular elements) to accurately model the crack tip singularity and hence, to obtain accurate contour integral values. However, it was necessary to use quadrilateral elements to ease the modelling of growing cracks. Fig. 4-17 and Fig. 4-18 show the CT model meshes using 2D (4 nodes) collapsed elements and 2D (8 nodes) quadrilateral elements, respectively. Due to symmetry, only the upper half of the specimen was modelled. The crack plane is the plane of symmetry on which the boundary conditions were applied. In both models, the plane of symmetry was constrained in the Y-direction while the load point was constrained in the X-direction; to prevent rigid body motion in the X-directions. Plane strain linear elements were used for the collapsed element model and plane strain quadratic elements were used for the quadrilateral elements model. The geometry and dimensions of the CT model are the same as those used for the experimental CT specimens, shown in Fig. 3-7 for single material (i.e. PM) CT specimens. P91 material properties and CT4 loading conditions were used in the FE analyses.

Fig. 4-19 compares the FE contour integrals obtained with the use of both models, i.e. collapsed 4-nodes elements model and quadrilateral 8-nodes elements model, when the initial crack was 15.5 mm. It can be seen that, the contour integral $C(t)$ decreases as time elapses, until it reaches an approximately constant value. This constant value is C^* . Moreover, it can be seen that, the contour integral obtained for both models are practically the same. These results reinforce the use of quadrilateral elements in the analyses in which crack

propagation is included; it is easier to model growing cracks using rectangular elements.

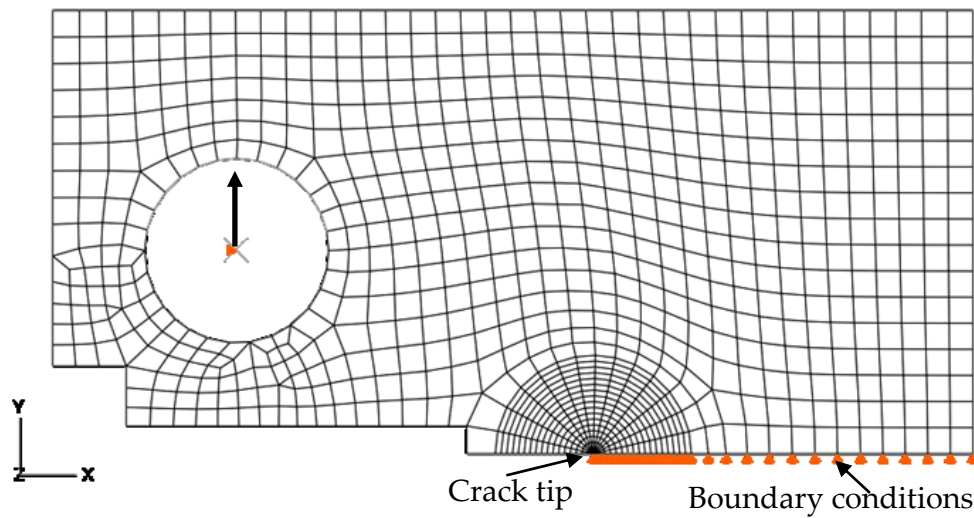


Fig. 4-17: Single material (PM) CT model using collapsed elements ahead of the crack tip.

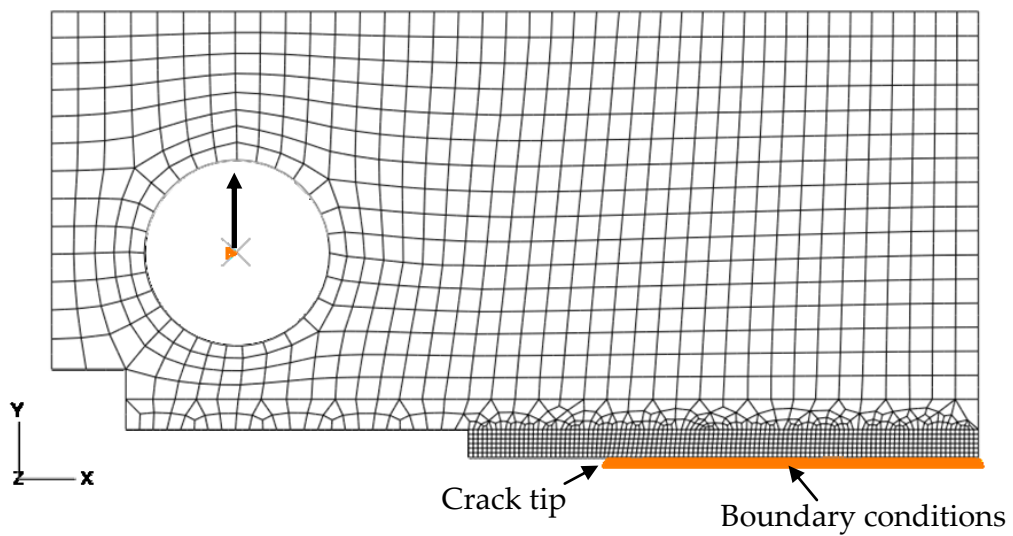


Fig. 4-18: Single material (PM) FE CT model using quadrilateral 4-node elements ahead of crack tip.

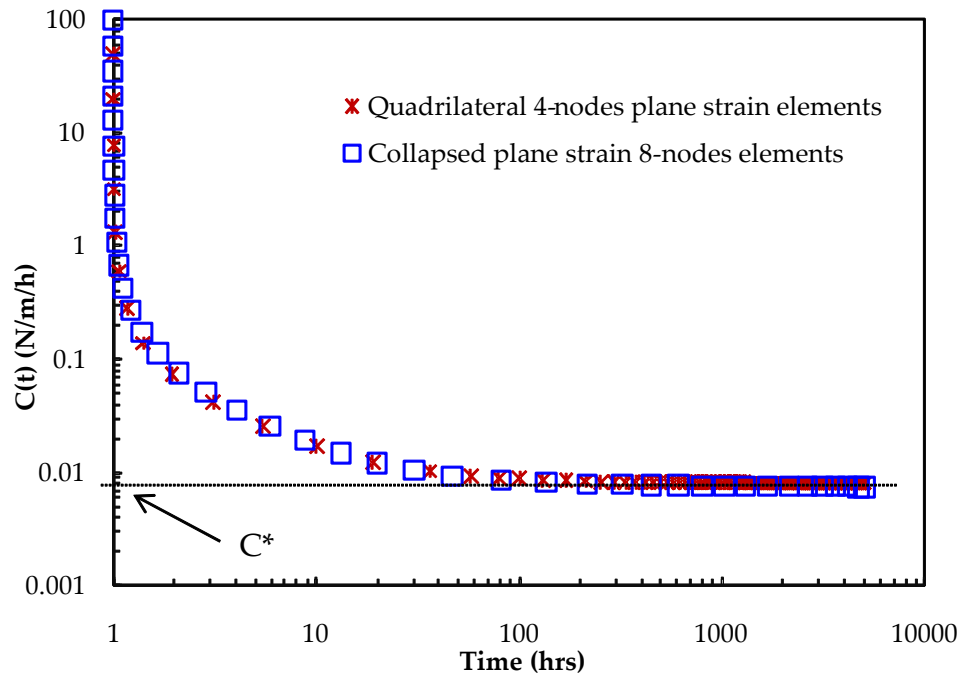


Fig. 4-19: Contour integral, $C(t)$, against time for collapsed element and 4-node elements for P91 CT4 at $a = 15.5$.

4.5.1 C^* for P91 PM CT specimens with stationary crack

FE C^* analyses were conducted for P91 PM CT specimens at nine different initial crack lengths. C^* values were taken as the steady state value of the contour integral $C(t)$. It is assumed that steady state is reached when the changes in the analysis time increments produce negligible changes in the $C(t)$ values. The resulting value of $C(t)$ is taken to be C^* and the corresponding time is taken to be the transient time, i.e. the time at which the creep zone is well spread in the CT specimen, as indicated in Fig. 4-20 for CT4 with a crack length of 16 mm.

Fig. 4-21 shows the variation of the FE C^* values with crack length, including comparison with the experimental results, for P91 CT4. Both of the results, i.e. the FE and Exp., were calculated using MSR material constants, i.e. A and n , and Ave. SR constants, i.e. A' and n' . It can be seen that, the FE C^* values calculated using MSR constants agree well with experimental results. However, the FE C^* values calculated using the Ave. SR constants are higher than all other results.

Table 4-4 shows, for each initial crack length, C^* value and the corresponding steady state time obtained from each of the nine analyses.

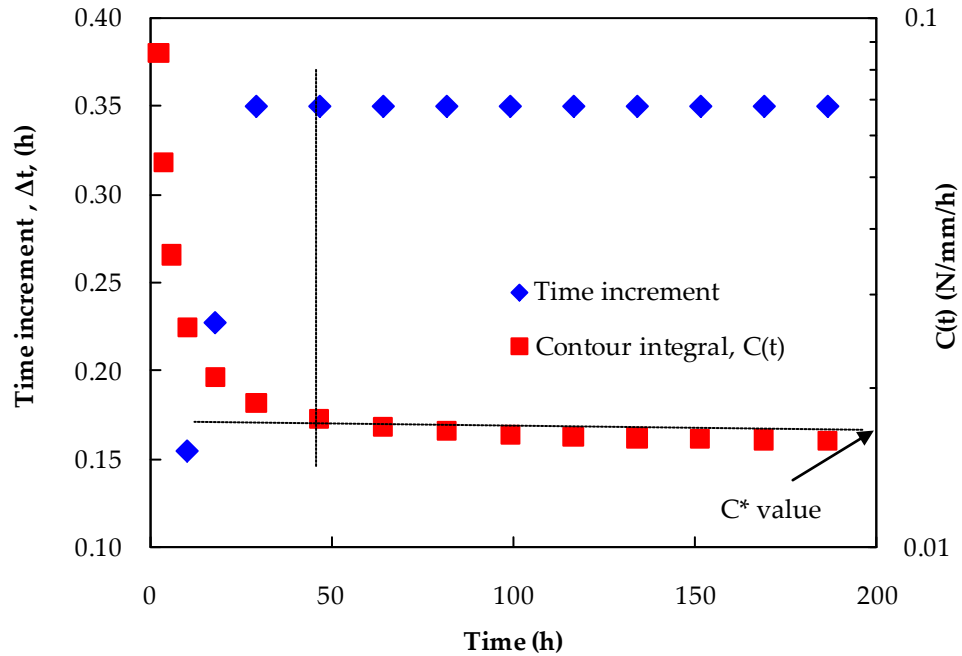


Fig. 4-20: Changing of time increment, Δt , and the contour integral, $C(t)$, with time for CT4 specimen with initial crack length of 16 mm.

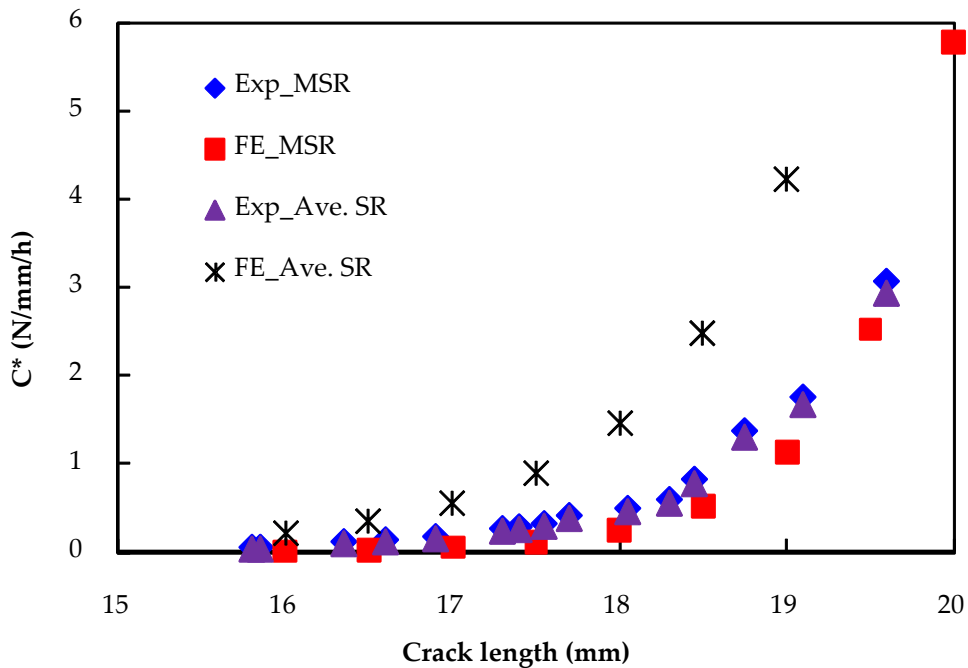


Fig. 4-21: FE C^* against crack length for CT4 using stationary crack models for P91, at 650°C, compared to Exp. results.

Crack length (mm)	C*(N/mm/h)	FE transient time (t_r) (h)
16	0.017745	46.6349
16.5	0.032376	44.2738
17	0.064431	21.907
17.5	0.125	21.5553
18	0.2569	12.9792
18.5	0.581901	3.5789
19	1.23376	2.72136
19.5	2.735	1.88238
20	6.202	1.4823

Table 4-4: C* values and the transient times for CT4, with nine initial crack lengths using stationary crack models (MSR constants were used to obtain C* values).

4.6 GROWING CRACK CT MODELS

4.6.1 FE modelling

The 2D CT growing crack model is shown in Fig. 4-22. Due to symmetry, only half the specimen was modelled. For quadrilateral elements, it was found that the values of C* obtained from using plane strain quadratic elements are closer to the corresponding experimentally obtained values than those obtained when using plane strain linear elements. Therefore, plane strain quadratic elements were used. Element thicknesses were taken to be 12mm, this being the actual CT specimen net thickness.

To grow the crack, the first 5mm ahead of the crack tip was divided into 20 segments, Δa , each being 0.25mm in length, see Fig. 4-23. Boundary conditions were applied to these segments to constrain them in the Y-direction. These boundary conditions were then released, during the analysis, one after another

allowing the crack to grow by 0.25mm each time. This technique is known as the node release technique, for growing cracks. This extension of the crack was modelled in a stepwise manner. Two steps are needed to grow the crack by one increment, Δa . The first step is to release the boundary condition; the time taken for this step is very small (about 0.01h). In the following step, creep takes place and a C^* value was obtained. A similar technique was used by (Xia *et al.*, 1998). Also, Laiarinandrasana *et al.* (2006) used the same technique to simulate crack growth in various specimens, such as CT and DENT. Contour integral values were calculated at each of the generated crack tips.

During an analysis, the boundary conditions are released in a step and the contour integral, $C(t)$, values were calculated in the subsequent step. The transient time for the corresponding stationary crack models, at the same crack length, were taken as the step time for the analysis steps, during which $C(t)$ was calculated, see Fig. 4-20 and Table 4-4.

Loading and boundary conditions for CT4 were used for the growing crack models analyses. Table 4-5 shows the loading, P , and the material constants, A and n , used in the analyses for the P91 CT analyses at 650°C. It is worth noting that only MSR constants were used, for the P91 CT analyses with growing cracks.

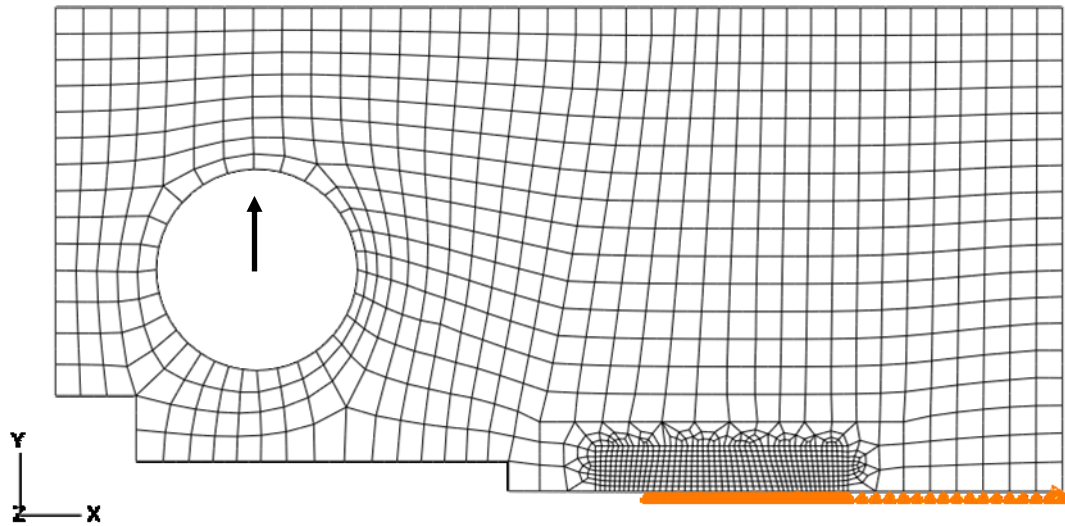


Fig. 4-22: FE mesh for growing crack model.

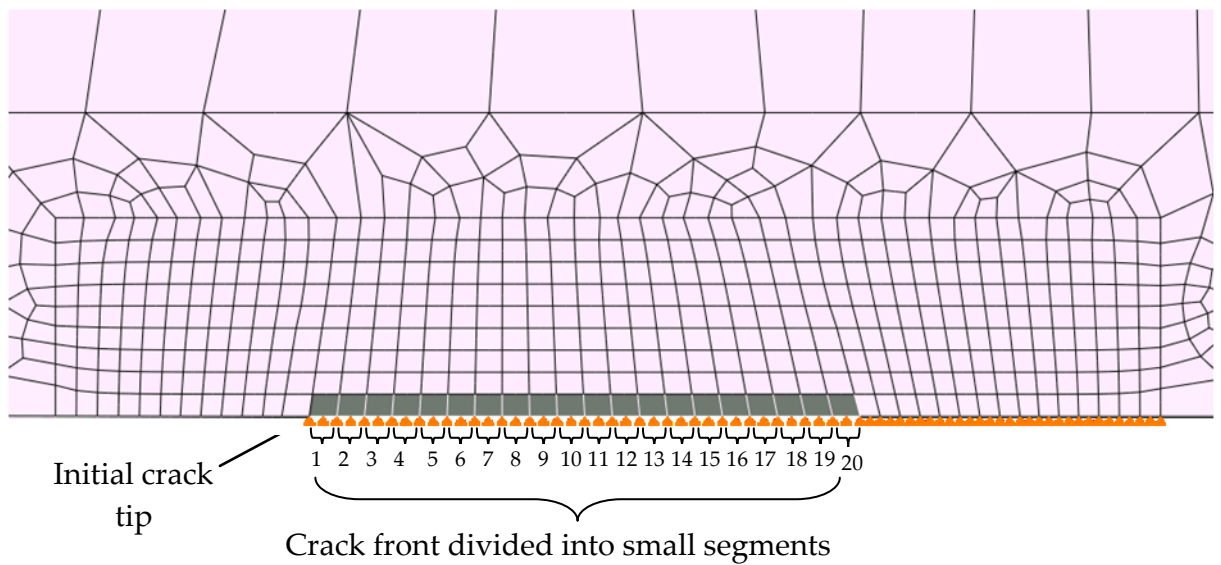


Fig. 4-23: Mesh ahead of the crack tip showing crack increments.

Load, P, (N)	3000
A	1.092×10^{-20}
n	8.462

Table 4-5: Load for CT4 and material constants for P91 at 650°C.

4.6.2 C^* calculations

Using the step times given in Table 4-4 and the growing crack model, an FE analysis was carried out to calculate C^* values. The boundary conditions applied to the elements ahead of the crack tip were released one after another, in order to grow the crack. Fig. 4-24 shows the deformed shape of the CT model and the released boundary conditions.

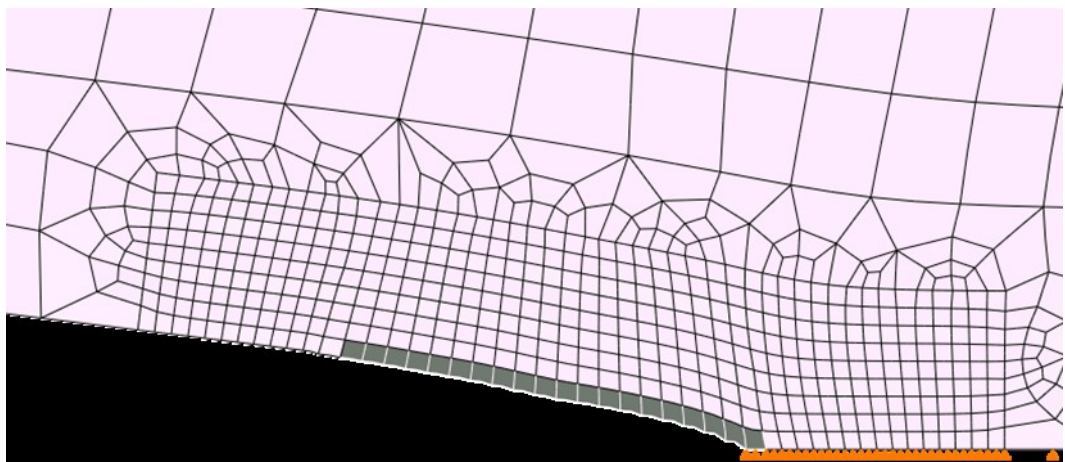


Fig. 4-24: Deformed shape of the growing crack model showing the released boundary conditions.

$C(t)$ contour integral values were obtained from the analysis at the end of each analysis step. Fig. 4-25 shows the progression of the $C(t)$ contour integral, with respect to time, for the growing crack model. The contour integral value at the end of each analysis step was taken to be the C^* value. Fig. 4-26 compares the values of C^* obtained from the growing crack model with those obtained from the stationary crack models; the experimental results are also included. It can be seen that the growing crack model gave the same C^* values as the stationary crack model at the same crack lengths. This indicates that the C^* values for the stationary crack models are equivalent to those determined for the growing crack model. Therefore, stationary crack models can be used in, for example,

cross-weld CT specimens where it is more difficult to use the growing crack model.

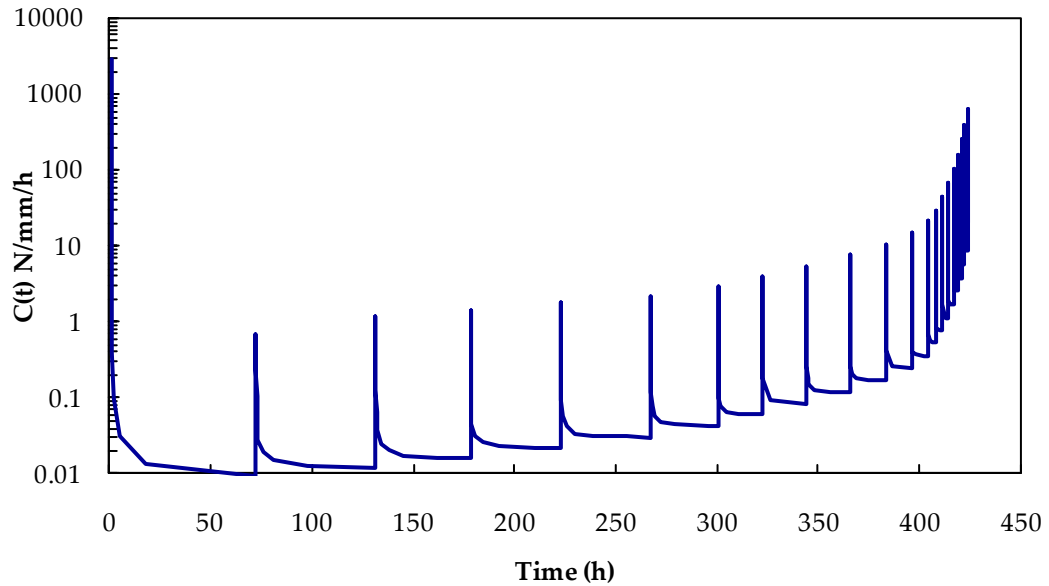


Fig. 4-25: Contour integral, $C(t)$, for the growing crack model using CT4 loading conditions.

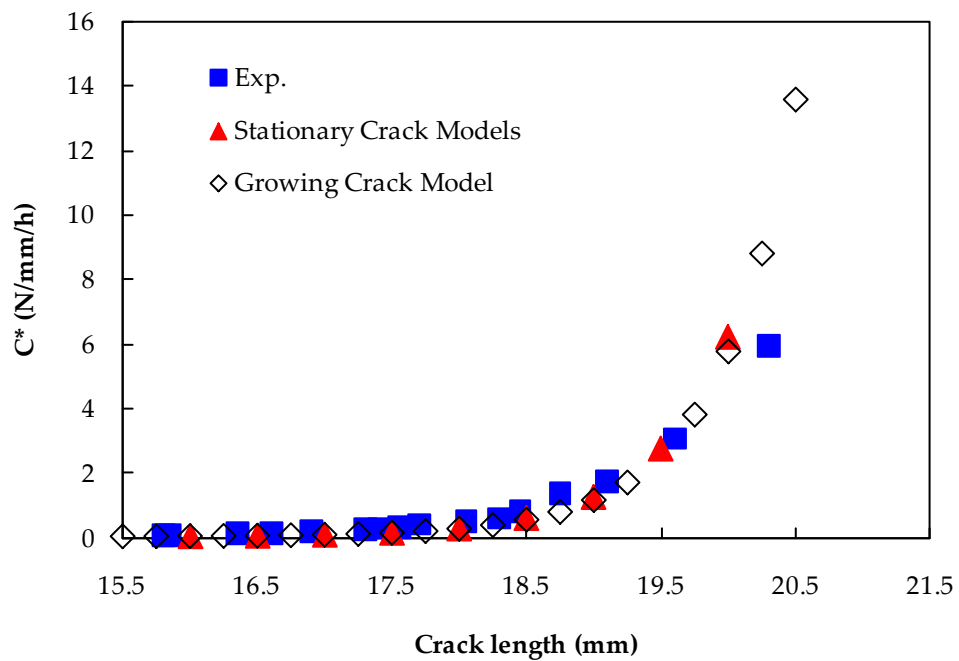


Fig. 4-26: C^* for the stationary crack models and the growing crack model compared to the experimental results for CT4.

4.6.3 Load line displacement (LLD)

Fig. 4-27 shows the LLD curves for the FE growing crack models compared to the experimental results. It can be seen that, during the steady state region, the FE LLD is always less than the experimental LLD. However, the FE and the experimental LLD curves have nearly the same gradients, for almost all of the analysis time.

The FE results shown in Fig. 4-27 are for plane strain elements, which were used for all of the growing crack and stationary crack analyses. Plane stress elements were used for one analysis of the growing crack model to see what its effect would be on load line displacements and, hence, the FE C^* values. The growing crack model was used again with the element type set to plane stress. Fig. 4-28 compares the load line displacement for plane strain conditions analysis, plane stress conditions analysis and the experimental results for CT4. It can be seen that the plane stress conditions, under the same σ_{nom} , produced much greater load line displacement.

Using the average strain material constants, A' and n' , resulted in higher values of C^* , as seen in Fig. 4-21 for steady cracks analyses. However, the resulted LLD displacement, for the growing crack model, agrees well the experimental results, see Fig. 4-29.

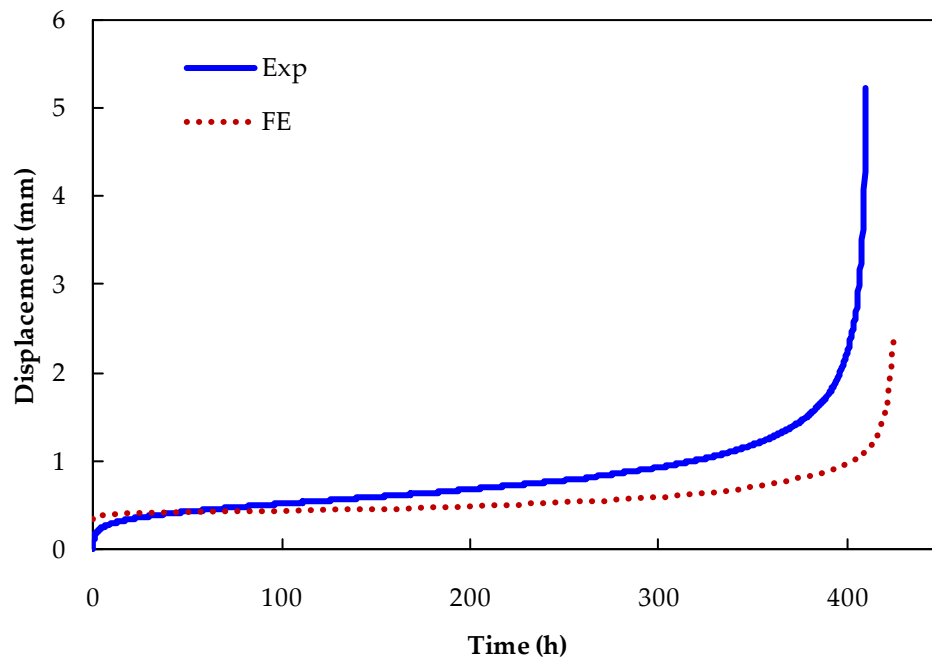


Fig. 4-27: FE load line displacement for the growing crack model, using **plane strain elements**, and the experimental results for CT4.

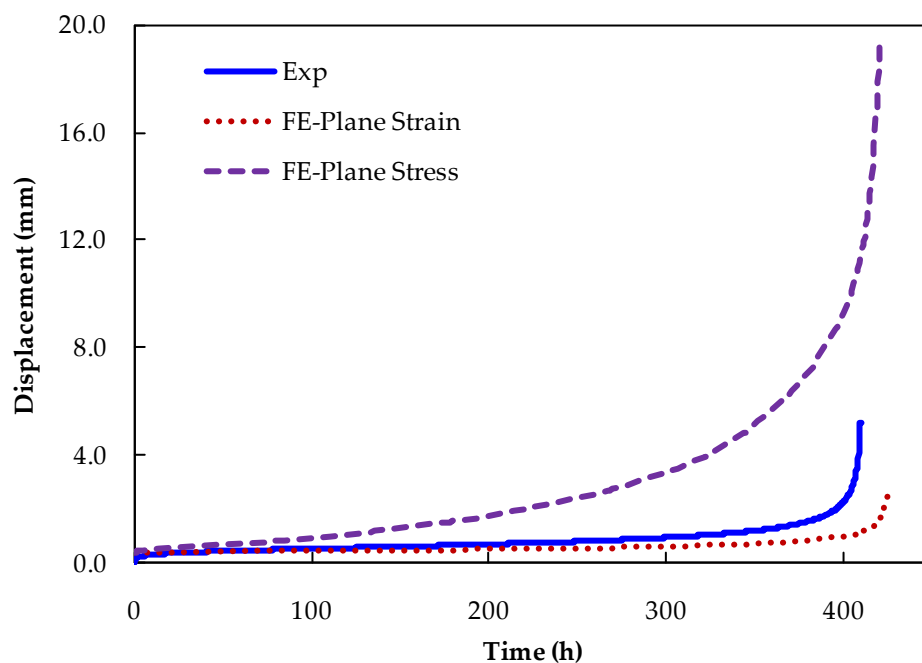


Fig. 4-28: FE load line displacement for growing crack model, using **plane strain** and **plane stress elements**, compared to the experimental results for CT4.

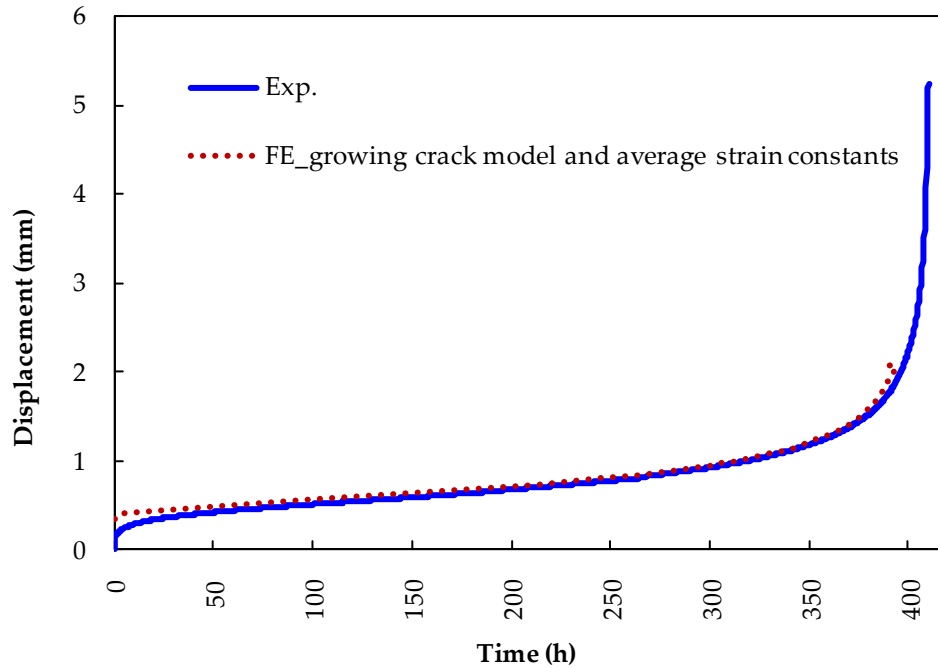


Fig. 4-29: FE load line displacement using the average strain rates constants, A' and n' .

4.6.4 C^* using the growing crack model and the experimental creep crack growth curve

ABAQUS allows the user to model a growing crack in CT specimens using a predefined fracture criterion. The fracture criterion could be an experimentally obtained crack opening displacement (COD) or experimental creep crack growth data. Providing one of these two criteria is available, users can model the growing crack and obtain FE load line displacement curves. These displacement curves can then be used to calculate displacement rates which can be used to calculate the corresponding C^* values. This approach was used by (Park *et al.*, 2001) and resulted in good correlation between experimental and FE load line displacement rates, and hence C^* values, as well. Becker *et al.*(1994) used the crack opening displacement as the fracture criterion to model creep crack growth in nickel-based alloy CT specimens at 700°C.

In this thesis, the growing crack model was used again to obtain the values of the $C(t)$ contour integral. Experimental creep crack growth curves, an example of which is shown in Fig. 4-30, were used to obtain the times needed to grow the crack with an increment, Δa , of 0.25mm each time. These times were then implemented into the FE analysis input file as step times for the analysis steps. The analyses were then allowed to run and the contour integral $C(t)$, which was calculated at the end of each step, was taken to be the C^* values. Resulted C^* values were then compared to those calculated using the same growing crack model but with the use of the transient times of stationary crack models.

Fig. 4-31 compares three different sets of results with corresponding experimental results. The first set is for C^* values calculated using nine models, each model having a different initial crack length, i.e. the stationary crack models. The second set of data is for the growing crack model, shown in Fig. 4-23 and Fig. 4-24, in which the C^* values were calculated at the transient times obtained from the previous nine stationary crack models analyses. The third set of results is for C^* values calculated using the growing crack model at times obtained from the experimental creep crack growth curves. It can be seen that all the predictions are consistent and have the same trends and practically the same values.

One advantage of using the growing crack model is the ability to obtain the load line displacement curves and to calculate the creep crack growth rates. This helps in comparing the da/dt vs. C^* from the experimental data with the FE results. Fig. 4-32 shows this comparison for the P91 CT4, at 650°C. It can be seen that the FE results, obtained using the growing crack model, are in good agreement with the experimentally calculated results.

Fig. 4-33 compares the load line displacement curves for the FE growing crack model with the experimental curve. It can be seen that the FE results, for the growing crack model, is always lower than the experimental results in its magnitude. However, the FE and experimental results have nearly the same gradients in the steady state region.

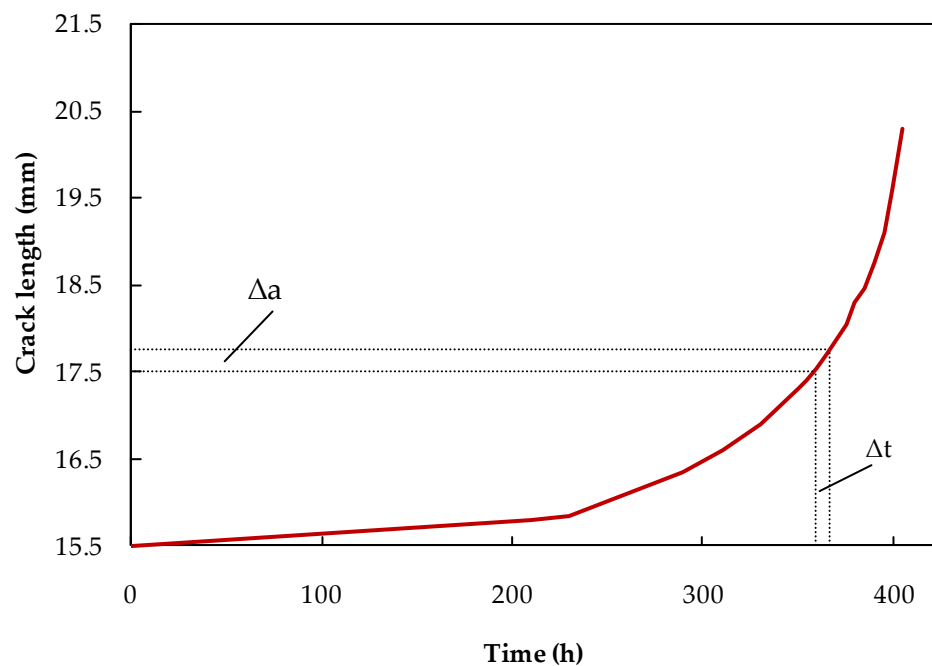


Fig. 4-30: Creep crack growth curve for CT4 used to calculate the step time, Δt .

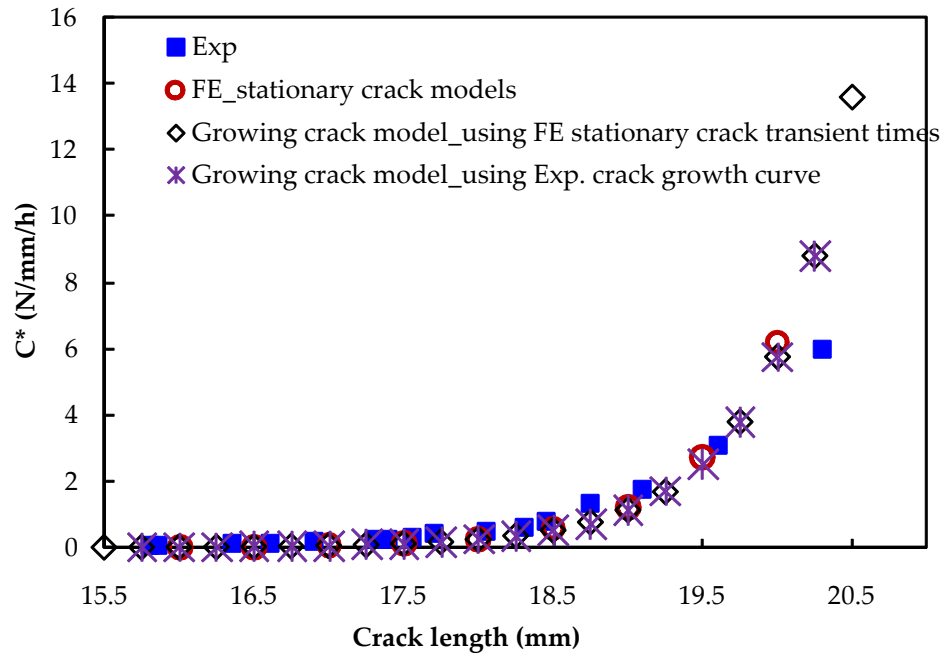


Fig. 4-31: FE C^* results for stationary crack and growing crack models compared to experimental results.

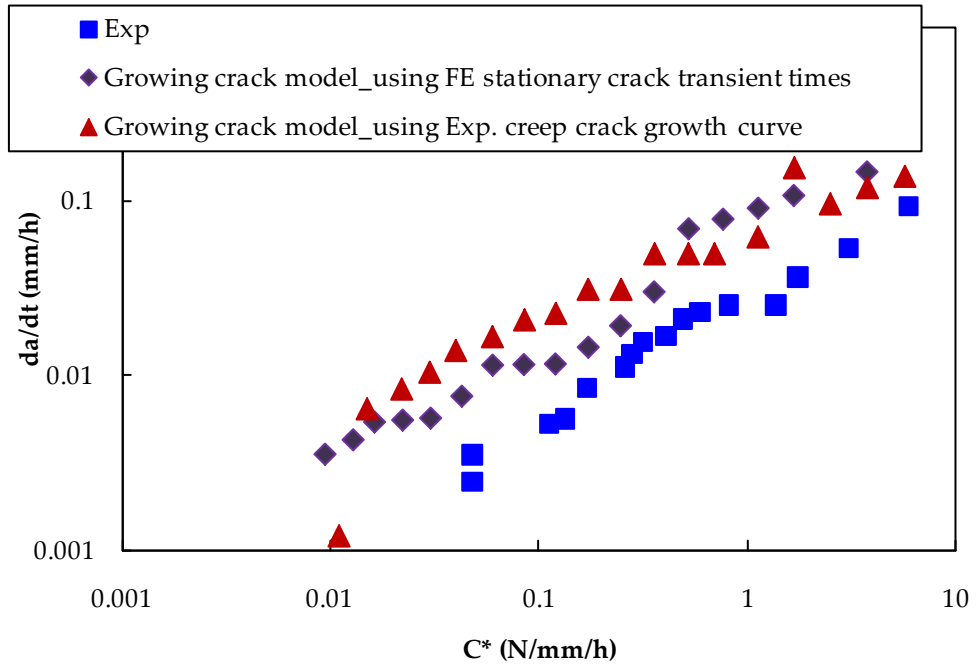


Fig. 4-32: Creep crack growth rate, da/dt , against C^* for the growing crack model and experimental results of CT4.

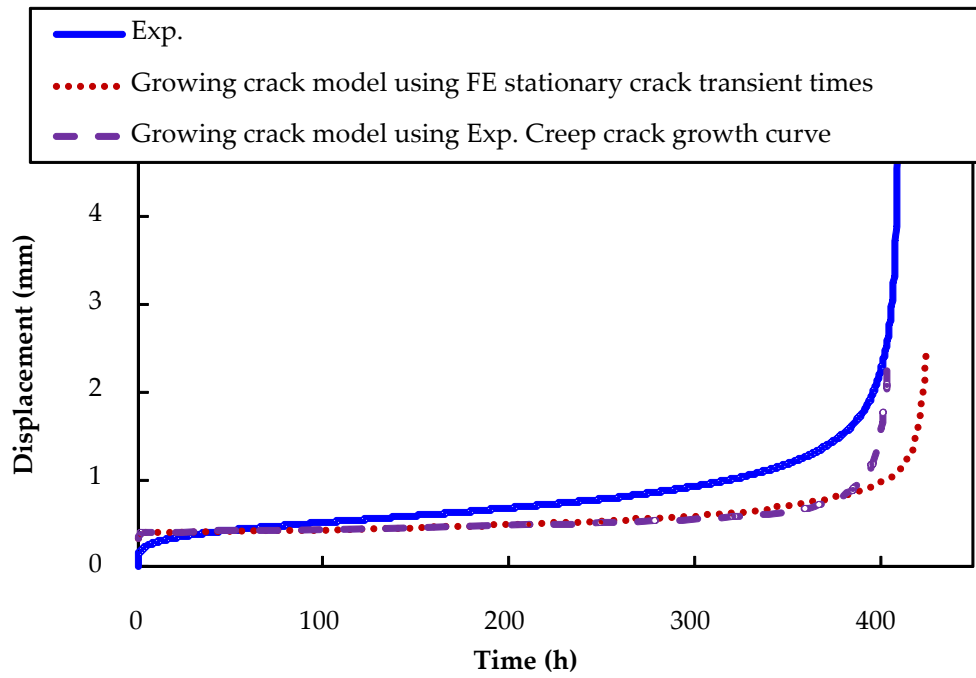


Fig. 4-33: Load line displacement for the growing crack model compared to the experimental results.

4.7 REFERENCE STRESS APPROACH TO PREDICT CREEP CRACK GROWTH IN P91 WELDMENTS

4.7.1 Introduction

The Reference Stress Method (RSM) is a technique used to relate the plastic or creep deformation and failure of a component to the plastic or creep deformation and failure of a single uniaxial test. This uniaxial test is carried out at a stress level referred to as Reference Stress (Penny and Marriott, 1995). The equations needed to calculate the Reference Stress are different from one component to another. In other words, the Reference Stress is geometry and loading dependent but material independent.

Norton's law is used to predict steady state creep behaviour in creeping component. Material constants, e.g. A and n , are needed to obtain the predictions. However, the procedures used to calculate these material constants could produce some uncertainties in the values of these constants and hence errors in the predictions. Boyle in (Wilshire and Owen, 1983) stated that the values of creep exponent n can be calculated by different methods from which :

- 1) By fitting a linear line to the $\text{Log}(\dot{\epsilon}_{min})\text{-Log}(\sigma)$ or
- 2) By fitting a non-linear curve to the original values of $\dot{\epsilon}_{min}$ and σ .

Values of A and n obtained from the use of these different methods are different, partly, due to the scatter of data, and produce different values of creep strain rates when they are used in the Norton's creep law at the same uniaxial stress. The values of A and n , for the P92 PM material, using method 1 (above) were found to be 4.33×10^{-20} and 7.659, respectively, while using method 2, they were found to be 1.134×10^{-20} and 7.96, respectively. Therefore, the objective of using the Reference Stress Method is to remove uncertainties in calculating creep strain (and rates) resulted from uncertainties in calculating material constants, specially the n value.

The Reference Stress can be estimated using the following generic form (Sim, 1970):-

$$\sigma_{ref} = \frac{P}{P_L} \sigma_Y \quad (4-25)$$

where, P is the nominal applied load acting on the component, P_L is the limiting load of P , in other words collapse load for an equivalent structure composed of perfectly plastic material with yield stress of σ_Y (Wilshire and Owen, 1983).

4.7.2 Reference Stress for thick-walled pipes

As an example, to explain the use of the Reference Stress Method, consider a thick-walled tube for which the Reference Stress is given in (Penny and Marriott, 1995) as:-

$$\sigma_{ref} = \frac{P_i}{\ln\left(\frac{D_o}{D_i}\right)} \quad (4-26)$$

where P_i is the applied internal pressure, D_o is the outer diameter and D_i is the inner diameter of the pipe.

Strain rate and failure time of a thick-walled tube are close to those obtained from a uniaxial test carried out at stress equal to the mean diameter hoop stress, σ_{mdh} , which is given by:-

$$\sigma_{mdh} = \frac{P_i \left(\frac{D_o}{D_i} + 1\right)}{2 \left(\frac{D_o}{D_i} - 1\right)} \quad (4-27)$$

Table 4-6, taken from (Penny and Marriott, 1995), shows the relationship between the Reference Stress and the mean diameter hoop stress at different ratios of D_o/D_i . It can be seen that for the same D_o/D_i ratio, the Reference Stress is almost the same as the mean diameter hoop stress. These results indicate that the Reference stress is only load and geometry dependent. It should be noted that the mean diameter hoop stress is used as the design stress for the pressure vessels in many design codes, e.g. R5.

D_o/D_i	$\frac{\sigma_{ref}}{P} = \frac{1}{Ln\left(\frac{D_o}{D_i}\right)}$	$\frac{\sigma_{mdh}}{P} = \frac{1}{2} \frac{\left(\frac{D_o}{D_i} + 1\right)}{\left(\frac{D_o}{D_i} - 1\right)}$
1.1	10.49	10.5
1.5	2.47	2.5
2	1.44	1.5
4	0.72	0.83

Table 4-6: Correlation between the reference stress, σ_{ref} , and the mean diameter hoop stress, σ_{mdh} .

To sum up, the Reference Stress Method is a powerful tool that can be used to predict the behaviour of any component undergoing creep or plastic deformation, by using the results of only one uniaxial test. Another great benefit is that, if the component is too complex to obtain an analytical solution, a simpler model can be used instead provided the same reference stress holds in each case (Penny and Marriott, 1995). Furthermore, attempts have been made to use the Reference Stress Method to correlate the creep crack growth for cracks in cracked bodies.

4.7.3 Prediction of creep crack growth using the Reference Stress Method

The Reference Stress Method has been used to predict creep crack growth in cracked bodies. Hyde (1988) compared the prediction of the creep crack growth in 316 steel CT specimens at 600°C using three parameters, i.e. the stress intensity factor, K , the Reference Stress and C^* . He found that the Reference Stress Method can be used to obtain C^* which correlates the creep crack growth rates very well. Moreover, the Reference Stress can be used directly to correlate the creep crack growth rates.

In this section, of the thesis, the Reference Stress Method has been used to predict the creep crack growth in P91 CT specimens, tested at 650°C. The Reference Stress for CT specimens is given by (Sim, 1970) as:-

$$\sigma_{ref} = \frac{P}{P_L} \sigma_Y \quad (4-28)$$

and, the limit load P_L is given in (Anderson, 2005) by:

$$P_L = 1.455\eta B(W - a)\sigma_Y \quad \text{For plane strain conditions.}$$

$$P_L = 1.072\eta B(W - a)\sigma_Y \quad \text{For plane stress conditions.}$$

$$\text{And} \quad \eta = \sqrt{\left(\frac{2a}{(w-a)}\right)^2 + \frac{4a}{(w-a)} + 2} - \left(\frac{2a}{(w-a)} + 1\right)$$

where W is the specimens width, a is the crack length and B is the specimens width.

The relationship between the Reference Stress and the creep crack growth rates in P91 CT specimens is shown in Fig. 4-34. It can be seen that the Reference Stress correlates the creep crack growth rates very well. Moreover, the creep crack growth rates in the cross-weld CT specimens are about ten times higher than these in the PM CT specimens, at the same Reference Stress. It is worth noting that the same results have been obtained using C^* . It can, also, be seen that the cross-weld CT specimens exhibit more scatter than the PM CT specimens do. Many factors could cause this scatter such as positioning the initial crack with respect to the PM/HAZ boundary and the material variability.

The Reference Stress values, shown in Fig. 4-34, were calculated using plane strain conditions. Plane strain conditions were used as the specimen thickness, 15 mm, is comparable to the specimen's dimensions. Fig. 4-35 compares the creep crack growth correlation when using plane strain and plane stress Reference Stresses. Clearly, it can be seen that for the same Reference Stress, the plane strain conditions produce higher creep crack growth rates than the plane stress conditions do. Likewise for the plane strain conditions, cross-weld CT specimens exhibit higher scatter than the PM CT specimens under the plane stress conditions. Moreover, both the plane strain and the plane stress conditions have the same slope for the PM and cross-weld CT specimens.

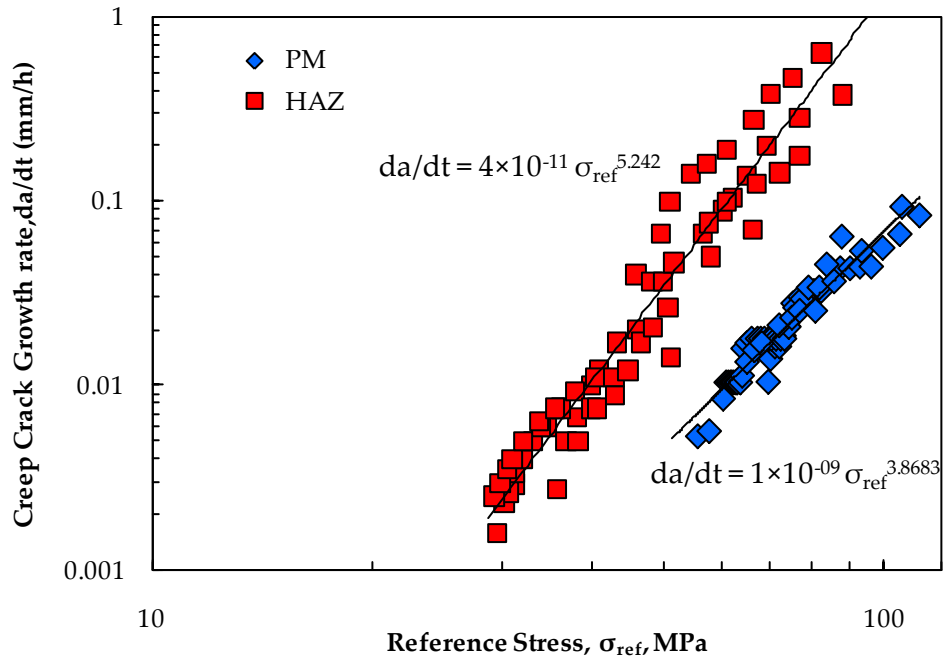


Fig. 4-34: Creep crack growth of P91 at 650°C against the Reference Stress.

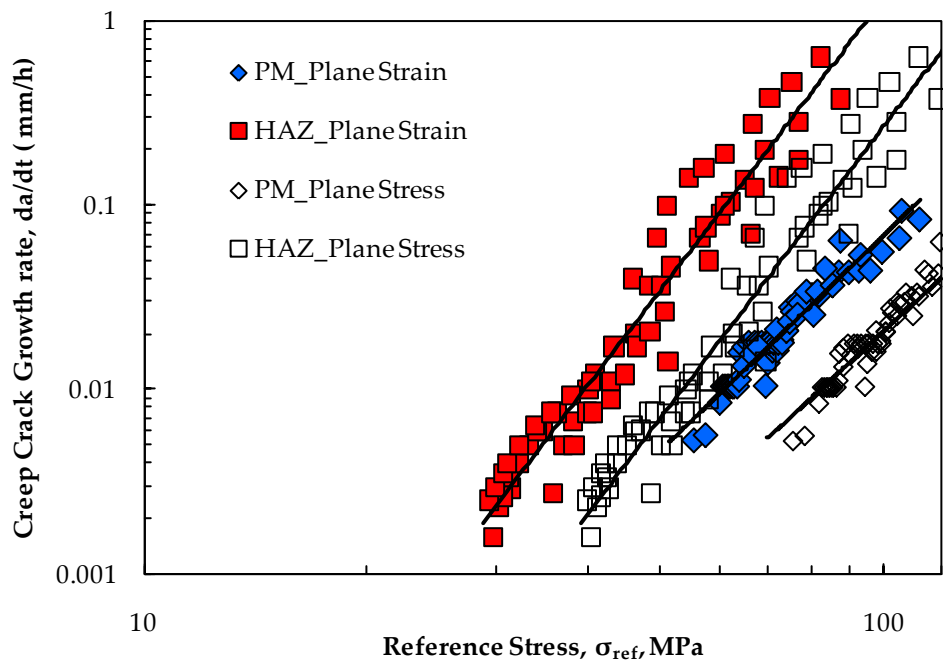


Fig. 4-35: Creep crack growth against Reference Stress using plane strain and plane stress conditions.

4.7.4 Discussion and Conclusions

The FE method was used to model PM CT specimens and to obtain C^* values. These C^* values can be used to characterise stresses and strains ahead of the crack tip and to correlate the creep crack growth rates in these specimens. To obtain C^* using the FE method, stationary crack 2D CT models were used. The FE results were in good agreement with the experimental results. However, cracks in actual components, including CT specimens, are not necessarily stationary; they grow with time at different rates. Therefore, it was important to model these growing cracks and to obtain C^* values. The node release technique was used to model growing cracks. Experimental creep crack growth curves could be used as the fracture criterion. Another fracture criterion can be used in which transient times of stationary crack model are used in growing crack model. The later fracture criterion can be used to predict C^* values, and to obtain creep crack growth rates and load line displacements.

It has been shown that, results obtained from stationary crack models are almost the same as those obtained from growing crack models. This means that, either model can be used and that the results are reliable and comparable to corresponding experimental results. This conclusion is very useful, especially, for use in the modelling of cross-weld CT specimens. Unlike PM CT specimens, cross-weld specimens are non-symmetric and so the whole specimen must be modelled. Therefore, node release techniques, i.e. the growing crack model, cannot be easily used. Instead, stationary crack models can be used successfully to predict C^* values.

The Reference Stress Method can be also used to correlate the creep crack growth in CT specimens. The only difficulty in using the Reference Stress technique is the determination of the appropriate Reference Stress for complicated components.

CHAPTER 5.

DETERMINATION OF MATERIALS' CREEP AND DAMAGE PROPERTIES

5.1 INTRODUCTION

In the previous chapter, fracture mechanics approaches have been used to predict creep crack growth in CT specimens for P91 and P92 weldments. However, it is difficult to use fracture mechanics for cases other than those used to predict the steady state behaviour of components. Therefore, damage mechanics approaches have been used to model all creep stages, i.e. primary, secondary and tertiary creep. Damage mechanics can, also, account for material deterioration which will allow accurate predictions of failure times and location of components. Different damage models have been currently used to predict deformation and lifetime of creeping components. In this thesis, two of these models are presented and used to predict creep crack growth in P91 and P92 CT specimens. These two models are (i) the Kachanov model and (ii) the Liu and Murakami model. In order to use these damage models it is necessary to determine several material constants. The experimental results given in Chapter 3 were used to determine these material constants.

This chapter details the creep damage models, the determination of the material constants and the verification the models' results with respect to the experimental results.

5.2 DAMAGE MECHANICS MODELS

Damage mechanics have been used to predict creep crack growth in CT specimens, using the commercial FE package, ABAQUS, (ABAQUS, 2007). A FORTRAN subroutine, CREEP subroutine, was used to implement the damage models for the FE analyses. Two sets of creep/damage coupled models were used, namely the Kachanov (Kachanov, 1958) model and the Liu and Murakami (Liu and Murakami, 1998) model.

5.2.1 Kachanov damage model

The Kachanov material behaviour model consists of a pair of coupled creep/damage equations, i.e.

$$\frac{d\varepsilon_{ij}^c}{dt} = \frac{3}{2} A \left(\frac{\sigma_{eq}}{1-\omega} \right)^n \frac{S_{ij}}{\sigma_{eq}} t^m \quad (5-1)$$

$$\frac{d\omega}{dt} = B \frac{(\sigma_r)^\chi}{(1-\omega)^\phi} t^m \quad (5-2)$$

where

$$\sigma_r = \alpha \sigma_1 + (1-\alpha) \sigma_{eq} \quad (5-3)$$

in which ε_{ij}^c is the creep strain tensor, t is the time, S_{ij} is the deviatoric stress tensor, ω is the damage parameter, where $0 < \omega < 1$, and σ_{eq} , σ_1 and σ_r are the equivalent (von-Mises), maximum principal and rupture stresses, respectively. A , n , B , χ , ϕ , m and α are material constants where α is a multiaxial stress state parameter, ($0 < \alpha < 1$).

Integration of equation (5-2) between the limits $\omega = 0$ (no damage) and $\omega = 1$ (failure), under uniaxial conditions, leads to an expression for the uniaxial failure time as follows:-

$$t_f = \left[\frac{m+1}{B(1+\phi)\sigma^\chi} \right]^{\frac{1}{m+1}} \quad (5-4)$$

Similarly, the uniaxial creep strain versus time relationship can be obtained, i.e.

$$\varepsilon^c = \frac{A\sigma^{(n-\chi)}}{B(n-\phi-1)} \left(\left[1 - \frac{B(1+\phi)\sigma^\chi t^{m+1}}{m+1} \right]^{\frac{\phi+1-n}{\phi+1}} - 1 \right) \quad (5-5)$$

The material constants A , n , B , χ , ϕ and m can be obtained from curve fitting to the experimental strain-time curves (Hyde *et al.*, 2004a).

5.2.2 Liu and Murakami model

In order to avoid the very high damage, and hence strain, rates which occur for the Kachanov model when ω approaches unity (these can cause convergence problems in FE creep analyses), an alternative creep damage model has been proposed by Liu and Murakami (Liu and Murakami, 1998). This model also consists of a pair of coupled creep/damage equations, i.e.

$$\frac{d\varepsilon_{ij}^c}{dt} = \frac{3}{2} A \sigma_{eq}^{n-1} S_{ij} \text{Exp} \left[\frac{2(n+1)}{\pi\sqrt{1+3/n}} \left(\frac{\sigma_1}{\sigma_{eq}} \right)^2 \omega^{3/2} \right] \quad (5-6)$$

$$\frac{d\omega}{dt} = \frac{M[1 - \text{Exp}(-q_2)]}{q_2} (\sigma_r)^\chi \text{Exp}(q_2\omega) \quad (5-7)$$

where

$$\sigma_r = \alpha \sigma_1 + (1 - \alpha) \sigma_{eq} \quad (5-8)$$

Integration of equation (5-7), under uniaxial conditions, leads to

$$\omega = -\frac{1}{q_2} Ln \left[1 - \left(1 - e^{-q_2} \right) \frac{t}{t_f} \right] \quad (5-9)$$

Where

$$t_f = \frac{1}{M \sigma^\chi} \quad (5-10)$$

The material constants A , n , M , χ and q_2 are obtained by curve fitting to the uniaxial creep curves and shown in the following section.

5.3 DETERMINATION OF MATERIAL CONSTANTS FOR DAMAGE MODELS

5.3.1 P91 material constants

5.3.1.1 A , n , M , χ , B , ϕ and α

P91 weldment materials constants, i.e. A , n , M , χ , B , ϕ and α , have been previously determined and are given in (Hyde *et al.*, 2004a). A and n are calculated by plotting the uniaxial minimum creep strain rates against the applied stresses on log-log scale and using the line of the best fit. The slope of that line is the n value and the intercept is $\text{Log}(A)$. For the HAZ material, results of impression creep tests were used to obtain the A and n values. The uniaxial failure times were plotted against the applied stress on a log-log scale and using the line of best fit to this data. The slope of that line was taken as $-\chi$ and the

intercept is $-\text{Log}(M)$. Creep strain curves have been obtained using Kachanov damage model and fitted to the experimental creep strain curves to obtain ϕ and B values ($M = B(1 + \phi)$). α values have been determined using the results of notched bar specimens and the results of the FE notched bar analyses. Detailed procedures of calculating these material constants are given in Section 5.3.3 for the P92 materials.

All of the above material constants, obtained for the Kachanov model, are used for the Liu and Murakami model, as well, with one more constant, q_2 . Procedures used in calculating q_2 for the P91 PM, WM and HAZ materials are given in the following three consecutive sections, respectively. Application of α into the Liu and Murakami model to predict failure times of notched bar specimens and creep crack growth in CT specimens are discussed later in Section 5.3.1.5.

All the material properties for the P91 weldment constituents are given in Table 5-1.

5.3.1.2 q_2 for the P91 PM

The damage, ω , for the Liu and Murakami model is given by:-

$$\omega = -\frac{1}{q_2} \text{Ln} \left[1 - \left(1 - e^{-q_2} \right) \frac{t}{t_f} \right] \quad (5-11)$$

where q_2 is a material constant

Creep strain was calculated numerically using a time marching technique, at different values of q_2 , keeping all the other material constants the same, and then

fitted to the experimental results. The value of q_2 that gives the best fit is then taken as the correct value.

Creep strain increments, in the uniaxial form, were calculated using the following relationship:-

$$\Delta \varepsilon^c = A \sigma E \exp \left[\frac{2(n+1)}{\pi \sqrt{1+3/n}} \omega^{3/2} \right] \Delta t \quad (5-12)$$

where A and n are material constants and ω is the damage obtained using equation (5-11). Δt is time increment. This time increment was taken as the experimental time increment using, i.e.

$$\Delta t = t_{i+1} - t_i \quad (5-13)$$

where t_i and t_{i+1} are the experimentally recorded times for the corresponding test. It is not necessary to use the experimental time record to define the Δt values; other small values of Δt can be used, instead.

Equation (5-12) is the uniaxial form of creep strain equation in the Liu and Murakami model and σ is the applied stress.

Using the time marching technique, creep strain curves for the P91 PM were obtained at different values of q_2 and for different stress levels. These fitted strain curves were then compared to the experimental results. The best fit was attained when $q_2 = 3.2$. Result of that fitting process is shown in Fig. 5-1. Very good agreement can be seen between the fitted curves and the experimental curves.

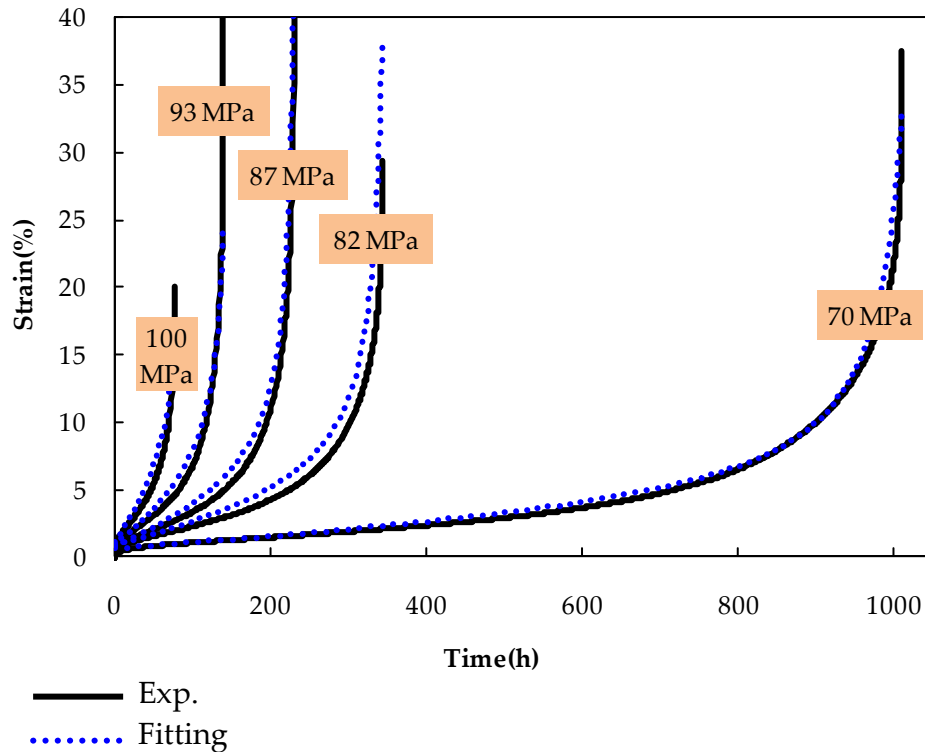


Fig. 5-1: Creep strain curves fitted to the experimental creep curve at $q_2 = 3.2$ for P91 PM.

5.3.1.3 q_2 for P91 WM

The experimental uniaxial creep test data for the P91 WM exhibit significant scatter as can be seen in Fig. 5-2 and Fig. 5-3. In particular, the 93 MPa appears to be in error. This scatter affects the accuracy with which the material constants can be determined. This in turn affects the accuracy of subsequent analytical and numerical solutions obtained using the constants. Consequently, it was difficult to obtain a unique value for q_2 for the WM using the time marching technique. As an alternative, FE uniaxial model was used in conjunction with the Liu and Murakami damage model. The analyses were repeated many times with different q_2 values and the predicted creep strain curves obtained were compared to the corresponding experimental creep strain curves. This procedure continued until a good fit to the data was obtained, for which $q_2 = 5.0$. Results of these FE analyses are compared to the experimental results in Fig. 5-4. Good agreements can be seen between the FE and the experimental results in

terms of the creep strain and the failure times for all the stress levels except for the 93 MPa test.

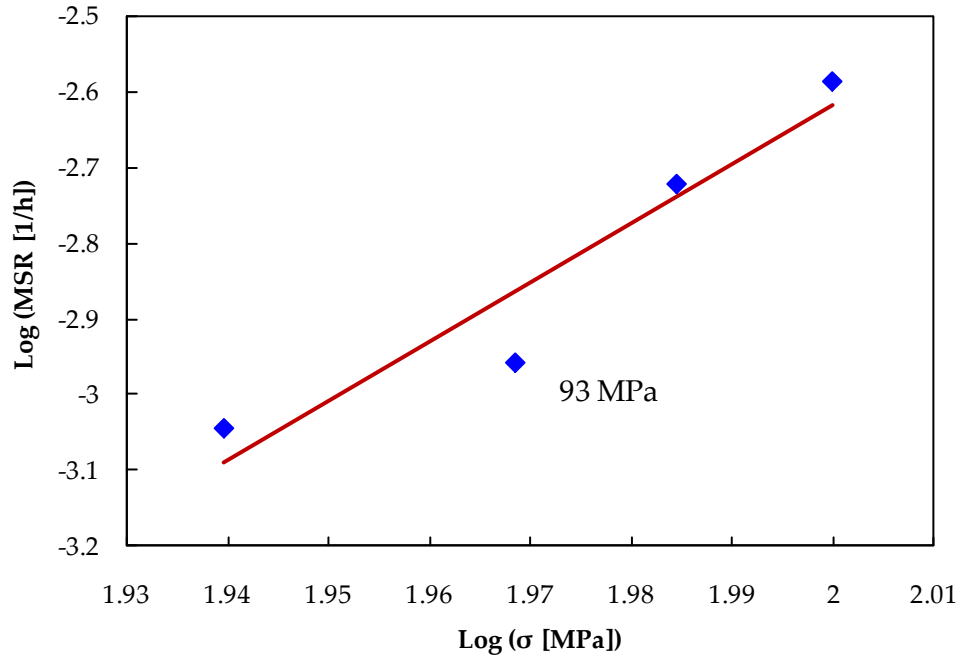


Fig. 5-2: Minimum Strain Rates (MSR) against applied stress for P91 WM at 650°C.

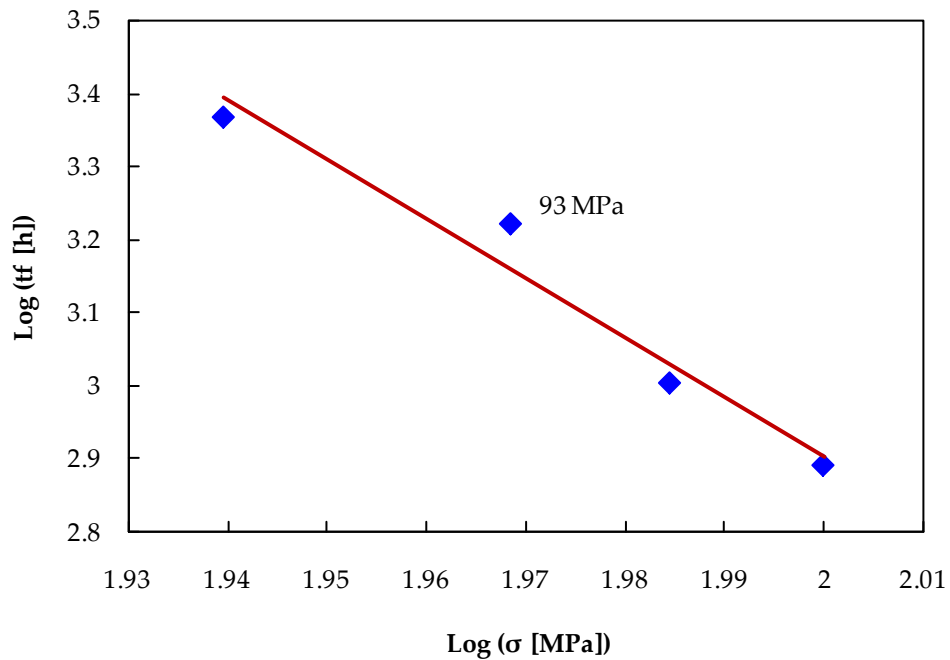


Fig. 5-3: Uniaxial failure times against applied stress for P91 WM at 650°C.

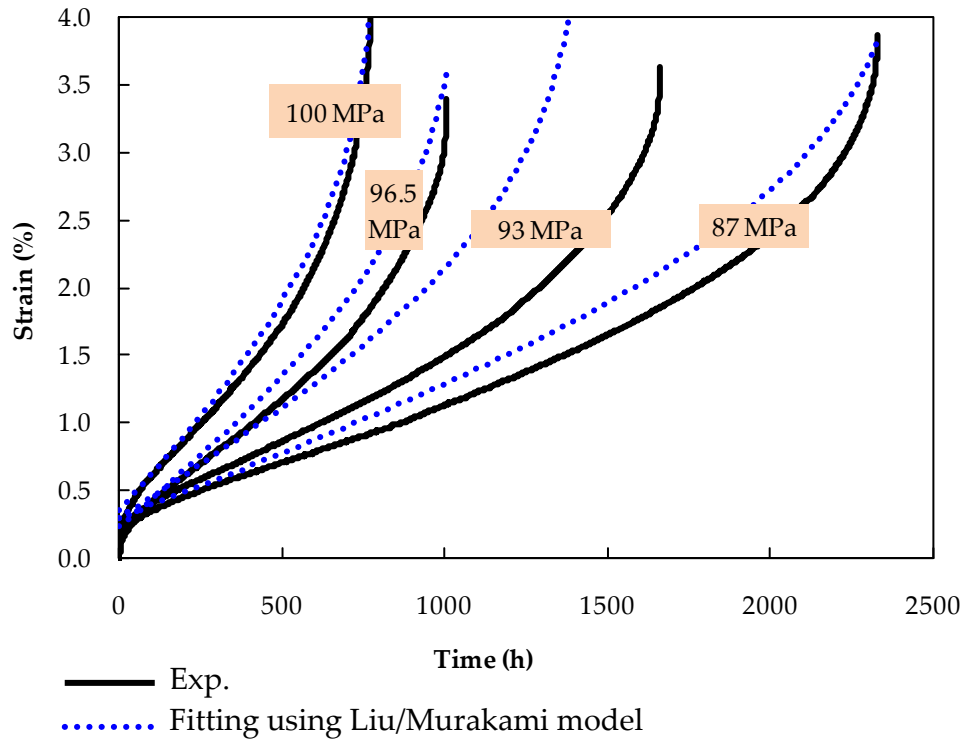


Fig. 5-4: Creep strain curves fitted to the experimental creep curve at $q_2 = 5.0$ for P91 WM using FE analyses.

5.3.1.4 q_2 for P91 HAZ

To define q_2 for the P91 HAZ material, a set of uniaxial creep strain curves have been generated using the Kachanov damage model. Creep strain curves were obtained using the Liu and Murakami model and fitted to those obtained using Kachanov at different q_2 values. The best fitting between the Liu and Murakami creep curves and the Kachanov creep curves has been achieved when $q_2 = 2.8$. Fig. 5-5 shows the reproduced creep strain curve using Kachanov model and the creep strain curves obtained using Liu and Murakami model.

The reason behind using the reproduced creep strain curves, using Kachanov model, as the analytical experimental curves is that, the HAZ material does not have experimental uniaxial creep strain curves. Instead, it has impression creep curves which were used mainly to obtain the A and n constants.

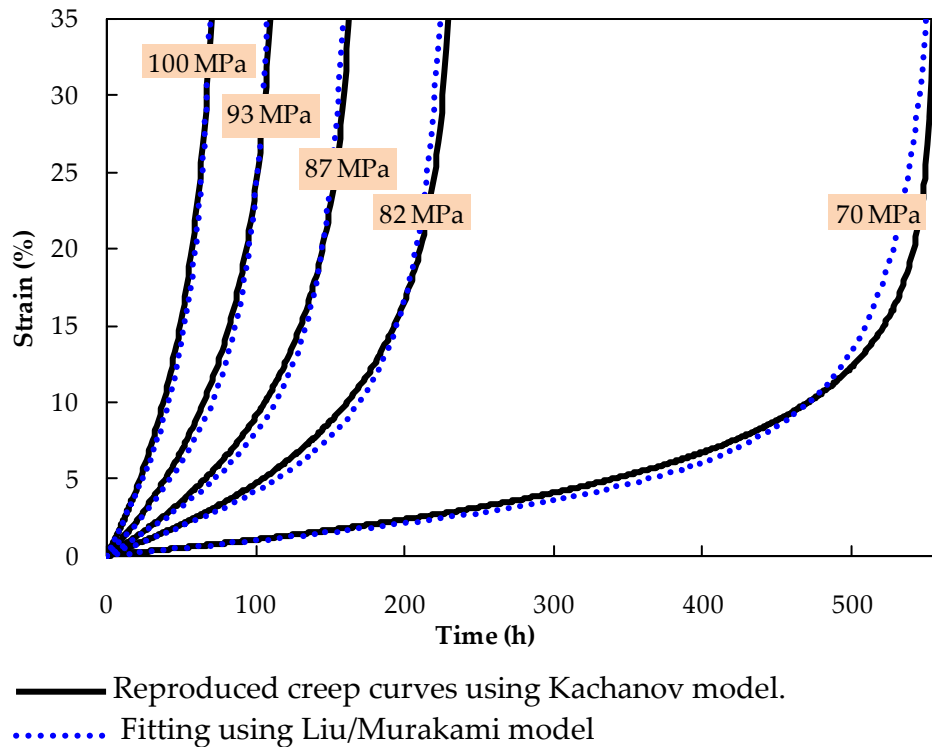


Fig. 5-5: Reproduced creep strain curves using Kachanov damage model and Liu and Murakami damage model at $q_2 = 2.8$ for the **P91 HAZ** material.

5.3.1.5 α for the Liu and Murakami model

Multiaxiality, in the Kachanov damage model and the Liu and Murakami damage model, has been accounted for by introducing a multiaxial parameter α . This parameter controls the rupture stress which is given by $\sigma_r = \alpha\sigma_1 + (1-\alpha)\sigma_{eq}$. To define the value of α , notched bar specimens were cut from the PM, WM and tested under creep conditions and their rupture times were recorded. Corresponding FE notched bar specimens were, also, modelled. Different α values were used in the FE analyses resulting in different rupture times of the FE notched bar models. The α value that gave failure times corresponding to the experimental failure times was taken as the correct α value.

Hyde *et al.* (2004a) calculated α values for the P91 weldment materials. These values of α are given in Table 5-1. It has been found that, using these values of α in the Liu and Murakami damage model resulted in lower creep crack growth in the CT specimens (prediction of CCG in CT specimens using the Liu and Murakami model is given in Chapter 6). Therefore, CT specimens have been used to define the correct α value by comparing creep crack growth in FE CT models to the corresponding experimental creep crack growth. This new approach was used for the P91 PM and the HAZ material, as well. For the P91 WM, the FE notched bar failure times were almost the same as the experimental failure time when $\alpha = 0.79$, see Fig. 5-6.

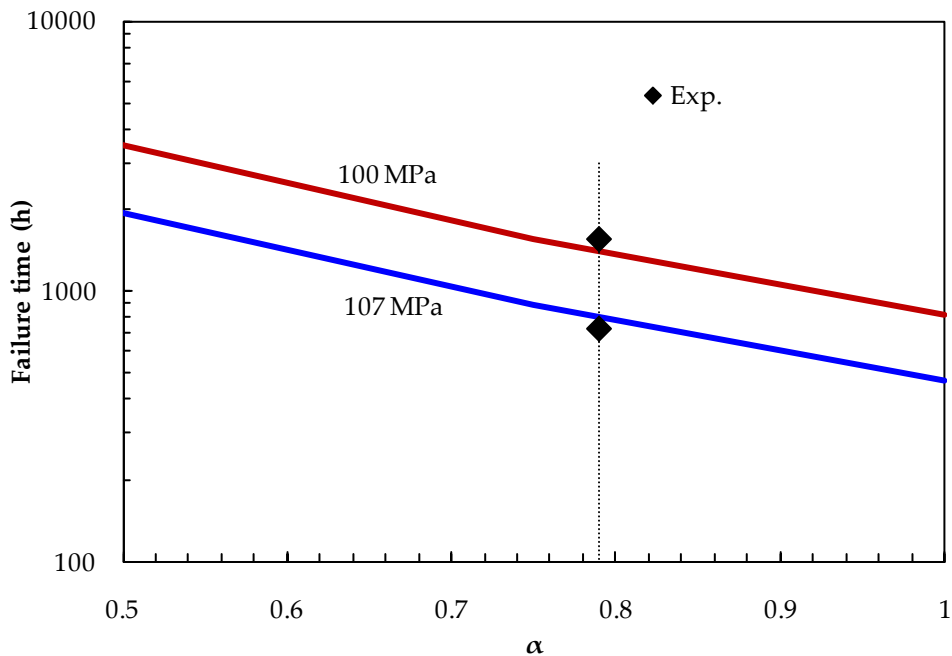


Fig. 5-6: FE notched bar failure times, for different α values, using the Liu and Murakami damage model for **P91 WM** at 650°C.

Material	A	n	m	B	ϕ	χ	α	q ₂	α_L
PM	1.092×10^{-20}	8.462	-4.754×10^{-4}	3.537×10^{-17}	7.346	6.789	0.215	3.2	0.3125
WM	1.370×10^{-20}	7.65	-0.0361	1.600×10^{-20}	11.463	7.950	0.59	5.0	0.79
HAZ	2.300×10^{-20}	8.462	0	1.522×10^{-14}	7.346	5.502	0.75	2.8	≈ 0.5

$\alpha_L = \alpha$ obtained using the Liu and Murakami model

Table 5-1: P91 Material constants for damage models at 650°C (σ in MPa and time in h)

5.3.2 P91 FE uniaxial creep strain

So far, the P91 material damage constants have been determined for the two damage models used, i.e. the Kachanov model and Liu/Murakami model. In order to verify the applicability of these results in the forthcoming FE creep crack growth analyses, a series of FE uniaxial analyses have been carried out using these material constants and the two damage models. Results obtained from the use of either model were compared with each other and were compared with experimental results. Good agreement was obtained between the FE results, on one hand, and between the FE and experimental results, on the other hand.

5.3.2.1 P91 parent material FE uniaxial creep strains

P91 material constants, given in Table 5-1, were implemented using the CREEP subroutine to obtain creep strain prediction of uniaxial FE analyses carried out using the FE commercial package, ABAQUS. Fig. 5-7 shows the FE uniaxial model used in creep strain analyses. This model consists of four axisymmetric elements, with the overall dimensions being the same as the gauge length dimensions of a standard uniaxial specimen (a standard uniaxial specimen is shown in Fig. 3-2). Boundary conditions were applied to the bottom edge to prevent the vertical translation and to the left hand edge of the model to prevent the transverse translation. Load was applied upward to the upper edge of the model.

Fig. 5-8 compares the FE uniaxial creep curves for the P91 PM to the experimental creep strain curves. Good agreement can be seen between the FE and the experimental results. This agreement validates the material constants and the uniaxial model used. It can, also, be seen that the FE curves which were obtained using the Liu/Murakami model are closer to the experimental results than those which were obtained using the Kachanov model.

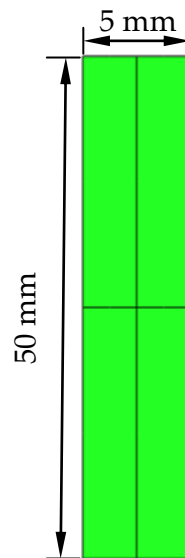


Fig. 5-7: FE uniaxial model

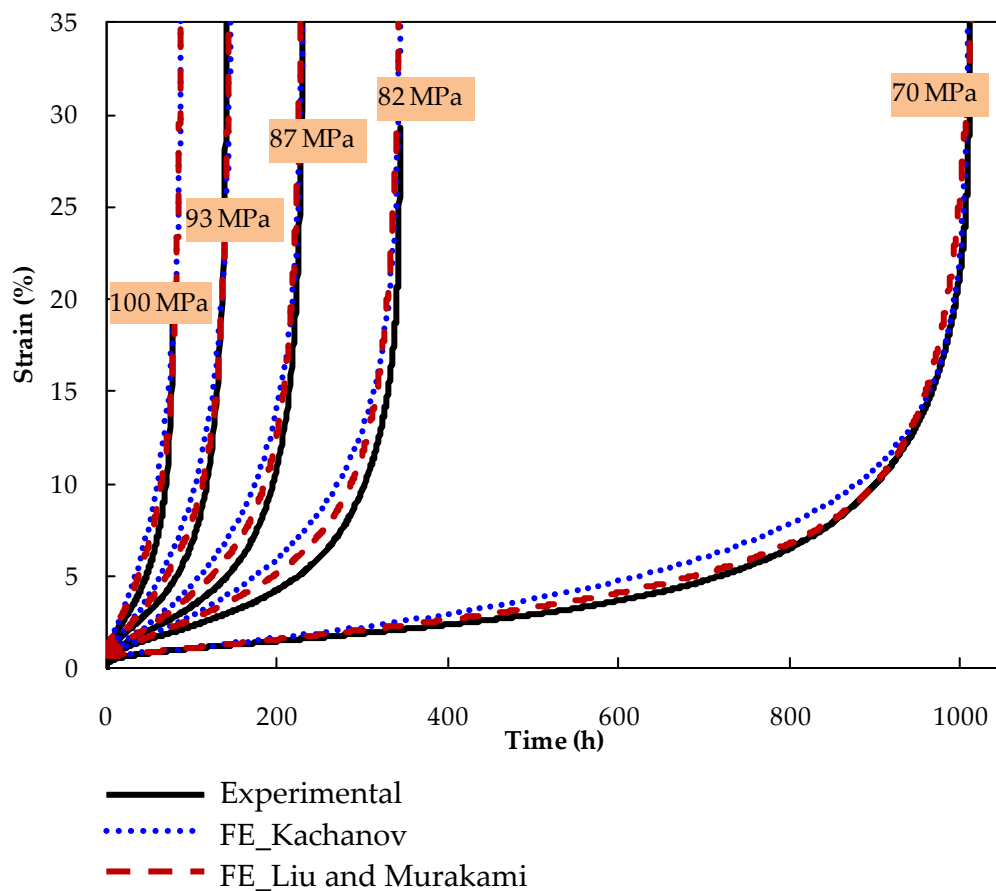


Fig. 5-8: Experimental and FE uniaxial creep strain curves for P91 PM at 650°C.

5.3.2.2 P91 weld metal FE uniaxial creep strains

Finite element creep strain curves for the P91 WM are compared with the corresponding experimental results in Fig. 5-9. It can be seen that the FE results using the Liu and Murakami model are closer to the experimental results than the FE results using Kachanov. Moreover, obvious differences can be seen between the two sets of FE results. This is due to the data scatter in the experimental results for the WM, which lead to uncertainties in calculating the material constants. Uncertainties in the WM material constants are, to some extent, acceptable as the PM and HAZ materials are the most important in simulating Type IV cracks.

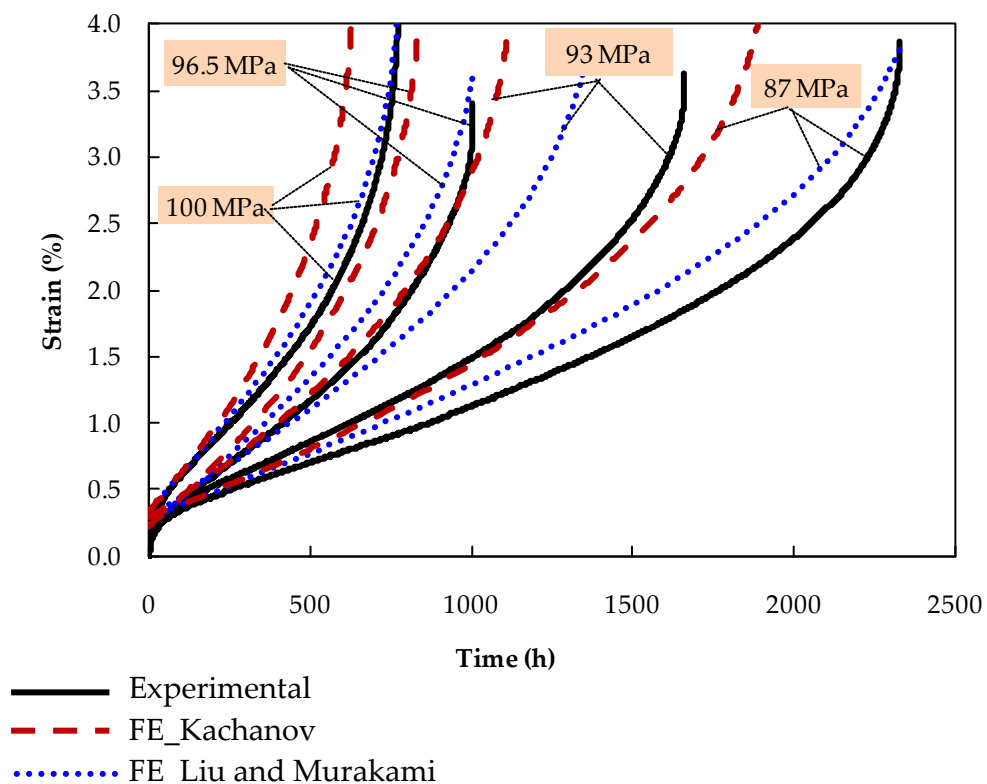


Fig. 5-9: Experimental and FE uniaxial creep strain curves for **P91 WM** at 650°C.

5.3.3 P92 material constants

The accurate determination of material constants is key to accurate modelling, and hence to the prediction of material behaviour. These constants are creep constants, i.e. A and n , and damage constants. Damage constants are those used for the Kachanov model, i.e. A , n , M , B , χ , ϕ , m and α , and for the Liu/Murakami model, i.e. A , n , M , χ , q_2 and α , where $M = B(1+\phi)$.

Experimental creep and creep rupture tests were used to obtain the P92 material constants. Testing conditions and the results of these tests are presented in Chapter 3.

5.3.3.1 A and n

It is assumed that the P92 material is a power law material and so it can be modelled using the Norton's power law (Penny and Marriott, 1995), i.e.

$$\dot{\epsilon}_{min} = A\sigma^n \quad (5-14)$$

where $\dot{\epsilon}_{min}$ is the minimum strain rate (MSR), A and n are material constants known as creep intercept and creep exponent, respectively.

Values of A and n can be obtained by taking the $\text{Log}(\)$ function of equation (5-14), i.e. ,

$$\text{Log}(\dot{\epsilon}_{min}) = \text{Log}(A) + n\text{Log}(\sigma) \quad (5-15)$$

then by plotting $\text{Log}(\dot{\epsilon}_{min})$ against $\text{Log}(\sigma)$ and then get the slope, n , and the intercept, $\text{Log}(A)$ of the line of the best fit.

Fig. 5-10 and Fig. 5-11 show $\text{Log}(\dot{\epsilon}_{min})$ against $\text{Log}(\sigma)$ for the P92 PM and P92

WM, respectively, tested at 675°C and at stress levels of 100, 95, 90, 85, 80 MPa. From these curves, A and n values were obtained. Values of A and n for P92 PM and P92 WM at 675°C are included in Table 5-2.

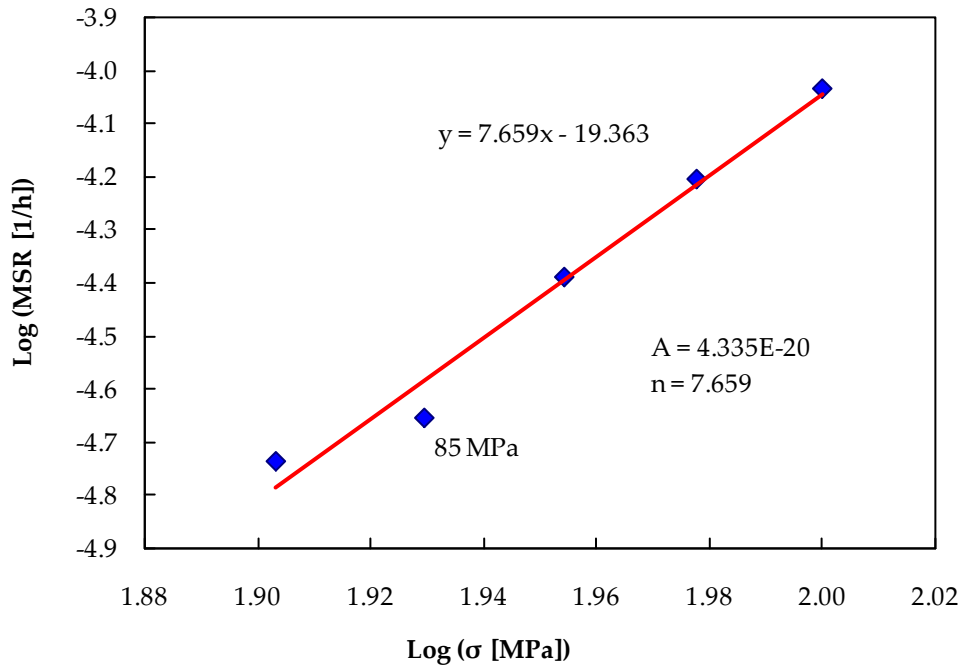


Fig. 5-10: Minimum strain rates (MSR) against stress (σ) for P92 PM, at 675°C.

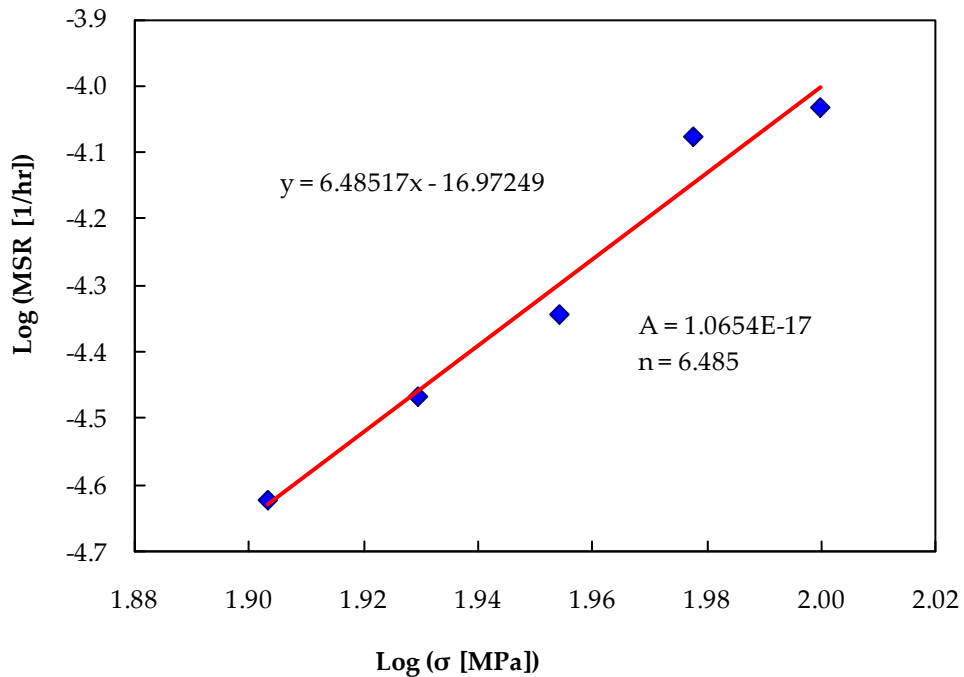


Fig. 5-11: Minimum strain rates (MSR) against stress (σ) for P92 WM, at 675°C.

5.3.3.2 M and χ

The uniaxial failure time, t_f , is given by:

$$t_f = \frac{1}{M\sigma^\chi} \quad (5-16)$$

where M and χ are material constants that can be determined by plotting $\text{Log}(t_f)$ against $\text{Log}(\sigma)$. By taking $\text{Log}(\)$ function to equation (5-16) it turns into

$$\text{Log}(t_f) = -\text{Log}(M) - \chi\text{Log}(\sigma) \quad (5-17)$$

then by plotting $\text{Log}(t_f)$ against $\text{Log}(\sigma)$, as shown in Fig. 5-12, M and χ values can be obtained. The slope of the line of the best fit is $-\chi$ and the intercept is $-\text{Log}(M)$. M and χ values for P92 PM are included in Table 5-2.

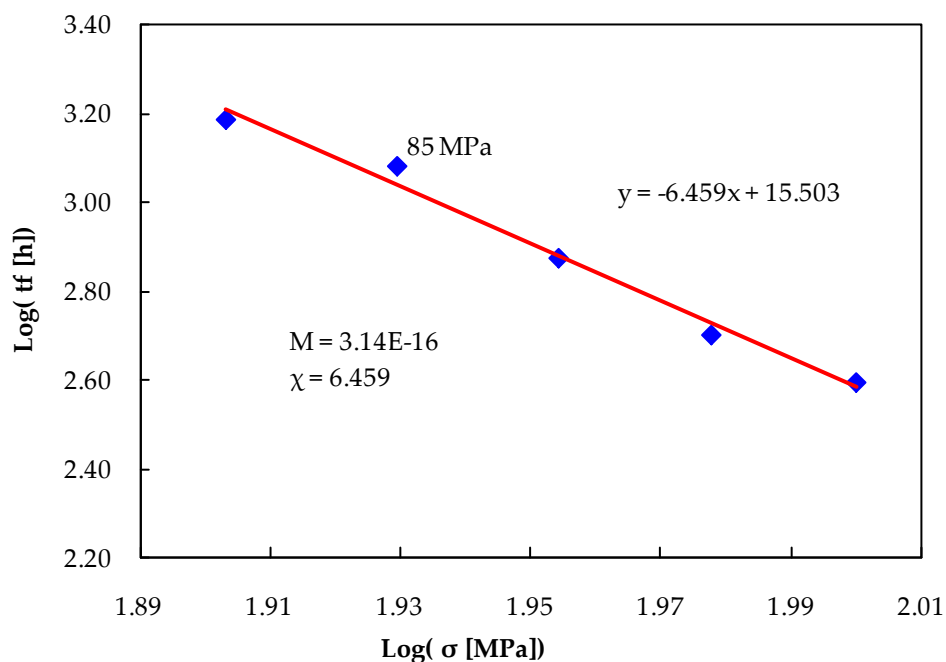


Fig. 5-12: Failure time (t_f) against applied stress (σ) for the **P92 PM** uniaxial creep tests at 675°C.

It is worth noting that, for the 85MPa test, the disk of the data logger, to which the test data were recorded, failed a few hours before the failure of the test. Therefore, it was not possible to define the exact failure time for that test. Therefore, the failure time of the test was estimated as the mid-point between time at which the disk failed and the predicted time using a characteristic creep curve. The disk failed at 1180 hrs and the estimated failure time is 1240 hrs and so the average failure time is 1210 hrs.

Fig. 5-13 is the plot of the uniaxial failure times against the applied stresses for the P92 WM, at 675°C. The values of M and χ for the P92 WM, at 675°C, are shown in Fig. 5-13 and are included in Table 5-2.

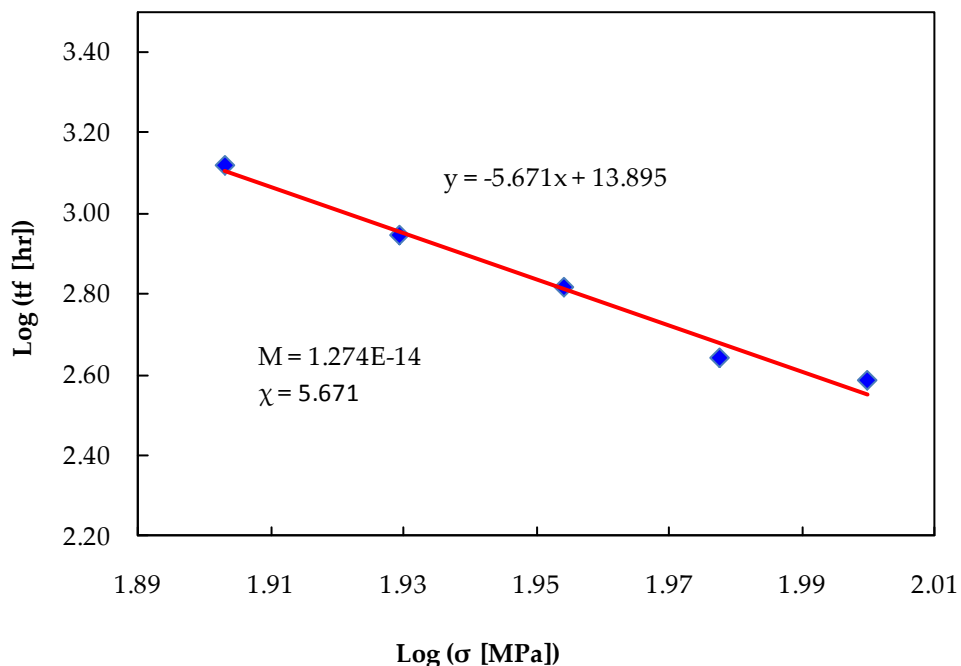


Fig. 5-13: Failure time (t_f) against applied stress (σ) for the P92 WM uniaxial creep tests at 675°C.

5.3.3.3 B , ϕ and m

Uniaxial creep strain is given by, using the Kachanov damage model:-

$$\varepsilon^c = \frac{A\sigma^{(n-\chi)}}{B(n-\phi-1)} \left(\left[1 - \frac{B(1+\phi)\sigma\chi t^{m+1}}{m+1} \right]^{\frac{\phi+1-n}{\phi+1}} - 1 \right) \quad (5-18)$$

where B and ϕ are material constants where

$$M = B(1 + \phi) \quad (5-19)$$

Material constant ϕ can be determined by fitting a set of uniaxial creep curves calculated using equation (5-18) to the corresponding experimental creep curves at different values of ϕ , keeping all the other material constants the same. The ϕ value that gives the best fitting is then taken as the correct value. Note, the B value is updated whenever the ϕ value changes, according to equation (5-19).

Fig. 5-14 shows the creep strain curves calculated using equation (5-18) fitted to the experimental uniaxial curves for the P92 PM, at 675°C. It should be noted that failure times are independent of the ϕ value. However, ϕ value significantly affects the strain values at the tertiary stage. Moreover, the minimum strain rates for all the fitted curves are quite similar to those for the experimental curves.

The material constant m is firstly set to zero until the correct value of ϕ was obtained. Then, the ϕ kept constant and the m value is changed slightly to enhance the fitting. It was found that, no improvement has been brought to the fitting when the m value was being changed, within a very small range. Therefore, the value for m was taken as zero. The values of B and ϕ are included in Table 5-2.

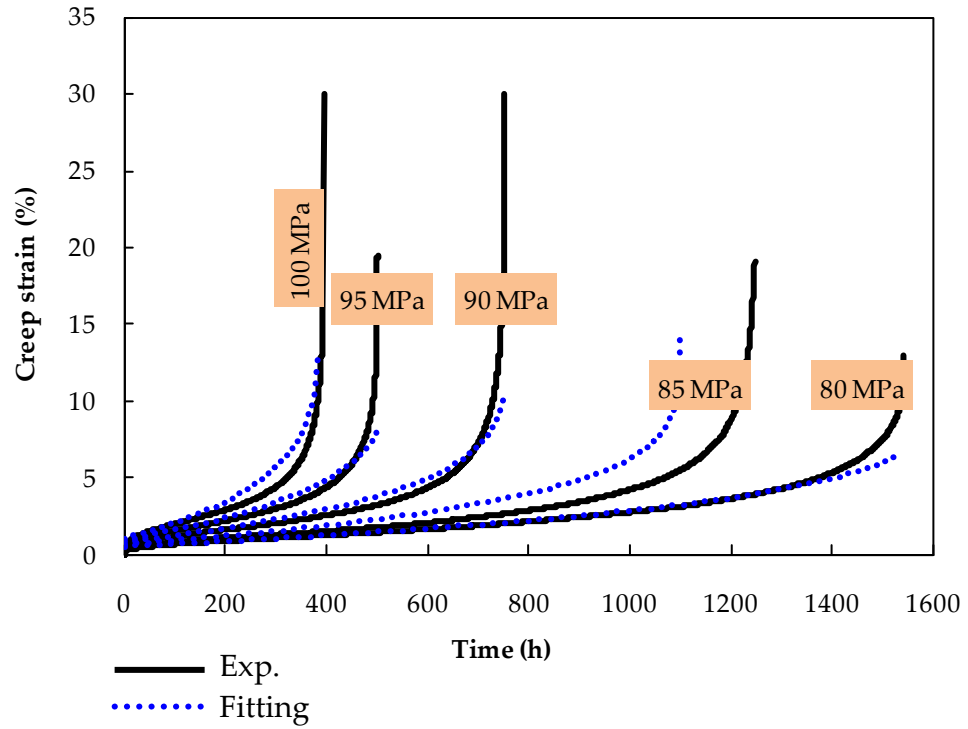


Fig. 5-14: Calculated creep strain curves fitted to the experimental creep curves, for the P92 PM, at $\phi = 8.3$.

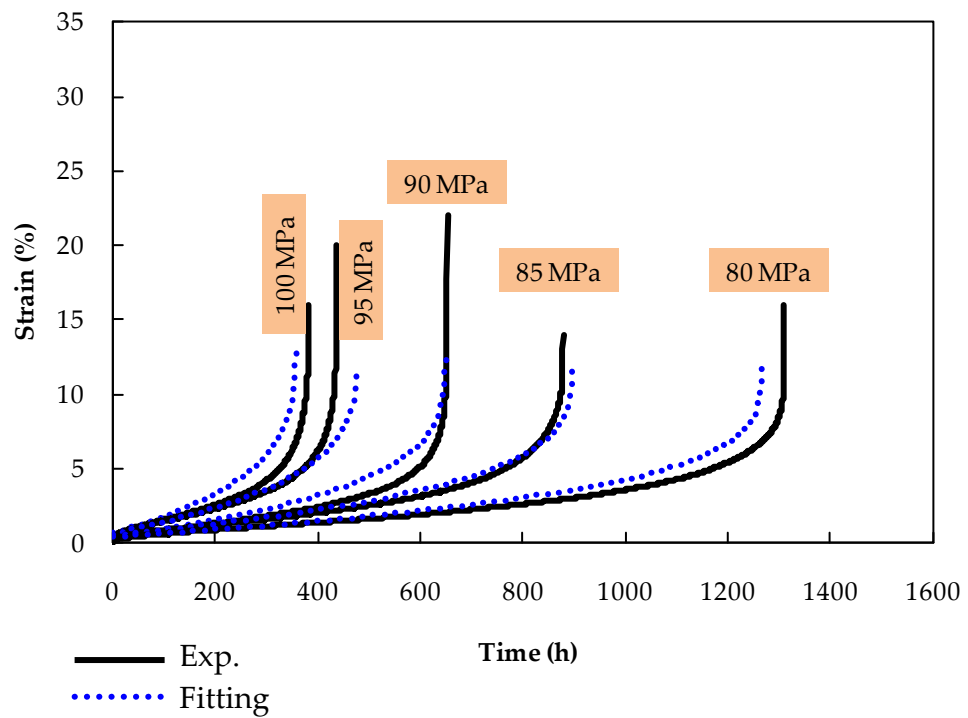


Fig. 5-15: Calculated creep strain curves fitted to the experimental creep curves, for the P92 WM, at $\phi = 7.5$.

5.3.3.4 α

The multiaxial parameter, α , is a material constant which defines the ratios by which equivalent stress, σ_{eq} , and maximum principal stress σ_1 , participate in the rupture stress according to the following relationship:-

$$\sigma_r = \alpha\sigma_1 + (1-\alpha)\sigma_{eq} \quad (5-20)$$

To define the α value for the P92 PM, at 675°C, notched bar creep rupture tests were carried out at stress levels of 125 MPa, 110 MPa. The geometry and dimensions of the notched bar specimens are shown in Fig. 3-3. The rupture times for these tests were found to be 350 and 679 h for the 125 MPa test and 110 MPa test, respectively.

FE notched bar model, as shown in Fig. 5-16 (a), has been used to obtain the α values. The notched bar model consists of 77 axisymmetric elements. The model dimensions are the same as those used in the experiment, shown in Fig. 3-3. FE analyses were carried out at the two stress levels (mean axial stress at the minimum notch cross-section), i.e. 125 and 110MPa, using various α values. The α value that gives the same failure times as the corresponding experimental tests is then taken as the correct α value. FE failure time was determined as the time at which about half of the elements at the specimen notch have failed, i.e. the damage variable (ω) reach a critical value, 0.99 in this study.

As the damage parameter, ω , reaches unity in Kachanov model, see equation (5-1), the creep strain rate, $\dot{\epsilon}_{ij}$, reaches infinity. This may cause numerical problems for the FE analyses. Therefore, a value less than one, say 0.99, was chosen as the maximum allowed (or a critical) value of damage. Because of the Liu and Murakami model was originally based on the Kachanov model, the critical value of damage for this model was taken as 0.99, as well. It is worth noting

that the FE obtained results are sensitive to that value of damage. Therefore, it must be kept the same throughout all of relevant analyses. An alternative approach is to calibrate that value to experimental results, for a specific material, then use the calibrated value for any analyses of that material.

FE notched bar failure times obtained using the Kachanov model are plotted against α values in Fig. 5-17 from which it can be seen that the average value of α is 0.370. Fig. 5-18 shows the FE failure times obtained using the Liu and Murakami model at different values of α compared to the experimental results. It can be seen that an average α value of 0.396 has been obtained for the P92 PM. A small difference was found between the α value obtained using the Kachanov model and that obtained using the Liu/Murakami model. For subsequent predictions, an average value of α (0.383) will be used.

Similar to the P92 PM, α value was determined for the P92 WM. Both damage models have been used. Fig. 5-19 and Fig. 5-20 show the FE notched bar failure times for the P92 WM for various α values using both the Kachanov and the Liu/Murakami damage models. It can be seen that the α values obtained from both models are very close (0.183 using the Kachanov model and 0.191 using the Liu and Murakami model). The average value of 0.187 will be used as the α value for the WM.

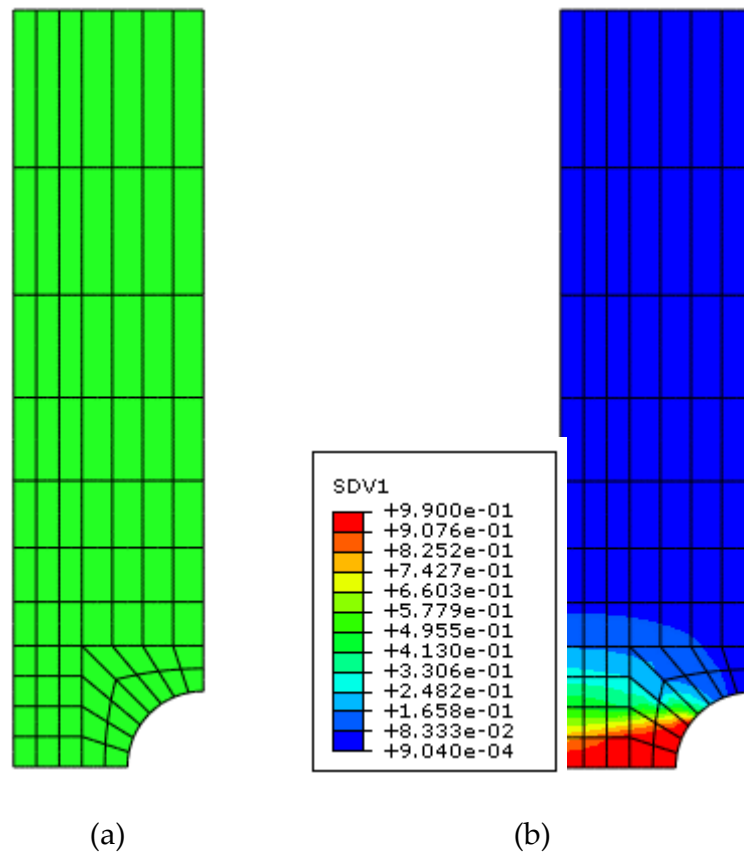


Fig. 5-16: FE notched bar model
(a) Notched bar mesh,
(b) Damage evolution at the notch at failure time using the Liu and Murakami model.

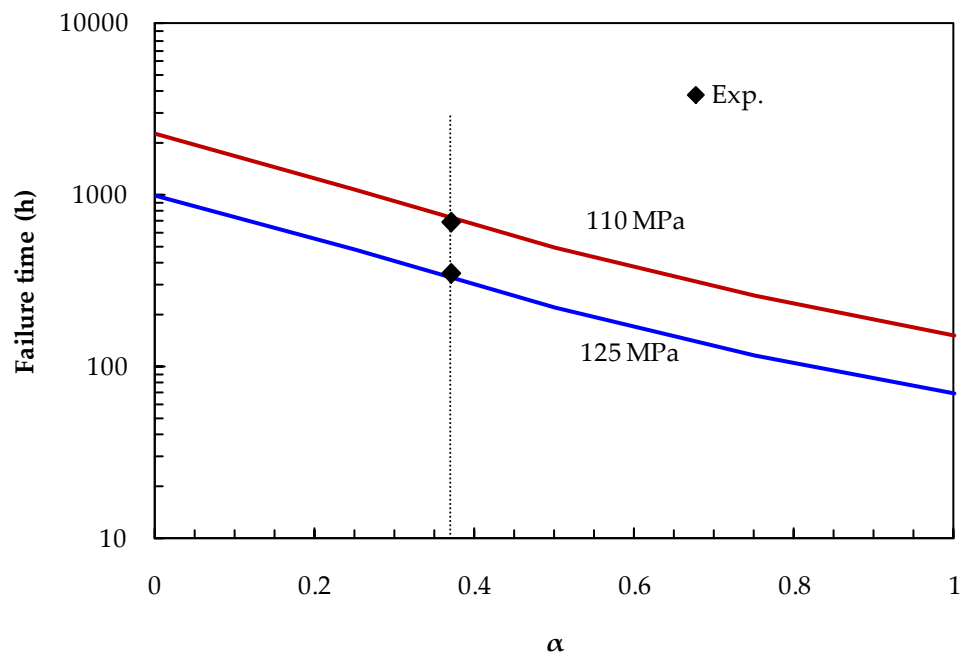


Fig. 5-17: FE notched bar failure times, for different α values, using the Kachanov model for P92 PM at 675°C.

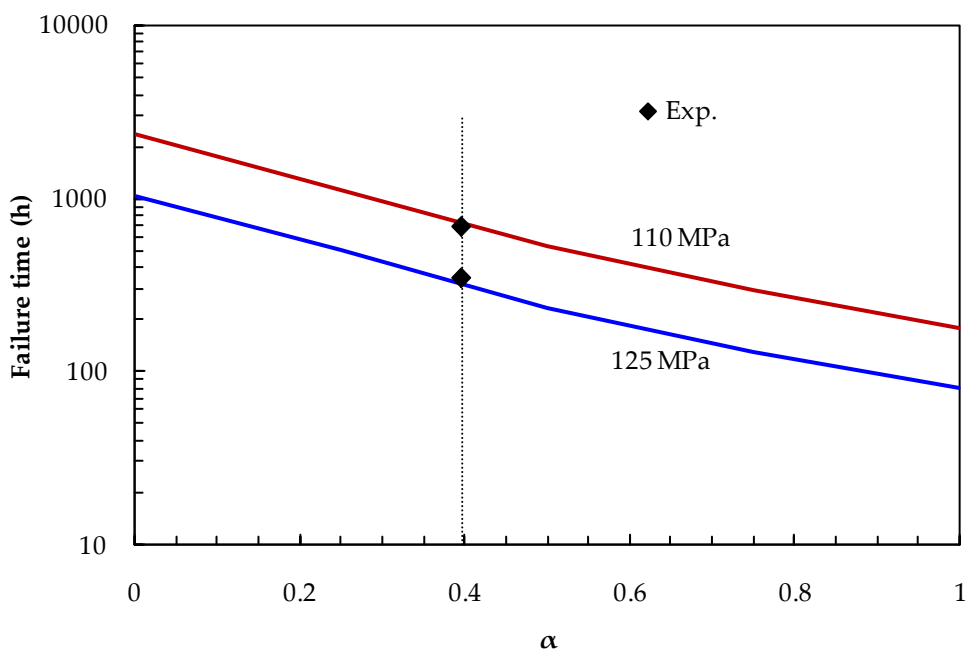


Fig. 5-18: FE notched bar failure times, for different α values, using the Liu/Murakami for P92 PM at 675°C.

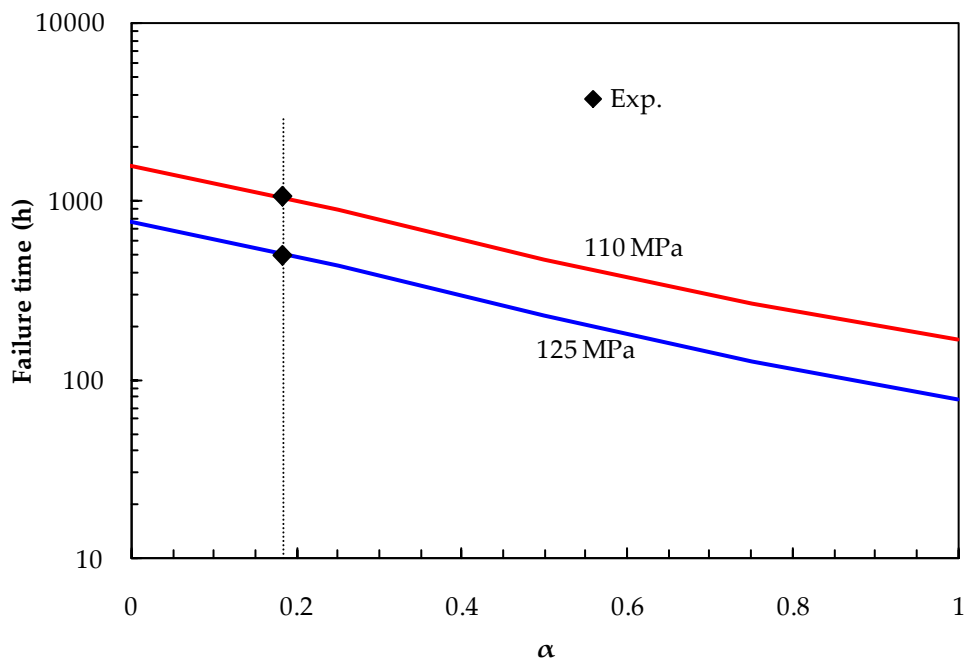


Fig. 5-19: FE notched bar failure times, for different α values, using the **Kachanov** model for **P92 WM** at 675°C.

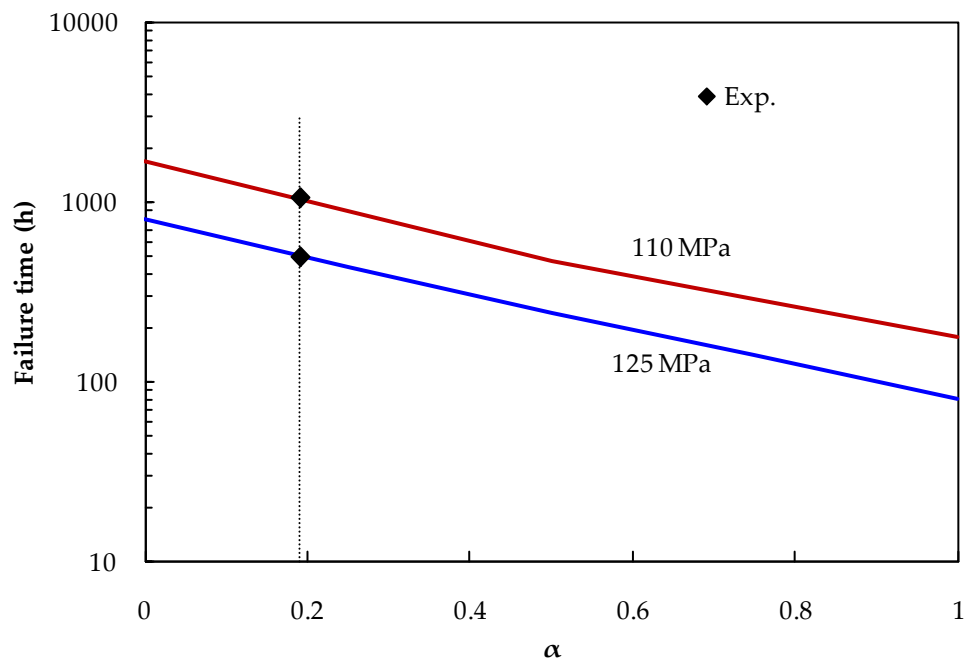


Fig. 5-20: FE notched bar failure times, for different α values, using the **Liu/Murakami** model for **P92 WM** at 675°C.

5.3.3.5 q_2

q_2 is a material constant used in determining the damage, ω , in the Liu/Murakami model, see equation (5-9). q_2 can be determined by fitting creep strain curves to the corresponding experimental curves. The fitting procedure has been detailed in Section 5.3.1.2. Fig. 5-21 and Fig. 5-22 show the creep strain curves, calculated using equation (5-12) and the fits to the experimental creep curves, with $q_2 = 3.0$ for P92 PM and P92 WM, respectively. The curves shown are the "best fit" obtained. All of the other material constants were kept the same during the fitting process. q_2 value for the P92 PM and P92 WM, at 675°C are included in Table 5-2.

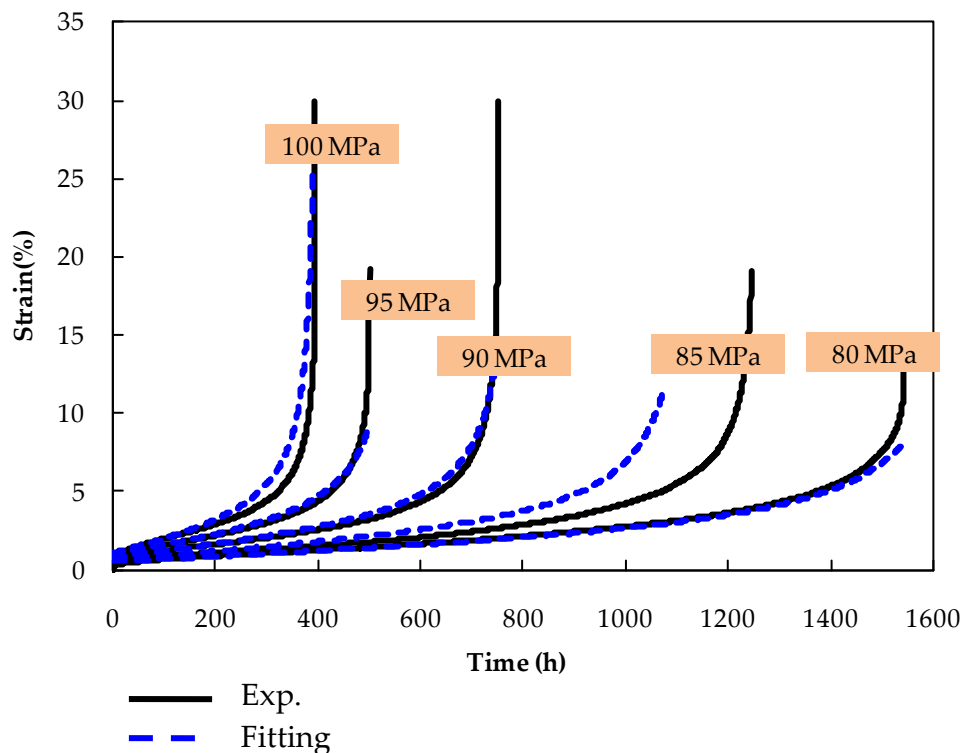


Fig. 5-21: Creep strain curves fitted to experimental creep curves at $q_2 = 3.0$, for P92 PM at 675°C.

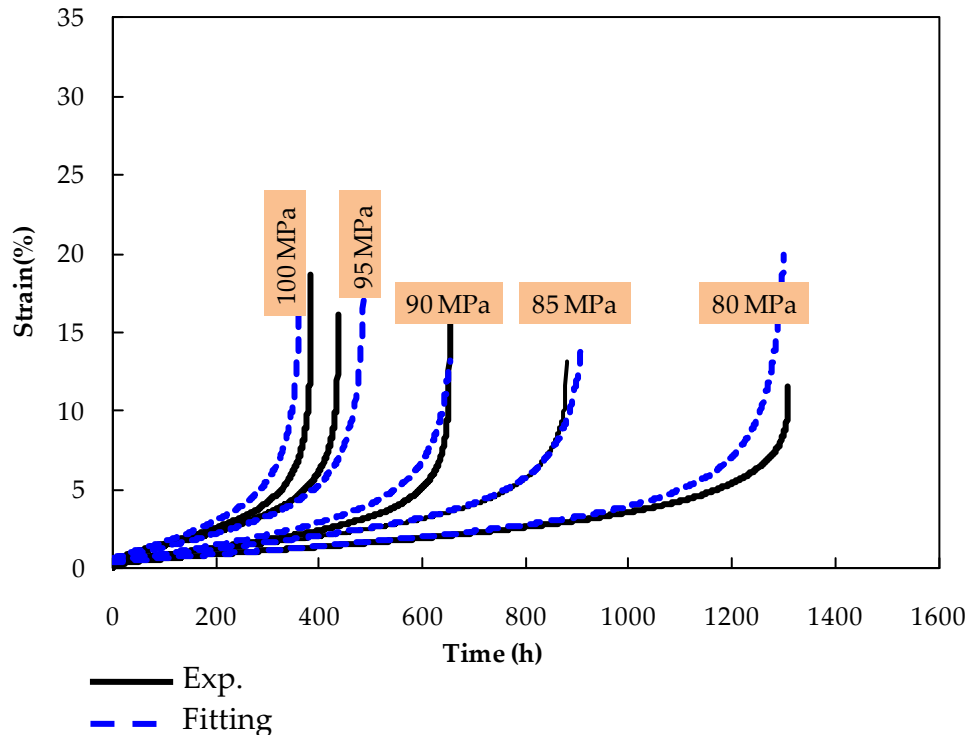


Fig. 5-22: Creep strain curves fitted to experimental creep curves at $q_2 = 3$, for P92 WM at 675°C.

Materi	A	n	m	B	ϕ	χ	α	q_2
PM	4.335×10^{-20}	7.659	0.0	3.377×10^{-17}	8.3	6.459	0.383	3.0
WM	1.065×10^{-17}	6.485	0.0	1.499×10^{-15}	7.5	5.67	0.187	3.0

Table 5-2: P92 Material constants for damage constitutive equations at 675°C (σ in MPa and time in h).

5.3.4 P92 FE uniaxial creep strain

FE uniaxial creep analyses have been carried out to validate the P92 material constants by comparing the results of these analyses to the corresponding experimental creep strain curves. Both damage models, i.e. the Kachanov and the Liu/Murakami models, were used. The FE model that was used for the P91 materials, and shown in Fig. 5-7, was also used for the P92 materials. Material constants for the P92, given in Table 5-2, were used.

Fig. 5-23 compares the FE uniaxial creep strain curves, obtained using the Kachanov model and those obtained using the Liu and Murakami model with the experimental creep strain curves for the P92 PM, at 675°C. The FE analyses have been run to times similar to the uniaxial failure times. It can be seen that, excluding the 85MPa test, all the FE results are in very good agreement with the experimental results. This validates the material properties obtained and the uniaxial FE models used.

The uniaxial FE creep strains for the P92 WM are compared with the experimental creep strains in Fig. 5-24. It can be seen that the FE creep strain curves obtained using either model, i.e. the Kachanov model or the Liu/Murakami model, agree with each other very well. They also fit the experimental data quite well.

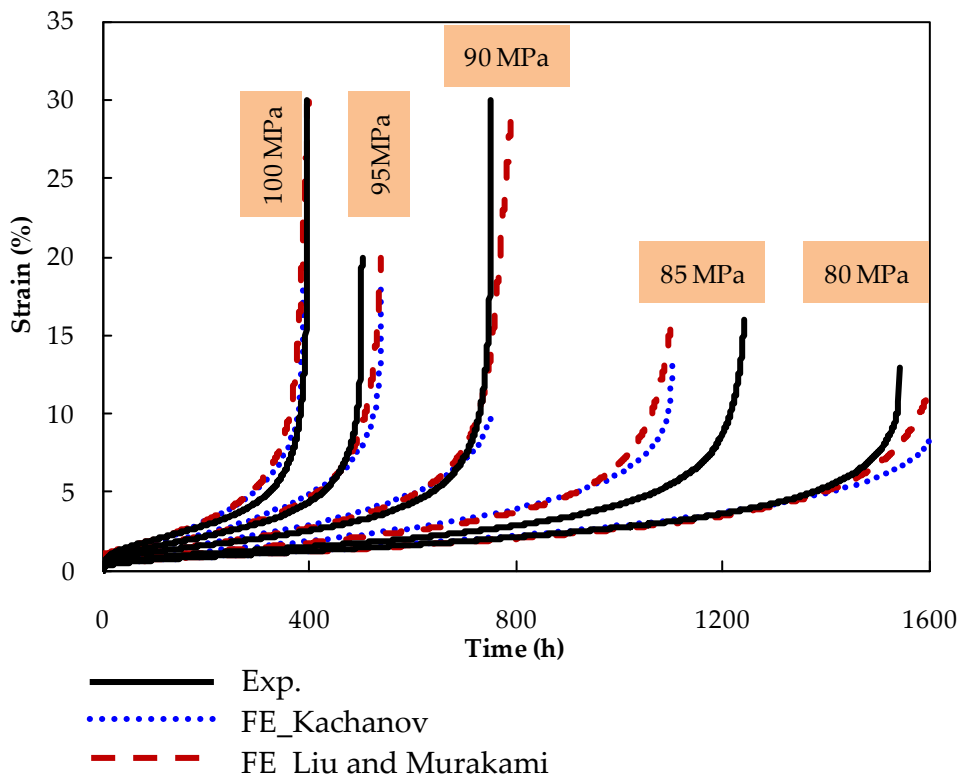


Fig. 5-23: Experimental and FE creep strain curves using the Kachanov and the Liu and Murakami Damage models for **P92 PM** at 675°C.

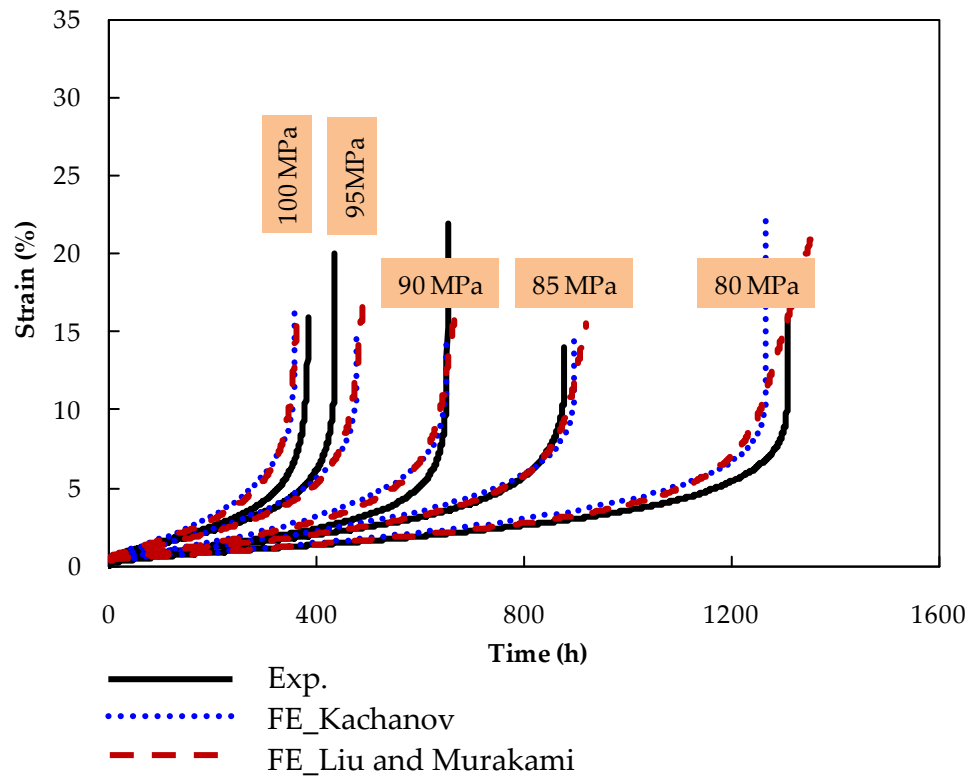


Fig. 5-24: Experimental and FE creep strain curves using the Kachanov and the Liu and Murakami Damage models for **P92 WM** at 675°C.

5.4 DISCUSSION AND CONCLUSIONS

Creep and creep rupture tests were carried out on P91 and P92 weldments and their results were given in Chapter 3. These results can be used to characterise the creep and creep rupture of these weldments and also to determine material constants which are needed to predict the creep behaviour of these weldments. In this chapter, the minimum strain rates (MSR) and failure times of the tested specimens are compared. Fig. 5-25 compares the MSR for the P91 weldment, at 650°C. These results were calculated using the Norton's law and the material constants given in Table 5-1. It can be seen that the HAZ is the weakest material whilst the WM is the strongest, in terms of creep resistance strength.

The minimum creep strain rates against the applied stress, for the P92 weldment, are shown in Fig. 5-26. Good fits can be seen between the MSR's and

the applied stresses for the PM and the WM. These fits were used to obtain the creep constants, A and n , for the PM and the WM, as shown in Fig. 5-10 and Fig. 5-11, respectively. Further, it can be seen that the slope of the PM curve and WM curve are similar. However, for the HAZ material, the results of the impression creep test show scatter. In order to avoid this inconsistency in the impression test results, it is suggested to cut the impression test specimens at the same time; more details are given in Section 7.3. The results of the cross-weld creep uniaxial tests are also shown in Fig. 5-26. Though the cross-weld uniaxial specimens failed at the HAZ region, their results are different from those obtained using the impression creep tests. For the same stress, e.g. 80 MPa, the MSR obtained from the impression test is more than two times that obtained from the cross-weld uniaxial test. It should be noted that the 80 MPa cross-weld specimens failed at the Type IV region on a plane perpendicular to the load direction while the 85 MPa specimen failed, also at the Type IV but, on a plane that was 45° to the loading direction, see Section 3.4.2.1. It is, therefore, suggested to manufacture a symmetric weld from which symmetrical cross-weld specimens to be cut. More investigations are needed to study the effects of constraints, of the PM and WM, on the deformation of the HAZ materials, in cross-weld specimens.

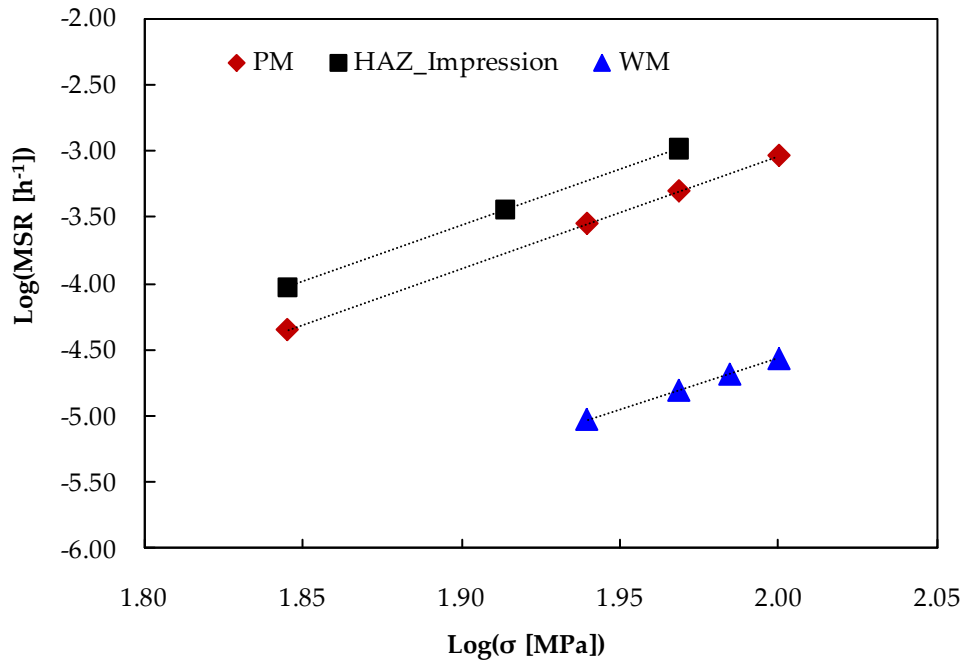


Fig. 5-25: Minimum creep strain rates, $\dot{\epsilon}_{min}$, against stress, σ , for the P91 weldment, at 650°C, (Hyde *et al.*, 2004a).

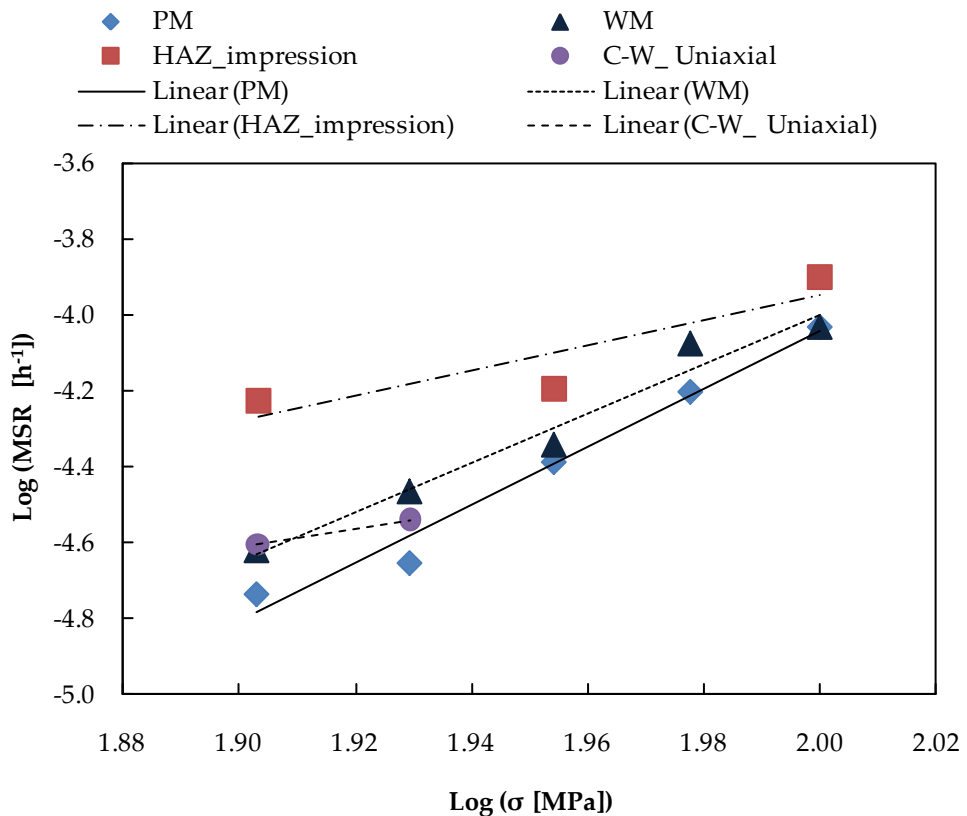


Fig. 5-26: Minimum creep strain rates, $\dot{\epsilon}_{min}$, against stress, σ , for the P92 weldment, at 675°C.

The failure times for the P91 weldment uniaxial, notched and waisted specimens, at 650°C, are shown in Fig. 5-27. It can be seen that the notch strengthening for the PM is more significant than that for the WM. Further, failure time for the WM uniaxial specimens is about one order of magnitude higher than that for the PM uniaxial specimens. It can also be seen that the failure times for the cross-weld notched and waisted specimens are similar, especially at lower stresses; failure times for both types of specimens are close to those for the PM uniaxial specimens. Failure times for the P92 PM and P92 WM creep uniaxial specimens, at 675°C, are similar, see Fig. 5-28. Three categories of results can be seen in Fig. 5-28. To the top of the figure, are the results for PM and WM notched bar specimens. In the middle, of the figure, are the results for the PM and WM uniaxial specimen. At the bottom, of the figure, are the results of cross-weld specimens. The consistency between the results of the PM specimens and corresponding WM specimens indicates that the P92 weld is an overmatched weld. This similarity in the properties of the weldment constituents improves the structure compatibility and integrity. From Fig. 5-28, it can, also, be seen that the failure times for the cross-weld uniaxial specimens are similar to those for the cross-weld waisted specimens.

Two damage mechanics models have been used in this thesis, i.e. the Kachanov and the Liu/Murakami models, to predict creep, creep rupture and CCG in P91 and P92 weldments. These models are known as single damage variable model, as only one variable, the damage, ω , controls strains and hence stresses. For non-cracked components, e.g. a pressurized pipe, both damage models can be used. However, for cracked components where stress state is very severe at the crack tip, the Kachanov model creates numerical problems. Moreover, the Kachanov model experiences mesh dependency problems (Liu and Murakami, 1998). Conversely, the Liu and Murakami model shows a much-improved numerical stability when modelling both cracked and un-cracked components.

Due to this reason, the Liu and Murakami model is used in this thesis to model the creep strain and creep crack growth in CT specimens.

Material constants A , n , M and χ can be determined in a straightforward manner using the MSR and failure times of uniaxial creep data. MSR and failure times can be determined accurately. Therefore, these material constants can be accurately determined. Other material constants, such as ϕ , q_2 and α , are determined using fitting to the overall experimental data.

Analytically obtained creep strain curves fit very well with those obtained from the FE analyses using the Kachanov and the Liu/Murakami model, for P91 and P92 materials. Both the analytical and FE curves fit well with the corresponding experimental curves.

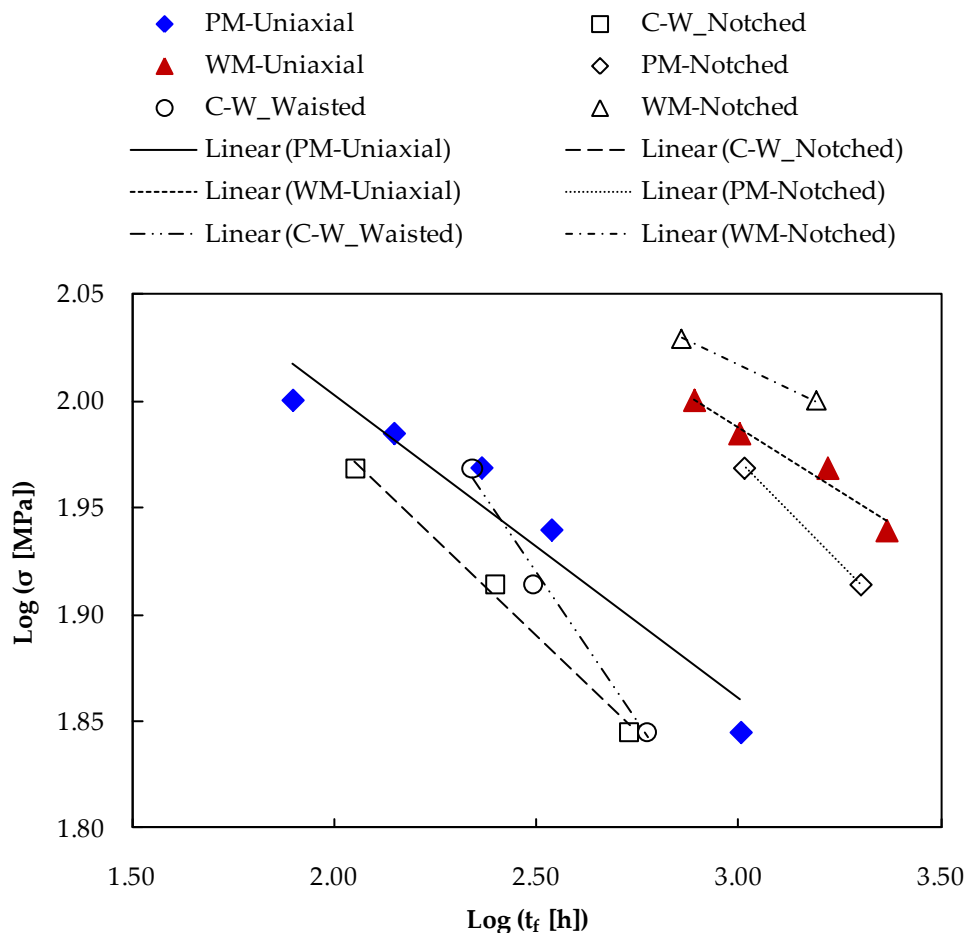


Fig. 5-27: Failure times, t_f , against stresses for the P91 weldment, at 650°C.

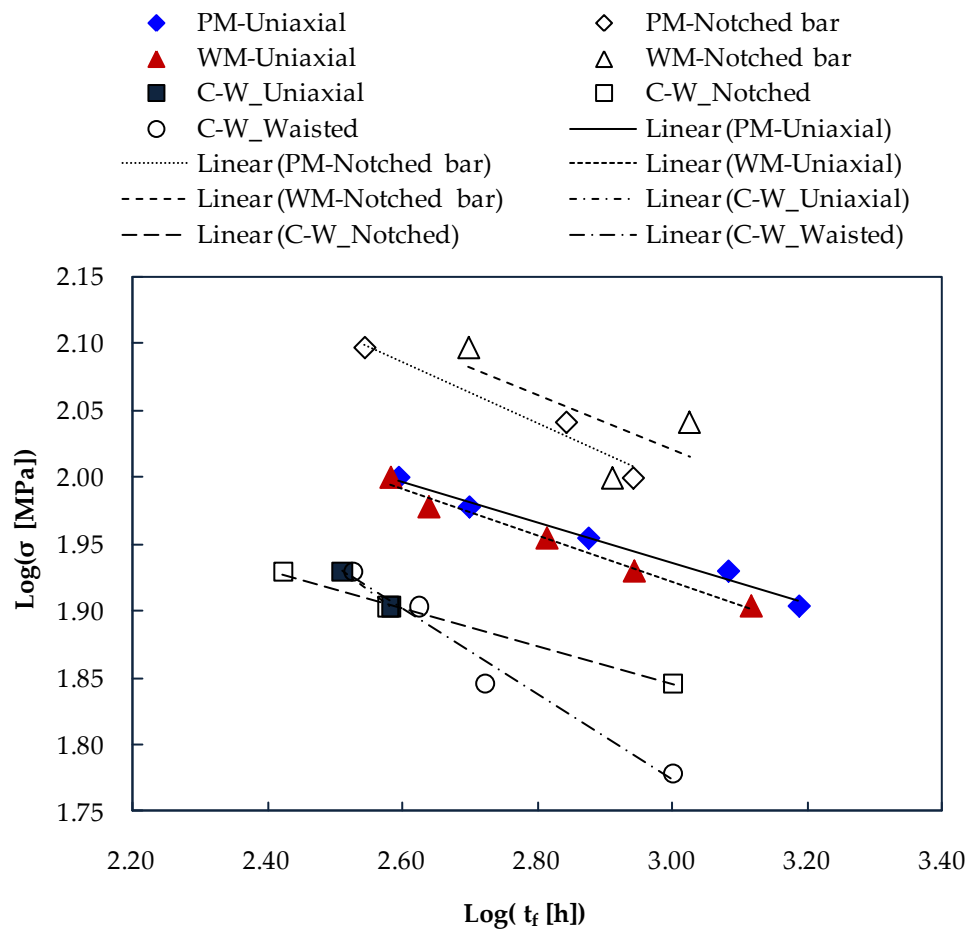


Fig. 5-28: Failure times, t_f , against stresses for the P92 weldment, at 675°C.

CHAPTER 6.

CREEP CRACK GROWTH PREDICTION USING DAMAGE MECHANICS

6.1 INTRODUCTION

Damage mechanics have been used to predict creep crack growth (CCG) in P91 and P92 CT specimens. In order to simulate the actual CT specimens, reported in Chapter 3, FE analyses were carried out using 3D CT models which have the same geometry and dimensions as the tested CT specimens. Another reason to use the 3D models is that the FE results are more sensitive to whether plane strain elements or plane stress elements were used. The FE analyses were carried out at the same loads as those used for the experiments. The appropriate boundary conditions were applied to the models. The Liu and Murakami damage model, presented in Section 5.2.2, was used, to obtain damage accumulation in the models. Experimentally determined material constants were used for the P91 and the P92 materials.

It was found that the Liu and Murakami model is capable of predicting the creep crack growth in the P91 and P92 CT specimens, but the predictions are sensitive to the material properties. The FE CCG analyses were used to verify the material constants obtained, for the P91 and P92 materials, by comparing the FE CCG predictions with the corresponding experimental results. Based on the FE CCG predictions for the P91 PM and for the cross-weld CT model, alternative values of the multiaxial parameter, α , were determined, for the PM and for the HAZ material. The new values of α were found to be 0.3125 and 0.5

for the P91 PM and HAZ material, respectively. However, for the P92 material, it was found that the values of α , that were determined by use of the notched bar specimens data were very similar to those obtained using the experimental CCG data.

6.2 PARENT MATERIAL CT MODEL

Based on the geometry and dimensions of the PM CT specimens, shown in Fig. 3-7, a 3D FE CT model has been created. Due to the symmetry of the PM CT model, only one-quarter of the specimen was modelled, as shown in Fig. 6-1. The C3D8R and C3D6 elements, as designated by ABAQUS, were used to model the specimens. Starter cracks were located at the mid-height position of the CT model. Fine elements, of size about 0.13mm, were used in the vicinity of the crack tip. This element size is less than one-third the element size that was used in (Liu and Murakami, 1998). The Liu/Murakami model was found to be mesh-independent (Liu and Murakami, 1998). Hyde *et al.* (2010) found that FE CCG predictions, using the Liu/Murakami model, fit the experimental CCG data well when small elements (0.2 mm or less) were used at the crack tip. Loading was applied to the load hole either by modelling a rigid pin which is attached to the nodes of the hole, or by using the multiple point constraints (mpc) facility, available in ABAQUS, which joins the hole centre to the nodes of the hole surface. Both methods produced practically the same results. Further details on the two loading methods are given in Appendix C. Boundary conditions were applied to the planes of symmetry of the model in the Y-direction and in the Z-direction, and to the load application point in the X-direction, as shown in Fig. 6-2. The load point was constrained in the X-direction to prevent the rigid body motion of the model.

The PM CT specimens, i.e. P91 CT1, P92 CT1 and P92 CT2, are plane specimens, i.e. without side grooves. All the other PM CT specimens are side-grooved. Both

the plane and the side-grooved CT specimens were modelled. For the grooved CT model, grooves of 1.5 mm depth with a 90° groove angle were applied. Fig. 6-1 shows a side-grooved CT model.

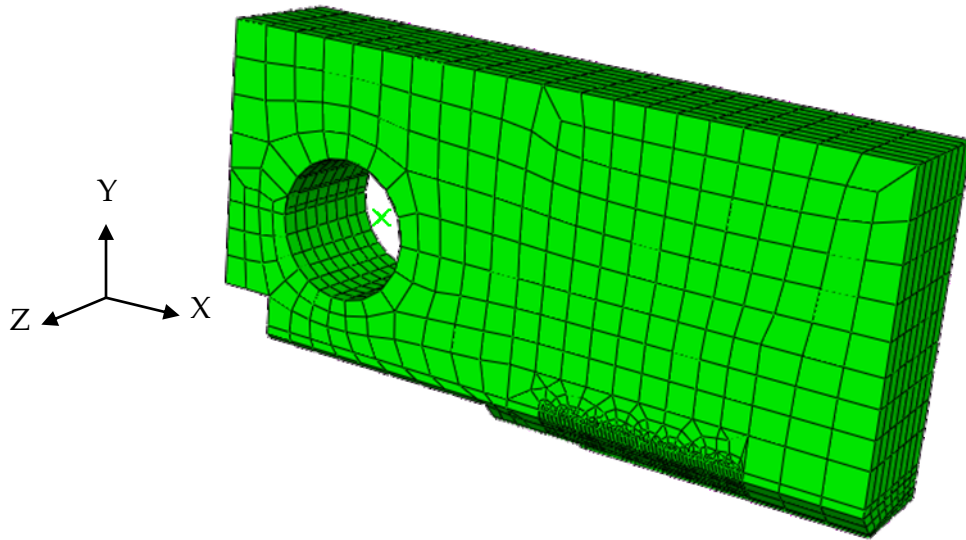


Fig. 6-1: PM CT specimen.

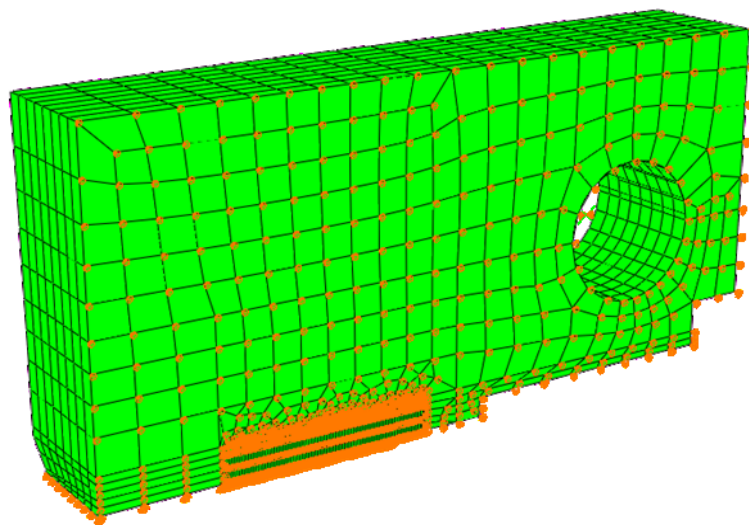


Fig. 6-2: Boundary conditions applied to the planes of symmetries.

6.3 CROSS-WELD CT MODEL

A cross-weld CT specimen consists of three distinctive materials, i.e. PM, HAZ and WM, as shown in Fig. 3-9. A 3D FE CT model was created, see Fig. 6-3, based on the geometry and dimensions of the cross-weld CT specimen, given in Fig. 3-9. Due to the symmetry of the specimens, it was only necessary to model one-half of the specimen. The cross-weld CT model consists of PM, HAZ and WM regions. As with the PM CT model, elements of type C3D8R and C3D6 were used. Fine elements were used in the region close to and ahead of the initial crack tip. The size of these elements is about 0.16 mm, which is slightly bigger than that used for the PM CT model. Load was applied to the upper hole of the model while the lower hole was kept fixed in the X, Y, and Z directions. Fig. 6-4 shows the load and the boundary conditions applied to the upper and lower holes, while Fig. 6-5 shows the boundary conditions applied to the vertical plane of symmetry. The load and boundary conditions were applied to the model via a rigid pin located at the upper and lower holes. Details of the modelling of the rigid pins are given in Appendix C. All of the cross-weld CT models are side-grooved models.

As with the experimentally tested cross-weld CT specimens, starter cracks were located on the boundary between the PM and the HAZ regions, i.e. in the Type IV region. The application of loads in the Y-direction, i.e. mode I loading, allows the crack to grow along the PM/HAZ boundary.

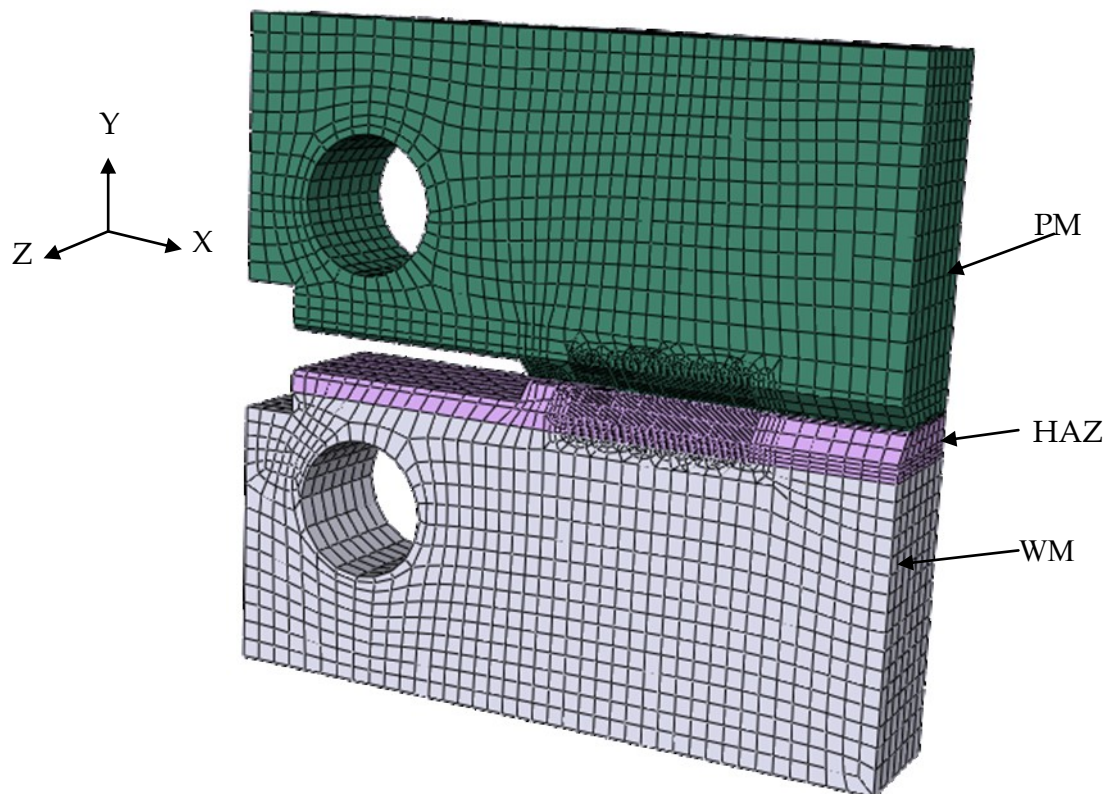


Fig. 6-3: The cross-weld CT model.

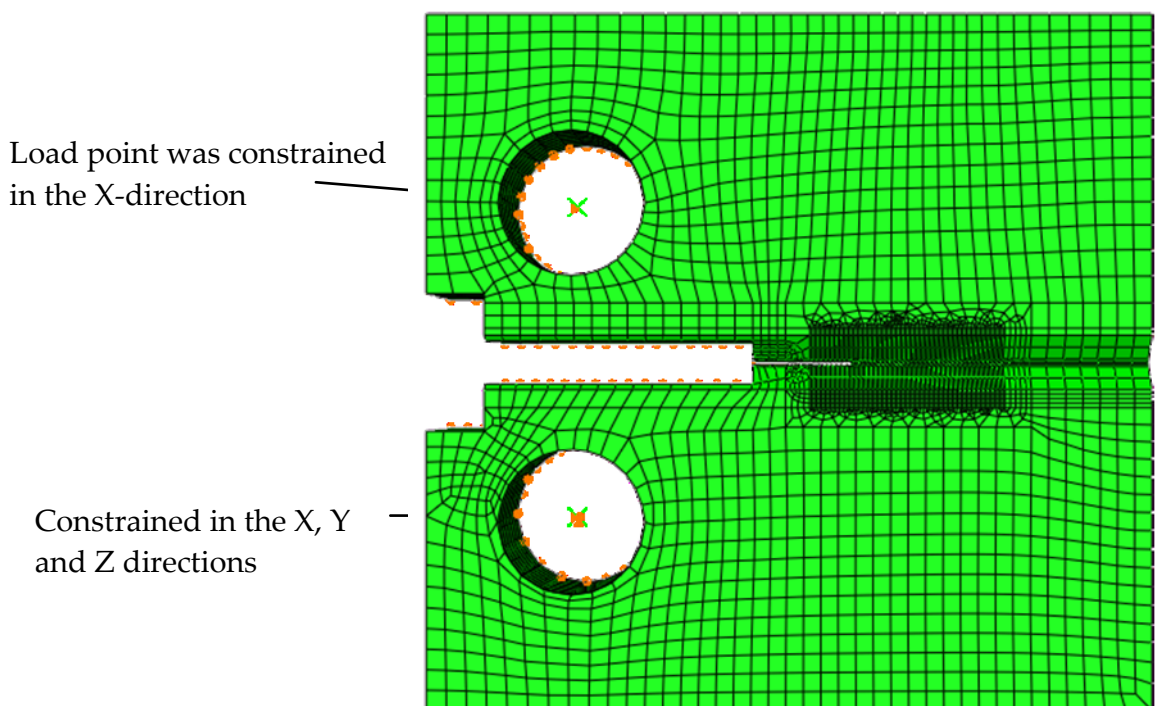


Fig. 6-4: The loading and boundary conditions at the load points.

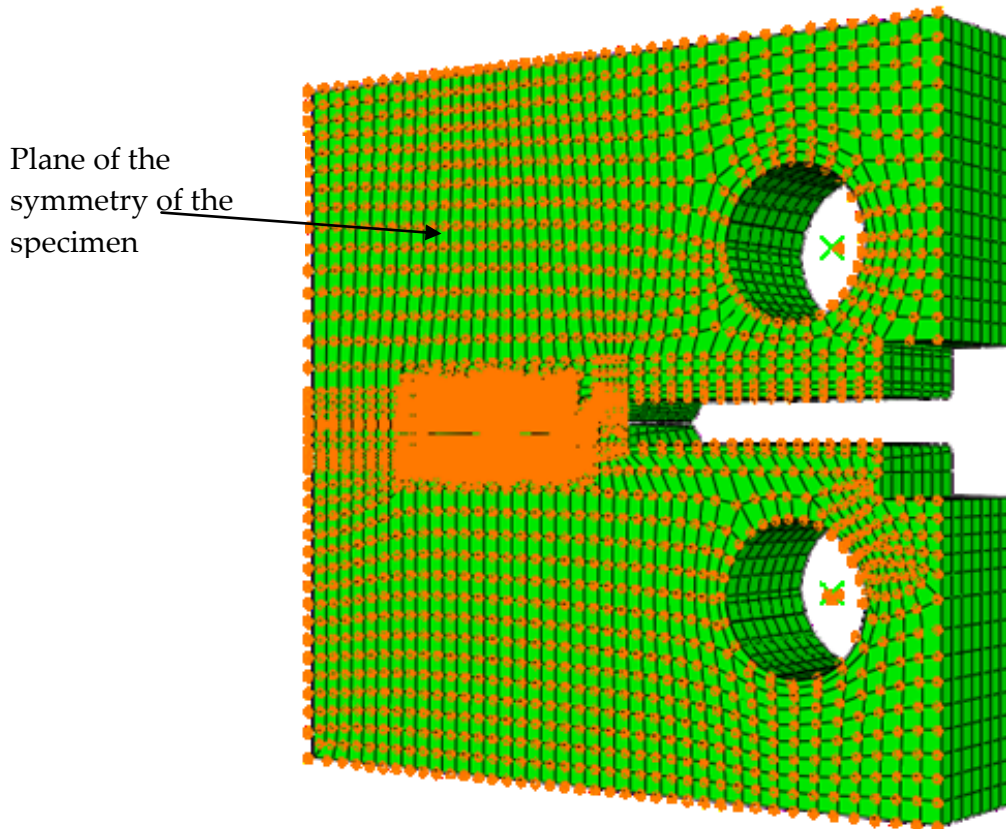


Fig. 6-5: The boundary conditions were applied to the plane of symmetry.

6.4 P91 FE PREDICTIONS

6.4.1 P91 PM

FE analyses were carried out, using the P91 PM CT models shown in Fig. 6-1, using the Liu and Murakami damage model, detailed in Section 5.2.2. Material constants which were used for the P91 PM analyses are given in Table 5-1. The FE analyses were carried out on the plane CT models and on the side grooved CT models. The CREEP subroutine was used to calculate the damage parameter, ω , for each element in the model. When the value of ω reached a specific value, 0.99 in this study, it was assumed that the element has failed and it is practically removed from the analysis. This is done by setting the element's modulus of elasticity, E , to a very small value close to zero, say 10; setting the value of E at failure to zero causes numerical problems for the FE analyses. This means that

in effect the element is no longer able to support any load. This technique is known, throughout this study, as the element deletion technique. Fig. 6-6 shows the global FE meshing used for the PM CT model together with damage contours on the plane of symmetry.

In the experiments, it was found that the cracks on the plane of symmetry for the plane specimens exhibit crack tunnelling, i.e. thumbnail cracked surface is produced. The side-grooved specimens exhibit an almost straight crack front, see Fig. 3-28 and Fig. 3-29. It was found that the FE analyses replicate these features. Fig. 6-7 shows the FE results obtained for the plane CT model, CT1, and the side-grooved CT model, CT4. Fully damaged elements, where $\omega = 0.99$, and non-damaged elements can be seen.

The multiaxiality parameter, α , used to define the rupture stress, σ_{rup} , is as follows:-

$$\sigma_{rup} = \alpha\sigma_1 + (1-\alpha)\sigma_{eq} \quad (6-1)$$

where σ_{rup} , σ_1 and σ_{eq} are the rupture stress, the maximum principal stress and the equivalent stress, respectively. It was found that the damage initiation, damage evolution and the failure time in the FE CCG analyses are strongly dependent on the α value used. Fig. 6-8 shows the predicted damaged zones in the CT4 model, using various α values, at the time equal to CT4 experimental failure time (410 h). A nonlinear relationship can be seen between extent of the damaged zone and the α value.

Fig. 6-9 compares the FE creep crack growth results to the corresponding experimental data, for CT3, using $\alpha = 0.3125$. Good agreement can be seen between the FE and the experimental results.

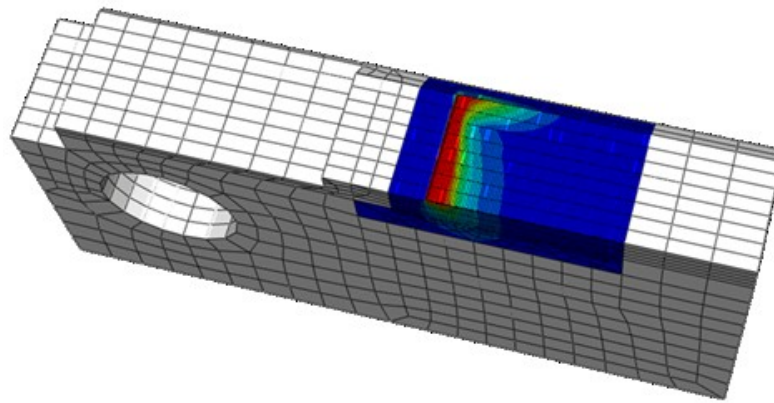


Fig. 6-6: Mesh for the 3D PM CT model showing damage contours.

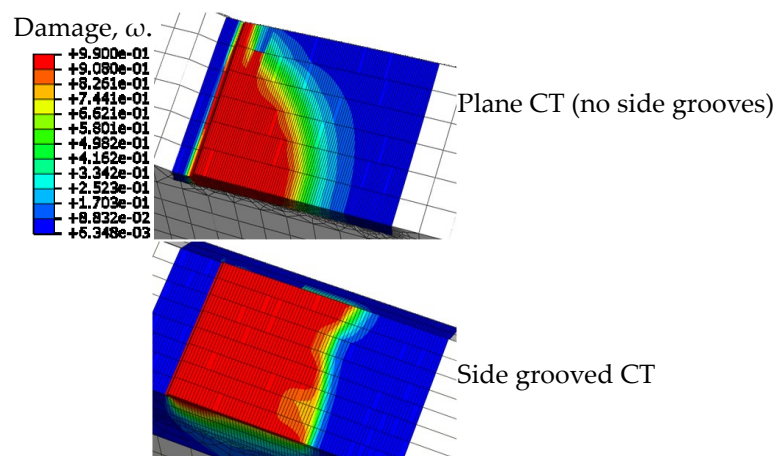


Fig. 6-7: FE damage contours for a plane CT model, CT1, and a side grooved CT model, CT4.

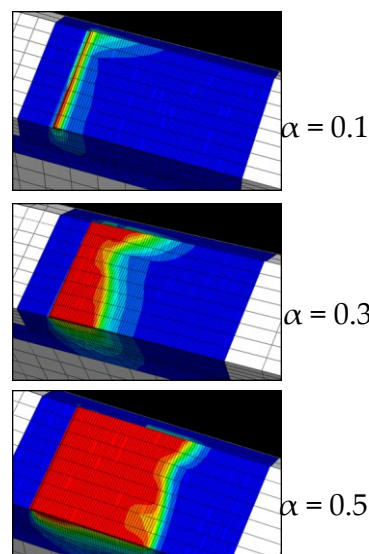


Fig. 6-8: Damage zones at various α values for the P91 PM CT model CT4.

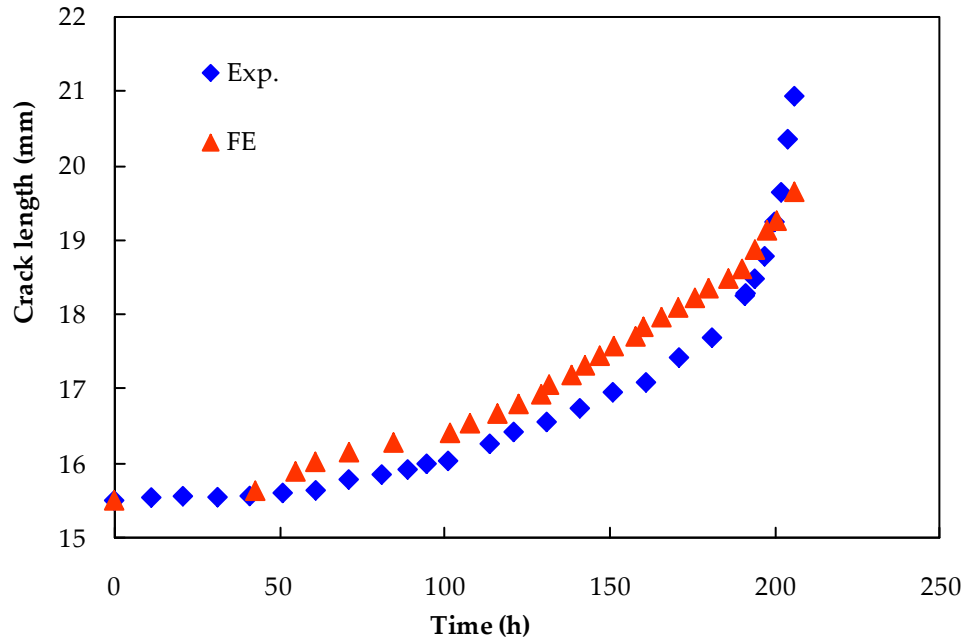


Fig. 6-9: FE creep crack growth for P91 PM CT3 compared to the experimental results.

6.4.2 P91 cross weld

Starter cracks in the P91 cross-weld CT test specimens were located in the Type IV region, i.e. on (or very close to) the boundary between the PM and the HAZ material. Therefore, material properties of the HAZ, particularly the α , control the damage initiation and damage evolution predicted in the cross-weld FE CCG analyses. It was found that when the α value of 0.215, given in (Hyde *et al.*, 2004a), was used for the HAZ material, it resulted in underestimate of the CCG in the cross-weld FE CCG analyses. Therefore, and in order to obtain a more suitable α value for the HAZ material, FE analyses were carried out on cross-weld CT models using various α values in conjunction with the Liu and Murakami model. All of the other materials constants for the HAZ and full set of constants for the PM and WM, already determined, were kept the same in the analyses.

When the damage, ω , reached the assigned critical value, which is 0.99 in this study, within an element, the element is taken to be fully damaged. The damage progression within these elements depends on the α value used for the HAZ material, when the load and other materials constants are kept the same. The α value that gives the same creep crack growth as that in the experiments was then taken to be the actual α value.

The results of the FE cross-weld CCG analyses were used to determine the multiaxial parameter, α , for the P91 HAZ material. Fig. 6-10 shows the predicted damaged area, where $\omega = 0.99$, when different α values were used in the FE analyses, for CT9. The progression of the $\omega = 0.99$ damaged area for CT9, with $\alpha = 0.52$, is shown in Fig. 6-11. It can be seen that the damaged area increases dramatically towards the end of the analysis, at a time close to that obtained from the corresponding experiment. This time was taken to be close to the time at which total failure occurs, as judged by the very high displacement and crack growth rates at this time. The average size of the 0.99-damaged area was determined at different times and this was taken to be the average crack length at those times.

Fig. 6-12 compares the CCG predictions for various α values, using the specimens CT9 and CT10 load magnitude, i.e. 1700 N; CT9 and CT10 were subjected to the same testing conditions. It can be seen that the FE CCG predictions are in good agreement with the experimental CCG data when $\alpha = 0.52$.

Fig. 6-13 shows the results of the FE CCG analyses for specimens CT7 and CT8 together with the corresponding experimental results. The loads applied to CT7 and CT8 were 2500 N and 2000 N, respectively. It can be seen that, when $\alpha = 0.48$, the results of the FE analyses agree well with the experimental results.

The comparisons between the damaged zones, which represent the FE cracked area, and the experimental results, shown in Fig. 6-10 to Fig. 6-13, indicate that the actual α value, for the P91 HAZ material, lies between 0.48 and 0.52. The α value has a significant effect on the predicted failure times for the specimens. Close to the failure time, the crack growth rate increases very sharply. The sensitivity of the crack growth rate prediction to the α value and the scatter which is observed in the experimental results, creates difficulty in obtaining a precise value for α which will give good fits to all of the experimental results.

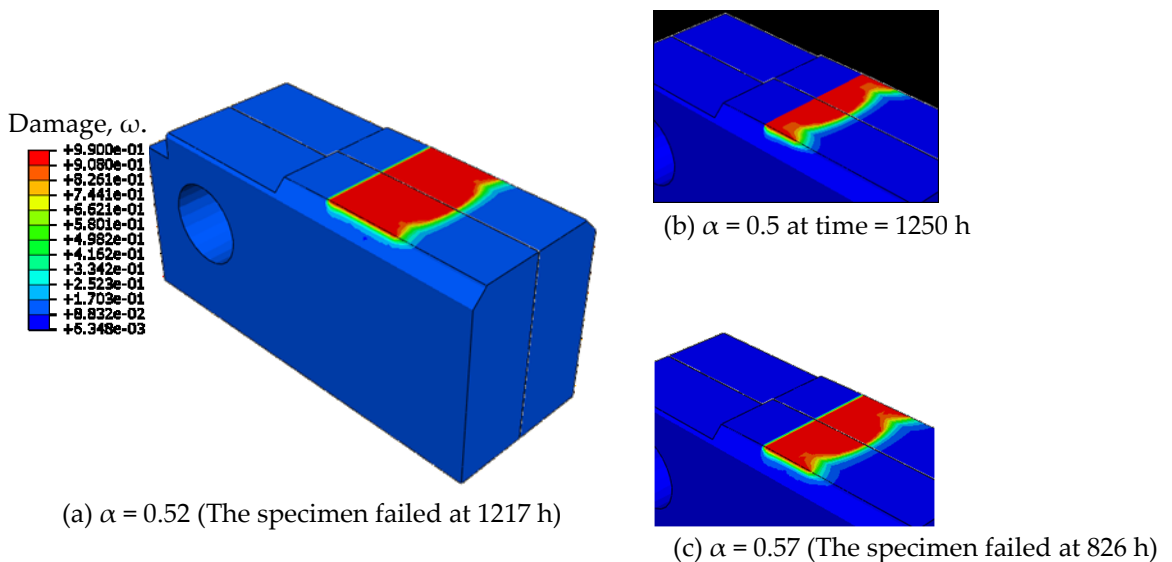


Fig. 6-10: Predicted damage zones on the PM/HAZ boundary for the CT9, with various α values for the HAZ material.

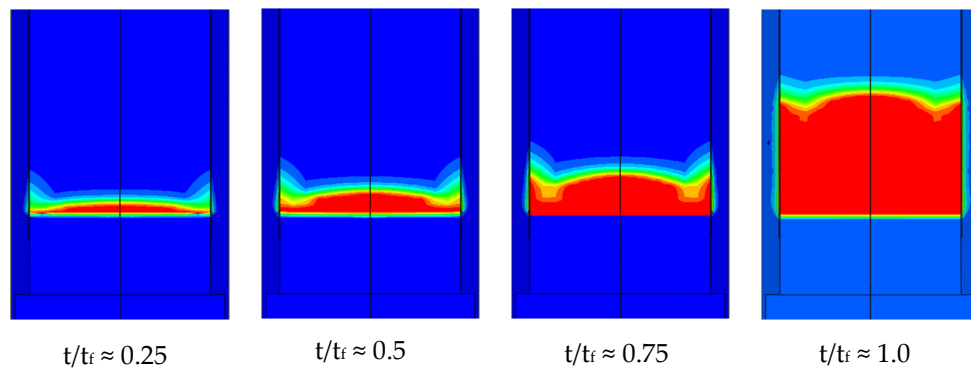


Fig. 6-11: Damage accumulation, indicating the progression of the creep crack growth with time, for CT9 with $\alpha = 0.52$, for various times, t , relative to the failure time, t_f .

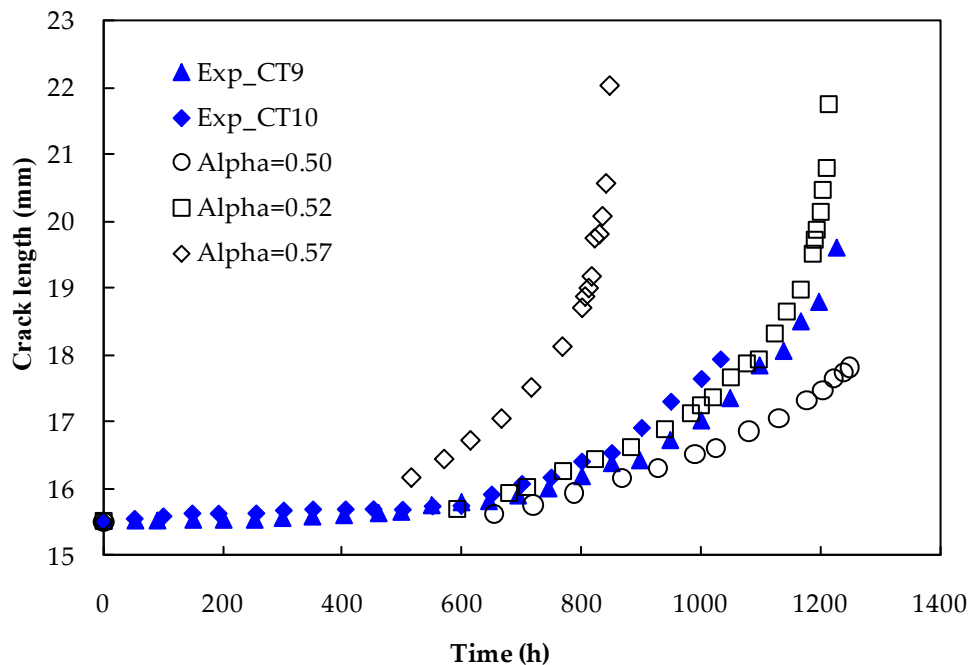


Fig. 6-12: Experimental and FE creep crack growth for the P91 CT9 and CT10 with various α values.

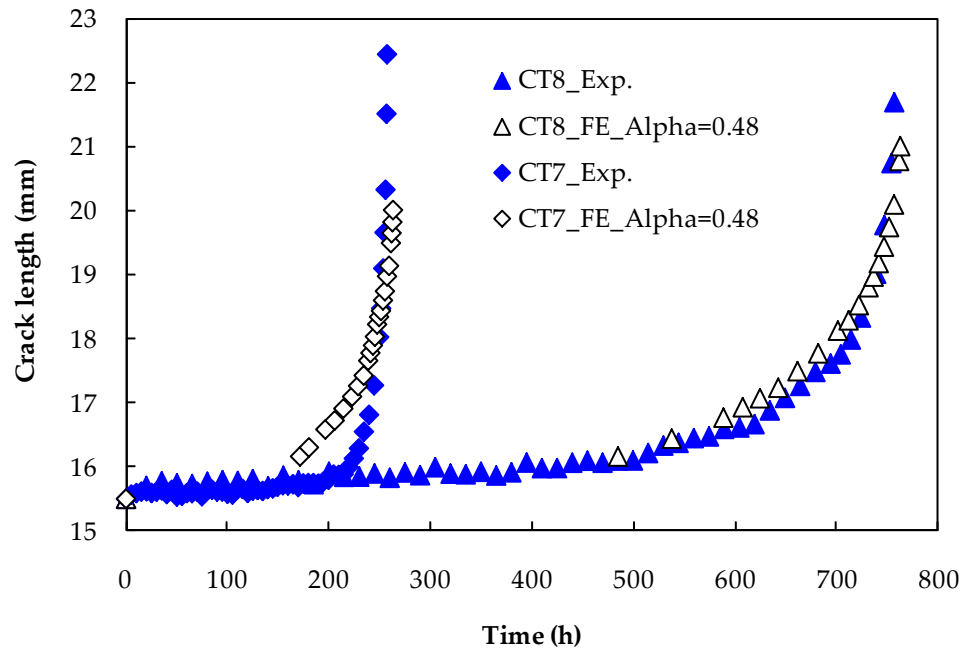


Fig. 6-13: Experimental and FE creep crack growth for CT7 and CT8 with $\alpha = 0.48$.

6.5 P92 FE PREDICTIONS

6.5.1 P92 PM

The determination of the α value for the P92 PM, at 675°C, using the results of notched bar tests was given in Section 5.3.3.4. The average α value for the P92 PM, at 675°C, was found to be 0.383. FE creep crack growth analyses were carried out using the Liu and Murakami model, with $\alpha = 0.383$, to predict the creep crack growth in the P92 PM CT models. The FE creep crack growth analyses were carried out on plane CT models and on side-grooved CT models. As with the P91 results, shown in Fig. 6-7, it was found that the plane CT models exhibit thumbnail cracking while the side grooved specimens show an almost straight crack front.

Fig. 6-14 shows the FE creep crack growth predictions for the P92 PM CT2 with $\alpha = 0.383$; the α value that was obtained from notched bar test results. It can be seen that the FE results agree reasonably well with the experimental results.

Moreover, the FE failure time is close to the experimental one. It should be noted that the P92 CT2 is a plane specimen, i.e. without side grooves; the FE model was also plane. Fig. 6-15 shows the FE creep crack growth predictions for the P92 PM CT3, with $\alpha = 0.383$, compared to the experimental results. It can be seen that the FE failure time compares favourably with the experimental failure time.

The results shown in Fig. 6-14 and Fig. 6-15 indicate that, creep crack growth can be accurately predicted using the α -value that was obtained using the results of notched bar tests. This confirms the reliability of the determination of α values using notched bar results, for P92 PM at 675°C.

The effect of the value of α on the creep crack growth is shown in Fig. 6-16, using CT3 loading conditions. It can be seen that the higher the α value the shorter the failure time. Moreover, the effect of the α value on the failure time is significant. It was also found that, for a close range of α values, the creep crack growth rates are similar at the same crack length, see Fig. 6-17.

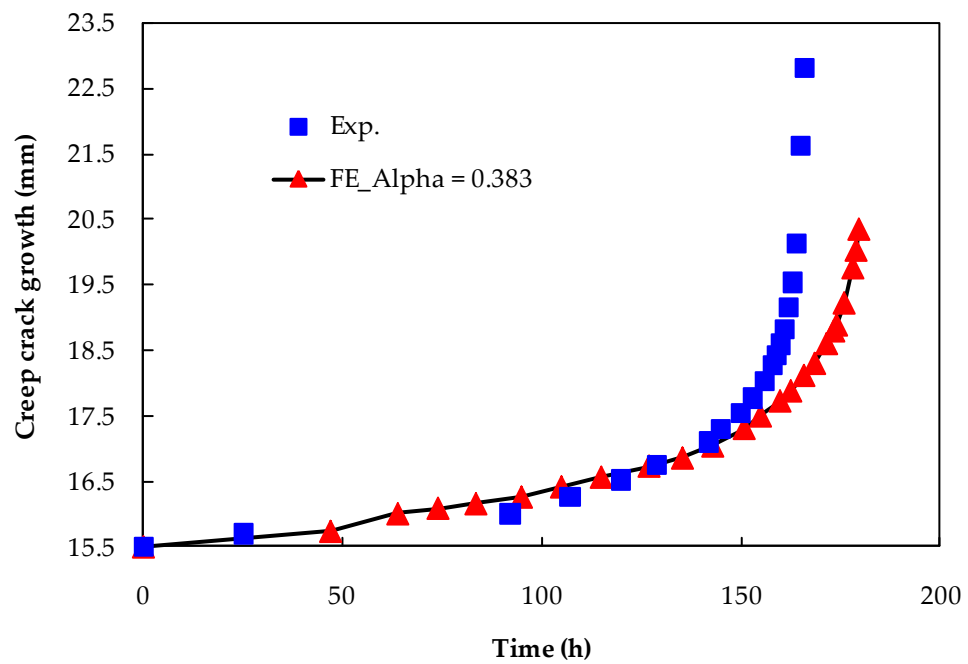


Fig. 6-14: Experimental and FE creep crack growth for the P92 CT2 with $\alpha = 0.383$.

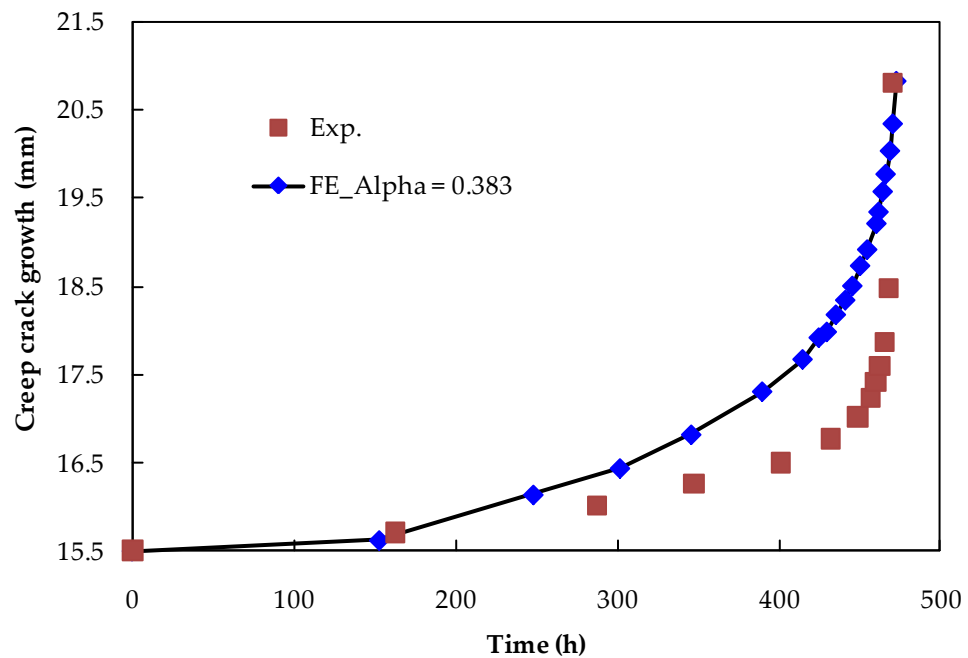


Fig. 6-15: Experimental and FE creep crack growth for the P92 CT3 with $\alpha = 0.383$.

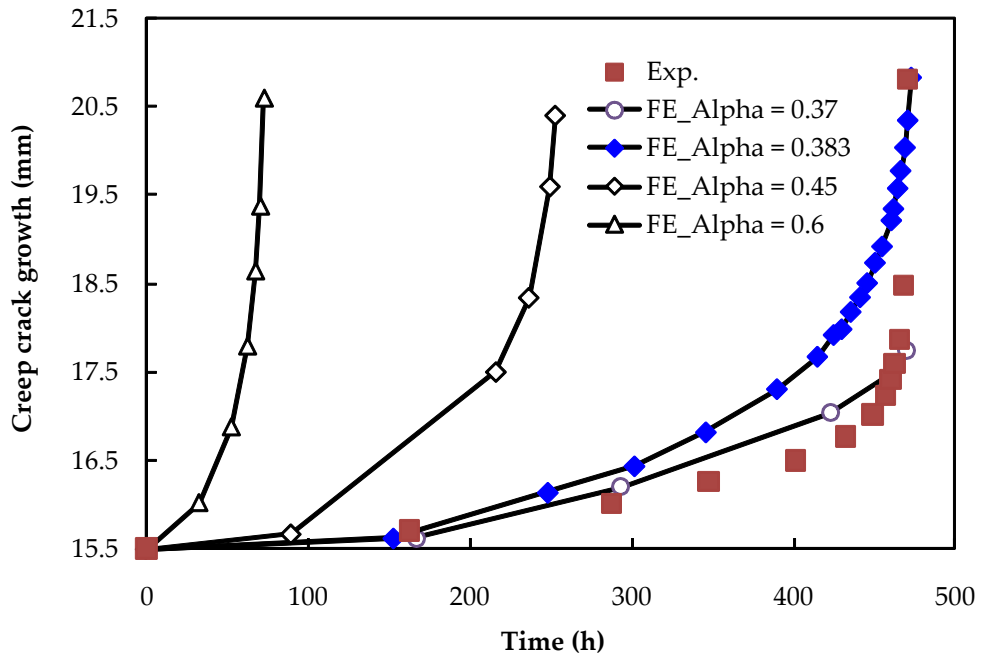


Fig. 6-16: FE creep crack growth with various α values compared to the P92 CT3 results.

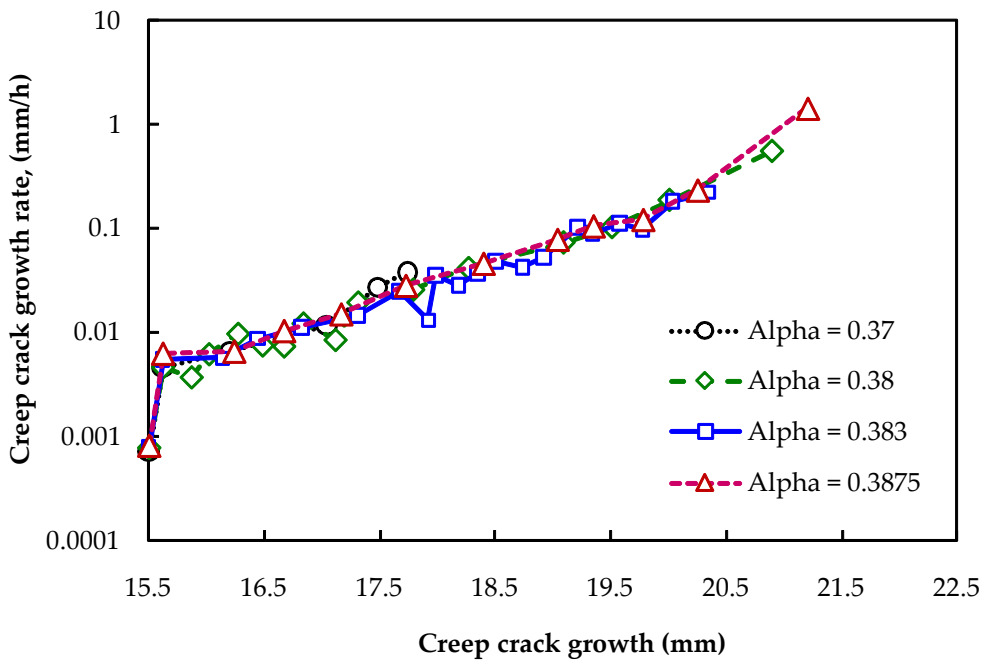


Fig. 6-17: FE creep crack growth rates for various α values, using CT3 loading conditions.

6.6 DISCUSSION AND CONCLUSION

The accurate determination of the multiaxiality parameter, α , is crucial if the initiation and evolution of damage in creeping components, and their failure times are to be accurately predicted. The α value is a material constant that can be determined by fitting failure times of FE notched bar models to corresponding experimental failure times. It can also be determined by fitting CCG predictions in CT models to the corresponding experimental CCG data.

Creep crack growth in PM and cross-weld CT specimens have been predicted using the FE method and the Liu/Murakami damage model. For the P91 PM CT models, good agreement was obtained between the FE CCG and the experimental CCG when $\alpha = 0.3125$ whereas for the P91 cross-weld CT models, the FE CCG fits the experimental CCG well when α value for the HAZ material is taken to be 0.5. However, these values of α are different from those obtained when using the notched bar results, i.e. 0.215 for the PM and 0.75 for the HAZ material. The α values that were obtained using CCG results are the most consistent. For example, the α value for the HAZ material (0.5), which was obtained using the results of the CCG tests, is the average of a narrow range of α values, i.e. 0.52 from the results of CT9 and CT10 and 0.48 from the results of CT7 and CT8, see Fig. 6-12 and Fig. 6-13. However, the α value obtained from the notched bar results (0.75) is the average of a relatively wide range of α values, i.e. 0.59 obtained for 93 MPa test, 0.75 for 82 MPa test and 0.85 for 70 MPa test, see Fig. 6-18. Further, as the α value is the last material constant to be determined, it will be significantly affected by the accuracy of the determination of all of the other material constants. Scatter in the experimental results significantly affects the accuracy of all of the material constants determined.

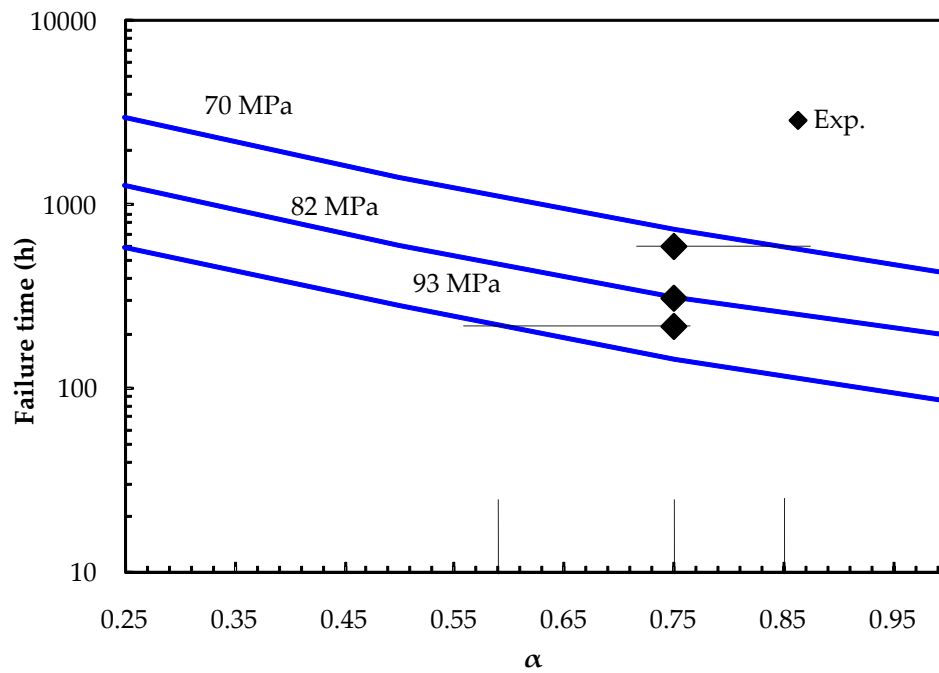


Fig. 6-18: FE notched bar failure times, for different α values, using the **Kachanov** model for the P91 cross-weld, at 650°C.

The α values for the P92 PM and WM, at 675°C, were obtained using the notched bar results (0.383 for the PM and 0.187 for the WM). These values were used to predict the CCG in the P92 PM CT specimens. Good agreement has been achieved between the FE CCG and the experimental CCG, as shown in Fig. 6-14 and Fig. 6-15.

In summary, it is possible to successfully predict CCG in cracked bodies using a damage mechanics approach. This requires accurate material properties and an appropriate material damage model. The Liu/Murakami damage model has been found to be suitable for use in predicting CCG in cracked bodies. Further, both the notched bar and the CT specimens approaches can be used to define the material multi-axiality parameter α .

CHAPTER 7.

DISCUSSION, CONCLUSIONS AND FUTURE WORK

7.1 DISCUSSION

The aim of this thesis is to study creep and creep crack growth in P91 and P92 steels. P91 and P92 steels are used to manufacture, for example, main steam pipes in power plants. They are also used in nuclear and chemical plants. Welds made from P91 and P92 materials are potential failure regions in piping systems. Therefore, the research has involved investigations into the creep and creep crack growth in welds and they have been compared with the behaviour of the corresponding base materials.

Creep tests were carried out on P91 material at 650°C; the nominal operating temperature of P91 material is 593°C. The results of these tests showed that, the P91 PM is a ductile material, with an average strain at failure of about 35%, while the P91 WM has a lower ductility, with an average strain at failure of about 5%. This difference in ductility, between the PM and the WM, results in a degree of mismatch in the P91 weldment. This mismatch complicates the evaluation of stresses and deformations which are produced in the weld. For the P91 weld, the Type IV region is the weakest region and, therefore, it is a potential failure position. Further, hardness tests showed that the Type IV region had the lowest hardness value compared with the other P91 weld regions. Impression creep tests were carried out on the P91 HAZ material region in order to obtain same creep data for the Type IV material. Notched bar tests

were carried out to obtain the creep rupture data of the P91 PM, WM and HAZ; for the HAZ material the notched bar specimens were cut across the weld. The results of creep and creep rupture tests for the P91 material are given in Chapter 3.

Supercritical and ultra-supercritical power stations work at higher than normal operating temperatures, i.e. more than 600°C. At such high temperatures, the allowable stress of the P91 material drops to the point that it is impractical to use it. To overcome this problem, P92 material has been introduced; P92 material can sustain operating temperatures of up to 620°C.

Creep tests were carried out on P92 material at 675°C; the nominal operating temperature for P92 material is 620°C. The P92 material was tested at a temperature which is higher than that used for the P91 material tests. At this temperature, it was found that the P92 PM is less ductile than the P91 PM; the average strain at failure for the P91 PM is about 35% and for the P92 PM is about 22%. The average strain at failure for the P92 WM (about 18%) is similar to that of the P92 PM. As with the P91 weld, hardness measurements across the P92 welds showed that the minimum hardness occurred in the Type IV region. Impression creep tests were carried out to obtain the creep data for the P92 HAZ material. However, the results obtained from the impression creep tests exhibit a high degree of inconsistency. It was found that the position of the indenter, with respect to PM, significantly, affects the results of the impression creep tests. In order to obtain consistent results from impression creep tests, a method has been proposed for sampling impression creep specimens, see Section 7.3. In addition, cross-weld uniaxial specimens were tested to obtain creep data for the P92 HAZ material. Only two cross-weld uniaxial specimens were tested. The results obtained do not appear to agree with those obtained from the impression creep tests. Moreover, due to asymmetry of the P92 weld, the two specimens

failed at different angles. Therefore, it is suggested to make a symmetric weld and cut the cross-weld uniaxial specimens out of that weld. In order to obtain the creep rupture data for the P92 materials, notched bar specimens were cut from the P92 PM and from the P92 WM and were tested, at 675°C.

Creep crack growth tests were carried out on the P91 PM and cross-weld CT specimens, at 650°C. The PM CT specimens were cut from a PM side of a P91 weldment while the cross-weld CT specimens were across the weld such that it consisted of PM, WM and HAZ materials. For the cross-weld CT specimens the starter cracks were located in the Type IV region. It was found that these cracks grew in the Type IV region where the lowest hardness was measured across the weldment. The fracture mechanics parameter C^* was used to correlate the CCG rates in both the PM and cross-weld CT specimens. The obtained results showed that, at the same C^* value, the CCG rate in the cross-weld CT specimens is about ten times higher than that in the PM specimens. This difference in the CCG rates highlights the effect of welding on the material properties.

Creep crack growth tests were also carried out on the P92 PM and cross-weld CT specimens. The testing procedure for the P92 CT specimens is the same as that used for the P91 CT specimens, with two differences. The first difference was in the sampling of the specimens. For the P91, the CT specimens were cut such that the specimen width (W) was parallel to the weld cross section while, for the P92 material, the CT specimens were cut so that the specimen width was perpendicular to the weld cross section. The second difference is the testing temperature; 650°C for the P91 material and 675°C for the P92 material. Hence, the results from the P91 and P92 tests are not, directly, comparable.

Creep crack growth can be predicted using, for example, the fracture mechanics parameter C^* . C^* values can be obtained using the load line displacement rates

and the CCG data of CCG tests of, for example, CT specimens. The calculated C^* values, for the P91 and P92 CT specimens, were found to correlate the CCG rates in these specimens. The procedure for calculating C^* values was presented in Chapter 4.

Continuum damage mechanics can be used to accurately predict the behaviour of a wide range of components and structures operating under creep conditions. Two damage models, named the Kachanov model and the Liu/Murakami model, have been presented in Chapter 5. Both of the models can be used successfully for predicting the deformation and failure of non-cracked components working under creep conditions. However, the Liu and Murakami model was favoured over the Kachanov model when they were applied to cracked bodies. It has been noticed that the FE CT analyses using the Liu and Murakami model were more stable and could be completed within a practical time. Nevertheless, when using the Kachanov model, for cracked bodies, time increments decreases to an impractical level and the analyses terminated issuing an error message.

Accurate determination of material properties is needed in order to, accurately, predict the creep behaviour of a component. The more accurate the material properties are, the more accurate the predicted component behaviour will be. For single material cases, such as PM and WM, it is straightforward to obtain material constants using creep and creep rupture data that were obtained from conventional uniaxial, notched bar specimens. However, where the amount of material available is not enough to manufacture conventional specimens, small and/or unconventional specimens are needed. In these instances, creep testing of impression creep specimens, small punch creep specimens and ring specimens may be necessary. These specimens can also be used to obtain creep data for HAZ material. To obtain creep rupture data for HAZ material, cross-weld

notched bar and waisted specimens can be used. Uniaxial, notched bar, cross-weld notched bar and waisted specimens are presented in Section 3.2.2, while small specimens are reviewed in Section 2.7.2.

7.2 CONCLUSIONS

The overall conclusions to be drawn are as follows:

- ✓ It was found that the C^* parameter correlates well the CCG rates in the P91 and the P92 CT specimens, for both the PM and cross-weld CT specimens. For a given C^* value, the creep crack growth rate, for the P91 PM CT specimens, was found to be about ten times lower than that for the cross-weld CT specimens. Further, the CCG rate for the P92 PM CT, at a specific C^* value, was found to two times lower than that of the cross-weld CT specimens. Though the CCG tests for the P92 CT specimens were carried out at higher temperature (675°C) than that for the P91 CT specimens (650°C), it was found that the CCG rates in the P92 cross-weld specimens are less than those in the P91 cross-weld specimens.

- ✓ The C^* parameter and the Reference Stress method were found to correlate the creep crack growth rates in homogenous CT specimens (the P91 PM CT's and P92 PM CT's in this thesis) and in heterogeneous CT specimens (P91 cross-weld CT's in this thesis).

- ✓ Damage mechanics analyses, using the FE method can successfully predict creep and creep rupture in P91 and P92 materials. Moreover, they can predict the CCG in homogenous and heterogeneous CT specimens made of these materials.

- ✓ Accurate determination of the material constants in damage laws, in particular the constants for the HAZ, is essential in order to obtain accurate creep crack growth predictions for welds.

7.3 FUTURE WORK

- FE C^* values have been obtained using stationary crack models. Growing crack models has been used, with the use of CCG data as a fracture criterion, to obtain FE C^* values and load line displacements. Further, research is needed to apply the growing crack model to actual pipe components with a crack.
- In this thesis, the CCG rates, \dot{a} , for the P91 and P92 materials, were correlated to the corresponding C^* values at a constant temperature, using CT specimens. However, some workers obtained a unique relationship between \dot{a} and C^* using different specimens geometries, different loads and different temperatures, e.g. (Laiarinandrasana *et al.*, 2006). Therefore, it is suggested to carry out some creep crack growth tests on, for example, CT, circumferentially cracked round bar (CCRB) and thumbnail crack specimens, and at different temperatures. This is, in order to study and investigate the effects of specimens geometry and temperatures on the \dot{a} - C^* correlation.
- Creep crack growth for the P91 and P92 welds has been studied, in this thesis, with the starter cracks being located in the Type IV region. The starter cracks were cut parallel to the PM/HAZ boundary. It is suggested that a study of CCG should be carried out when the starter cracks are cut perpendicular (or inclined) to the PM/HAZ interface, as shown in Fig. 7-1. This involves studying the effect of the distance between the crack

tip and PM/HAZ boundary, on the CCG and failure times. Further, the effect of the inclination angle can also be investigated.

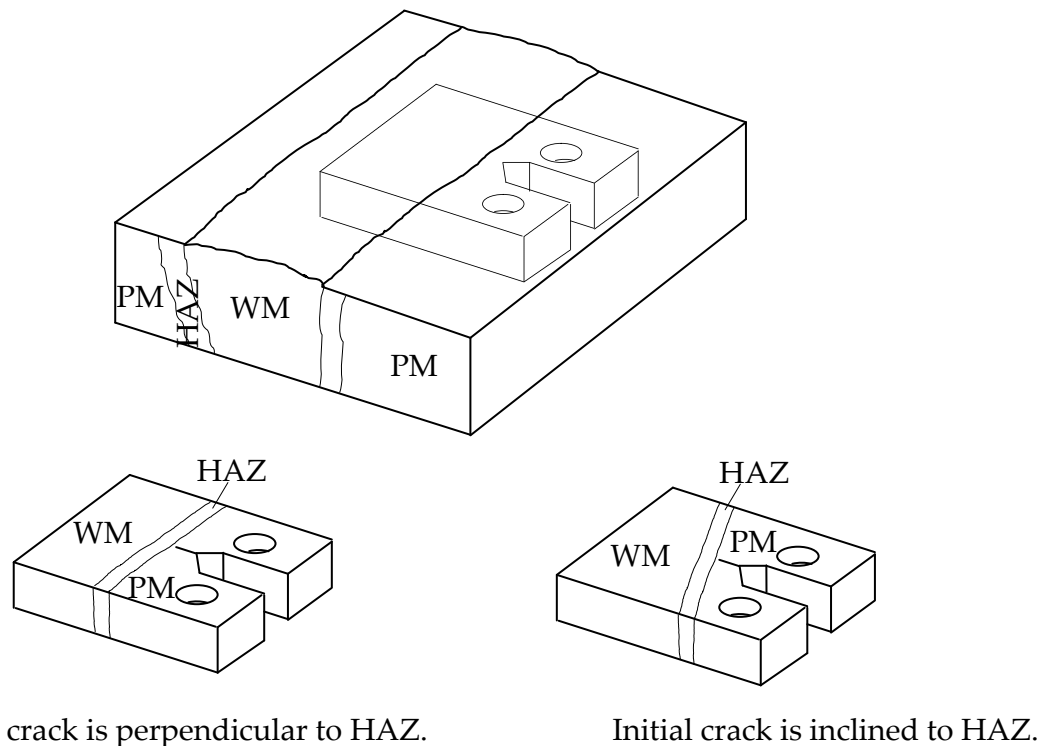


Fig. 7-1: Proposed CT specimens sampling.

- The determination of material constants for HAZ material is extremely important in the prediction of creep, creep rupture and CCG in cross-weld specimens. Different techniques and specimens designs are involved in the determination of material constants for HAZ material. Examples of these specimens are impression, small punch, cross-weld waisted and cross-weld notched creep tests. A number of complications arise during these tests, such as loading, alignments and oxidation of small specimens. Also, the use of simulated HAZ material with conventional specimens has been approved by many workers, e.g. (Smith

et al., 2003, Tabuchi *et al.*, 2010, Hongo *et al.*, 2009, Wang *et al.*, 2009). Simulating the HAZ material can be done by heat treating the parent material in a furnace or by using weld simulator (Wang *et al.*, 2009). Simulated HAZ can be used to determine the material constants, for the HAZ material, and to investigate the constraint applied to the HAZ material in welds. This can be done by comparing the creep strain of a simulated HAZ creep test to that of cross-weld creep test under the same testing conditions.

- It is recommended to machine all the impression creep specimens at the same time. This can be done by cutting a quite long strip of HAZ material. The sides of the strip are to be polished and etched to define the Type IV region and then grind the strip surface until reaching the Type IV region. This strip is then cut into standard impression creep specimens. Fig. 7-2 describes the proposed sampling method of the impression creep specimens.
- The FE analyses and the Liu and Murakami model were found to be able to, successfully, predict the CCG in the P91 and P92 CT specimens. Therefore, it is suggested to use the FE analyses and the damage model to predict the CCG in cracked pipes. The pipes could have, for example, a circumferential crack in the Type IV region. The results of such analyses could help in determining the remaining lifetime of a potentially cracked pipes or components.

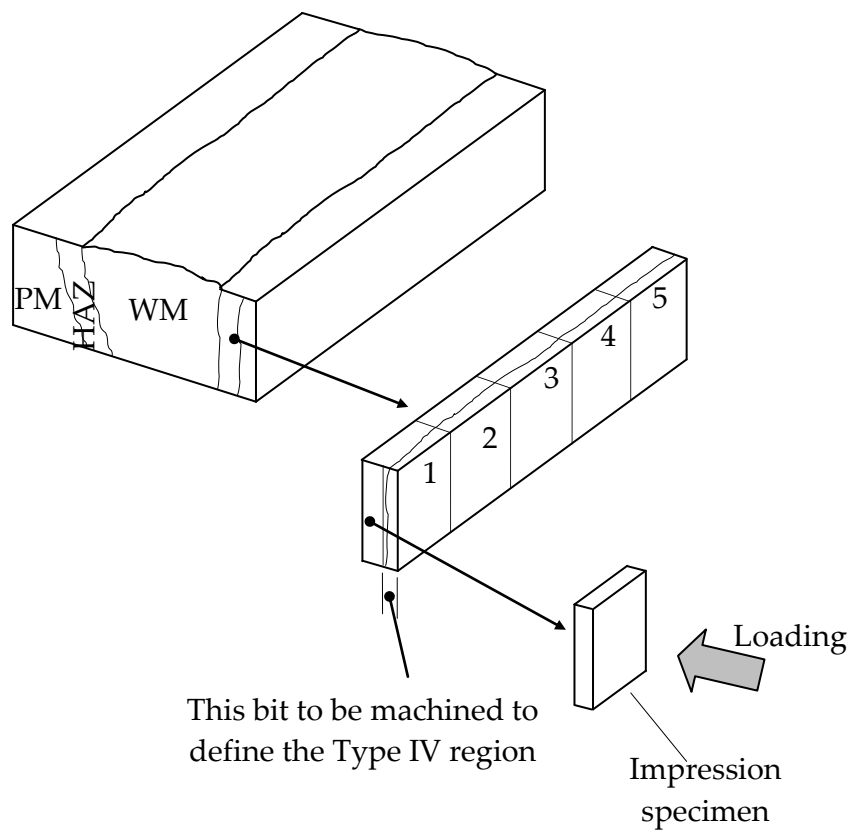


Fig. 7-2: It is suggested to cut impression creep specimens in one go; to obtain consistent specimens.

REFERENCES

- Abaqus**, (2007), *Abaqus 6.7 Standard User Manual*, USA, ABAQUS, Inc.
- Anderson, T. L.**, (2005), *Fracture Mechanics Fundamentals and Applications*, CRC Press.
- Ashby, M. F. and Jones, D. R. H.**, (1996), *Engineering Materials 1: An Introduction to Their Properties and Applications*, Butterworth Heinemann.
- Astm E 1457-00**, (2001), *Standard Test Method for Measurement of Creep Crack Growth Rates in Metals*, Annual book of ASTM standards.
- Becker, A., Hyde, T. and Xia, L.**, (1994), Numerical Analysis of Creep in Components, *The Journal of Strain Analysis for Engineering Design*, 29, 185-192.
- Dogan, B. and Petrovski, B.**, (2001), Creep Crack Growth of High Temperature Weldments, *International Journal of Pressure Vessels and Piping*, 78, 795-805.
- Evans, R. W. and Wilshire, B.**, (1985), *Creep of Metals and Alloys*.
- Falat, L., Výrostková, A., Homolová, V. and Svoboda, M.**, (2009), Creep Deformation and Failure of E911/E911 and P92/P92 Similar Weld-Joints, *Engineering Failure Analysis*, 16, 2114-2120.
- Francis, J. A., Mazur, W. and Bhadeshia, H. K. D. H.**, (2006), Type Iv Cracking in Ferritic Power Plant Steels, *Materials Science and Technology*, 22, 1387-1395.
- Gopala Krishna, M. S., Sriramamurthy, A. M. and Radhakrishnan, V. M.**, (1998), Application Software for Analyses of Creep Crack Growth Data, *Engineering Fracture Mechanics*, 59, 137-150.
- Halighongde, S.**, (2009), Simulation of High Temperature Crack Growth in Welds Using Finite Element Analysis. *Mechanical, Materials and Manufacturing Engineering*. Nottingham, UK, University of Nottingham, PhD thesis.
- Halighongde, S., Becker, A. and Hyde, T. H.**, (2010), Finite Element Analysis of Creep Crack Growth Using C* Parameter in Multi-Domain Problems. IN Tizani, W. (Ed.) *computing in civil and building engineering*. Nottingham, UK, Nottingham University Press.
- Hayhurst, D. R.**, (1972), Creep Rupture under Multi-Axial States of Stress *J.Mech.Phys.Solids* 20, 9.

- Hayhurst, D. R.**, (2001), Computational Continuum Damage Mechanics: Its Use in the Prediction of Creep in Structures - Past, Present and Future, *S.Murakami and N.Ohno(eds.),IUMAT Symposium on Creep in Structures*, 13.
- Hongo, H., Tabuchi, M. and Takahashi, Y.**, (2009), Microstructures and Type-Iv Creep Damage of High Cr Steel Welds, *Journal of Solid Mechanics and Materials Engineering*, 3, 464-474.
- Hyde, C. J., Hyde, T. H., Sun, W. and Becker, A. A.**, (2010), Damage Mechanics Based Predictions of Creep Crack Growth in 316 Stainless Steel, *Engineering Fracture Mechanics*, 77, 2385-2402.
- Hyde, T., Sun, W., Becker, A. and Williams, J.**, (2004a), Creep Properties and Failure Assessment of New and Fully Repaired P91 Pipe Welds at 923 K, *Proceedings of the Institution of Mechanical Engineers, Part L: Journal of Materials: Design and Applications*, 218, 211-222.
- Hyde, T., Tang, A. and Sun, W.**, (1998), Analytical and Computational Stress Analysis of Welded Components under Creep Conditions *Integrity of High-Temperature Welds*. Nottingham, UK, Professional Engineering Publishing Limited, London and Bury St, Edmunds, UK.
- Hyde, T. H.**, (1988), Creep Crack Growth in 316 Stainless Steel at 600 C, *High Temperature Technology*, 6, 51-61.
- Hyde, T. H., Becker, A. A., Song, Y. and Sun, W.**, (2006a), Failure Estimation of Tig Butt-Welded Inco718 Sheets at 620 °C under Creep and Plasticity Conditions, *Computational Materials Science*, 35, 6.
- Hyde, T. H., Becker, A. A., Sun, W. and J.A.Williams**, (2006b), Finite-Element Creep Damage Analyses of P91 Pipes, *International Journal of Pressure Vessels and Piping*, 83, 10.
- Hyde, T. H., Becker, A. A., Sun, W. and Williams, J. A.**, (2006c), Finite-Element Creep Damage Analyses of P91 Pipes, *International Journal of Pressure Vessels and Piping*, 83, 853-863.
- Hyde, T. H., Becker, A. A., Sun, W., Yaghi, A., A.Thomas and Seliger, P.**, (2006d), Finite Element Creep Failure Analyses of P91 Large Tensile Cross-Weld Specimens Tested at 625 °C. IN Gomes, J. F. S. and Meguid, S. A. (Eds.) *5th International Conference on Mechanics and Materials in Design*. Porto-Portugal.

- Hyde, T. H. and Sun, W.**, (2000), Determining High Temperature Properties of Weld Materials, *JSME International Journal of Solid Mechanics & Material Engineering*, 43, 408-414.
- Hyde, T. H. and Sun, W.**, (2009a), Evaluation of Conversion Relationships for Impression Creep Test at Elevated Temperatures, *International Journal of Pressure Vessels and Piping*, 86, 757-763.
- Hyde, T. H. and Sun, W.**, (2009b), A Novel, High-Sensitivity, Small Specimen Creep Test, *The Journal of Strain Analysis for Engineering Design*, 44, 171-185.
- Hyde, T. H., Sun, W., Becker, A. A. and Williams, J. A.**, (2004b), Creep Properties and Failure Assessment of New and Fully-Repaired P91 Pipe Welds at 923 K, *Journal of Material: Design and Applications(IMEchE Proceedings Part L)*, 23.
- Hyde, T. H., Xia, L. and Becker, A. A.**, (1996), Prediction of Creep Failure in Aeroengine Materials under Multi-Axial Stress States, *International Journal of Mechanical Sciences*, 38, 385-403.
- Jason Dobson, P.**, (2006), Why New U.S. Supercritical Units Should Consider T/P92 Piping. Cummins & Barnard Inc.
- Kachanov, L. M.**, (1958), Time of the Fracture Process under Creep Conditions *SSSR*, 8.
- Kim, B., Jeong, C. and Lim, B.**, (2008), Creep Behavior and Microstructural Damage of Martensitic P92 Steel Weldment, *Materials Science and Engineering: A*, 483-484, 544-546.
- Kim, B. and Lim, B.**, (2008), Local Creep Evaluation of P92 Steel Weldment by Small Punch Creep Test, *Acta Mechanica Solida Sinica*, 21, 312-317.
- Laha, K.**, (2007), Type Iv Cracking in Modified 9cr-1mo Steel Weld Joint.
- Laiarinandrasana, L., Kabiri, M. R. and Reytier, M.**, (2006), Effect of Specimen Geometries on the C* Versus Da/Dt Master Curve for Type 316l Stainless Steel, *Engineering Fracture Mechanics*, 73, 726-737.
- Landes, J. D. and Schwalbe, K.-H.**, (2004), An Analysis of Creep Deformation Parameters. Part 1: Background, *Engineering Fracture Mechanics*, 71, 2449-2461.
- Le Mat Hamata, N. and Shibli, I. A.**, (2001), Creep Crack Growth of Seam-Welded P22 and P91 Pipes with Artificial Defects. Part I. Experimental

- Study and Post-Test Metallography, *International Journal of Pressure Vessels and Piping*, 78, 819-826.
- Ling, X., Tu, S.-T. and Gong, J.-M.**, (2000), Damage Mechanics Considerations for Life Extension of High-Temperature Components, *Journal of Pressure Vessel Technology*, 122, 174-179.
- Liu, Y. and Murakami, S.**, (1998), Damage Localization of Conventional Creep Damage Models and Proposition of a New Model for Creep Damage Analysis, *JSME International Journal* 41, 57-65.
- Nikbin, K. M.**, (2009), Predicting Creep and Creep/Fatigue Crack Initiation and Growth for Virtual Testing and Life Assessment of Components, *Virtual Testing and Predictive Modeling*.
- Ogata, T., Sakai, T. and Yaguchi, M.**, (2009), Damage Characterization of a P91 Steel Weldment under Uniaxial and Multiaxial Creep, *Materials Science and Engineering: A*, 510-511, 238-243.
- Ohgami, M., Naoi, H., Kinbara, S., Mimura, H., Ikemoto, T. and Fujita, T.**, (1997), Development of 9crw Tube, Pipe and Frogging for Ultra Supercritical Power Plant Boilers. *Nippon Steel Technical Report No. 72*.
- P. Jason Dobson, P.**, (2006), Why New U.S. Supercritical Units Should Consider T/P92 Piping. Cummins & Barnard Inc.
- Park, Y. K., Kim, K. S., Chung, Y. K. and Park, J. J.**, (2001), Creep Crack Growth in X20crmov 12 1 Steel and Its Weld Joint, *Journal of Pressure Vessel Technology*, 123, 191-197.
- Penny, R. K. and Marriott, D. L.**, (1995), *Design for Creep*, London, Chapman & Hall.
- Perrin, I. and Hayhurst, D.**, (1996), Creep Constitutive Equations for a 0.5cr–0.5mo–0.25v Ferritic Steel in the Temperature Range 600–675°C, *The Journal of Strain Analysis for Engineering Design*, 31, 299-314.
- Perrin, I. J. and Hayhurst, D. R.**, (1999), Continuum Damage Mechanics Analyses of Type Iv Creep Failure in Ferritic Steel Crossweld Specimens, *International Journal of Pressure Vessels and Piping*, 76, 599-617.
- Rice, J. R.**, (1968), A Path Independent Integral and the Approximate Analysis of Stress Concentration by Notches and Cracks *Journal of applied Mechanics* 35, 7.
- Saha, P. K.**, (2003), Comparing Materials for High-Temperature Steam Piping; the Use of X20 and P91 in Power Stations.

- Seliger, P. and Gampe, U.**, (2002), Life Assessment of Creep Exposed Components, New Challenges for Condition Monitoring of 9cr Steels, *Power Plants: Operation, Maintenance and Material Issues, OMMI*, 1.
- Shibli, I. A. and Le Mat Hamata, N.**, (2001), Creep Crack Growth in P22 and P91 Welds -- Overview from Sota and Hida Projects, *International Journal of Pressure Vessels and Piping*, 78, 785-793.
- Sim, R. G.**, (1970), Reference Stress Concepts in the Analysis of Structures During Creep, *International Journal of Mechanical Sciences*, 12, 561-573.
- Smith, D. J., Walker, N. S. and Kimmins, S. T.**, (2003), Type Iv Creep Cavity Accumulation and Failure in Steel Welds, *International Journal of Pressure Vessels and Piping*, 80, 617-627.
- Storesund, J. and Tu, S. T.**, (1995), Geometrical Effect on Creep in Cross Weld Specimens, *International Journal of Pressure Vessels and Piping*, 62, 179-193.
- Sugiura, R., Toshimitsu Yokobori Jr, A., Suzuki, K. and Tabuchi, M.**, (2010), Characterization of Incubation Time on Creep Crack Growth for Weldments of P92, *Engineering Fracture Mechanics*, 77, 3053-3065.
- Sun, W., Hyde, T. H., Becker, A. A. and Williams, J. A.**, (2000), Comparison of the Creep and Damage Failure Prediction of the New, Service-Aged and Repaired Thick-Walled Circumferential Crmov Pipe Welds Using Material Properties at 6408c, *International Journal of Pressure Vessels and Piping*, 77, 9.
- Tabuchi, M., Watanabe, T., Kubo, K., Matsui, M., Kinugawa, J. and Abe, F.**, (2001), Creep Crack Growth Behavior in the Haz of Weldments of W Containing High Cr Steel, *International Journal of Pressure Vessels and Piping*, 78, 779-784.
- Tabuchi, M., Yokobori, A. T., Sugiura, R., Yatomi, M., Fuji, A. and Kobayashi, K.**, (2009), Results of Japanese Round Robin Program for Creep Crack Growth Using Gr.92 Steel Welds. *WELDS Sanibel Harbour Resort & Spa, Fort Myers, Florida, USA*.
- Tabuchi, M., Yokobori Jr, A. T., Sugiura, R., Yatomi, M., Fuji, A. and Kobayashi, K.**, (2010), Results of a Japanese Round Robin Program for Creep Crack Growth Using Gr.92 Steel Welds, *Engineering Fracture Mechanics*, In Press, Corrected Proof.
- Tu, S. T.**, (2002), Creep Behavior of Crack near Bi-Material Interface Characterized by Integral Parameters, *Theoretical and Applied Fracture Mechanics*, 38, 203-209.

- Vaillant, J. C., Vandenberghe, B., Hahn, B., Heuser, H. and Jochum, C.,** (2008), T/P23, 24, 911 and 92: New Grades for Advanced Coal-Fired Power Plants--Properties and Experience, *International Journal of Pressure Vessels and Piping*, 85, 38-46.
- Viswanathan, V., Purgert, R. and Rawls, P.,** (2008), Coal-Fired Power Materials.
- Wang, X., Shi, Z., Pan, Q.-G. and Wu, H.-L.,** (2009), High-Temperature Creep Properties of Fine Grained Heat-Affected Zone in P92 Weldment, *Transactions of Nonferrous Metals Society of China*, 19, s772-s775.
- Wilshire, B. and Owen, D. R. J.,** (1983), *Engineering Approaches to High Temperature Design : Recent Advances in Creep and Fracture of Engineering Materials and Structures 2*, Swansea, Pineridge press,1983.
- Xia, L., Becker, A. A. and Hyde, T. H.,** (1998), An Assessment of the C* and K_i Parameters for Predicting Creep Crack Growth in a Ni-Base Superalloy (Waspaloy) at 700 °C, *International Journal of Fracture*, 92, 39-54.
- Yamamoto, M., Miura, N. and Ogata, T.,** (2009), Effect of Constraint on Creep Crack Propagation of Mod. 9cr-1mo Steel Weld Joint. *ASME Pressure Vessels and Piping Division Conference*. Prague, Czech Republic, ASME.
- Yamamoto, M., Miura, N. and Ogata, T.,** (2010), Applicability of C* Parameter in Assessing Type Iv Creep Cracking in Mod. 9cr-1mo Steel Welded Joint, *Engineering Fracture Mechanics*, In Press, Corrected Proof.
- Yatomi, M., Nikbin, K. M. and O'dowd, N. P.,** (2003), Creep Crack Growth Prediction Using a Damage Based Approach, *International Journal of Pressure Vessels and Piping*, 80, 10.
- Yokobori, A. T.,** (1999), Difference in the Creep and Creep Crack Growth Behaviour between Creep Ductile and Brittle Materials, *Engineering Fracture Mechanics*, 62, 61-78.
- Zhao, L. G., Tong, J. and Byrne, J.,** (2001), Finite Element Simulation of Creep-Crack Growth in a Nickel Base Superalloy, *Engineering Fracture Mechanics*, 68, 1157-1170.

APPENDICES

Appendix A

Derivation of the uniaxial form of the damage models

A.1. Kachanov model

The multiaxial form of Kachanov model is given by

$$\frac{d\varepsilon_{ij}^c}{dt} = \frac{3}{2} A \left(\frac{\sigma_{eq}}{1-\omega} \right)^n \frac{S_{ij}}{\sigma_{eq}} t^m \quad (\text{A-1})$$

where S_{ij} is the deviatoric stress that is given by

$$S_{ij} = \sigma_{ij} - \delta_{ij} \sigma_m \quad (\text{A-2})$$

where

σ_{ij} is the stress tensor and δ_{ij} is the Kronecker delta where

$$\delta_{ij} = \begin{cases} 1 & i = j \\ 0 & i \neq j \end{cases}$$

and σ_m is the hydrostatic stress where

$$\sigma_m = \frac{\sigma_{11} + \sigma_{22} + \sigma_{33}}{3} \quad (\text{A-3})$$

For the uniaxial form of the Kachanov damage equations, assume $\sigma_{22} = \sigma_{33} = \sigma_{12} = \sigma_{23} = \sigma_{13} = 0$ and $\sigma_{11} = \sigma_{eq} \neq 0$.

Then the uniaxial form of Kachanov model can be given by

$$\frac{d\varepsilon_{11}^c}{dt} = \frac{3}{2} A \left(\frac{\sigma_{eq}}{1-\omega} \right)^n \frac{\sigma_{11} - \sigma_m}{\sigma_{eq}} t^m$$

$$\text{where } \sigma_{eq} = \sqrt{\frac{1}{2} [(\sigma_1 - \sigma_2)^2 + (\sigma_1 - \sigma_3)^2 + (\sigma_2 - \sigma_3)^2]}$$

Substitute equation (A-3) gives

$$\frac{d\varepsilon_{11}^c}{dt} = \frac{3}{2} A \left(\frac{\sigma_{eq}}{1-\omega} \right)^n \frac{\sigma_{11} - \frac{\sigma_{11} + \sigma_{22} + \sigma_{33}}{3}}{\sigma_{eq}} t^m \quad \text{where } \sigma_{22} = \sigma_{33} = 0$$

i.e.

$$\frac{d\varepsilon_{11}^c}{dt} = \frac{3}{2} A \left(\frac{\sigma_{eq}}{1-\omega} \right)^n \frac{2\sigma_{11}}{3\sigma_{eq}} t^m \quad \text{where } \sigma_{11} = \sigma_{eq} \text{ and } \varepsilon_{11}^c = \varepsilon_{eq}^c = \varepsilon^c.$$

So the uniaxial form of the Kachanov damage model is given by

$$\frac{d\varepsilon^c}{dt} = A \left(\frac{\sigma}{1-\omega} \right)^n t^m \quad (\text{A-4})$$

A.2. Liu and Murakami model

The multiaxial form of the Liu and Murakami model is given by:-

$$\frac{d\varepsilon_{ij}^c}{dt} = \frac{3}{2} A \sigma_{eq}^{n-1} S_{ij} \text{Exp} \left[\frac{2(n+1)}{\pi \sqrt{1+3/n}} \left(\frac{\sigma_1}{\sigma_{eq}} \right)^2 \omega^{3/2} \right] \quad (\text{A-5})$$

where S_{ij} is the deviatoric stress.

By substituting the values of deviatoric stress, S_{ij} , and the hydrostatic stress, σ_m , as shown in equation (A-2) and equation (A-3), respectively,

$$\text{then } S_{11} = \sigma_{11} - \frac{\sigma_{11} + \sigma_{22} + \sigma_{33}}{3} \text{ and } \sigma_{22} = \sigma_{33} = 0,$$

i.e.

$$S_{11} = \frac{2\sigma_{11}}{3} = \frac{2\sigma_1}{3} = \frac{2\sigma_{eq}}{3}. \quad \text{where } \sigma_{11} = \sigma_1 = \sigma_{eq}$$

Then the uniaxial form of Liu and Murakami damage model is given by

$$\frac{d\varepsilon_{11}^c}{dt} = \frac{3}{2} A \sigma_{eq}^{n-1} \frac{2\sigma_{eq}}{3} \text{Exp} \left[\frac{2(n+1)}{\pi\sqrt{1+3/n}} \left(\frac{\sigma_{eq}}{\sigma_{eq}} \right)^2 \omega^{3/2} \right] \quad (\text{A-6})$$

i.e.

$$\frac{d\varepsilon^c}{dt} = A \sigma^n \text{Exp} \left[\frac{2(n+1)}{\pi\sqrt{1+3/n}} \omega^{3/2} \right] \quad (\text{A-7})$$

Appendix B

Numerical error in FE CT damage analyses

B.1. System error code 144

For CCG FE analyses, some analyses aborted issuing an error message which is known, in ABAQUS, by "System error code 144". It was found that, a numerical error caused the analyses to abort. This numerical error was caused by raising negative numbers to a fraction; this lead to an imaginary component. In the CCG FE analyses, using CT models, the rupture stress had negative values at some integration points at the end of un-cracked ligament, where the maximum stress is negative (i.e. compression). When the rupture stress (SRUP) is a negative value and raised to X , a material constant which is usually a fraction number, the result is then a complex number. This causes the analyses to abort.

Within the CREEP subroutine (given in Appendix B.2.), the damage increment is defined as:

$$DW = B*(1.0 - \exp(-q2))*(SRUP**X) * ((\exp(q2*W))/q2)**TT**M*DTIME$$

where DW is the damage increment; B, PHI, X and M are material constants; TT is the total analyses time; DTIME is the time increment; W is the damage; and SRUP is the rupture stress which is given by:

$$SRUP = ALPHA*SI+ (1.0-ALPHA)*QTILD$$

where ALPHA is a material constant; SI is the maximum principal stress and QTILD is the equivalent stress.

To avoid the negative values of the rupture stress, one of the the following suggestions can be used:

- 1) **If the rupture stress is negative, ignore the damage calculations at that point.** This can be done by adding an **IF** statement after the rupture stress calculation statement as follows:

```
SRUP = ALPHA*SI+ (1.0-ALPHA)*QTILD
```

```
IF (SRUP.LT.0.0) go to 60
```

```
-----
```

```
-----
```

```
-----
```

```
60  Return
```

```
End
```

- 2) **Consider only the positive values of the rupture stress.** This can be done by applying the **ABSOLUTE** function to the rupture stress as follows:

```
SRUP = ABS (ALPHA*SI+ (1.0-ALPHA)*QTILD)
```

```
-----
```

```
-----
```

```
-----
```

```
Return
```

```
End
```

- 3) **Define the rupture stress as a complex number.** This can be done by defining the parameter **SRUP** as complex in the parameter declaration section at the beginning of the subroutine as follows:

```

Complex  SRUP
REAL    N, M, X, q2, ALPHA, WMAX, I
REAL*8  TT, A, B, SI, DW, W
    
```

All of these modifications allow the analysis to run without interruption by numerical errors.

B.2. CREEP Subroutine

The following is the CREEP subroutine based on the Liu and Murakami damage model and written in FORTRAN.

```

SUBROUTINE CREEP (DECRA, DESWA, STATEV, SERD, ECO, ESWO, P, QTILD,
1 TEMP, DTEMP, PREDEF, DPRED, TIME, DTIME, CMNAME, LEXIMP, LEND,
2 COORDS, NSTATV, NOEL, NPT, LAYER, KSPT, KSTEP, KINC)
INCLUDE 'ABA_PARAM.INC'
CHARACTER*80 CMNAME
REAL N, M, X, q2, ALPHA, WMAX, I
REAL*8 TT, A, B, SI, DW, W
REAL*8 SRUP, L, V
DIMENSION DECRA(5), DESWA(5), STATEV(*), PREDEF(*), DPRED(*)
1 TIME(2), COORDS(*), EC(2), ESW(2)

DO I=1, 5
DECRA(I) = 0.0D0
DESWA(I) = 0.0D0
ENDDO

IF (CMNAME.EQ.'"WM"') goto 20
IF (CMNAME.EQ.'"PM"') goto 30
IF (CMNAME.EQ.'"HAZ"') goto 40

20 A=1.37e-20
N=7.224
X=8.1457
B=6.427e-20
q2=5.0
ALPHA=0.81
M=-0.0361
GOTO 50

30 A = 1.09e-20
    
```

```

N = 8.4617
X = 6.789
B = 2.95162e-16
q2 = 3.2
ALPHA = 0.3125
M = -4.754e-4
GOTO 50
40 A = 2.3e-20
N = 8.462
X = 5.502
B = 1.2703e-13
q2 = 2.8
ALPHA = 0.52
M = 0
GOTO 50
WMAX = 0.99

50 IF (KINC.EQ.1.AND.KSTEP.EQ.2) THEN
TATEV(1) = 0.0
ENDIF
W = STATEV(1)
TT = TIME(2)
IF (LEND.EQ.0) THEN
TT = TIME(2)-DTIME
ENDIF

SI = STATEV(2)

IF (LEXIMP.EQ.1) THEN

DECRA(5) = (A*N*QTILD**(N-1.0))*
2exp ((2.0*(N+1.0))/(3.143*sqrt(1.0+3.0/N))*W**1.5)*TT**M*DTIME

ENDIF

SRUP = ALPHA*SI + (1.0-ALPHA)*QTILD

IF (SRUP.LT.0.0) goto 60

DW=B*(1.0 - exp (-q2))*(SRUP**X)*((exp (q2*W))/q2)*TT**M*DTIME

W=W+DW

DECRA(1) = A*QTILD**N*exp((2.0*(N+1.0))/(3.143*sqrt(1.0+3.0/N))*
2W**1.5)*TT**M*DTIME

IF(W.GE.WMAX)W=WMAX

STATEV(1)=W

```

```
STATEV(2)=SI  
STATEV(3)=SRUP
```

```
60 RETURN  
END
```

```
C*****  
SUBROUTINE USDFLD (FIELD, STATEV, PNEWDT, DIRECT, T, CELENT,  
1 TIME, DTIME, CMNAME, ORNAME, NFIELD, NSTATV, NOEL, NPT, LAYER,  
2 KSPT, KSTEP, KINC, NDI, NSHR, COORD, JMAC, JMATYP,  
3 MATLAYO, LACCFLA)  
INCLUDE 'ABA_PARAM.INC'  
CHARACTER*80 CMNAME, ORNAME  
CHARACTER*3 FLGRAY(15)  
DIMENSION FIELD(NFIELD), STATEV(NSTATV), DIRECT(3,3),  
1 T(3,3), TIME(2)  
DIMENSION ARRAY(15), JARRAY(15), JMAC(*), JMATYP(*), COORD(*)  
  
IF (KINC.EQ.1) THEN  
    FIELD(1) = 0.0  
    ELSEIF(STATEV(1)>=0.0) THEN  
FIELD(1) = STATEV(1)  
  
ELSE  
    FIELD(1) = 0.0  
    END IF  
  
CALL GETVRM('SP',ARRAY,JARRAY,FLGRAY,JRCD,JMAC,JMATYP,  
1 MATLAYO,LACCFLA)  
  
STATEV(2) = ARRAY(3)  
  
RETURN  
END
```

Appendix C

Load application to the FE CT models

For the CT models used in this research, the load and the boundary conditions were applied to the centre of the load hole and transmitted to the specimens via a linkage between that centre and the nodes of the hole. This linkage can be done by creating a pin whose centre coincides with the centre of the hole and its circumference contacts the inner surface of the hole or by using multiple points constraints (mpc) option, which is available in ABAQUS.

C.1. Rigid pin

An analytical rigid shell was modelled as a pin with radius the same as the load hole itself. This pin was modelled as an individual part and assembled with the CT in one assembly. A reference point was assigned for this analytical body and connected to it forming a rigid body. A contact pair was then created between that rigid body and the nodes of the inner surface of the hole. As the load or the boundary conditions are applied to the reference point, they transmit directly to specimen body. Fig. C-1 shows the assembly of the rigid pin and the CT specimen.

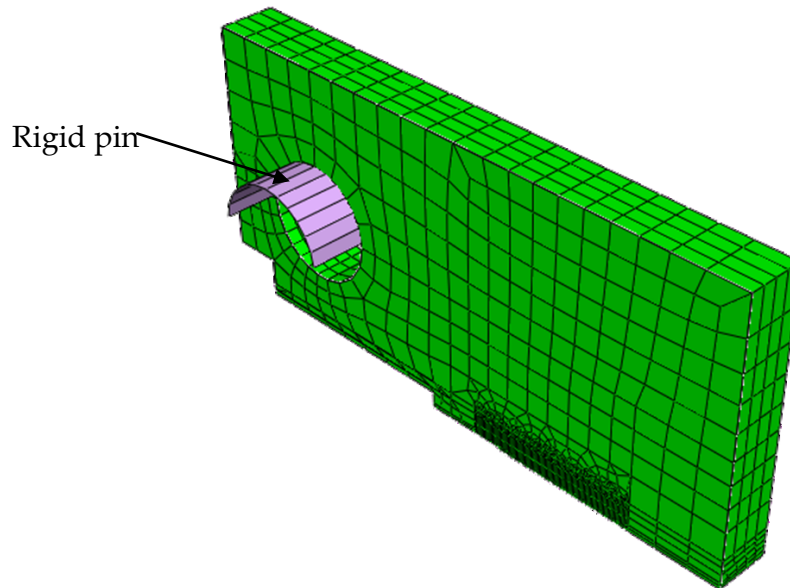


Fig. C-1: Modelling the load pin as a rigid body.

C.2. Multiple point constraints (mpc)

The second option to apply load and boundary conditions to CT models is the use of the multiple point constraints (mpc) facility, available in ABAQUS. The centre of the load hole was selected as a datum point. The nodes of upper-half of the upper hole is defined as a node set. In the input file, the selected datum point was connected to that node set using the *mpc key word. This line of code appears like

```
*mpc
```

```
link, pin hole node set, datum point
```

```
*End Assembly
```

This means that the "pin hole node set" follows the motion of "datum point". In such case the loads and/or the boundary conditions are applied to the datum point. Fig. C-2 shows the CT model with the load hole linked to the hole centre.

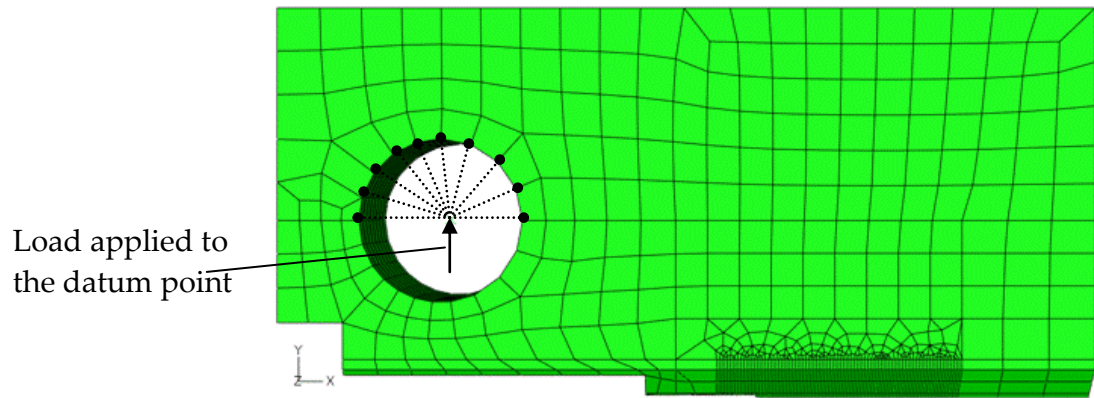


Fig. C-2: Multiple points constraint to link the hole centre to the hole nodes.

Author's Biography



Mohammed Saber was born in Mansoura, Egypt, in 1977. He graduated from the Department of Production and Mechanical Design, Mansoura University, Egypt, in 2000. From 2000 to 2003, he was working as a mechanical engineer in a naval shipyard. From 2003 to 2010, Mohammed was working as an academic for the Faculty of Engineering at Port Said campus, Suez Canal University, Egypt. Since 2010, the Port Said campus has become an independent university, named Port Said University, and since then Mohammed is working for the Port Said University, Egypt. In 2007, Mohammed was awarded a governmental scholarship to study PhD at the University of Nottingham, UK, and he got his degree in 2011.

Mohammed can be contacted via his email address: mssaber77@yahoo.com or via his facebook account: [facebook.com/mssaber77](https://www.facebook.com/mssaber77)